UNIVERSITY OF CALIFORNIA
SANTA CRUZ

SMALL POLARON CONDUCTION IN TRANSITION METAL OXIDES AND EXCITED STATE RECOMBINATION IN TWO-DIMENSIONAL MATERIALS FROM FIRST-PRINCIPLES

A dissertation submitted in partial satisfaction of the
requirements for the degree of

DOCTOR OF PHILOSOPHY

in

PHYSICS

by

Tyler J. Smart

June 2021

The Dissertation of Tyler J. Smart
is approved:

Prof. Frank Bridges, Chair

Prof. Yuan Ping

Prof. Yat Li

Quentin Williams
Interim Vice Provost and Dean of Graduate Studies

Table of Contents

List of Figures

List of Tables

Abstract

Small Polaron Conduction in Transition Metal Oxides and Excited State Recombination in Two-Dimensional Materials from First-Principles

by

Tyler J. Smart

State-of-the-art first-principles calculations are implemented and utilized in order to optimize or give insight into material properties for various technologies and applications. These applications, and therefore the research, have two primary focuses. The first is energy conversion and storage using transition metal oxides and the second is quantum defects in two-dimensional materials as qubits and single photon emitters.

Regarding the first, the limitation of transition metal oxides is in their poor carrier conduction due to the formation of small polarons. Here I have developed our understanding of how to compute small polaron properties such as optical absorption, polaron transport, and carrier concentrations, especially in the presence of dopants and defects. Polaron transport has been investigated under both macroscopic (dielectric continuum) and microscopic (explicit hopping) models within small polaron theory. Primary focus has been given to the Fe_2O_3 system, where I have extensively researched polaron formation in the presence of many intrinsic defects and external dopants. Furthermore, I have discovered a novel form of dopant clustering mediated by small polaron and dopant interactions which has been experimentally validated. Outside of Fe_2O_3, I have demonstrated the origin of the optical gap in Co_3O_4 is due to small hole polaron formation, and in CuO I have detailed the formation and transport of spin polarons. Lastly, in various other systems (*e.g.* $BiFeO_3$ and $LaFeO_3$) we have provided insight on how

dopants impact polaron properties which are relevant to experimentally observed enhancements.

For the second research focus, the design of single photon emitters and spin-based qubits in hexagonal boron nitride is presented. Here, both static and dynamic properties are computed for the first time for defects in two-dimensional materials. For static properties, we have developed methods to deal with more accurate electron correlation beyond standard density functional theory (e.g. GW approximation and hybrid functional) and charged defect interaction for systems with highly anisotropic and weak dielectric screening. I have also implemented computing the zero-field splitting of $S \geq 1$ systems, an essential quantity in defect based-qubit systems like NV center in diamond. For dynamical properties, we included exciton-defect coupling for radiative lifetime from solving the Bethe-Salpeter equation and electron-phonon interactions for nonradiative lifetime. In addition, I have implemented computing intersystem crossing (necessary for spin initialization and readout) with spin-orbit coupling and electron-phonon interaction. With these computed static and dynamical properties, we are able to predict spin qubits read-out efficiency and new quantum spin defect systems in hexagonal boron nitride which can be potential candidates for spin-based quantum technologies.

To my parents,

Steven and Penelope Smart.

Acknowledgments

The research presented here is not the result of my effort alone. Here I make my best attempt to acknowledge those whose impact was pivotal in bringing this research to fruition.

First, and foremost, I would like to thank my advisor Prof. Yuan Ping. Her passion, wisdom, and creativity are unparalleled, I am extremely grateful for all that she has taught me in these five years. I am thankful to Dr. Feng Wu, who was a great mentor to me, his patience and excitement in sharing his knowledge was very inspiring to me. I would also like to thank Mingpeng Chen, who not only provided me incredible insight into experiment but also was an amazing friend to share a meal with. I would like to thank Kejun Li, who I worked on various two-dimensional material projects and Valentin Urena Baltazar, who I worked with on various transition metal oxide projects. To the entire Ping Group I am thankful for the many conversations we had in which I learned so much.

Next, I thank several collaborators outside of the Ping Group. Dr. Tuan Anh Pham, was an amazing mentor to me, going beyond just research advice and often providing me with invaluable life and career advice. Dr. Tadashi Ogitsu and him had a huge impact in my PhD, giving me the opportunity to work at LLNL. I am thankful to Dr. Marco Govoni at Argonne National Laboratory for facilitating the opportunity to be a part of the Quantum Information Science and Engineering Network. I am thankful to several experimentalist whose discussions and collaborations with I learned a lot from including, but not limited to, Prof. Kyoung-Shin Choi, Prof. Yat Li, Prof. Shaowei Chen, Prof. Frank 'Bud' Bridges, and also their graduate students such as, Dr. Allison Cardiel, Dr. Tianyi Kou, Dr. Bingzhang Lu.

I am thankful to my committee members, Prof. Frank 'Bud' Bridges, Prof.

Yat Li, and Prof. Yuan Ping, in particular Bud for agreeing to be the chair and my department advisor. There are also many members of the physics department who were invaluable to my PhD experience. Specifically, I am thankful to Dr. Ben Miller, Dr. Katie Hellier, and Prof. Stephano Profumo who provided me with a much needed guidance during my PhD. I thank Carey Williams and all the students in my year, for the fun times and terrific friendships.

I am thankful to the physics department faculty at Humboldt State University who taught me physics such as Prof. Monty Mola, Prof. Wes Blivens, and Prof. C.D. Hoyle. I still remember the day I decided I wanted to major in Physics from a short discussion with Monty.

Lastly, I am thankful to my family. My mother and father, who taught me that trying your best is the best way to enjoy life. My wife, Channey for being my best friend, and the ultimate source of wisdom and support. And my son Alden, who made life enjoyable and fun, even as I finished out the PhD during the coronavirus pandemic.

-TJS :)

Chapter 1

Introduction

Understanding and developing material properties is essential to solving some of societies greatest concerns. One such concern of particular interest is the desperate need for renewable energy resources. Advancing novel technologies for energy harvesting, conversion, and storage is critical to ensure the economic viability of U.S. energy and chemical industries. [1, 2] For many of these technologies, a detailed understanding of chemical processes at electrochemical interfaces is essential. For instance, optimizing water splitting reactions at the semiconductor-water interface in photoelectrochemical cells is key for improving the device efficiency and stability for generating hydrogen fuel from water and sunlight. [3] Alternatively, the causes of oxidation and corrosion at the interface can be illuminated via chemical degradation processes. [4] Last but not least, understanding the relationship between reactivity and electronic properties of liquid electrolytes at the interface with electrode materials is also one of the prerequisites for manipulating the electrochemical stability of electrode-electrolyte interfaces in ion batteries and supercapacitors. [5]

However, the development of renewable energy resources is only a single example of the type of problem in which material design is crucial. As another

example, material science is unsurprisingly at the very heart of developing brand new technologies, particularly those in the realm of quantum information science. The development of innovative quantum technologies is immanent and will make broad impacts on our national technology sector. [6] For example, point defects in two-dimensional materials are hosts for emerging quantum phenomena such as single-photon emitters and defect-based spin qubits. Both of these technologies necessitate the development of material design.

With the intention to expand these fields, the role of computational material science has grown immensely alongside ever-growing supercomputing facilities. These facilities enable calculations of large-scale simulations which provide improved theoretical understanding of these aforementioned fields. In particular, first-principles simulations allow us to better understand the quantum mechanical nature of materials, which is an essential part of their application. These simulations have proven to be pivotal in the evolution of many fields all the way from renewable energy to quantum technology.

As such, my research in modeling materials from first-principles calculations is bifurcated into two branches of motivation: 1. renewable energy and energy conversion with transition metal oxides (TMOs) and 2. quantum information sciences in two-dimensional (2D) materials. In this dissertation I will discuss my research within both of these fields by covering the motivation behind my research, discussing progress achieved thus far and finally how these efforts have culminated or are being extended.

1.1 Density Functional Theory

1.1.1 Background

In the interrelated field of physics, chemistry, and material science, there is no greater problem than that of the electron. The electron can determine so many of the properties of a material, from its ability to absorb light, conduct electrical currents, thermally or electrically insulate, and so much more. Hence, in order to have a grasp on fundamental material properties we must understand the electron and the quantum mechanical nature by which it lives by solving the multi-electron Schrödinger equation (SE). The multi-electron problem essentially refers to any problem involving interactions between more than one electron, often in an external field. In principle, the problem is well understood in the formalism of Schrödinger quantum mechanics, where the Hamiltonian of the multi-electron system within the Born-Oppenheimer approximation (rigid ion approximation) is given by:

$$\left[-\frac{\hbar^2}{2m}\sum_i \nabla_i^2 + \sum_i V_{ext}(\mathbf{r}_i) + \frac{1}{2}\sum_{i\neq j}\frac{e^2}{|\mathbf{r}_i - \mathbf{r}_j|}\right]\Psi(\mathbf{r}_1, \mathbf{r}_2, \ldots \mathbf{r}_N) = E\ \Psi(\mathbf{r}_1, \mathbf{r}_2, \ldots \mathbf{r}_N) \tag{1.1}$$

However, this has its immediate challenges. Namely, even the classical (non-quantum) three body problem has no general solution! Clearly a non-analytical approach is needed. Such a non-analytical approach is discussed below and is the foundation of all density functional theory (DFT) calculations.

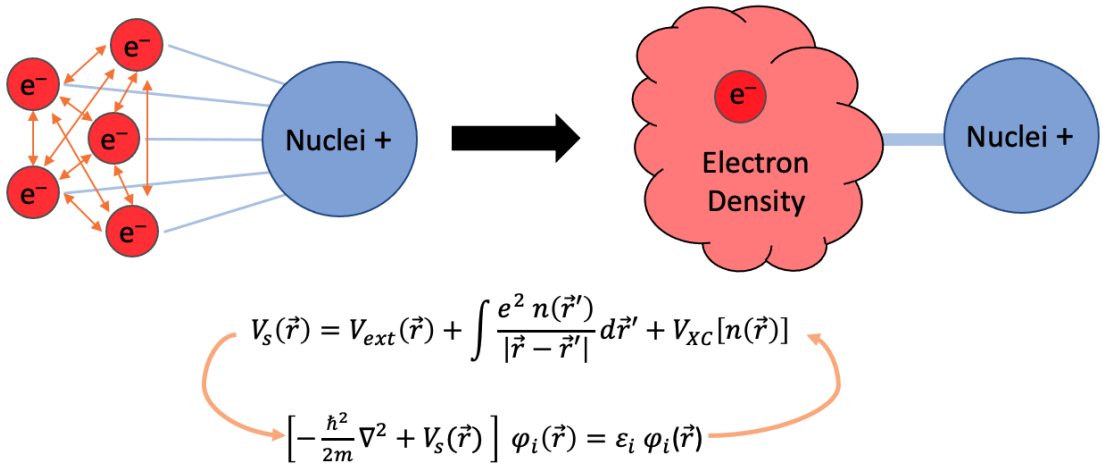

Figure 1.1: Density functional theory is a mean field approach which replaces the many-electron problem with one of a single electron interacting with a mean-field electron density at a significantly reduced complexity while maintaining remarkable predictive power.

1.1.2 Hohenberg Kohn and Sham

Typically, one may envision that given an external potential $V_{ext}(\mathbf{r})$, one may solve the multi-electron SE as in Eq. 1.1, determining all of the eigenstates of the SE, $\Psi_i(\mathbf{r})$. This would include a ground state $\Psi_0(\mathbf{r})$ wavefunction and corresponding ground-state density $n_0(\mathbf{r})$. This process logically demonstrates that given an external potential, a unique ground state density can be found ($V_{ext}(\mathbf{r}) \Rightarrow n_0(\mathbf{r})$). Hohenberg and Kohn's first theorem, [7] demonstrates that the reverse is also true, namely that given a ground state density, one can find (up to a constant), a unique external potential, *e.g.* $n_0(\mathbf{r}) \Rightarrow V_{ext}(\mathbf{r})$. In other words, all properties of the system are completely determined by the ground state density. Secondly, Hohenberg and Kohn defined that a universal functional of the energy $E[n]$ can be constructed for any external potential. And the ground state density is a global minimum of this functional, $E[n] \geq E[n_0]$.

Following these theorems by Hohenberg and Kohn, Kohn and Sham were able

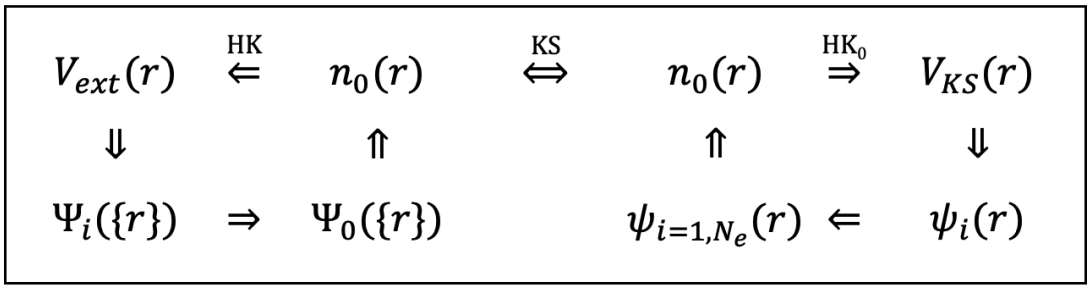

$$H_{KS}\,\psi_i(r) = \varepsilon_i\,\psi_i(r)$$

$$H_{KS} = -\frac{1}{2}\nabla^2 + V_{KS}(r) \quad V_{KS}(r) = V_{ext}(r) + V_H(r) + V_{xc}(r)$$

Figure 1.2: Top left, the true multi-particle potential and wavefunctions are replaced by an auxiliary single-particle system, as in the top right. At the end the Kohn-Sham method involves solving the Schrödinger equation for the auxiliary Hamiltonian (H_{KS}) as defined in the bottom panel. Adapted from Ref. [8].

to demonstrate the very basis of density functional theory. [9] Namely, they proved that there exists an auxiliary single-particle Hamiltonian (H_{KS}) with the exact same electron density ($n_0(\mathbf{r})$) as would be obtained by solving the multi-particle system. Schematically the theorems of Hohenberg and Kohn (HK) as well as Kohn and Sham (KS) are shown in Figure 1.2.

1.1.3 Self-Consistent Approach

Today, there are many density functional theory (DFT) codes which are built upon the theory presented by Hohenberg, Kohn, and Sham. The exact procedure is shown in Figure 1.3. Specifically, an initial guess of the electron density is constructed. Here a basis set of gaussians (for molecular systems) or plane waves (for crystal systems) is constructed to represent the density and make the computation efficient and cheap. The typical guess of the electron density may involve a com-

pletely random guess or one utilizing a linear combination of atomic orbitals (or both). From this initial guess, the effective potential can be constructed, which is then solved by typical diagonalization methods such as Davidson or conjugate gradient. This will yield eigenfunctions $\psi_i(\mathbf{r})$ and a new electron density $n(\mathbf{r})$. This electron density can be checked for self consistency (for example do they produce a similar total energy) and if not then they are mixed to create a new guess. Once self-consistency is reached we can obtain energy, forces, stress, eigenvalues, and so much more from the DFT approach.

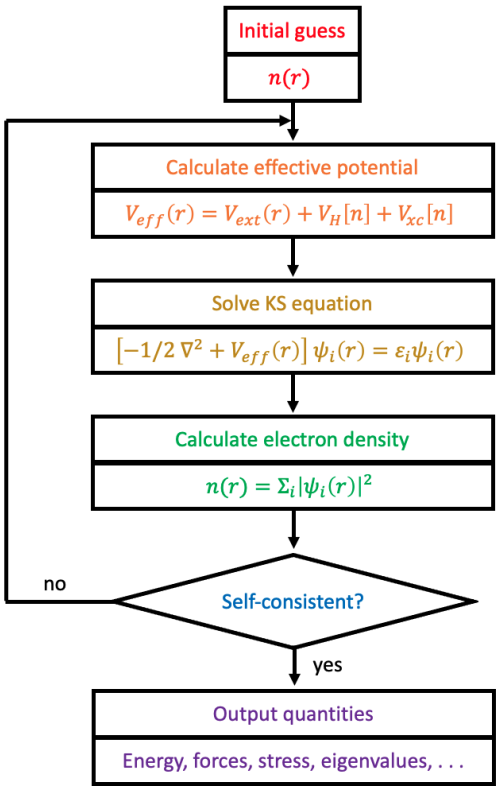

Figure 1.3: The procedure of the self-consistent loop implemented in various density functional theory codes existing today.

1.1.4 Electron-Electron interactions

In the auxiliary approach, there is a single functional component which is expected to capture the full many-body interacting electron problem, the exchange-correlation energy $E_{xc}[n]$. And much of the success of density functional theory must be paid to the success in finding an approximate exchange-correlation functional which yields reliable results. To cover all the many methods of exchange and correlation would be an unbearably difficult task. In practice, a very popular method is that of the local density approximation (LDA) which uses the approximate form of exchange-correlation one can obtain for a homogeneous electron gas. Alternatively, the PBE functional is an immensely popular GGA (generalized gradient approximation) which is widely used today. [10]

The shortcoming of LDA and GGA, comes for systems where the electrons in the system deviate significantly from that of an electron gas. For example, transition metal oxides, which possess $3d$ orbitals exhibit strong correlation, and have been more successfully treated by including a Hubbard correction. [11]

$$E_{\mathrm{DFT+U}} = E_{\mathrm{DFT}} + \frac{U_{\mathrm{eff}}}{2} \sum_{I,\sigma} \sum_{i} \lambda_i^{I\sigma}(1 - \lambda_i^{I\sigma}) \tag{1.2}$$

Here, E_{DFT} is the energy obtained from standard DFT methods which is corrected by the following term which includes the occupation matrix $\lambda_i^{I\sigma}$ (I ranges over all ions, i ranges over $3d$ orbitals and σ is for spin up or down). For example, we have shown that applying a U of 4.3 eV on Fe $3d$ orbitals in Fe_2O_3 yields bandgap, electron localization, hopping barrier, and ionization energies which agree with experiment. [12]

An alternative method, is built upon a mixture of the semi-local PBE exchange-

correlation functional and that of the non-local exact Hartree-Fock exchange:

$$E_x^{HF} = -\frac{1}{2}\sum_{i,j}\int\int \psi_i^*(\mathbf{r}_1)\psi_j^*(\mathbf{r}_2)\frac{1}{r_{12}}\psi_j(\mathbf{r}_1)\psi_i(\mathbf{r}_2)d\mathbf{r}_1 d\mathbf{r}_2 \tag{1.3}$$

A popular and most simple hybrid functional method (PBE0(α)) mixes E_x^{HF} with that obtained from PBE:

$$E_x^{PBE0}(\alpha) = (1-\alpha)E_x^{PBE} + \alpha E_x^{HF}, \tag{1.4}$$

where most commonly $\alpha = 0.25$ (denoted simply PBE0). Other variations of hybrid functionals, including HSE, B3LYP, and B3PW, will be discussed in necessary detail as they pertain to the research in later sections.

More exact methods of including many-body interactions include the GW approximation. In the one-shot G_0W_0 (here all cases will be one-shot, so I will simply write GW instead of explicitly G_0W_0) approach the self energy Σ perturbatively replaces the XC functional obtained in DFT. First the single particle Green's function is constructed:

$$G_0 = \sum_i \frac{\varphi_i(r)\varphi_i^*(r')}{\omega - \varepsilon_i \pm i\eta}, \tag{1.5}$$

where φ_i and ε_i are eigenfunctions and eigenvalues obtained from DFT. Then the screened Coulomb interaction can be obtained where the vertex $\Gamma = 1$, $W = v/(1+\chi_0 v) = \epsilon^{-1}v$. Here the polarizability is obtained directly from the Green's function $P_0 = G_0G_0$. The new self energy is then obtained as $\Sigma = iG_0W_0$, and quasi-particle corrections are obtained from 1^{st} order perturbation theory with $V_p = \Sigma - V_{xc}$.

1.2 Formalism of Charged Defect Formation

The below research takes special interest into the formation of impurities into crystal lattices. These impurities could include native vacancies, interstitials, and antisites but also extrinsic dopants and localized carriers (small polarons will be discussed later). The most fundamental properties of these impurities are their formation energy (how easily the impurity can form in the lattice) and their ionization energy (how easily the impurity changes charge state and contributes electrons or holes). Below an overview is provided on computing formation energies from First-Principles.

1.2.1 Elemental Chemical Potentials

In order to evaluate the formation of atomic impurities the source of the impurities need to be evaluated in the form of a chemical potential. Rather than introduce this notion abstractly, below I present the procedure for obtaining chemical potential energies for the $CsPbBr_3$ compound. The discussion can easily be extended to other cases. For, $CsPbBr_3$ the chemical potential of atomic Cs, Pb, and Br can be evaluated by determining the stability of the parent compound $CsPbBr_3$ against its byproducts. Namely in thermodynamic equilibrium growth conditions, the chemical potentials μ_{Cs}, μ_{Pb} and μ_{Br} must satisfy Eq. 1.6−1.7:

$$\Delta\mu_{\mathrm{Cs}} + \Delta\mu_{\mathrm{Pb}} + 3\Delta\mu_{\mathrm{Br}} = \Delta H_{\mathrm{CsPbBr_3}} \tag{1.6}$$

$$i\Delta\mu_{\mathrm{Cs}} + j\Delta\mu_{\mathrm{Pb}} + k\Delta\mu_{\mathrm{Br}} \leq \Delta H_{\mathrm{Cs}_i\mathrm{Pb}_j\mathrm{Br}_k}, \quad (i,j,k) \in \mathbb{N}. \tag{1.7}$$

Here $\Delta\mu_{\mathrm{X}}$ is the chemical potential of species X referenced to its most stable phase. In Eq. 1.7, $\mathrm{Cs}_i\mathrm{Pb}_j\mathrm{Br}_k$ refers to possible byproducts of $CsPbBr_3$, e.g. Cs, Pb, Br_2, CsBr, $CsBr_3$, $PbBr_2$, Cs_4Pb_9, and Cs_4PbBr_6. From Eq. 1.6−1.7 and

considering each of these byproducts we obtained a phase diagram as shown in the main text Figure 2a. The results are in good agreement with previous reported diagrams for $CsPbBr_3$. [13, 14] More details can be found at `https://github.com/Ping-Group-UCSC/PhaseDiagram` and in particular see the $CsPbBr_3$ tutorial (NOTE: at the time of this writing, this link is only available internally within the Ping Group).

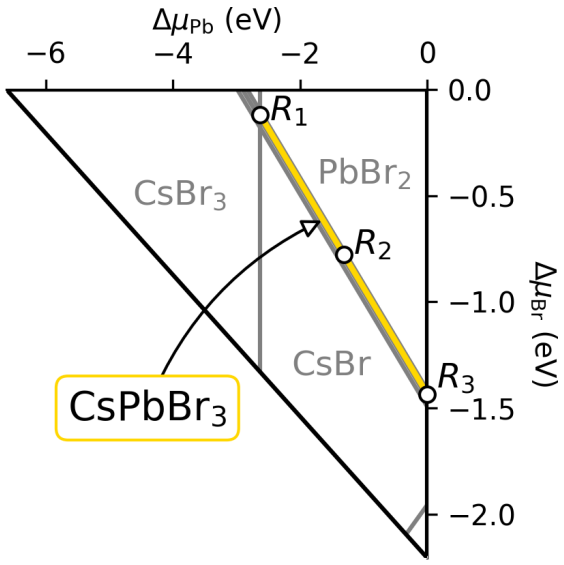

Figure 1.4: Phase diagram of $CsPbBr_3$.

1.2.2 Defect Formation Energy and Ionization Energy

The charge defect formation energy (E_q^f) provides insight into the charge states of dopants providing some insight into the influence on carrier concentration and is given by:

$$E_q^f(X;\varepsilon_F) = E_q(X) - E_{prist} + \sum_i \mu_i \Delta N_i + q\varepsilon_F + \Delta_q, \tag{1.8}$$

where $E_q(X)$ is the total energy of the defect system (X) with charge q, E_{prist} is the total energy of the pristine system, μ_i and ΔN_i are the chemical potential and change in the number of atomic species i, and ε_F is the electron chemical potential. A charged defect correction Δ_q must be computed for charged cell calculations. This correction is computed with the JDFTx code [15] by employing the techniques developed in Ref. [16, 17]. Meanwhile, chemical potentials can be carefully evaluated against the stability of byproduct compounds as detailed above. Finally, the corresponding charge transition levels of the defects can be obtained from the value of ε_F where the stable charge state transitions from q to q'.

$$\epsilon_{q|q'} = \frac{E_q^f - E_{q'}^f}{q' - q} \tag{1.9}$$

Typically, for a semiconductor or insulator the ionization energy of a p-type/n-type dopant is given by the value(s) of its charge transition level(s) referenced to the valence/conduction band edge of the host materials. However, in systems which form small polarons the ionization energy should be referenced to the free polaron state. [12, 18] For example, the free electron small electron polaron level is defined as the $\epsilon_{0|-1}$ transition level in the pristine system.

1.2.3 Defect Concentration

In order to simultaneously consider defect, dopant, and carrier formation, I implemented the procedure of defect concentrations via a self-consistent approach based on charge neutrality. Following the formalism presented in Ref. [19], the

charged defect concentration (c_q) is computed as:

$$c_q(X;\varepsilon_F) = g\exp\Big[-E_q^f(X;\varepsilon_F)/k_BT\Big], \tag{1.10}$$

where g is the degeneracy factor accounting for the internal degrees of freedom of the point defect, k_B is the Boltzmann factor, and T is temperature. In order to maintain neutrality, the introduction of defect X with charge q into the lattice must be compensated by defects of opposing charge or through the generation of free carriers. Specifically charge neutrality must be held:

$$\sum_{X,q} c_q(X;\varepsilon_F) + n_h - n_e = 0, \tag{1.11}$$

where the concentration of free delocalized holes (n_h) and free delocalized electrons (n_e) can be evaluated via:

$$n_e - n_h = \int_{-\infty}^{\infty} dE \frac{D(E)}{1+\exp[(E-\varepsilon_F)/k_BT]}. \tag{1.12}$$

Here $D(E)$ is the electronic density of states of the pristine system. Eq. 1.11 can be evaluated by standard root-finding algorithms to obtain ε_F where charge neutrality is held. Note, for systems where free carriers will localize into small polarons, the formation of free electron small polarons is entered in a similar way to a defect, i.e. with a formation energy. Finally, in order to relate to experimental measurements, concentrations are first computed at a synthesis temperature (T_S) and then charge neutrality is recomputed at room temperature (T_O = 300 K) while fixing the total defect concentration to that obtained at synthesis condition as employed by Ref. [20]. The software computing defect concentrations can be found (for Ping Group members) at `https://github.com/Ping-Group-UCSC/`

`DefectConcentration`.

1.3 Defect Mediated Carrier Recombination

In many fields, properties of carrier dynamics are essential to understand. For example, single-photon emitters (discussed in more detail later) require efficient radiative recombination which must occur at a faster time-scale than those of nonradiative processes. As another example, spin qubits (again will be discussed more later) require intricate arrangements of intersystem crossing in order to ascertain efficient spin polarization for initialization, as well as, photoluminescent contrast for readout. Methods for computing such properties from first-principles are summarized here.

1.3.1 Radiative Recombination

In order to quantitatively study radiative processes, we computed the radiative rate Γ_R from Fermi's Golden Rule and considered the excitonic effects by solving BSE [21]:

$$\Gamma_R(\mathbf{Q}_{ex}) = \frac{2\pi}{\hbar} \sum_{q_L,\lambda} \Big| \langle G, 1_{q_L,\lambda} | H^R | S(\mathbf{Q}_{ex}), 0 \rangle \Big|^2 \delta(E(\mathbf{Q}_{ex}) - \hbar c q_L). \tag{1.13}$$

Here, the radiative recombination rate is computed between the ground state G and the two-particle excited state $S(\mathbf{Q}_{ex})$, $1_{q_L,\lambda}$ and 0 denote the presence and absence of a photon, H^R is the electron-photon coupling (electromagnetic) Hamiltonian, $E(\mathbf{Q}_{ex})$ is the exciton energy, and c is the speed of light. The summation indices in Eq. 1.13 run over all possible wavevector (q_L) and polarization (λ) of the photon. Following the approach described in Ref. [21], the radiative rate (inverse of radiative lifetime τ_R) in SI units at zero temperature can be computed

for isolated defect-defect transitions as:

$$\Gamma_R = \frac{n_D e^2}{3\pi\epsilon_0 \hbar^4 c^3} E_0^3 \mu_{e-h}^2, \tag{1.14}$$

where e is the charge of an electron, ϵ_0 is vacuum permittivity, E_0 is the exciton energy at $\mathbf{Q}_{ex} = 0$, n_D is the refractive index of the host material and μ_{e-h}^2 is the modulus square of exciton dipole moment with length^2 unit. Note that Eq. 1.14 considers defect-defect transitions in the dilute limit; therefore the lifetime formula for zero-dimensional systems embedded in a host material is used [22, 23] (also considering n_D is unity in isolated 2D systems at the long-wavelength limit).

1.3.2 Nonradiative Recombination

Phonon-assisted nonradiative recombination rates are computed via a Fermi's golden rule approach:

$$\Gamma_{NR} = \frac{2\pi}{\hbar} g \sum_{n,m} p_{in} \left| \langle fm | H^{e-ph} | in \rangle \right|^2 \delta(E_{in} - E_{fm}) \tag{1.15}$$

Here, Γ_{NR} is the nonradiative recombination rate between electron state i in phonon state n and electron state f in phonon state m, p_{in} is the thermal probability distribution of the initial state $|in\rangle$, H^{e-ph} is the electron-phonon coupling Hamiltonian, g is the degeneracy factor and E_{in} is the energy of vibronic state $|in\rangle$. Within the static coupling and one-dimensional (1D) effective phonon ap-

proximations, the nonradiative recombination can be reduced to:

$$\Gamma_{NR} = \frac{2\pi}{\hbar} g |W_{if}|^2 X_{if}(T), \tag{1.16}$$

$$X_{if}(T) = \sum_{n,m} p_{in} \left| \langle \phi_{fm}(\mathbf{R}) | Q - Q_a | \phi_{in}(\mathbf{R}) \rangle \right|^2 \delta(m\hbar\omega_f - n\hbar\omega_i + \Delta E_{if}), \tag{1.17}$$

$$W_{if} = \langle \psi_i(\mathbf{r}, \mathbf{R}) | \frac{\partial H}{\partial Q} | \psi_f(\mathbf{r}, \mathbf{R}) \rangle \Big|_{\mathbf{R}=\mathbf{R}_a}. \tag{1.18}$$

Here, the static coupling approximation naturally separates the nonradiative recombination rate into phonon and electronic terms, X_{if} and W_{if}, respectively. The 1D phonon approximation introduces a generalized coordinate Q, with effective frequency ω_i and ω_f. The phonon overlap in Eq. 1.17 can be computed using the quantum harmonic oscillator wavefunctions with $Q - Q_a$ from the configuration diagram. Meanwhile the electronic overlap in Eq. 1.18 is computed by finite difference using the Kohn-Sham orbitals from DFT at the Γ point. The nonradiative lifetime τ_{NR} is given by taking the inverse of the rate Γ_{NR}. Additional details of nonradiative recombination are provided in the appendix. Implementation of nonradiative recombination can be found here (for Ping Group): `https://github.com/Ping-Group-UCSC/NonRad`.

1.3.3 Intersystem Crossing

In a very similar way to the above formalism, the intersystem crossing (ISC) rate is computed as:

$$\Gamma_{ISC} = 4\pi\hbar\lambda_{\perp}^2 \widetilde{X}_{if}(T) \tag{1.19}$$

$$\widetilde{X}_{if}(T) = \sum_{n,m} p_{in} \left| \langle \phi_{fm}(\mathbf{R}) \rangle \, \phi_{in}(\mathbf{R}) \right|^2 \delta(m\hbar\omega_f - n\hbar\omega_i + \Delta E_{if}) \tag{1.20}$$

Implementation of intersystem crossing can be found here (for Ping Group): `https://github.com/Ping-Group-UCSC/NonRad`. Compared with previous formalism [24], this method allows for different values of the initial state vibrational frequency (ω_i) and final state one (ω_f) through explicit calculations of phonon wavefunction overlap. Here spin-orbit coupling (SOC) can entangle triplet and singlet states yielding the possibility for a spin-flip transition. The SOC operator is given to zero-order by [25]:

$$H_{so} = \frac{1}{2}\frac{1}{c^2 m_e^2}\sum_i \left(\nabla_i V \times \mathbf{p}_i\right)\mathbf{S}_i \tag{1.21}$$

where c is the speed of light, m_e is the mass of an electron, $\mathbf{p}$ and $\mathbf{S}$ are the momentum and spin of electron i and V is the nuclear potential energy. The spin-orbit interaction can be rewritten in terms of the angular momentum L and the SOC strength λ as [25],

$$H_{so} = \sum_i \lambda_\perp (L_{x,i}S_{x,i} + L_{y,i}S_{y,i}) + \lambda_z L_{z,i}S_{z,i}. \tag{1.22}$$

where $\lambda_\perp$ and λ_z denote the non-axial and axial SOC strength, respectively. In practice, SOC strengths were computed using the ORCA code by TD-DFT [26, 27].

Chapter 2

Designing Efficient Transition Metal Oxides

2.1 Overview

Solar water splitting, the process of utilizing the Sun's energy by converting water to hydrogen fuel represents the most promising and sustainable means of harvesting renewable energies [28, 29, 30]. In particular, many transition metal oxide (TMO) based photoelectrochemcial (PEC) devices (such as Fe_2O_3 and $BiVO_4$) are capable of achieving the highest solar-to-hydrogen efficiencies and offer the greatest avenue of developing this field, while simultaneously utilizing cheap and abundant sources [31, 32, 33]. Unfortunately, progress within this field has been stunted by the formation of small polarons (hereinafter referred to simply as polarons) which conduct via a thermally activated hopping mechanism and yield very poor conduction when compared to typical band conduction [34]. Hence, polarons are the chief bottleneck in the development of TMO-based PEC devices, as poor conduction leads to low efficiency.

Therefore, my research focuses on the development of our understanding of polarons in TMOs and the discovery of methods for facilitating polaron conduction in TMOs for improved solar-to-hydrogen efficiency. In particular, atomic doping in TMOs has been highly successful for improving the solar-to-hydrogen efficiency of TMOs. For example, in my first publication we studied how several defects in Fe_2O_3 influence carrier conduction [12]. This work formulated methods for studying polaron transport in doped systems and showed how Sn doping in Fe_2O_3 can improve carrier concentration. Following this, we developed mechanistic insights into how Li doping facilitates novel spin polaron conduction in CuO, which was validated by experimental measurement of enhanced photocathode performance by Li-doped CuO [35]. Our work demonstrating how the intrinsic band gap of Co_3O_4 had been misidentified due to the formation of optically active hole polarons caught a lot of attention [36]. In particular, this work received a Lawrence Livermore National Laboratory (LLNL) summer student poster symposium award, was highlighted in LLNL notable news, and was pivotal in my reception of the Graduate Student Scholar Program fellowship from LLNL. Recently, I have done two in-depth studies on the Fe_2O_3 system, the first extensively details polaron formation in the presence of many intrinsic defects and external dopants by computing defect, carrier, and dopant concentrations and reveals best doping practices. Furthermore, I have discovered a novel form of dopant clustering mediated by small polaron and dopant interactions which has been experimentally validated. Finally, I have collaborated in many experimental works where our abilities to simulate polarons [37, 38] and chemical reactions [39, 40, 41, 42] have proven vital in our understanding of how atomic doping enhances the performance of these materials.

2.2 Polaron Formation and Transport in Fe_2O_3

In our 2017 work published in Journal of Physics: Condensed Matter [12], we investigated polaron formation and transport in Fe_2O_3, demonstrating the notation of a 'free polaron' level and detailing polaron hopping in pristine and doped Fe_2O_3. Several transition metal oxides, such as TiO_2, $BiVO_4$, WO_3 and hematite Fe_2O_3, have exemplified some of the desirable characteristics of an efficient photoanode for solar-driven photoelectrochemical (PEC) water splitting [43, 44]. In particular, hematite (Fe_2O_3) is a low cost, earth abundant, n-type semiconductor with a relatively smaller band gap in the visible range (~ 2 eV) compared with other oxides; thus it has been established as a promising candidate for photoanodes. However, application of hematite as a photoanode has been hindered from low carrier denstiy, low carrier mobility and high electron-hole recombination rate. Collectively, this results in the solar to fuel efficiency being substantially lower than the theoretical value, i.e. hematite typically yields a solar to hydrogen efficiency of 1-2% despite having a theoretical efficiency for water splitting of 13% [45].

Extensive research has been conducted on the introduction of certain defects or dopants into hematite which could enhance PEC performance. In particular it has been shown that the introduction of defects such as V_O, Sn and Ti can improve the photocurrents of Fe_3O_3. [46, 47, 48] Despite this, the underlying mechanism is not well understood. Specifically, whether the dopants improved the bulk properties or the interface charge separation, and how they affected light absorption, carrier concentration and carrier mobility of the bulk hematite, etc. Answering these questions is crucial for further optimization of chemical composition and morphology of hematite for higher PEC efficiency.

Recently, the joint experimental and theory work by Ref. [49] provided a de-

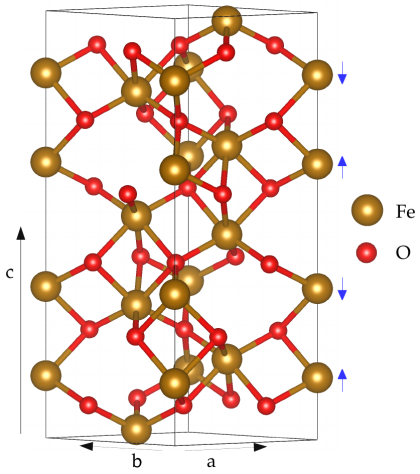

Figure 2.1: The crystal structure of Fe_2O_3 with lattice coordinates a, b and c. The blue arrows are to indicate the anti-ferromagnetic ordering of the iron ab layers.

tailed explanation for how nitrogen doping and oxygen vacancies in bismuth vanadate have led to improved photo-to-current efficiency by a simultaneous improvement of carrier density, carrier mobility and visible light absorption. In Ref. [49], it has been found that the enhanced mobility is tightly connected to the small polaron transport properties in $BiVO_4$, *i.e.* the N doping lowered the small polaron hopping barrier and improved the hopping mobility. Similarly, small polaron transport is the main carrier conduction mechanism in hematite, which causes its carrier mobility and conductivity to be extremely low. In the past, certain defects such as oxygen vacancies in bulk hematite have been discussed by computing their defect formation energies [20, 50] but have not provided insights related to small polaron formation and conduction, which is the key to understand experimental observations (throughout this paper we will simply write polarons when referring to electron small polarons).

Therefore we plan to illuminate the mechanism responsible for the enhancement of efficiency in doped hematite and provide a quantitative depiction of the

roles of these dopants in terms of the small polaron formation and transport mobility in bulk hematite. We will discuss the electronic structure, defect charge transition levels and ionization energies for these individual defects as well as defect complex. Although several studies have been carried out on the formation energies of doped hematite [20, 50], their dependence on the choice of U parameters has not been examined in details. As we will show below, we have computed defect formation energies and ionization energies for different U parameters to investigate how the results vary as a function of U. Besides the defect ionization energies which are closely related to the carrier concentration, it is crucial to understand the effect of defects or dopants on the small polaron transport mobility in hematite which is another factor determining the carrier conductivity. To our best knowledge, discussion of small polaron transport in hematite from first principles is limited to pristine systems and there are few studies of small polaron transport in defective hematite [51].In this work, we will examine how defects effect the small polaron hopping barriers for carrier conduction in doped hematite. By this means we can answer important experimental questions related to the effects of defects on hematite and also provide extending insights for other doped transition metal oxides, supplying guidance for future experimental design of improved small polaron transport properties in metal oxides.

2.2.1 Methods

We obtained the electronic structure of pristine and doped hematite with Density Functional Theory (DFT) calculations including Hubbard U corrections in order to take into account of strong on-site d electron interactions. Total energy, geometry relaxation and electronic structure calculations were performed with open source, plane wave codes Quantum ESPRESSO [52]. We used ultrasoft

pseudopotentials [53] including Fe $3s$ and $3d$ semicore electrons, which in our case yielded identical results to norm-conserving alternatives [54, 55]. For the plane wave basis we individually used cutoff energies of 40 Ry for wave functions and 240 Ry for charge density. The Brillouin zone was sampled with a $4 \times 4 \times 2$ Monkhorst-Pack k-point mesh for geometry optimization of the 30 atom unit cell and the k-point mesh was doubled in density of states calculations. Methfessel-Paxton first-order spreading was used to expedite Brillouin zone integration with a smearing width of 0.001 Ry [56]. Total energy was calculated self consistently until a convergence of 10^{-8} Ry was achieved and geometry was optimized until the net force per atom reached less than 10^{-3} Ry/au. For the hopping activation barrier calculations, a linear extrapolation scheme of atomic structure between initial and final hopping centers was employed for pristine and defective systems.

Fe_2O_3 is arranged in the hexagonal corundum structure with a space group of $R\bar{3}c$ [57] (Figure 2.1). The unit cell consists of 30 atoms where iron, Fe^{3+}, is six coordinated and oxygen, O^{2-}, is four coordinated. The system is anti-ferromagnetic where the Fe^{3+} ions have a high spin configuration of partially occupied $3d$ orbitals with aligned spin between ions within ab-planes and anti-aligned along the c direction. We first optimized the initial geometry of pristine hematite with a variable cell relaxation which obtained cell parameters of $a = 5.13\,\text{Å}$ and $c = 13.99\,\text{Å}$ with bond lengths and angles of Fe-O = 1.99, 2.14 Å, O-Fe-O = 90.7, 86.0, 78.6 °, which agree well with other work in both experiment [58] and theory [59]. The pristine structure and fundamental values that we obtained are collected in Table 2.1.

Pristine Hematite Fundamental Values		
Value	Present Work	Experiment [58]
a (Å)	5.13	5.04
c (Å)	13.99	13.75
Fe-O (Å)	1.99, 2.14	1.94, 2.11
O-Fe-O (°)	90.7, 86.0, 78.6	90.5, 85.0, 78.2
μ_{Fe} (μ_B)	4.0	4.6 [60]
E_{gap} (eV)	2.21	2.2 [61]

Table 2.1: Computed and experimental lattice constants a and c ($b = a$), nearest neighbor bond lengths Fe-O, bond angles O-Fe-O and the band gap energy E_{gap}.

Hematite is a charge transfer insulator [62, 63] and in accordance with the strong correlation of electrons in $3d$ orbitals we apply the Hubbard correction [11] to the Fe $3d$ orbitals. The U_{eff} parameter, which sets the strength of this correction, was determined empirically to be 4.3 eV, in order to best fit the band gap of hematite to be 2.2 eV as measured by soft x-ray spectroscopy [61]. It is notable that Hubbard parameters used in previous calculations of this material vary, although most used a U_{eff} between 4 eV to 4.3 eV. [20, 59, 64, 50, 65, 66, 51] In particular, one study also used a non-empirical method, on the basis of unrestricted Hartree Fock theory, to determine a converged value of $U_{\text{eff}} = 4.3$ eV for Fe_2O_3, which they also showed to provide results in good agreement with experiment. [65]

The introduction of any extra electrons into Fe_2O_3 will form strongly localized small polarons due to large electron phonon couplings (the electrons are self-trapped by local lattice distortions) and the small polaron radius is typically no farther than the next-nearest neighbors. [67] The formation of small polarons have been found in several metal oxides, such as Fe_2O_3, $BiVO_4$, [49] and ABO_3 perovskites [68], where the small polarons must be thermally activated and then

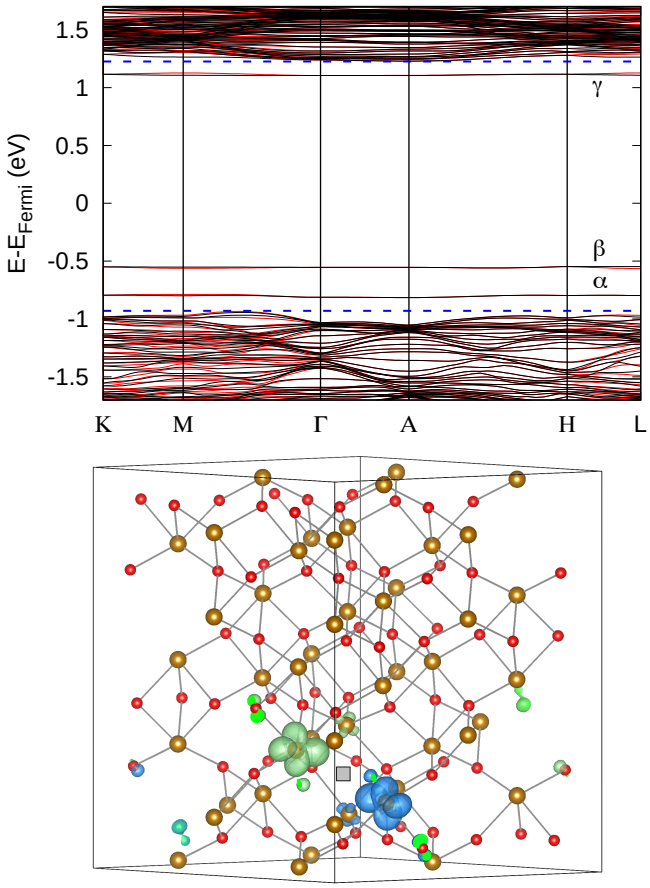

Figure 2.2: (Left) The band structure of Vo:Fe_2O_3 with unperturbed band edges and the creation of three isolated defect states α, β and γ (red curves: spin up; black curves: spin down; blue dashed lines mark VBM and CBM). Defect states are states which are away from the band edges and correspond to localized states as in this case. (Right) Isosurface plot of the two highest occupied orbitals present in Vo:Fe_2O_3 with an isosurface of $\sim 2\%$ the maximum value. These two degenerate small polarons form at nearest neighbor Fe of V_O (grey box) and are referred to as β polarons throughout this paper (green isosurface spin up and blue isosurface spin down).

hop between metal sites in order to conduct currents. In this work we plan to study the relative stability and hopping barriers between different polaron configurations, where controlling the position of small polaron formation with/without defects is the key. We controlled the placement of the small polaron through local geometry adjustments that break the symmetry of the ground state system, such as moving the oxygen atoms surrounding an Fe ion away from it to ensure localization of polarons at that site and then relaxing the geometry to energy minimum. This bias initiates the localization of polarons which will expand the local metal-oxygen bonds slightly ($\sim$0.1 Å). The small polarons form both in pristine systems (without explicit defects) and defective systems. For the latter, the small polaron and defect center often interact and possibly form a complex as we will discuss later.

For calculations with defects and excess charge, a $2 \times 2 \times 1$ supercell with a $2 \times 2 \times 2$ k-point mesh was adopted and internal geometries were relaxed keeping cell parameters fixed to simulate an isolated defect within the periodic system. We found the $2 \times 2 \times 1$ supercell is large enough to avoid periodic interactions between neutral defects. The charged defect formation energies have a slow convergence with supercell size (scale as 1/L) due to image charge interactions. We corrected the charge defect formation energies using the charge correction scheme similar to Ref. [19] and our recent development in Ref. [69] where the proper treatment for electrostatic potential alignment at presence of strong geometry relaxation by defects is included, which has been a general issue for charged defect calculations [70].

2.2.2 Electronic Structure of Defective Hematite

Oxygen vacancy is an important intrinsic defect in Fe_2O_3, whose concentration can be controlled through experimental conditions. Recently, it has been found that the introduction of oxygen vacancies in Fe_2O_3 can improve the overall photocurrents of hematite based photoanodes in solar water splitting cells. [46] Yet, the role of oxygen vacancies is unclear, and two possible explanations are present: (1) oxygen vacancies improve the bulk carrier conductivity properties or (2) oxygen vacancies improve the electron hole separation at electrode/electrolyte interfaces. In this work we focus on (1), *i.e.* the effect of oxygen vacancies on the bulk properties of Fe_2O_3.

The role of oxygen vacancies is simulated through the removal of one oxygen atom within our supercell (120 atoms) and allowing the internal geometry to relax. Since the oxygen within Fe_2O_3 has an oxidation state of O^{2-}, oxygen vacancy is an n-type dopant, which donates two electrons to the system. The band structure of hematite with one neutral oxygen vacancy (Figure 2.2) displays the creation of three defect states within the band gap α, β, γ in agreement with previous theoretical work [20]. The corresponding projected density of states is included in SI figure 2. Defect states are considered to be lozalized states (over a few nearest neighbor atoms – see SI figure 7) and have no dispersion as seen by the band structure and density of states. We found the two electrons are spontaneously ionized from oxygen vacancy site and form localized small polarons at nearby Fe ion (no charge density appears at the center of the vacancy, unlike the case of $SrTiO_3$ [71]). The β state in the band structure corresponds to the two polaron states (one spin up and one spin down) in which the extra electrons from V_O occupy (the wave functions are shown in Figure 2.2). They are $d_{x^2-y^2}$ type orbitals of the two nearest neighbors of the four-coordinated V_O. The α

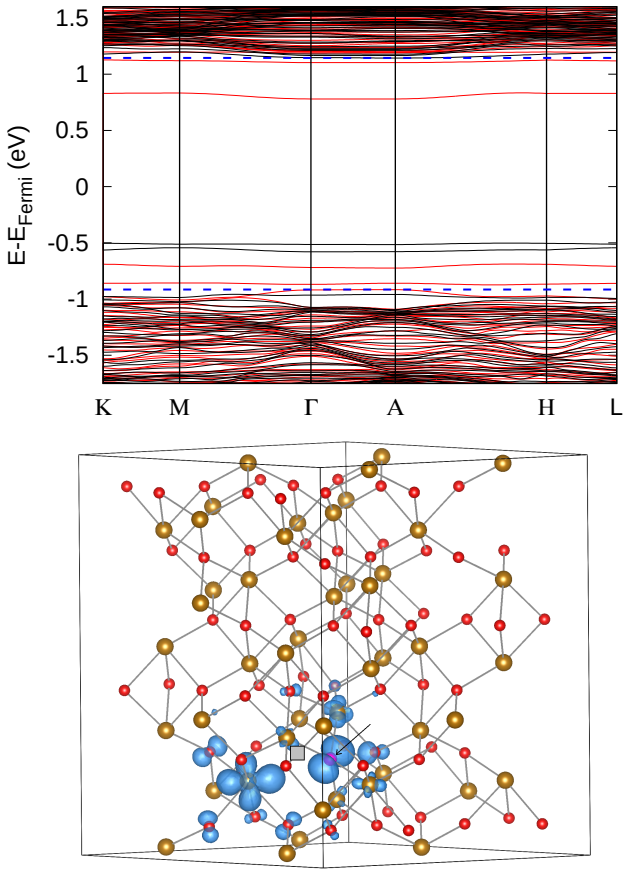

Figure 2.3: (Top) The band structure of N+Vo:Fe_2O_3 with a perturbed valence band edge (right below the lower dashed blue line), creating a reduced gap and an indirect to direct gap transition (red curves: spin up and black curves: spin down; blue dashed lines mark VBM and CBM). There are several defect states introduced in the gap (between two blue dashed lines), including occupied defect states which are primarily hybridized Fe 3*d* and N 2*p* states. (Bottom) Isosurface plot (blue) of the highest occupied orbital present in N+Vo:Fe_2O_3, a combination of a β polaron from the presence of V_O (grey box) and N 2*p* orbital (pink atom with arrow).

state is a perturbed valence state of O $2p$ orbitals surrounding the site at which the extra electrons go, while the γ state is a perturbed conduction state which is unoccupied and corresponds to e_g orbitals of the next nearest Fe neighbors of V_O. Overall, the oxygen vacancy did not modify the band edge positions and band dispersion of the pristine systems, except introducing isolated defect levels in the band gap. Therefore, we do not expect it will affect the main optical absorption spectra (as the defect states have low density of states) but it may affect the transport properties of the system, i.e. the carrier concentration or mobility as we will discuss later.

Atomic nitrogen has been found to be a promising dopant to improve visible light absorption properties of metal oxides, such as in TiO_2 [72] and $BiVO_4$. [49] Recently, we found N doping in the presence of oxygen vacancies can also improve the carrier mobility of $BiVO_4$, where the small polaron hopping barrier was lowered. Yet, N doping in Fe_2O_3 with/without oxygen vacancies has not been studied both theoretically and experimentally to our best knowledge. We will firstly discuss the effects of N doping and then discuss the combination effect of N doping with oxygen vacancies.

For N-doped hematite we replaced one O in our system with N, a p-type dopant since N has one fewer valence electron than O. This substitution results in a deep defect state created corresponding to an unoccupied N $2p$ orbital and results in slightly perturbed valence band states (See SI Figure 3 for band structure and projected density of states.) The deep defect state introduced by N doping has minimal overlap with the O $2p$ states, which may introduce defect state involved transitions in the optical spectra but will not affect the main absorption edge. In the meanwhile, the VBM in N-doped hematite is raised by 0.1 eV due to the hybridization between N and O 2p states, and interestingly, the indirect band gap

2N:1V_O Hematite configurations			
β polarons	N-N (Å)	N-Fe-N (°)	ΔE_{tot} (eV)
2	2.4025	74.578	0.44
1	2.7482	86.841	0.23
0	3.8606	151.269	0

Table 2.2: Summary of 2N:1V_O configurations, displaying the relation between number of β polarons from V_O formed, distance between N (N-N (Å)), atomic angle (N-Fe-N (°)) and the total energy difference (ΔE_{tot}) with the most stable system (the configuration with 0 β polarons formed).

for the pristine Fe_2O_3 becomes a direct band gap after N doping. This could both shift the absorption edge to lower energy slightly and also enhance the absorption coefficient at the same energy range compared to the pristine case.

Next, we considered nitrogen doping coupled with oxygen vacancy in both a (1N:1V_O) ratio and a (2N:1V_O) charge-balanced ratio. In the (1:1) doping regime the overall effect is still n-type yet one of the polaron states is absorbed by the nitrogen into the previously unoccupied N 2p state (Figure 2.3). We found that the defects prefer to be close-by, rather than far away, with $E_{near} - E_{far} \approx -0.67$ eV, with only small variations in the E_{near} based on N and V_O orientation and distance. Tested configurations had the distance between V_O and N in the 'near' case as about $\sim$2.5-3.0 Å and $\sim$7-10 Å in the 'far' case. The resulting electronic structure of N+V_O:Fe_2O_3 is shown in Figure 2.3 and displays a slightly reduced band gap of 2.1 eV (see SI Figure 4 for details). Again, as in N-doped hematite, we see a shift at the VBM of N+V_O:Fe_2O_3, resulting in a direct band gap introduced from N-doping.

We also tested nitrogen doping coupled with oxygen vacancy in a (2:1) ratio and we found three possible electronic configurations based on the orientation of the defects within the lattice (in each case they are attached to the same Fe ion). These configurations are nicely characterized by the number of β type states (β

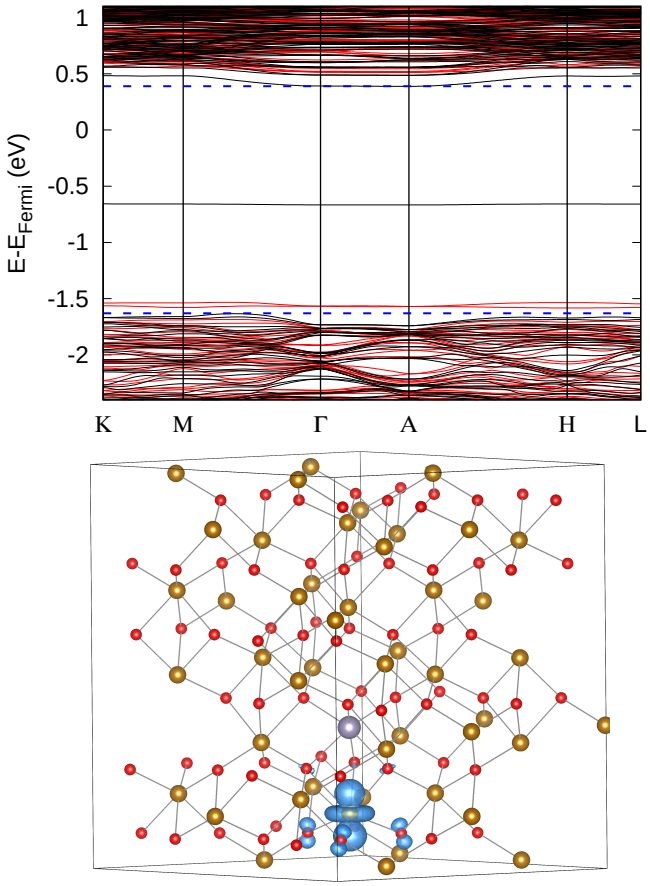

Figure 2.4: (Top) The band structure of Sn:Fe_2O_3 with a perturbed conduction band edge of Fe 3*d* states creating a reduced gap of 2.0 eV (see SI figure 6 for details). There is a single isolated defect introduced in the gap which corresponds to a small polaron formed at Fe site near Sn. (Bottom) Isosurface plot (blue) of the highest occupied orbital present in Sn:Fe_2O_3, a small polaron formed directly below Sn (grey atom).

polarons) created by V_O. A summary of these configurations is collected in Table 2.2. We found that if all three defects are as close as possible (with N-N distance 2.40Å) then both small polarons are formed (the number of β polarons is 2 as shown in Table 2.2). If all three are still close yet the nitrogen atoms are on opposite sides of V_O (with N-N distance 3.86Å)then both small polarons are absorbed by the nitrogen (the number of β polarons is 0 as shown in Table 2.2; see detailed structures in SI figure 8). Lastly, it is possible to form a configuration somewhere in between these two states and have only one small polaron state formed (the number of β polarons is 1 as shown in Table 2.2). Ultimately, the most stable configuration for the (2:1) ratio is to have the nitrogen on opposite sides of V_O so that they may absorb the two electrons of V_O with minimal interaction between nitrogen sites. This configuration is minimal in energy because the absorption of these extra electrons allows the nitrogen to achieve filled valence bands while keeping their repulsive electrostatic interaction at a minimum. In any of these configurations, several defect states are still present within the band gap (see the corresponding band structure and projected density of states in SI figure 5). Although both electrons donated from V_O are absorbed by the nitrogen atoms in the most stable configuration of $2N{:}1V_O$, these dopants still introduced extra defect states inside the gap. This is unlike the case of $BiVO_4$, where the charge balanced N doping with oxygen vacancy results in the shift of valance band edges but no isolated defect states formed in the band gap [49]. Meanwhile, the valence band edge shifts up by 0.2 eV in this case resulting in a reduced band gap size of 2.0 eV, and is also accompanied by an indirect to direct gap transition.

Sn substitution has been shown experimentally to be a promising dopant for improving photocurrents in Fe_2O_3 photoanodes [47]. However, similar to the case of oxygen vacancies, it is unclear whether this is because the bulk carrier

conductivity has been improved. Sn is a n-type dopant since the substitution $Fe^{3+} \rightarrow Sn^{4+}$ donates an electron into the system. The atomic number of tin is nearly double that of iron (50:26) yet the atomic radius of Sn^{4+} (83.0 pm) is only slightly larger than that of Fe^{3+} (78.5 pm). Since the Fe ions in hematite have a high spin configuration of half-filled $3d$ orbitals, the main modification of the electronic structure upon the introduction of Sn substitution is that Sn has no unpaired spin which creates a hole in the magnetic ordering of the anti-ferromagnetic arrangement of Fe_2O_3. Additionally, Sn valence orbitals are less localized than Fe $3d$ orbitals, which results in the excess electron easily moving away from Sn and localizing on a nearby Fe ion. Therefore, the excess electron contributed from Sn substitution forms a small polaron at the Fe site located either directly below or directly above Sn (depending on the location of Sn in the lattice, Figure 2.4). Alignment of Fe 3s semi-core states between the pristine and doped systems reveals the conduction band edge down-shift of unoccupied Fe $3d$ orbitals in Sn-doped hematite resulting in a slightly smaller band gap (2.0 eV) than pristine Fe_2O_3 (see Figure 2.4 for the band structure and SI Figure 6 for the projected density of states). Overall, Sn doping causes one small polaron defect state in the gap and perturbs the states close to the band edges, unlike the case of oxygen vacancies which only results in several isolated defect states in the gap with no perturbation of band edges.

2.2.3 Formation Energy of Charged Defects

To understand whether the defects can be ionized easily at the room temperature (and therefore contribute to the carrier concentrations), we calculated thermodynamical charge transition levels $\epsilon_{0/+1}$ and $\epsilon_{+1/+2}$ of the doped systems considered. The chemical potentials of elements Fe, Sn, O and N were estimated

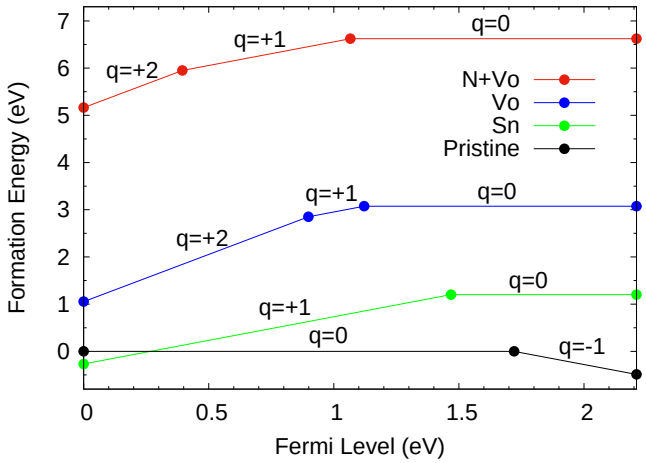

Figure 2.5: Formation energy displaying the most stable charge states of the different doped systems considered with respect to the Fermi level. The zero Fermi level is the VBM of the pristine system.

Ionization Energies in Doped Hematite		
Doping	(+1/+2) eV	(0/+1) eV
V_O	1.31	1.09
N+V_O	1.82	1.14
Sn	–	0.74

Table 2.3: Corresponding ionization energies obtained from the energy difference between the charge transition level to the conduction band for different doping cases.

as the total energy per atom of the natural occurrence of the element. In this paper we focus on the charge transition levels of the defects which will not depend on the chemical potential of elements (*e.g.* oxygen poor or rich conditions).

We obtained the charged defect formation energies and charge transition levels for the doped systems as displayed in Figure 2.5. Typically, one obtains the ionization energies of these states by the difference of the conduction band minimum 2.21 eV (of the pristine system) to the Fermi level at which the charge transitions occur, summarized in Table 2.3. We see that V_O introduces deep defects into

the system with large ionization energies 1.31 eV (+1/+2) and 1.09 eV (0/+1), consistent with previous theoretical work which reported 1.08 eV for (0/+1) [20]. Meanwhile we see that N+V_O deepens the (+1/+2) transition by 0.51 eV yet does not significantly change the (0/+1) ionization energy. Sn has the lowest ionization energy of 0.74 eV (0/+1), which is larger than previously reported values by 0.22 eV [50]; yet, they also reported a smaller band gap (2.15 eV) than ours (2.21 eV) due to a lower U value (4 eV). It is important to note that these ionization energies indirectly depend on the Hubbard U parameter. Specifically, a lower U parameter will lower the conduction band minimum position and hence result in lower defect ionization energies. We find that the charge transition levels are not expected to change much with respect to the valence band maximum, yet the band gap can have a range from 1.8 eV to 2.2 eV for a Hubbard U of 3.0 eV to 4.3 eV (see Figure 2.6). Nonetheless, the overall defect property does not change qualitatively, i.e. the oxygen vacancy has an ionization energy ranging from 1.09 eV (at U=4.3 eV) to 0.79 eV (at U=3.0 eV), which is still a deep impurity compared with the ionization energy of a small polaron in the pristine hematite (0.49 eV at U=4.3 eV and 0.09 eV at U=3.0 eV.)

We note that although the absolute Sn-doping ionization energy is still large (0.74 eV), if we compare its ionization energy with the ionization energy of one small polaron in a pristine system (0.49 eV; black line in Figure 2.5), the difference is only 0.25 eV. This implies that it takes 0.25 eV to excite the small polaron from a defect-bound polaron to an unbound polaron (or 'free' polaron), which can be considered as a shallow impurity. And because electrons naturally form small polarons even in the pristine Fe_2O_3 and it takes 0.49 eV to ionize the electrons from self-trapped to free electrons in the conduction bands, absolute 'shallow' n-type defects (where the ionization energy relative to the CBM is at the order of kT)

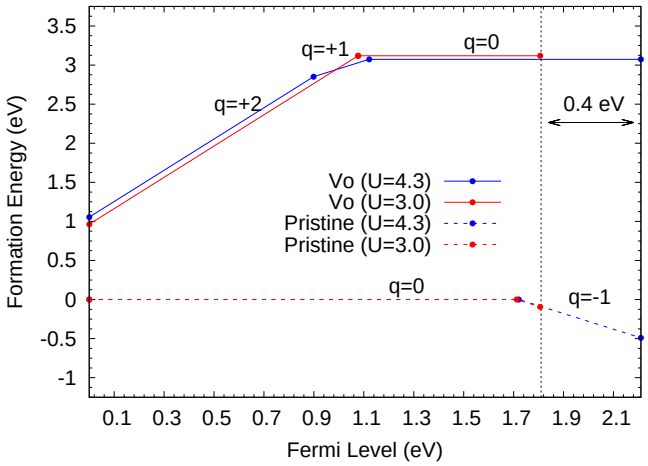

Figure 2.6: Formation energy plot for pristine hematite and hematite with V_O with different U parameters, 3.0 and 4.3 eV. The reference zero of the Fermi level is the VBM of the pristine system. The charge transitions still occur at the similar Fermi level with respect to the VBM in the respective systems, however, a smaller U parameter results in a smaller band gap. In particular E_{gap} = 1.81 eV in the U = 3.0 eV system, 0.4 eV smaller than E_{gap} = 2.21 eV in the U = 4.3 eV system. As a result, the defect ionization energy is lowered by 0.4 eV at U= 3.0 eV compared with U=4.3 eV.

can hardly form in Fe_2O_3. In particular,this is evident for the ionization energies of V_O and N+V_O which are still $\sim$0.6-0.7 eV away from the ionization energy of one small polaron in the pristine system. Therefore, even when considering the ionization energy of a small polaron in the pristine system, the polarons formed in these systems (V_O and N+V_O) are still difficult to ionize and contribute to carrier concentrations at room temperature, unlike the case of Sn doping.

2.2.4 Small Polaron Transport in Pristine and Defective Hematite

From the ionization energy calculations above, we have found Sn is a promising dopant for carrier concentration improvement. As the carrier conductivity depends on both the carrier concentration and mobility, in this section we will discuss whether Sn doping improves the carrier mobility as well. Previous work [73] found that in pristine Fe_2O_3 the coupling of small polaron hopping sites (V_{AB}) is large relative to the reorganization energy ΔG^* ($V_{AB} > \Delta G^*/4$), implying the small polaron hopping conduction of Fe_2O_3 is in the adiabatic regime. We then computed the small polaron hopping activation energy of pristine and Sn-doped hematite using a linear extrapolation technique, which includes the coupling V_{AB} implicitly. We start from the initial configuration q_a where the small polaron is located on a Fe ion and then using geometrical techniques described in the method section determine a configuration q_b in which the small polaron is located on a nearest neighbor Fe ion in the same ab-plane. Then, in accordance with Eq. 2.1 we linearly extrapolated from q_a to q_b, allowing the electron density of the system to equilibrate at each step but keeping the geometry q_x fixed.

$$q_x = q_a(1 - x) + x\, q_b \tag{2.1}$$

The computed total energies (referenced to the starting configuration) as a function of reaction coordination are shown in Figure 2.7. The peak of the barrier is the saddle point between the two hopping sites and the true activation energy E_A is obtained from relaxing the geometry from this point. In the pristine system the saddle sits at the $q_{0.5}$ reaction coordinate due to the symmetry of two hopping centers and in Sn:Fe_2O_3 it sits at the $q_{0.56}$ reaction coordinate. The latter relates

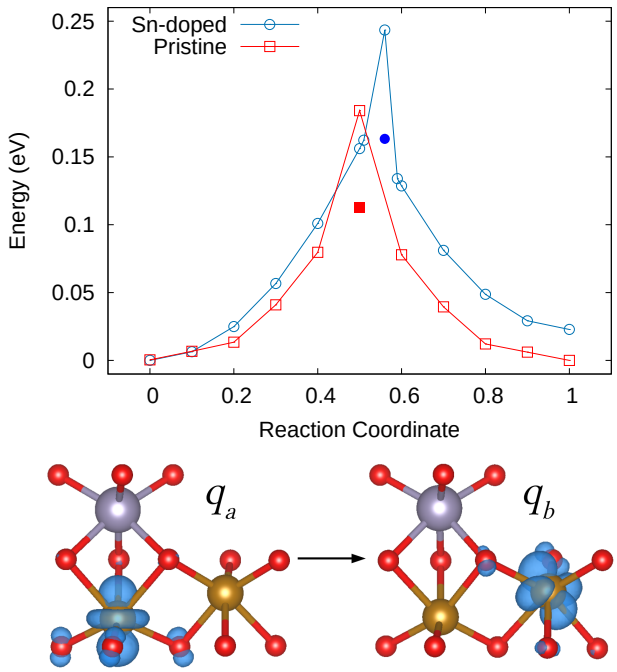

Figure 2.7: (Top) Small polaron hopping barrier in the pristine and Sn-doped systems where the solid square and dot indicate the activation energy. (Bottom) Schematic of polaron hopping in the Sn-doped system (left is the initial a configuration and b is the final configuration).

to the different distances from the small polaron center to the Sn defect center.

For the pristine system we obtain an activation energy of $E_{A,Fe} = 0.11$ eV, consistent with previously calculated results of 0.11 eV [73] and 0.13 eV [59]. In the Sn-doped system we computed an activation energy of $E_{A,Sn} = 0.16$ eV. This higher activation energy is quite significant when compared with kT at room temperature (k is the Boltzmann constant and T is temperature). In particular the electron transfer rate is proportional to the exponential of the activation energy over kT as shown in Eq.2.2.

$$\tau = Ae^{-E_A/kT} \tag{2.2}$$

where τ is the electron transfer rate and A is the prefactor which depends on the number of nearest neighbors and the attempt frequency. Considering that both systems have 3 nearest neighbors and Sn disrupts the geometry only slightly, the prefactor A of these two systems should be on the same order of magnitude. The hopping mobility is related to the electron transfer rates through the Einstein relation and one dimensional random walk i.e. $\mu = eR^2\tau/(2kT)$, where R is the electron transfer distance and τ is the electron transfer rate[59, 74]. Therefore we can determine the ratio of the mobility in these two systems to be solely dependent on the difference of their activation energies.

$$\frac{\mu_{Sn}}{\mu_{Fe}} \simeq e^{-(E_{A,Sn}-E_{A,Fe})/kT} \tag{2.3}$$

Eq.2.3 gives a ratio $\mu_{Sn}/\mu_{Fe} = 0.14$, which implies a decrease in carrier mobility in Sn:Fe_2O_3. We note that the effect of defects on the carrier mobility depends on the distance to the defect center, i.e. the hopping barriers between the pristine and Sn-doped systems will be similar when the hopping centers are far away from the defects (Sn). Therefore what we estimate here is the lower bound of carrier mobility at presence of Sn.

We also investigated the hopping barriers at presence of V_O and N+V_O by using similar procedures; yet we found the small polaron centers are unstable away from the defects (the electrons tend to localize closest to the defect centers, despite any applied local distortion at the positions far away from the defects.) This again indicates these defects in bulk Fe_2O_3 are deep and extra electrons from V_O and N+V_O tend to form small polarons tightly bounded to the positive charged defect centers.

2.2.5 Conclusions

In summary, this work discussed the effects of defects on the small polaron formation, ionization and hopping transport properties in bulk Fe_2O_3 through first-principles calculations, where the choice of dopants is inspired by recent experimental and theoretical work[46, 47, 48, 49]. Our calculations of the electronic structure of pristine and doped Fe_2O_3 show that the small polarons will naturally form at Fe ions if there are any excess electrons (unless there are dopants with stronger correlated electrons available than the $3d$ electrons of Fe). These small polarons can be tightly bounded to the defect centers (strongly preferred to locate at Fe closest to the defects) or possibly conduct through thermally activated small polaron hopping, depending on the corresponding ionization energies.

Electronic structure calculations show the defects we investigated here have different effects on the band structures: for V_O, only deep defect levels are introduced in the band gap and the bulk band structure did not change compared with the pristine hematite. For the cases of N, ($1N{:}1V_O$) and ($2N{:}1V_O$) doping, we observe 1. defect levels appear in the band structure; 2. the valence band maximum shifts up by $0.1 - 0.2$ eV, accompanied by an indirect to direct gap transition, which could improve the visible light absorption at the same energy range as before, but also lower the absorption spectra edge than the pristine hematite. The enhancement of visible light absorption may be further confirmed by computing absorption spectra for these doped systems in the future work. For Sn doping, we found related defect states in the gap and also a band gap reduction by 0.2 eV by lowering of the conduction band position.

Formation energy as a function of Fermi level reveals most stable charge configurations of the several doped systems of hematite considered: V_O, $N{+}V_O$ and Sn. From our defect formation energy calculations, we see that V_O and $N{+}V_O$

bind the small polarons strongly with relatively large ionization energies. In the Sn-doped system we see a much lower ionization energy (it takes 0.25 eV from a defect-bound polaron to a "free" polaron) compared to the pristine system. This shows Sn doping could contribute to the carrier concentrations at room temperature. We note that due to the spontaneous formation of small polarons even in pristine systems (with an ionization energy of 0.49 eV to become free electrons in CBM), an absolute shallow n-type impurity can hardly form in Fe_2O_3 since this would require an ionization energy relative to CBM more comparable to kT at room temperature ($\sim$0.026 eV).

Calculations of the small polaron hopping activation energy were conducted in pristine and Sn-doped hematite and we found that the introduction of Sn may lower the hopping mobility due to a higher hopping activation barrier. However, the improved carrier concentration and possibly improved light absorption by Sn doping can improve the overall photocurrents as observed experimentally. We note that although experimentally they also found V_O improved the photocurrents of Fe_2O_3 [46, 47] (which is not supported by our theoretical results that V_O is a deep impurity and does not modify the band structure of the pristine system except introducing defect bands), the measurements are based on an average of bulk and surface defects, at the presence of electrode/electrolyte interfaces. In order to further elucidate the roles of V_O, N+V_O and Sn doping in Fe_2O_3 for solar water splitting applications, the ionization energies of charged defects at surfaces as well as the interaction between small polarons, defects and water at the Fe_2O_3/water interface needs to be investigated in the future work.

2.3 Carrier Concentrations in Fe_2O_3

Outstanding questions remain in the pursuit of highly-efficient Fe_2O_3-based devices with atomic doping. For example, the identity of intrinsic free carrier donor remains under debate. Specifically, various experimental works have claimed that oxygen vacancies (V_O) are the source of extra carriers in n-type Fe_2O_3, [75] whereas theoretical works have shown that V_O have an unreasonably large ionization energy,[12] which suggests that they cannot be the primary contributor of free carriers. Meanwhile, some theoretical works have supported that iron interstitials (Fe_i) are the major carrier donors due to a significantly smaller ionization energy than that of V_O. [20] Another important question, which is more general to oxides than particularly Fe_2O_3, is how to determine dopants which will yield the best performances of oxide based devices? Insights into the design of efficient oxide based devices by simple yet practical prediction of atomic doping are highly desired. [76]

There have been some theoretical works on intrinsic defects and atomic doping in Fe_2O_3, for example, defect formation energy and charge transition levels have been computed for Fe_2O_3, which can help determine dopants with low ionization energy such as Sn, Ge, and Ti. [12, 50] However, these works cannot yet address the above questions since directly obtaining carrier concentrations requires understanding the combined effects of dopant solubility and dopant ionization energy. Furthermore, intrinsic defects should be considered simultaneously as they may compensate n-type dopants, and yet, the effects of intrinsic defects with or without external doping are not well-established in Fe_2O_3, as mentioned above.

In this work, we provide answers to these questions by investigating carrier concentrations in Fe_2O_3 from first-principles. By careful evaluation of defect concentrations including the presence of small electron polarons we can reliably predict

the concentrations of free carriers in Fe_2O_3, in excellent agreement with experiments. Further detailed computational analysis of dopant solubility, ionization energy, chemical condition, and synthesis temperature are provided in order to answer outstanding questions such as: What are the intrinsic carrier donors in pristine Fe_2O_3? Which dopants are the best at raising carrier concentrations? What makes a dopant effective in raising carrier concentrations (*e.g.* solubility or ionization energy)? The work is organized as follows, first we briefly present our computational methodology. Second we discuss intrinsic defects in undoped Fe_2O_3. Third we systematically study several tetravalent and pentavalent dopants idenitifying the best dopants for this system. Finally we analyze the importance of solubility against ionization energy in determining which dopants will be the best at enhancing carrier concentrations. The contribution of entropy to the formation energy is rigorously studied and the general trends of formation energy (ionization energy) within each group with respect to ionic radius is also presented. This work provides detailed understanding of the interactions between intrinsic defects, extrinsic dopants, and small polarons in polaronic oxides.

Density functional theory calculations were performed in the open-source plane-wave code QuantumESPRESSO [52] using ultrasoft GBRV pseudopotentials [53] and an effective Hubbard U [11] value of 4.3 eV for Fe $3d$ orbitals [12, 59]. Plane-wave cutoff energies of 40 Ry and 240 Ry were used for wavefunctions and charge density, respectively. All calculations employed a $2 \times 2 \times 1$ supercell (120 atoms) of the hexagonal unit cell with a $2 \times 2 \times 2$ k-point mesh for integration over the Brillouin zone. Charged defect formation energies and defect concentrations, including free carrier concentrations were evaluated from first-principles.

2.3.1 Intrinsic Defect Contributions to Polaron Concentration

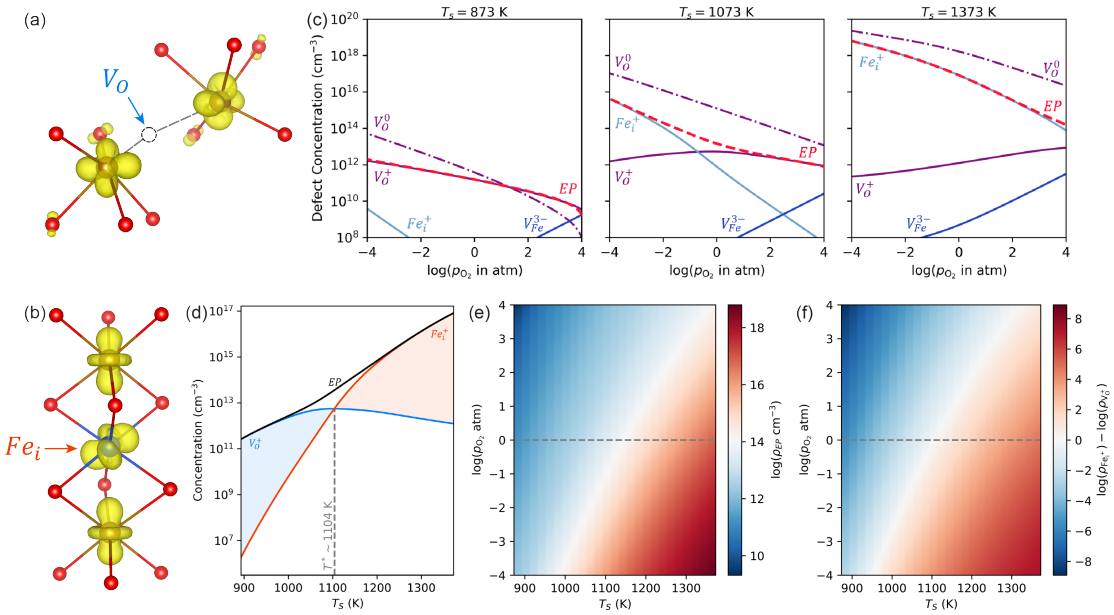

Figure 2.8: Identification of the source of free carriers in undoped Fe_2O_3. (a) Local structure and electron wavefunctions (yellow cloud) of V_O with two EPs. (b) Local structure and electron wavefunctions of Fe_i with three EPs (one of which forms at the interstitial site). (c) Intrinsic defect concentrations as a function of O_2 partial pressure in undoped hematite computed at room temperature with synthesis at $T_S = 873$, 1073, 1373 K. (d) V_O^+, Fe_i^+ and EP concentration at room temperature and $p_{O_2} = 1$ atm, as a function of synthesis temperature. (e) Polaron concentration and (f) difference between Fe_i^+ and V_O^+ at room temperature as a function of synthesis temperature (T_S) and oxygen partial pressure (p_{O_2}). In the atomic plots, gold=Fe, red=O, and blue=Fe_i. The yellow cloud is an isosurface of the polaron wavefunction with an isosurface level of 5% its maximum.

In undoped hematite, intrinsic defects such as vacancies (V_O, V_{Fe}), and interstitials (O_i, Fe_i) may form within the lattice along with the generation of carriers such as free small electron polarons (EP). Since V_O and Fe_i are n-type defects, they introduce small electron polarons into the lattice as shown in Figure 2.8a-b. In Figure 2.8c, intrinsic defect concentrations are provided at room temperature (300 K) as a function of oxygen partial pressure (p_{O_2}) in pristine hematite for

three synthesis temperatures (T_S = 873, 1073, and 1373 K). First we note that the largest presence of any defect is V_O (lowest formation energy in Table 2.4), which grows monotonically with decreasing p_{O_2}, and should be chiefly responsible for the non-stoichiometry observed in Fe_2O_3. [77] Second, we find that intrinsically excess electrons can form into free electron polarons (dashed red line labeled as EP) whereas the concentrations of free delocalized band electrons and holes are negligible (less than 10^8 cm^{-3}), consistent with experimental measurements of photoexcited electrons in Fe_2O_3.[78] Also, the intrinsic n-type nature of Fe_2O_3 is consistent with the lower formation energy of V_O and Fe_i compared with p-type defects in Table 2.4.

In terms of identifying the primary donor of these EP, the conclusions are dependent on the synthesis conditions and cannot be determined from formation energy or ionization energies alone. At T_S = 873 K, it is the case that ionized oxygen vacancies (V_O^+, solid purple line) are the primary donor to free electron polaron concentrations (overlaps with the dashed red line labeled EP). Interestingly, as the synthesis temperature is elevated, for example to T_S = 1373 K, free electron polaron concentrations are not just more abundant, they are also originating from a different source, namely, Fe interstitials (Fe_i^+, solid light blue line) in Figure 2.8c. The change in electron polaron concentration versus synthesis temperature is directly shown in Figure 2.8d at atmospheric pressure (p_{O_2} = 1 atm). We find that for synthesis temperatures below a critical temperature of ∼1104 K, V_O^+ is the primary donor, whereas above this threshold Fe_i^+ will become the primary donor. To simultaneously show the effect of oxygen partial pressure we plot a heat map of electron polaron concentration and the difference between Fe_i^+ and V_O^+ concentration in Figure 2.8e-f. The correspondence between the two figures reveals the importance of forming Fe_i in achieving higher carrier concentrations

in Fe_2O_3.

Defect	E^f (eV)	IE (eV)
V_O	2.06	0.70
Fe_i	3.46	-0.01
V_{Fe}	4.14	–
O_i	3.15	–

Table 2.4: The formation energy and first ionization energy of intrinsic defects at $p_{O_2} = 1$ atm in undoped Fe_2O_3.

The observation above is important in resolving the long-standing confusion about which defect acts as the major carrier donor in pristine hematite. Our results here suggest that previous debate over the primary donor can be explained by the transition from V_O^+ to Fe_i^+ which has not been previously identified. Furthermore, this transition highlights the varying importance of defect solubility versus ionization energy. While the ionization energy of V_O is 0.7 eV, it has the highest solubility amongst intrinsic defects, with a formation energy 1.4 eV lower than that of Fe_i. At lower synthesis temperatures (*e.g.* below 1100 K), the formation of Fe_i is sparse (less than 10^{10} cm^{-3} when $T_S = 873$ K as shown in Figure 2.8c) and by consequence V_O is the primary source of carriers. In this situation the carrier concentrations are extremely low, $\sim 10^{12}$ cm^{-3} because the Fermi level is pinned at the first charge transition level of V_O at $\sim$0.94 eV. This observation is in good agreement with recent measurements of undoped Fe_2O_3 which exhibit Fermi level positions between 0.8 and 1.2 eV. [79] When the synthesis temperature is increased or the oxygen partial pressure is decreased, the formation of Fe_i is more achievable and eventually it can act as the major donor in Fe_2O_3. In this situation, Fe_i is always ionized Fe_i^+ due to a negative ionization energy, -0.01 eV, and so the carrier concentrations of hematite can be dramatically increased

(red regions in Figure 2.8d-f where Fe_i^+ is the primary donor, EP concentrations can reach $\sim 10^{18}$ cm^{-3}). In this situation the Fermi level will approach the free polaron limit as experimentally observed. [79] It has to be noted that there is some difference between our computed polaron concentration and expeimentally measured polaron concentration for pristine hematite, which could be related to two perspectives0.[48, 80] First, experimentally, hematite are often grown and measured on substrate such as fluorine doped hematite (FTO). The interface between hematite film and substrate could actually play an important role in shifting Fermi level (carrier concentration), i.e. low and high work function contact materials could raise and lower the Fermi level at the interface, respectively.[79] Second, the carrier concentration (or Fermi level) of pristine system is very sensitive to temperature and pressure. The experimental vacuum synthesis condition is not easy to be correctly defined in simulation.

2.3.2 Tetravalent and Pentavalent Dopant Raise Carrier Concentrations

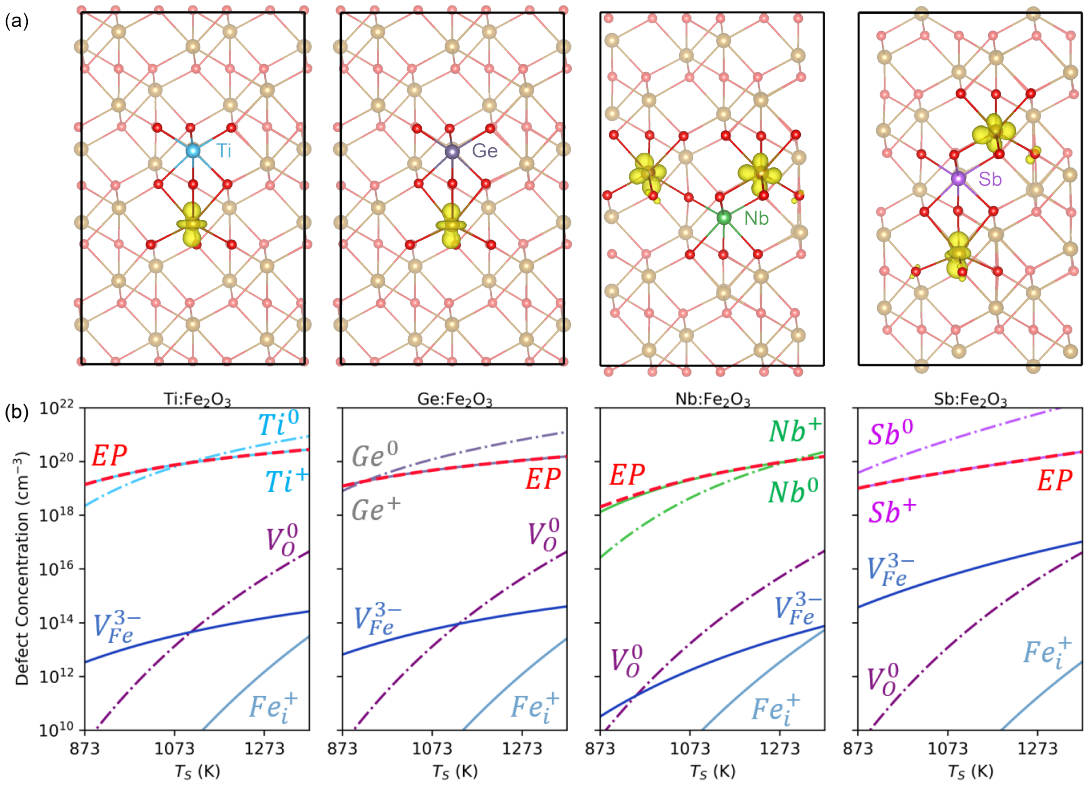

Figure 2.9: Atomic structures and defect concentrations of extrinsic dopants which are best at raising carrier concentrations in Fe_2O_3. (a) Atomic structures of Fe_2O_3 with neutral dopants Ti, Ge, Nb, and Sb. In the case of tetravalent and pentavalent the yellow cloud(s) represent the one or two nearby electron polaron(s), respectively. (b) Room temperature defect, dopant, and carrier concentrations of Ti, Ge, Nb and Sb doped hematite at $p_{O_2} = 1$ atm and as a function of synthesis temperature. In the atomic plots, gold=Fe, red=O, and the remaining colored atom is the dopant as labeled within each figure. The yellow cloud is an isosurface of the polaron wavefunction with an isosurface level of 5% its maximum.

In order to achieve higher carrier concentrations and optimize the efficiency of Fe_2O_3-based devices, extrinsic doping will be necessary. In order to broadly survey potential dopants and identify optimal doping strategies we studied all group IV, V, XIV, and XV elements. Intuitively substituting trivalent Fe ions by

Dopant	E^f (eV)	IE (eV)	ρ_{EP}(cm^{-3})	ρ_{EP}^{exp}(cm^{-3})
Ti	0.884	0.157	7.4×10^{19}	1.4×10^{19}-3.3×10^{20} [48, 81, 82, 83, 84, 45]
Ge	0.810	0.197	4.7×10^{19}	3.0×10^{19} [85]
Sb	0.546	0.247	4.1×10^{19}	1.1×10^{20} [86]
Nb	1.461	0.153	2.2×10^{19}	5.0×10^{19} [87]
Bi	1.155	0.198	1.4×10^{19}	N/A
As	0.808	0.268	1.3×10^{19}	N/A
Sn	0.883	0.255	1.2×10^{19}	6.5×10^{18}-1.1×10^{20} [88, 89, 47, 90]
Pb	1.061	0.241	9.0×10^{18}	N/A
Ta	1.224	0.260	6.1×10^{18}	N/A
Hf	1.143	0.267	4.2×10^{18}	N/A
Zr	1.230	0.259	3.7×10^{18}	N/A
V	1.137	0.344	1.0×10^{18}	N/A
P	1.926	0.348	1.8×10^{17}	N/A
Si	1.949	0.165	1.4×10^{17}	N/A

Table 2.5: Summary of representative dopants considered in this work with their formation energy (E^f), first ionization energy (IE), and induced polaron concentration (ρ_{EP}) computed at room temperature with synthesis at $T_S = 1073$ K and $p_{O_2} = 1$ atm.

tetravalent or pentavalent ions will donate electrons due to the increased valence count. In Figure 2.9 we show the results of four dopants (Ti, Ge, Nb, Sb) that we found enhance carrier concentration of Fe_2O_3 the most, at room temperature and under typical synthesis conditions, $p_{O_2} = 1$ atm and $T_S = 1073$ K. [89] We find dramatic enhancement in electron polaron concentration of Fe_2O_3 after atomic doping (dashed red line in Figure 2.9b). Specifically, whereas in undoped Fe_2O_3 free electron polaron concentrations are maximally $\sim10^{18}$ cm^{-3}, many dopants can raise electron polaron concentrations higher. When comparing all of the studied dopants together (see Table 2.5) we find that Ti-doped Fe_2O_3 has the highest yield for enhancing polaron concentration which exhibits concentrations of 10^{20} cm^{-3}, in great agreement with experimental measurement. [83, 45, 81, 91, 82] Meanwhile our predictions of Ge and Sb as effective dopants in raising carrier concentrations to $10^{19} - 10^{20}$ cm^{-3} are consistent with experimental measurements as well.[86, 85] The excellent agreement with experiments on various dopants highlight the robustness of our first-principles prediction of defect properties and the depiction of

carriers as small electron polarons. Based on our carrier concentration calculation results, we predict that Ti, Ge, Nb and Sb are excellent candidates for further investigation as potentially promising dopants for enhancing PEC performance in hematite.

In Table 2.5, some correlation between the dopant formation energy and the carrier concentration (ρ_{EP}) is apparent, while the ionization energy seems less important. The best example of this is the case of P and Si which have nearly identical formation energies (1.926 and 1.949 eV), and despite a remarkable difference in their ionization energy (0.35 and 0.17 eV), P doping is predicted to have only slightly larger electron polaron concentrations than Si ($1.8\times\ 10^{17}$ and $1.4\times\ 10^{17}$ cm^{-3}). Meanwhile, in Figure 2.10a we show there is a dramatic change in carrier concentrations for Si doping as a function of synthesis temperature, which underperforms P doping at low temperatures but then outperforms at higher temperatures. This result is reminiscent of Figure 2.8d, and touches on the outstanding question of what is most important in determining the ability for a dopant or defect to raise carrier concentrations, *e.g.* low formation energy or low ionization energy?

2.3.3 Critical Role of Synthesis Temperature

In order to directly address this question, we performed linear regression on the larger data sets obtained from dopant calculations to analyze the importance of dopant formation energy or solubility against that of ionization energy. Figure 2.10b shows the predictive score (*e.g.* the coefficient of determination R^2) of modeling the data sets such as those shown in Figure 2.10c-e by three cases. First (red line in Figure 2.10b) the polaron concentration is predicted by a single exponential term from the dopants ionization energy (e^{IE}). Second (in blue) a single

exponential from the dopants formation energy (e^{FE}) was used to predict the polaron concentration. Finally (in black) the polaron concentration is predicted by both terms ($e^{IE} + e^{FE}$). When using both terms (black), the predictive score is typically exceeding 0.85 which signifies that these two dopant properties uniquely determine the induced electron polaron concentrations. Formation energy determines how much dopants can be incorporated into the crystal lattice of hematite while ionization energy determins how much dopants can be ionized.

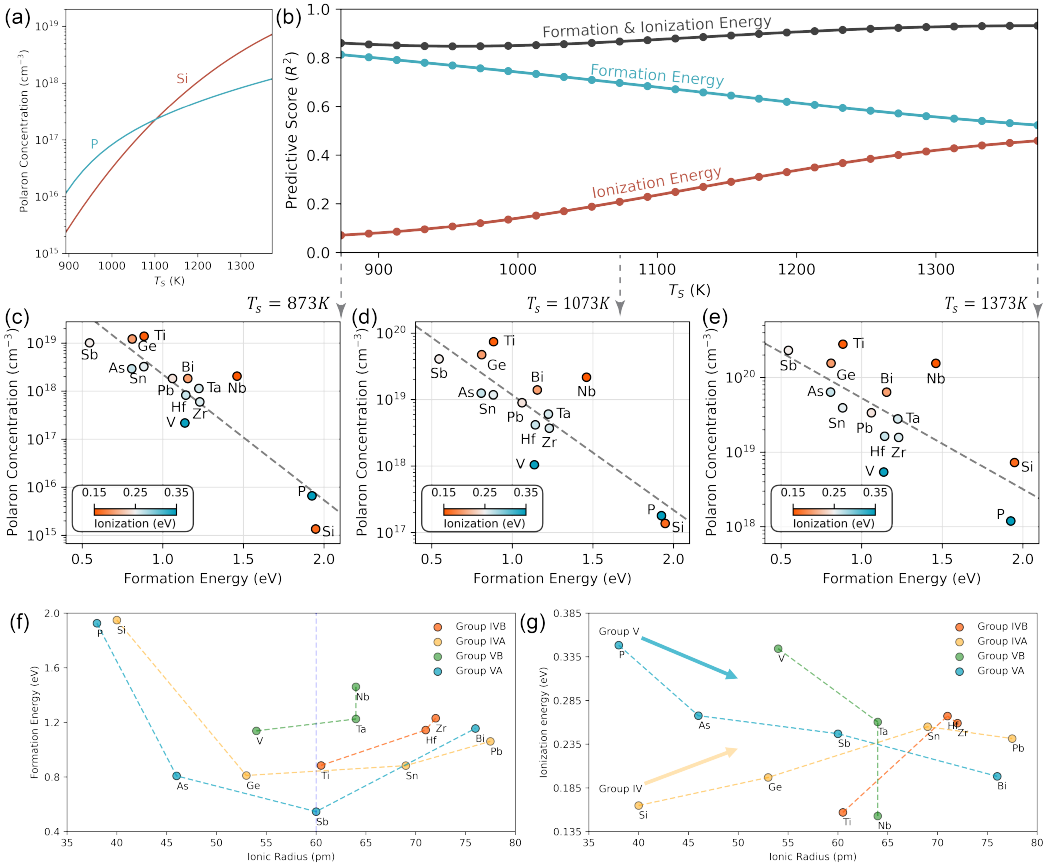

Figure 2.10: Resolving the importance of dopant formation energy and ionization energy in determining carrier concentrations of Fe_2O_3. (a) Electron polaron concentration change of Si (red) and P (blue) doped hematite at room temperature and $p_{O_2} = 1$ atm as a function of synthesis temperature (T_S). (b) Predictive score of linear regression models on the induced carrier concentrations using dopants formation energy (blue), dopants ionization energy (red), or both (black). Electron polaron concentrations at room temperature and $p_{O_2} = 1$ atm for various synthesis temperatures: (c) 873, (d) 1073, and (e) 1373 K, plotted against dopant formation energies and with dopant ionization energies distinguished in colors. (f) The correlation between formation energy and ionic radius of different dopants. (g) The correlation between ionization energy and ionic radius of different dopants.

More importantly, the decomposition into dopant formation energy (blue) or dopant ionization energy (red) reveals the relative importance of these two factors in determining the induced carrier concentrations. For lower temperatures the solubility of the dopant (formation energy, $R^2 \sim 0.8$) almost uniquely deter-

mines how well the dopant is able to raise carrier concentrations, while ionization energy is significantly less important ($R^2 \sim 0.1$). This explains the above observation that P and Si, which have similar formation energy (1.926 and 1.949 eV), have nearly identical polaron concentrations ($\sim 10^{17}$ cm^{-3}) at low synthesis temperature, despite significant difference in their ionization energy (0.348 and 0.165 eV). It can also explain how V_O, despite a significantly larger ionization energy (0.7 eV) than Fe_i (-0.01 eV), is still the major donor in Fe_2O_3 at lower synthesis temperatures due to its lower formation energy (2.06 vs. 3.46 eV). Meanwhile, as the synthesis temperature is elevated poor solubility can be overcome and dopants ability to ionize is weighted equally with its formation energy (blue and red lines approach $R^2 \sim 0.5$ as synthesis temperature is increased in Figure 2.10b). This helps to explain the dramatic increase in polaron concentration under Si doping shown in Figure 2.10a, as well as the transition from V_O to Fe_i as the source of carriers in undoped Fe_2O_3 shown in Figure 2.8c-f. Beyond this we conclude that less soluble dopants such as Si, require higher synthesis temperatures to reach carrier concentrations seen for more soluble dopants such as Ti, Ge, and Sb (Figure 2.9b).

We also explicitly consider the effect of entropy to the total formation energy. Entropy contributes formation energy from two aspects: configurational entropy and vibrational entropy. Configurational entropy is depending on the number of different possible configurations for the defect to be placed in hematite lattice, which always stabilizes the dopant formation. It can be separated into two parts, entropy from ideal solution and excess entropy of mixing. Since the second term is small compared to the first term,[92, 93] in this work, the configurational entropy of ideal solution is used to approximate the total configurational entropy. On the other hand, the vibrational entropy is computed by taking the difference of vibrational entropy between doped species and undoped species. We chose Sn and

Nb as two representatives for group IV and V elements and computed the entropy correction of them to the formation energy and found that their contribution to the total formation energy is 0.1-0.2 eV, which does not affect the defect concentration significantly. Based on that, formation energy without entropy correction is used across the whole paper.

Some general trends between formation energy/ionization energy and ionic radius of dopants within each group are also observed. The formation energies of dopants in each group have a parabolic shape with respect to their ionic radius (Figure 2.10f). Some dopants such as Ti and Sb have small formation energies, while some others such as P and Pb have much lower solubility. A radius around 60 pm seems to be a sweet spot, which is slightly smaller than that of the ionic radius of Fe^{3+} (64.5 pm) due to the repulsion caused by polaron formation. A dashed line at 60 pm is drawn to guide the eyes. On the other hand, in Figure 2.10g, it can be noted that the trends for group IV and group V elements are different. For group V elements, ionization energy is generally getting smaller with ionic radius. However, the trend is opposite for group IV elements, ionization energy is generally increasing with ionic radius, which could be related to the electronic configurations of the dopants after ionization. For instance, group IV dopants have inert gas electronic configurations after ionization energy, which are very stable and lower the ionization energy compared to group V dopants overall. In addition, with the increase of ionic radius, the electronic configurations of ionized group IV dopants are getting less stable, which explains the upside trend of them. These trends could help experimentalists make reasonable choices about what dopants to choose when there is only very limited information such as ionic radius.

2.3.4 Conclusions

In summary, this work demonstrates the role of defects, dopants, and small polarons in determining carrier concentrations in a prototypical oxide, Fe_2O_3. This work identifies from first-principles calculations that the critical role of synthesis temperature on small polaron carrier concentration in hematite, both pristine and doped. For pristine hematite, the major electron polaron donor switches from V_O to Fe_i with the ramp up of synthesis temperature because the high formation energy of Fe_i can be overcome at higher temperature and its low ionization energy makes it easier to be ionized compared to V_O. From our survey of all group IV and V dopants, we find that Ti, Ge, Sb, and Nb, are able to achieve the highest free carrier concentration in Fe_2O_3. The linear regression on our data set of these dopants under different chemical conditions and synthesis temperatures reveals that dopant solubility is more important in determining the improvement on carrier concentration in Fe_2O_3. Our study suggests that lower solubility dopants such as Si will require elevated synthesis temperatures for them to be incorporated into the lattice. This work addresses several outstanding questions for hematite but will also be applicable to other polaronic oxides, therefore, our study has broader interests to fundamentally designing more efficient oxide-based energy conversion and storage devices.

2.4 Dopant Clustering in Fe_2O_3

In our 2021 work published in Chemistry of Materials [94], we investigated the doping bottleneck in Fe_2O_3 and demonstrated it is caused by a novel form of dopant clustering which is mediated by dopant and small polaron interactions which give rise to dopant pairs which resemble electric quadrupoles and can form at very low concentrations. As we have discussed above, applications of hematite and other transition metal oxides are limited by small polaron formation. To overcome these limitations, several efforts have been made to dope hematite by tetravalent ions that yield improved photoelectrochemical performance of hematite photoelectrodes [79, 95, 47, 88, 96, 91, 82, 97, 89, 98]. While the performance can be moderately improved via group IV and XIV dopants, the optimal doping concentration strongly varies with each individual dopant,[96, 91, 82, 97, 89, 98] thereby requiring extensive experimental testing each time [99].

For example, researchers[91, 82] have found that Ti-doped hematite photoanodes had the highest carrier density and photocurrent at a doping concentration of around 0.1%. Meanwhile, several works[97, 89, 100] have found that optimal PEC performance with Sn-doped hematite photoanodes was achieved at 3% Sn doping concentration. In all of these cases there is a direct correlation between optimizing carrier density and PEC performance; however, the mystery of extremely low optimal doping concentration for certain dopants remains elusive. Two possible mechanisms could be responsible for the doping bottleneck: compensation by oppositely-charged defects or the clustering of dopants. However, the concentration of intrinsic p-type defects is expected to be negligible in Fe_2O_3[20], which leaves a strong rationale for the clustering of dopants being the cause of low optimal doping concentration. On the theoretical side, group IV and XIV dopants in Fe_2O_3 have been previously investigated from first-principles,

focusing on their electronic structure, formation energy, and polaron hopping barrier[12, 101, 50, 51]. However, these studies cannot explain the low optimal doping concentration observed experimentally.

In this work, we will reveal the origin of the extremely low optimal doping concentration in Fe_2O_3 through a joint theoretical and experimental study. We suggest a novel form of dopant clustering in polaronic oxides and conclude its critical role on determining carrier concentration. We begin by detailing our computational methodology, including our proposed model for disentangling the effects of dopant clustering. Next, the electronic structure of isolated and clustered Sn dopant formation is provided, which resembles an electric dipole and quadrupole, respectively. The binding energy of the clustered dopants as quadrupoles is computed to validate their thermodynamic stability. Then, the formation of the theoretically predicted Sn-Sn pairs are confirmed by experimental EXAFS, and their mechanistic origin is unraveled theoretically in terms of electrostatic, magnetostatic and strain effects. Finally, carrier concentrations of Fe_2O_3 with and without dopant clustering are computed to elucidate the underlying mechanism of the doping bottleneck. At the end, essential design principles are provided to yield higher conductivity in polaronic oxides for the advancement of energy conversion applications.

2.4.1 First-Principles Calculations

All Density Functional Theory (DFT) calculations were carried out using the open source plane-wave code QuantumESPRESSO [52] with ultrasoft pseudopotentials [53] and an effective Hubbard U [11] value of 4.3 eV for Fe $3d$ orbitals [12, 59]. This U value is chosen for its ability to reproduce the bandgap of hematite ($\sim$ 2.21 eV) but also has shown to capture physics of small polarons such as the

polaron hopping barrier [59, 12]. Plane-wave cutoff energies of 40 Ry and 240 Ry were used for wavefunctions and charge density, respectively. All calculations were performed with a $2 \times 2 \times 1$ supercell (120 atoms) of the hexagonal unit cell with a $2 \times 2 \times 2$ k-point mesh for integration over the Brillouin zone. A $3 \times 3 \times 1$ supercell was also tested to ensure convergence with supercell sizes (see supercell convergence in SI Table S1). The consistency between these supercell sizes also validates that the present calculations are in the dilute limit and while the Sn at Fe concentrations of the aforementioned supercells are 2.08% and 0.93%, respectively, these concentrations do not yield interactions between dopant periodic images (even for systems with two dopants, see SI Figure S1). The actual concentrations of dopants are determined by evaluating charge neutrality directly from dopant formation energies at a synthesis condition as discussed later in this section. Finally, we note that we use the same U value for systems with dopants. While it is true that changing U will vary the bandgap (in this case the conduction band shifts due to U correction on Fe $3d$), it has been shown that the formation energies computed with different U values were very similar and the ionization energies changed little when referenced to the free polaron level instead of the CBM for Fe_2O_3. [12]

2.4.2 Electrostatic, Magnetostatic, and Strain Model of Binding Energy

We will later demonstrate that single dopants resemble dipoles, while dopant-pairs resemble quadrupoles. Here, we demonstrate our analysis on the physical contributions to the quadrupole binding energies computed from first-principles as we will discuss later, by using an electrostatic, magnetostatic, and strain (EMS) model. In this model, the binding energy is obtained by separately computing

electrostatic (Δ_{quad}^{elec}), magnetostatic (Δ_{quad}^{mag}), and strain (Δ_{quad}^{strain}) contributions. For the electrostatic effect, we compute the electrostatic potential contribution to binding energy (Δ_{quad}^{elec}) by taking the difference between the quadrupole (quad) and twice the dipole configuration (dipole):

$$\Delta_{quad}^{elec} = \frac{k\alpha}{2\epsilon_r}\left(\sum_{ij}^{quad}\frac{q_i q_j}{r_{ij}} - 2\sum_{ij}^{dipole}\frac{q_i q_j}{r_{ij}}\right). \tag{2.4}$$

Here k is the Coulomb constant, α is the Madelung constant, and ϵ_r is the relative permeability (22.9 for hematite). [102] The summation goes over all polarons and dopants i and j, with relative charges q_i and q_j, and physical separation r_{ij}.

Magnetic effects were computed using the Heisenberg Hamiltonian $H_{spin} = -\frac{1}{2}\sum_{ij} J_{ij}\hat{S}_i \cdot \hat{S}_j$, where J_{ij} is the magnetic coupling between the spins of the i^{th} and j^{th} ion, and $\hat{S}_i$ is the spin of the i^{th} ion. Here we use the magnetic exchange coupling constants computed from Ref. [103], which provided magnetic couplings for both the superexchange between two Fe(3+) or between two Fe(2+), as well as the double-exchange between Fe(3+) and Fe(2+). For high-spin Fe(3+) and Fe(2+), the value of $\hat{S}_i$ is 5/2 and 2, respectively, while the spin of the tetravalent dopants is zero (hence the magnetic interaction with these dopants is always zero). In this way, we can compute the magnetic contribution to the binding energy from the magnetic energy of the quadrupole system subtracted by two times of the dipole system:

$$\Delta_{quad}^{mag} = -\frac{1}{2}\left(\sum_{ij}^{quad} J_{ij}\mathbf{S}_i \cdot \mathbf{S}_j - 2\sum_{ij}^{dipole} J_{ij}\mathbf{S}_i \cdot \mathbf{S}_j\right). \tag{2.5}$$

In this work, we assume J_{ij} between two Fe ions before and after doping are the same, as lattice distortions are generally small compared to Fe distances. With

the above consideration and the non-magnetic nature of dopants, our computed magnetic energy is identical for all the dopants.

Finally, in order to compute the strain contribution to the binding energy, we evaluated the change in energy induced by lattice distortions before and after doping. As usual, taking this energy for the quadrupole system and subtracting twice the dipole system:

$$\Delta_{quad}^{strain} = E_{quad}^{strain} - 2E_{dipole}^{strain}. \tag{2.6}$$

Here E_X^{strain} is the strain energy of system X, computed as a difference of total energy of the pristine system with its equilibrium geometry and with relaxed geometry from the doped system (first relax with dopants then substitute back Fe atoms to keep the same composition as pristine Fe_2O_3). We note a similar approach was used in Ref. [104] to evaluate strain energies.

2.4.3 Dopant Clustering by Multipole Formation

Substitutional doping by group IV and XIV elements was investigated theoretically by replacing a single Fe site by the dopant (X). Consistent with previous studies [12, 50] and experimental observation,[47, 88] we found this process yields the formation of small electron polarons corresponding to the identification of Fe(2+) after replacing Fe(3+) by the tetravalent dopant $X(4+)$. (Note in this paper we use the notation $X(i)$ to denote an ion X with valency i). The electronic structure of the single Sn-doped system is shown in Figure 2.11b right panel, wherein the band structure exhibits a flat isolated occupied state in the gap corresponding to the small electron polaron (EP) with tight spatial localization similar in size to the Fe−O bond lengths. Likewise, the projected density of states (PDOS) in Figure 2.11b shows a sharp isolated peak composed mostly

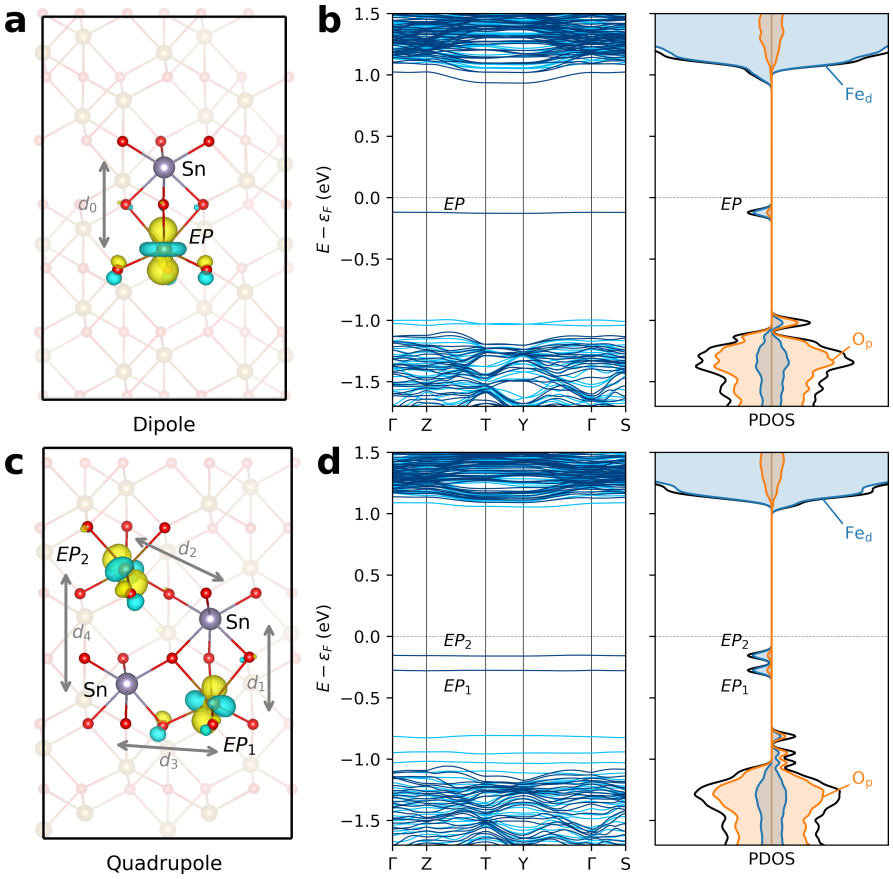

Figure 2.11: Electronic structure of Sn-doped Fe_2O_3. (**a**) Wavefunction of the small electron polaron (EP) in the single Sn-dopant system where the EP and Sn form a dipole. (**b**) Band structure and projected density of states (PDOS) of the dipole Sn system. (**c**) Wavefunctions of the two EP in the two Sn-dopant system where the two EP and two Sn form a quadrupole. The Sn-Sn separation is 3.784 Å. (**d**) Band structure and PDOS of the quadrupole Sn system. For the atomistic plots, gold=Fe, red=O, grey=Sn, and the yellow/blue (+/−) cloud is the isosurface of the polaron wavefunction (the isosurface level is 1% of the maximum). In the band structures, dark/light blue is spin up/down and ε_F is the Fermi energy.

by Fe $3d$. The wavefunction of the EP is shown in Figure 2.11a with a clear d_{z^2} character. The EP forms at the Fe site nearest to the Sn dopant with a Sn$-EP$ distance of 2.981 Å (d_0 in Figure 2.11a).

To investigate dopant-dopant interactions, we placed a second Sn dopant in the lattice. All possible Sn-Sn pair configurations were tested, and the lowest energy configuration was clearly identified (see SI Figure S2, S3 and Table S2). The electronic structure of this corresponding configuration is shown in Figure 2.11c-d, which exhibit the formation of two EP states. We find the asymmetry of the local structure, which is a natural consequence of the corundum crystalline form, causes a noticeable energetic difference of 0.12 eV between EP_1 and EP_2. Specifically, in Figure 2.11c, EP_1 has distances to the two adjacent Sn of $d_1 = 3.011$ and $d_2 = 3.129$ Å, whereas EP_2 has distances of $d_3 = 3.510$ and $d_4 = 4.112$ Å. The proximity of EP_1 to the Sn yields a lower energy state relative to EP_2. Lastly, the theoretically predicted Sn-Sn distance of 3.784 Å closely matches experimentally observed Sn-Sn peak in EXAFS data of Sn-doped hematite samples (as discussed in next section).

The remaining group IV (Ti, Zr, Hf) and XIV (Si, Ge, Sn, Pb) dopants were also simulated in both single and pair dopant configurations with negligible differences in their electronic structure and polaron configurations from Sn (all electronic structures are presented in SI Figure S4-S9). Note for the present study, the configuration of two dopants is chosen to be the same for all dopants for the purpose of discussing chemical trends, as predicted by the case of Sn. It is possible that dopants may vary in their exact pair dopant configuration, for example see SI Table S3. This variation does not affect the main implications on carrier concentration we conclude later. Most importantly, the stable configuration of a single tetravalent dopant (such as Sn) resembles an electric dipole where the Sn

and EP represent positive and negative charge centers, respectively. In this way the system with two dopants resembles an electric quadrupole (two positive Sn centers and two negative EP centers). Therefore, we will denote the single doped system as a first-order multipole (dipole) system and the pair doped systems as a second-order multipole (quadrupole) system. To examine the thermodynamic stability of dopant-polaron quadrupole, we studied their binding energy (Δ_{quad}) from two separate dipoles:

$$\Delta_{quad} = E^f(quad) - 2E^f(dipole). \tag{2.7}$$

Here, $E^f(X)$ is the formation energy of the system with neutral dopants in a configuration X (e.g. quadrupole or dipole dopant system). The quadrupole binding energy was evaluated for all group IV and XIV dopants considered in this study. We observed that the binding energy for all dopants is negative (~ -0.1 to -0.2 eV), as shown in Table 2.6 (Δ^{DFT}_{quad}), indicative of a strong tendency for dopants and polarons to aggregate. We note that we expect dopant clustering occurs during the cooling process from synthesis temperature (over one thousand K here) down to room temperature. At a synthesis condition, dopants will be all ionized and the binding of dopants into quadrupoles will not occur. Since all the binding energies are lower than kT at room temperature, it is expected that the quadrupoles are stable at room temperature.

2.4.4 Experimental Evidence for Dopant-Pair Formations

Extended x-ray absorption fine structure (EXAFS) data at the Sn edge were collected at SSRL for two Sn doped Fe_2O_3 samples, with Sn nominal concentrations of 0.1% and 1.0%. (Sn concentration of 1% corresponds to replacing 1 out of 100 Fe with Sn; measured concentrations are 10-20% lower, see Table S4 in SI

for details). Synthesis methods are detailed in the SI. A standard fluorescence set-up (32 element Ge fluorescent detector) was used with the sample set at 45° to the beam, and an Oxford helium cryostat maintained the temperature at 10 K. Details about the data collection and reduction are in the SI section on EXAFS characterization. The r-space data are plotted in Figure 2.12 for the 0.1% Sn and 1.0% Sn samples. For the 0.1% Sn sample (Figure 2.12a), the amplitudes of the further neighbor peaks are quite large and the data can be well fit (solid orange line) to the hematite structure, with a small expansion for the Sn-Fe pairs compared to hematite; roughly 0.1 Å for closer pairs but only 0.02 Å for Fe neighbors near 3.7 Å. This is the expected behavior around a substitutional dopant site when the dopant valence Sn(4+) is higher that the host valence Fe(3+), and this behavior has been observed in other similar situations.[105]. The further neighbor Sn-O peaks are expected to contract very slightly, but because these small peaks overlap the larger Sn-Fe peaks, the pair-distances fluctuate too much. The first O shell, although split in hematite, collapses to a single peak with an average Sn-O distance of 2.05 Å, very close to the averaged first neighbor distance in hematite, 2.03 Å; this is a competition between a larger ionic radius for Sn(4+), and larger electrostatic force between Sn(4+) and O(2−).

On the other hand, the EXAFS r-space plot for 1% Sn sample is quite different (Figure 2.12b). The data up to 3 Å are very similar to that for 0.1% Sn - i.e. the phase of the real part of the Fourier transform, R(r), is the same. However in the range 3-3.8 Å, the phase changes dramatically and a dip develops in the amplitude near 3.3 Å which has the shape of an interference dip. It occurs close to the expected position for the Sn-Fe peak in an EXAFS plot (actual distance ∼3.7 Å: note that there is a calculable phase shift of peaks in r-space plots to lower r). These data can't be fit to a simple distorted hematite model and the shape of

R(r) suggests that another peak is present (see SI Figure S11). Consequently, an additional peak, corresponding to one Sn-Sn pair with a distance close to 3.7 Å, was included in the fit. The number of Sn-Fe pairs was correspondingly reduced from 6 to 5. This yielded the good fit (details in SI) shown in Figure 2.12b, and is a clear evidence that Sn-Sn pairs have formed. Remarkably, this Sn-Sn pair distance (∼3.7 Å) matches the theoretically predicted distance of Sn-Sn pair (3.784 Å) shown above.

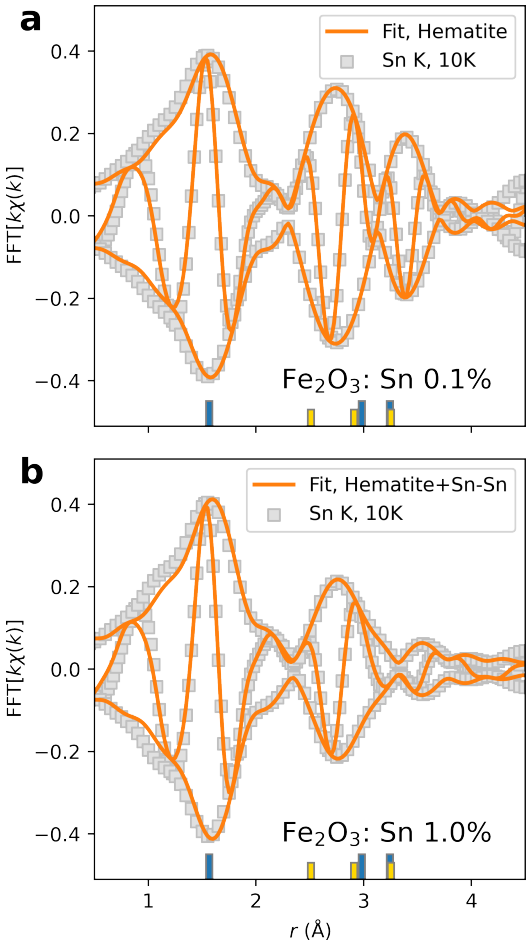

Figure 2.12: EXAFS r-space data at the Sn K edge, for (**a**) 0.1% and (**b**) 1% Sn in Fe_2O_3. The plot for 0.1% Sn also shows a fit to the hematite structure; good agreement is obtained with a slight contraction of the Sn-O pairs and a slight expansion of the Sn-Fe pairs. At 1% Sn, the EXAFS changes significantly. Although the first two peaks are very similar, the region from 3-3.8 Å is quite different, particularly the shape of the phase (fast oscillating function), and a dip develops near 3.3 Å. These data cannot be fit to the hematite structure. The data suggest that there is another peak present; in the fit shown in part (**b**), one of the Fe neighbors at ∼3.7 Å is replaced with a Sn atom, forming a Sn-Sn pair. This leads to the excellent fit shown in (**b**). Fourier transform range, 3.5-13 $Å^{-1}$; fit range in r-space, 1.1-4.2 Å for both plots. In both figures, the blue and gold bars at the bottom indicate the position of Sn-O and Sn-Fe peaks, respectively, in undistorted hematite. The bar positions include the known shifts in r.

2.4.5 Mechanisms of Dopant-Polaron Binding into Quadrupoles

After confirming the existence of Sn-Sn clustering both theoretically and experimentally, we turn to investigate the mechanisms of their formation. Above the analogy was made between the single Sn-doped system and electric dipoles, so in order to probe this electrostatic interaction, we plotted the total energy of the single Sn-doped system as a function of Sn-polaron distance, as shown in Figure 2.13a. The computed total energies were fitted to a Coulomb potential ($-a/r + b$) with the fitted values of $a = 0.658$ eV $\cdot$ Å and $b = 0.230$ eV, and a coefficient of determination (R^2) of 0.85. This validates a clear electrostatic attraction between the two bodies with opposite charges like a dipole. Furthermore, we find that b is close to the value of ionization energy of Sn (0.25 eV), as expected.

However, this Coulombic interaction competes with other factors. For example in Mo doped $BiVO_4$[106], strain causes short-range repulsion between the dopant and polaron, and dominates over the Coulombic attraction.[106, 107] We find this was also reflected in the computed quadrupole binding energies (Δ_{quad}), as shown in Figure 2.13b, where we plotted them versus the ionic radius (R_I) of each dopant. Specifically, there is a roughly positive correlation between the ionic radius and the quadrupole binding energy. We attribute this to the compensatory size effects of the dopant and the polarons. Namely, the replacement of Fe(3+) with ionic radius of 64.5 pm by Fe(2+) with ionic radius of 78.0 pm, yields an expansion strain at the lattice site. This strain can be reduced by smaller radii dopants (e.g. Ti, Ge, Si) that will increase the magnitude of Δ_{quad} as shown in Figure 2.13b, or enhanced by larger radii dopants (e.g. Sn, Hf, Zr, Pb) that will decrease the magnitude of Δ_{quad} towards zero. We note that the case of Ti, an outlier in Figure 2.13b, possess stronger correlated $3d$ orbitals, which in turn exhibit stronger electron localization, may compensate local expansion from small

polarons and lower its binding energy (similar to Si which intrinsically is smaller than the rest).

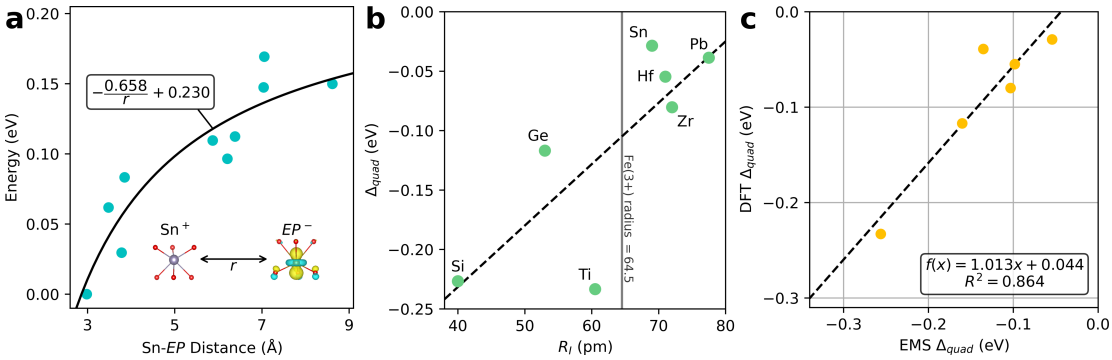

Figure 2.13: Mechanisms of dopant-polaron binding in Fe_2O_3. (**a**) Total energy of Sn-doped hematite system as a function of the Sn$-EP$ distance. The black curve represents a simple Coulomb potential fit which has an R^2 value 0.85, supporting the intuition of an electrostatic interaction between the Sn (positive charge) and EP (negative charge) centers. (**b**) Quadrupole binding energy (Δ_{quad}) of group IV and XIV dopants in hematite computed by Eq. 2.7, plotted against the ionic radius of the dopant [108] (R_I; valency 4+, coordination VI). (**c**) Computed Δ_{quad} by Eq. 2.7 plotted against those computed with the EMS model in Eq. 2.8. The linear fit relation ($f(x)$) between these models is shown in the inset box.

Therefore, it is necessary to consider electrostatic and strain effects simultaneously, and also include magnetic effects (binding energies may also be modified by the antiferromagnetism of Fe_2O_3). Hence, we propose a model of the quadrupole binding energy based on electrostatic, magnetostatic, and strain effects (abbreviated to EMS), in order to analyze the importance of each contribution:

$$\Delta_{quad}^{EMS} = \Delta_{quad}^{elec} + \Delta_{quad}^{mag} + \Delta_{quad}^{strain}. \tag{2.8}$$

Here Δ_{quad}^{elec}, Δ_{quad}^{mag}, Δ_{quad}^{strain}, correspond to electrostatic, magnetostatic, and strain contributions to the quadrupole binding energy, respectively. The exact formulation for each component of the EMS model is detailed in the methods section

(Eq. 2.4−2.6) and the results are summarized in Table 2.6. We evaluate how well this model reproduces DFT calculations by plotting them against each other in Figure 2.13c. The linear fitting shows adequate agreement between the simple EMS model and our exact DFT calculations (with a slope near unity and an R^2 value of 0.864), which justifies its use for interpreting the DFT binding energies.

As shown in Table 2.6, each of the three components contributes significantly to the overall quadrupole binding energy. The electrostatic interaction (Δ_{quad}^{elec}) is typically the most dominant factor, and intuitively it is chiefly responsible for the attraction of dopants into the quadrupole configuration. Interestingly, we also found a non-negligible contribution from magnetostatic interactions (Δ_{quad}^{mag}, 42 meV) which further participates in the binding of quadrupoles. This effect is non-trivial but is an indirect consequence of placing non-magnetic dopants next to each other, which in-turn breaks fewer antiferromagnetic interactions and yields a lower energy configuration when dopant-pairs form. In contrast, the effect of strain (Δ_{quad}^{strain}) typically mitigates the formation of dopant-pairs (increases the system's energy with clustering) due to the accumulation of lattice distortion. However, as aforementioned, this effect can be compensatory in the dopant cases with smaller ionic radii than Fe(3+), which can pack more efficiently next to the polarons with larger ionic radius as specified in Figure 2.13b.

Dopant	Δ_{quad}^{elec}	Δ_{quad}^{mag}	Δ_{quad}^{strain}	Δ_{quad}^{EMS}	Δ_{quad}^{DFT}
Si	-0.184	-0.042	-0.33	-0.553	-0.227
Ge	-0.188	-0.042	0.07	-0.160	-0.117
Ti	-0.175	-0.042	-0.04	-0.256	-0.233
Sn	-0.188	-0.042	0.18	-0.054	-0.029
Hf	-0.188	-0.042	0.13	-0.098	-0.055
Zr	-0.192	-0.042	0.13	-0.103	-0.080
Pb	-0.204	-0.042	0.11	-0.135	-0.039

Table 2.6: Collected values of the binding energy for group IV and XIV dopants in Fe_2O_3 computed by DFT (Δ_{quad}^{DFT}) or with the EMS model (Δ_{quad}^{EMS}) as in Eq. 2.8. The various components of the EMS model are tabulated as well including the electronic (Δ_{quad}^{elec}), magnetic (Δ_{quad}^{mag}), and strain (Δ_{quad}^{strain}). All values are given in eV.

2.4.6 Effects of Dopant Clustering on Polaron Concentrations

Lastly, we discuss the effects of dopant clustering, which we will show to be responsible for the low optimal doping concentrations of Fe_2O_3 observed experimentally. The computed thermodynamic charge transition levels (CTLs) are displayed in Figure 2.14a for both the dipole (single dopant) and quadrupole (pair dopants) systems. In quadrupole systems, there are two charge transition levels (gold and orange lines) which correspond to the ionization energies of two electron polarons (as shown in Figure 2.11c). Because quadrupoles yield consistently lower second CTLs, they possess very high second ionization energy ranging from 0.34 eV to 0.48 eV (the orange lines in Figure 2.14a, nearly doubled the ionization energies of corresponding single-doped systems denoted by the blue lines). Therefore, the ionization of both electrons after quadrupole formation is nearly impossible. On the other hand, the first ionization energies of quadrupoles com-

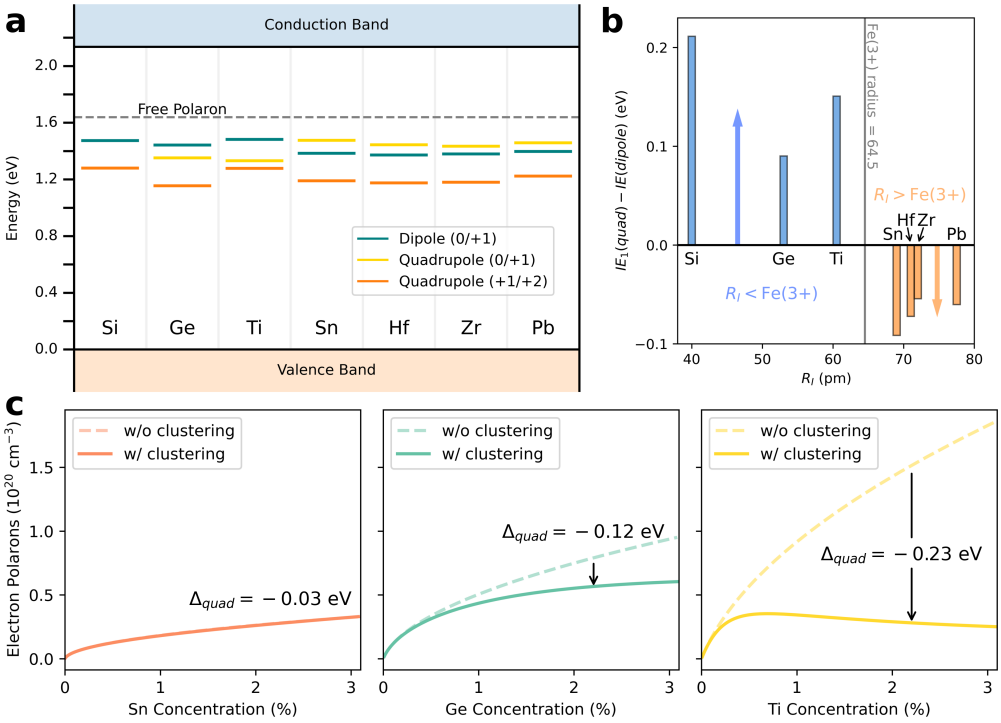

Figure 2.14: Effects of quadrupole binding on carrier concentration in Fe_2O_3. (**a**) Band diagram of various doped systems either single-doped (dipole) or with two dopants (quadrupole), the solid horizontal lines represent the thermodynamic charge transition levels (CTLs), and the ionization energy corresponds to the separation of the CTLs to the free polaron line (dashed grey line). (**b**) Change in the first ionization energy when quadrupoles are formed vs. ionic radius (R_I). Notably, when the ionic radius of dopants is below that of Fe(3+), the ionization energy is increased (as shown in blue bars), whereas it is decreased when the dopant radius is larger (as shown in orange bars). (**c**) Computed free electron polaron concentration as a function of dopant concentration for Sn, Ge, and Ti, with and without the effect of clustering (i.e. quadrupole formation).

pared to the ones of dipoles shift in a manner correlated with the ionic radius as shown in Figure 2.14b. In particular, dopants with a radius larger than the host site (Fe(3+)) have a lower first ionization after quadrupole formation (orange bars in Figure 2.14b) and vice versa.

To show how dopant clustering affects carrier concentration quantitatively, we compute the polaron concentrations with and without the effect of dopant clustering for three representative cases: Sn, Ge, and Ti in Figure 2.14c. Equilibrium polaron concentrations are computed following the defect formation energy and charge neutrality approach as detailed in the method section.[20, 19]. We then introduce clustering in the theoretical synthesis process, by considering the probability at which two dopants form into a quadrupole following a thermal Boltzmann distribution (details in the SI section on probability of quadrupole formation). As dopant-dopant pairs form during cooling process from synthesis temperature to room temperature, an intermediate temperature of $T = 500$ K is chosen as an approximate temperature where pairs start to form. We show the trends among different dopants remain the same for different temperatures (see SI Figure S13). In Figure 2.14c, we show that polaron concentration is reduced due to clustering (solid lines) compared to the case without clustering(dashed lines), and the magnitude of this reduction is closely related to their binding energy (Δ_{quad}) in Table 2.6. Specifically, dopants such as Ge and Ti with large binding energies show significant trapping of polarons due to clustering in the second and third panels of Figure 2.14c.

In order to avoid the adverse effects of clustering, Ti will be better suited to be doped at very low concentrations into hematite. This explains the experimentally observed very low optimal doping concentration of Ti in hematite (about 0.1%).[91, 82] Furthermore, co-doping Ti with another dopant less prone

to clustering may offer higher performance in hematite, which explains the success of recent co-doping strategies.[109, 110, 111] On the other hand, the small quadrupole binding energy of Sn makes it easier to dope Sn into hematite to higher concentrations without experiencing an immediate bottleneck. This explains why the optimal doping of Sn into hematite (3%) is an order of magnitude larger than Ti.[97, 89, 100] If neglecting the effect of clustering, Ti would be a better dopant than both Sn and Ge (see dashed lines in Figure 4c, which shows that Ti has predicted to contribute the highest carrier concentration without clustering). Therefore, to unlock the potential of Ti, it is necessary to mitigate its strong tendency of clustering. A strategy of co-doping Sn and Ti in hematite may offer the most effective strategy for maximizing performance of hematite photoanodes. Alternatively, co-doping of divalent dopants, such as Mg, has been shown to relieve lattice distortion and can also offer further improvement to PEC performance [112]. Ultimately, Ge is seen as the best dopant in group IV and XIV with the highest polaron concentration, which outperforms Sn and Ti in Figure 2.14c.

Finally, we remark that here we have focused on formations of dopant clustering at an early stage, which dominate at relatively low concentrations of doping in hematite. We also tested higher-order multipole clustering such as 'hexapole' formation in hematite (e.g. three Sn dopants with the three introduced EP, details in SI section on higher-order multipoles and SI Figure S14). We found that hexapoles also have a negative binding energy, and thus it is entirely possible that dopant clustering may grow even larger than the second-order multipoles we considered here. However, there will also be larger and more complicated strain effects and configurational entropy which can compensate binding energies of larger sized aggregations. Eventually, at even larger doping concentrations, the precipitation of different phases may occur, for example at 6% Sn-doping in hematite XRD shows

SnO_2 secondary phases form [89]. Future theoretical work should provide further insights to PEC experiments by investigating the role of dopants and dopant clustering on polaron mobility via small polaron hopping [106, 107, 12, 35] and optical absorption[36, 37, 113], which together, along with carrier concentrations studied here, directly impact the photoconductivity of transition metal oxide based photoelectrodes.

2.4.7 Conclusions

This work discovers a new mechanism of dopant clustering via the aggregation of n-type dopants and electron polarons into dopant-pairs which resemble electric multipoles. These pairs are thermodynamically stable due to several contributions which we disentangle by a simple model involving three components: electronic, magnetic, and strain. Our model illuminates that binding occurs predominantly through electrostatic interactions but surprisingly is also mediated by magnetic interactions which together overcome strain to yield the consistently negative binding energies of tetravalent dopants in Fe_2O_3. EXAFS experiments confirm the existence of these Sn-Sn pairs which formed at 1% doping and have an identical interatomic distance compared to those predicted theoretically (~ 3.7 Å).

The effect of doping with and without clustering on carrier (small electron polaron) concentration is carefully examined. We find doping in Fe_2O_3 is limited by dopant clustering which traps electron polarons and severely lowers the carrier concentration with respect to doping concentration. This clustering is shown to be responsible for the doping bottleneck in hematite, where dopants such as Ti exhibit extremely low optimal doping concentration (i.e. 0.1%) for PEC application. Strategies to overcome this doping bottleneck are proposed; specifically

codoping with dopants that exhibit low binding energies for clustering (e.g. Sn-Ti codoping) is seen as an ultimate solution. Lastly, for single-type doping in group IV and XIV, we found Ge is the best dopant which can contribute the highest polaron concentrations even at presence of dopant clustering. These findings provide a cohesive picture of the doping bottleneck in hematite and help to establish an improved rationale for further development of hematite photoanodes usage in renewable energy applications.

2.5 Spin Polaron Conduction in CuO

In our 2018 work published in npj Computational Materials [35], we investigated hole transport in cupric oxide (CuO), a p-type semiconductor. Due to its relatively small bandgap (1.2-1.8 eV) and a conduction band minimum located at a more negative potential than that of water reduction, [114, 115, 116, 117, 118, 119, 120, 121, 122, 123] it has the potential to serve as an inexpensive and environmentally benign photocathode for a water splitting PEC. However, like other TMO's, CuO suffers from poor carrier conductivity, which limits the effectiveness of CuO-based devices.[121, 122, 124, 119] Additionally, cathodic photocorrosion of CuO can also limit the use of CuO for photoelectrochemical applications. Fortunately, a recent study demonstrated that the photocorrosion of CuO can be effectively suppressed by depositing a thin protection layer that prevents direct contact of CuO and the electrolyte,[123] which encourages studies on further improving charge transport and photoelectrochemical properties of CuO. Facilitated charge transport in CuO can also be advantageous for the use of CuO in other electrochemical devices such as gas sensors.[125, 126]

The development of charge transport in CuO depends on the understanding and optimization of the small polaron hopping process. Strong electron-phonon coupling in many transition metal oxides (Fe_2O_3, $BiVO_4$, TiO_2) leads to the localization of carriers into polarons, a quasi-particle representing the carrier and local lattice distortion.[127, 128, 78] Due to this localization, carriers are no longer transported through the system via typical band mechanisms. Rather, carriers must be thermally activated in order to "hop" between sites, a process known as polaron hopping conduction.[129, 130] This type of conduction leads to an extremely low carrier mobility (e.g. 0.1 $cm^2/V/s$ for CuO) [127] several orders of magnitude lower than band-like semiconductors such as Si (1000 $cm^2/V/s$).

Previous experimental studies have indicated that polaron formation also occurs in CuO. [131, 132, 133, 134, 135] Interestingly, more exotic properties such as "one-dimensional charge stripes" and "spin polarons" have been found in CuO due to strong spin-charge-lattice interactions,[133] which distinguishes its conduction mechanism from the common electron polaron hopping conduction in non-magnetic oxides such as $BiVO_4$. However, there has yet to be a theoretical investigation on the existence and transport of polarons in CuO, which would provide deeper understanding of carrier transport and therefore offer effective doping strategies to improve the carrier transport properties in CuO and other magnetic oxides in general. Finally, although there have been a few experimental doping studies of CuO to date,[136, 135, 137, 138, 139, 140, 141, 142, 143] the role of dopants in improving hole conduction in CuO has not been clearly understood.

In this study, we address these fundamental questions by comparatively investigating hole conduction in pristine and Li-doped CuO. Our focus is on the elucidation of the mechanisms by which Li doping improves hole concentration and mobility through a combined theoretical and experimental effort. Our work is organized as follows, first we provide theoretical background on CuO and discuss the mechanism of hole conduction which involves a unique spin-flip hopping process of spin polarons. Second, we show how Li doping enhances hole concentrations and hole mobility in CuO. Finally, we confirm our theoretical results by preparing CuO and Li-doped CuO electrodes and experimentally compare their photoelectrochemical properties.

2.5.1 Polaron formation and hole conduction in CuO from first-principles

Several experimental studies have shown that CuO has an Arrhenius dependence of conductivity to temperature. [131, 132, 133, 134, 135] This dependence is expected for materials which form small polarons (a trapped electron or hole due to local lattice distortion) which must be thermally activated in order to hop between lattice sites in the material, a process known as polaron hopping. [130] The mobility of small polaron hopping follows the relationship shown in Eq. 2.9,

$$\mu \propto e^{-E_a/kT} \tag{2.9}$$

where E_a is the activation energy, k is the Boltzmann constant, T is the temperature, and μ is the carrier mobility which is related to the conductivity σ, by $\sigma = en\mu$ (n is majority carrier concentration, which are holes in this case). To confirm the presence of polarons in CuO, we computed the electronic structure of pristine CuO with a single electron removed from a 96 atom system ($2 \times 3 \times 2$ supercell), corresponding to a hole concentration of 2% (at. % of hole = 100 $\times$ [mol of hole] / [mol of O]). Detailed descriptions of our electronic structure calculations can be found below under the Computational Methods section and SI. From the density of states and wave function of the hole state, we determine that holes form localized polaron states. These polaron states are predominantly O $2p$ mixed with Cu $3d$ as seen from the partial density of states (Figure S2) in agreement with previous studies on the electronic structure of CuO. [144]

An intriguing consequence of hole localization around a single Cu $3d^9$ ion is that the Cu magnetic moment will flip, forming a "spin polaron" (SP).[145, 146, 147, 148, 149, 150] Such states are common in copper oxides as the combination of two

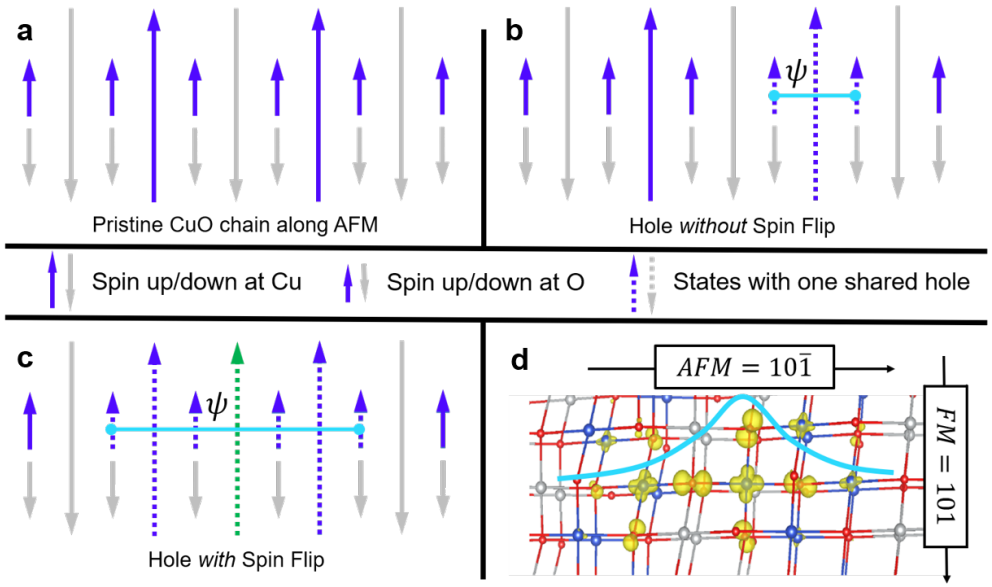

Figure 2.15: Spin Polaron Formation in CuO. a. Pristine Cu and O chain with antiferromagnetic (AFM) ordering. **b**. If a hole forms (without a spin flip) it will be highly localized as it can only distribute on one Cu atom (other neighboring Cu atoms do not have an available state of the appropriate spin as explained in the main text). **c**. After a Cu's moment flips, the hole can redistribute over several Cu atoms lowering the kinetic energy. **d**. The wavefunction of a hole in CuO which has formed a SP with a flipped Cu spin so that it may redistribute over several atoms, in accordance with panel C. An isosurface of 10% of the maximum is used. (Blue ball = Cu with up spin, Grey ball = Cu with down spin, and Red ball = O). (In the panels a-c large arrows denote the unpaired spin of Cu, small arrows denote two spin states of O which are often paired, dashed arrows denote states with a shared hole, blue/grey arrows= up/down, and green arrow= flipped Cu spin.)

SPs will create a spinless Cooper pair state which obeys Bose-Einstein statistics and is the basis of superconducting.[147, 151] In general, a SP forms in polaronic materials where the kinetic energy of the state can be lowered substantially from the increased delocalization of the electron or hole wavefunction after the spin-flip occurs. [152] For example, after an electron at a spin-up state is removed, a hole is created at the same spin state. As a fermion, the hole obeys the Pauli exclusion principle like electrons and can only be added to a state which is already occupied (i.e. a state must be occupied by an electron of the same spin for a hole to form). Therefore, in an anti-ferromagnetic system, the delocalization of a spin-up hole is limited by the availability of neighboring atoms' spin-up occupied states. As shown in Figure 2.15B, with anti-ferromagnetic ordering, the hole polaron may form into a highly localized state (limited to forming over a single Cu atom and its bonding O atoms that have up spins, as neighboring Cu atoms do not have an available spin-up state at which the hole can form). But after a neighboring Cu ion's moment flips (Figure 2.15C) an extra channel is created, and the spin-up hole can redistribute over several sites that all have an up spin, lowering the kinetic energy of the hole polaron. The resulting flipped Cu ion with a distributed polaron state over several Cu and O atoms is shown in Figure 2.15D. As discussed in Ref. [152], this lowering of kinetic energy through wavefunction delocalization dominates over the energy cost of the spin flip and facilitates the formation of spin polarons in CuO. Additional explanations can be found in the SI (Figures S3-S4).

Considering that the magnetic couplings between Cu ions in CuO are significantly large ($J \sim 100$ meV), spin-spin interactions will have an important effect on the conduction of holes in CuO. To address this point, we consider the total

kinetic rate κ of the hopping process in Eq. 2.10,

$$\kappa = \left(\sum_i e^{-E_i/kT} \kappa_i \right) / \left(\sum_i e^{-E_i/kT} \right) \tag{2.10}$$

where E_i is the energy of the i^{th} configuration and κ_i is the hopping rate between configurations (for full details see SI). For the case of CuO, we found that the formation of a polaron at a site without a flipped spin was not possible, and, presumably, the total energy of such a state is very high, which reduces the possible configurations entering Eq. 2.10. Then we define hopping that does not involve a spin-flip process to have a rate given by $\kappa_i = e^{-E_a^{e-ph}/kT}$, with E_a^{e-ph} being the usual hopping activation energy barrier due to electron-phonon interactions. We have shown that the Boltzmann factors that are related to the energies of different spin configurations will be dominated by the most probable hopping path (Figure S9). As a result, the full hopping rate κ then reduces to Eq. 2.11,

$$\kappa \sim e^{-(E_a^{e-ph} + E_a^{spin})/kT} \tag{2.11}$$

Namely as holes are conducted through the system they will invoke a spin-flip process which will cost energy equal to the cost of flipping a spin of a Cu ion (illustrated in Figure 2.16). In final, we see that the energy of this spin-flip process E_a^{spin} can be simply added to the electron-phonon process E_a^{e-ph} to give the full activation energy E_a, given in Eq. 2.12.

$$E_a = E_a^{e-ph} + E_a^{spin} \tag{2.12}$$

Intuitively, a spin-flip hopping process will not have a well-defined transition state; if there was a transition state, it would be a spin delocalized state which is not fa-

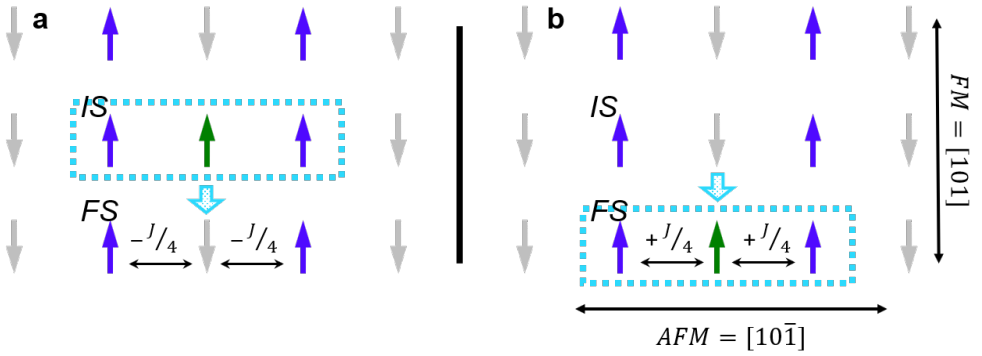

Figure 2.16: Spin Polaron Hopping in Pristine CuO. Diagram describing the interplay of spin and polaron hopping in CuO. As opposed to Figure 2.15, only Cu spins are shown here for simplicity. **a**. Initially the spin polaron has formed at the initial site (IS), while the moment of Cu ions at the final site (FS) are aligned anti-ferromagnetically (AFM) $(-J/4)$. **b**. After the polaron hops to the final site (FS) the center Cu moment is flipped, costing energy according to the strength of J. (Blue = Cu with up spin, Grey = Cu with down spin, Green = Cu with flipped spin, Dashed Light Blue box = polaron state).

vored to form in a polaronic oxide. To confirm this point, we employed the newly-developed constrained density functional theory (CDFT) technique for solids in which an external potential is added to the Kohn-Sham potentials, and its strength is varied self-consistently in order to localize a desired number of charges on a specific site. [153, 154] This allows for a direct calculation of the electronic coupling constant between initial and final states $|H_{ab}|$ in CuO, which we obtained to be 1.01 meV (the numerical accuracy is 0.01 meV). This is two orders of magnitude smaller than the computed activation energy (shown later), implying that transport in CuO is indeed non-adiabatic, which cannot be described by a semi-classical transition state theory.

The energy of this spin-flip (E_a^{spin}) can be obtained directly using the Heisenberg Hamiltonian $H_{spin} = -\sum_{i<j} J_{ij} \hat{S}_i \hat{S}_j$, where J_{ij} is the magnetic coupling between the spin of the i^{th} and j^{th} Cu ion and $\hat{S}_i$ is the spin of the i^{th} Cu ion (taken to be 1/2 as Cu is in a $3d^9$ configuration with one unpaired electron).

The use of this model is well-established in accurate modeling of the magnetic couplings of CuO, [155, 156, 157] and our calculations show that fitting the total energy of different magnetic configurations of CuO with this Hamiltonian yields an R-squared of 0.999 (Figure S7). Following a previous work, [155] we considered five magnetic couplings in CuO: J_z, J_x, J_a, J_b, J_2. Of these five couplings, the coupling J_z is dominant over the rest with a value of -111 meV and is responsible for the long-range antiferromagnetic transition of CuO at 230 K. Note that in CuO the magnetic correlation length remains large at temperatures above the transition temperature T_N, so magnetic coupling is still relevant to our discussion of hole conduction in CuO at room temperature. [133, 158] Second is the super-superexchange J_2 which is -39 meV yet is still three times smaller than J_z. The remaining values are -17.4 meV for J_a, $+3.0$ meV for J_x, and $+2.6$ meV for J_b. From this we can directly compute E_a^{spin} according to Eq. 2.13.

$$E_a^{spin} = -\sum_{i<j} J_{ij} \Delta \left(\hat{S}_i \hat{S}_j \right) \tag{2.13}$$

In CuO, $-\sum_{i<j} J_{ij} \Delta \left(\hat{S}_i \hat{S}_j \right) = -(J_z + J_x + J_a + 2J_b + J_2)$, which gives E_a^{spin} to be 160 meV, a similar magnitude to E_a^{e-ph} (99 meV) as shown in Table 2.7. This result validates that E_a^{spin} contributes significantly to the overall activation energy. Therefore, this result suggests that dopants that can reduce the magnetic coupling contribution E_a^{spin} as well as the electron-phonon contribution E_a^{e-ph} to the activation energy can more effectively improve hole mobility in CuO. Note that here we consider hopping along the ferromagnetic (FM) [101] direction (see Figure 2.16) due to shorter Cu-Cu distances and superior orbital overlap between initial and final states. Meanwhile, we find that hopping along the anti-ferromagnetic (AFM) $[10\bar{1}]$ direction is energetically unlikely to occur (Figure S10-S12).

Li (%)	ε_∞	ε_0	ε_p	E_a^{e-ph} (meV)
0	6.4	11.0	15.5	99
6.25	7.9	13.0	16.7	92
12.5	8.4	16.3	17.5	88

Table 2.7: Electron-Phonon Activation Energy. Effect of Li doping on the electron-phonon activation energy from Eq. 2.14.

2.5.2 Spin polaron conduction in Li-doped CuO from first-principles

Our experimental work (discussed later) shows Li-doped CuO electrodes have significantly increased photocurrent and show a positive shift of onset potential, while also retaining a similar crystallinity and photon absorption to the pristine CuO electrodes. Thus, it is anticipated that Li doping in CuO improves electron-hole separation and/or carrier conduction (concentration and/or mobility). To confirm this postulation, we applied our theoretical techniques discussed above to clarify how Li doping improves hole conduction in CuO.

The enhancement of carrier concentration after Li doping can be confirmed by the low hole ionization energy in Li-doped CuO, which is comparable to kT. Specifically, the ionization energy for a p-type dopant is defined by the difference between its charge transition level (CTL) and the valence band maximum. We computed the hole ionization energy of Li-doped CuO to be 55 meV (corresponding to the $-1|0$ transition level). Since this energy is small and comparable to kT at room temperature, it indicates that Li introduces shallow hole states which can be ionized at room temperature to increase the hole concentration. This indicates a shift of the Fermi level towards the valence band maximum as has been experimentally shown with a positive shift of the onset potential by ~ 210

mV. The introduction of shallow states from Li doping is also in agreement with previous theoretical and experimental works.[135, 137]

To investigate the effects of Li doping on the transport of holes in CuO (*i.e.* the effect of Li on hole hopping mobility) we first focused on the electron-phonon contribution to the activation energy, E_a^{e-ph}. For this part, we computed the electron-phonon activation energy of pristine and Li-doped CuO via Eq. 2.14. This method represents an averaged doping effect in a continuum polarization medium and avoids the sampling of all possible doping configurations and hopping paths. [67]

$$E_q^{e-ph} = \frac{e^2}{4\varepsilon_p}\left(1/r_p - 1/R\right) \tag{2.14}$$

Here r_p is the polaron radius which is approximated as $r_p = 1/2(\pi/6)^{1/3}V^{1/3}$, R is the average hopping distance, and $1/\varepsilon_p = 1/varepsilon_\infty - 1/\varepsilon_0$ where ε_∞ is the high frequency dielectric constant and ε_0 is the static dielectric constant. The results of this calculation (Table 2.7) show that Li doping increased the high frequency dielectric constant (ε_∞) due to increased carrier concentrations after Li doping. Although the static dielectric constant (ε_0) is also increased due to weaker Li-O bonds (ε_0 is inversely proportional to the bonding energy squared)[159], an increased ε_∞ dominated and resulted in an overall lower barrier (E_a^{e-ph}). For example, the barrier decreases by 11 meV after 12.5% Li doping, which corresponds to 1.5 times improvement on hopping mobility based on the $\mu \propto e^{-E_a/kT}$ relation between E_a and mobility μ. Therefore, Li doping assists the electron-phonon kinetics of carriers in CuO.

To consider the effect of Li on the magnetic contribution to the activation energy E_a^{spin}, we first recalculated the magnetic couplings in CuO after a significant amount of Li doping (12.5%) using the same methods as before (Figure S8,

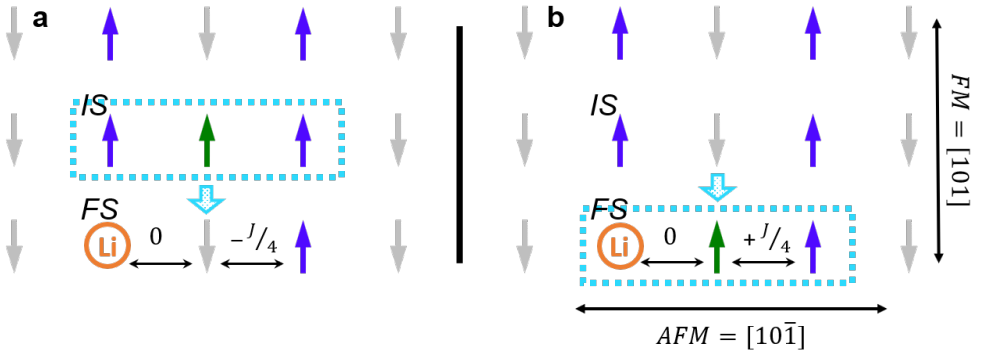

Figure 2.17: Spin Polaron Hopping in Li-Doped CuO. Diagram describing the interplay of spin and polaron hopping in CuO after Li doping (Orange = Li). As the spin polaron hops through the lattice, its interaction with Li will result in a lower magnetic barrier E_a^{spin} due to broken magnetic couplings between Cu ions and non-magnetic Li ions (E_{spin}=0).

Table S3-S4). We find that the predominate magnetic coupling J_z is nearly the same after Li doping, although overall Li suppresses the anti-ferromagnetism of CuO due to the spinless character of Li, which has also been seen experimentally. [135] The resulting energy of the spin-flip process in Li-doped CuO from Eq. 2.13 (assuming that there are no Li near the polarons) would be 137 meV, which is smaller than 160 meV in pristine CuO (mentioned above). We note that the largest benefit of Li doping is seen when we consider the interaction of neighboring SPs and Li. An analogue of the spin-flip hopping process after Li doping in CuO is shown in Figure 2.17. Since Li is non-magnetic, it does not interact with a SP when it passes by, and a single Li site can reduce the local hopping barrier of the SP by up to 55 meV which corresponds to approximately 9 times improvement of hopping mobility based on the $\mu \propto e^{-E_a/kT}$ relation (the case of Li breaking J_z coupling). This larger effect of Li doping on the activation energy describes how Li doping significantly enhances the hole mobility in CuO, in agreement with previous experimental measurements of the activation energy of Li-doped CuO.[135, 138, 140, 141] For example in Ref. [135], a monotonic decrease

of activation energy has been observed as a function of Li doping concentration (up to 16%), accompanied by strong suppression of the anti-ferromagnetism of CuO. The activation energy decreases from 0.23 eV for pristine CuO to 0.035 eV for $Cu_{0.92}Li_{0.08}O$, which leads to a three order of magnitude decrease of resistivity in experiments. [135] Since what we have discussed is relevant for isolated Li doping (Li-Li interaction is neglected in our magnetic interaction models), even a small amount of Li doping will have a significant impact on the conduction of holes in CuO and can dramatically increase the photocurrent density of CuO as we have seen in our experimental investigation. [141]

2.5.3 Experimental comparison of CuO and Li-doped CuO electrodes

Since the direct measurement of charge transport properties of our high surface area, nanofibrous polycrystalline electrodes was not possible, the effect of Li doping on charge transport properties was evaluated by comparing photocurrent generation of CuO and Li-doped CuO electrodes. Since these electrodes have the same absorbance (Figure S15B), the number of electron-hole pairs generated in these electrodes under illumination must be identical. Then, if an interfacial charge transfer reaction that can quickly consume almost all the surface reaching electrons is chosen for photocurrent measurement, any change in photocurrent generation caused by Li doping must be due to a change in the number of surface-reaching electrons caused by a change in the charge transport properties, which affects electron-hole separation.

For this purpose, comparing photocurrent for water reduction may not be proper because the surface of CuO is not catalytic for water reduction, and a significant portion of the surface reaching electrons can be lost to surface recom-

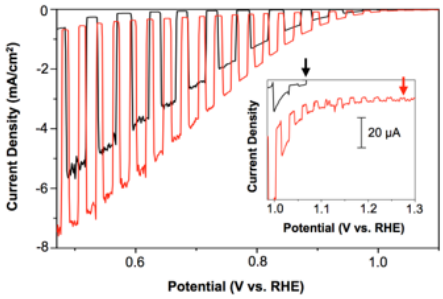

Figure 2.18: J-V Plots of CuO and Li-Doped CuO. J-V plots (scan rate = 10 mV/s) of CuO (black) and Li-doped CuO (red) electrodes for O_2 reduction in 0.1 M KOH (pH 13) solution with O_2 purging under AM1.5G,100 mW/cm^2 illumination. The inset shows the enlarged current in the potential region near the photocurrent onset potentials indicated by arrows.

bination, making it difficult to accurately evaluate the change in the number of surface-reaching electrons. In this study, we used oxygen reduction as the photoelectrochemical reduction reaction that occurs on the CuO surface as the kinetics of this reaction is typically much faster than water reduction on oxide-based photocathodes. [160, 161, 162, 163] The J-V plots of CuO and Li-doped CuO for oxygen reduction obtained in a 0.1 M KOH (pH 13) solution purged with O_2 under standard illumination conditions (AM1.5G, 100 mW/cm2) are shown in Figure 2.18.

The pristine CuO electrode already shows efficient photocurrent generation for O_2 reduction as its bandgap allows for the utilization of a great portion of the visible solar spectrum, and its nanostructure reduces bulk electron-hole recombination. For example, it achieved a photocurrent density of $\sim$ 1.2 mA/cm^2 at a potential as positive as 0.8 V vs. RHE, and it increased up to $\sim$ 4.0 mA/cm^2 when the potential was swept to 0.6 V. (The dark current initiating around 0.65 V vs. RHE is due to electrochemical reduction of O_2 which was subtracted from the photocurrent to determine overall photocurrent.) The photocurrent observed for O_2 reduction can be considered the upper limit of photocurrent that can be ob-

served for water reduction when an efficient hydrogen evolution catalyst is placed on the CuO surface to improve the water reduction kinetics.

The Li-doped CuO electrode significantly enhanced photocurrent generation. For example, the Li-doped CuO electrode achieved a photocurrent density of $\sim$ 2.0 mA/cm^2 at a potential as positive as 0.8 V vs. RHE, and it increased up to $\sim$ 5.6 mA/cm^2 when the potential was swept to 0.6 V. In addition to the evident increase in magnitude of photocurrent density, Li-doped CuO electrodes demonstrated a considerable shift in photocurrent onset to the positive direction by $\sim$ 210 mV. The photocurrent onset potential for a reaction that has high interfacial charge transfer kinetics, such as O_2 reduction on an oxide photocathode, can be considered the flatband potential. This is because for such reactions the loss of the surface-reaching minority carriers to surface recombination is negligible. In this case, it can be assumed that photocurrent disappears when the applied potential is the same as the flatband potential, where electron-hole separation is no longer possible. The fact that the J-V plots of CuO and Li-doped CuO electrodes measured with chopped illumination do not show any transient photocurrent even when the applied potential is near the photocurrent onset potential is a good indication that recombination on the CuO surface during O_2 reduction is negligible. This confirms that the photocurrent onset potentials of these electrodes can be regarded as their flatband potentials. Since the flatband potential is the same as the Fermi level after accounting for the Helmholtz layer potential drop at the semiconductor/electrolyte interface, and the Helmholtz layer potential drop should not be altered by 0.1 at. % Li doping, the shift of the onset potential of Li-doped CuO directly indicates that Li doping shifted the Fermi level of CuO to the positive direction, closer to the valance band maximum. [164]

These experimentally obtained results agree well with computational results

that Li doping generates shallow acceptors that effectively increase the hole concentration. The increase in hole concentration, which improves the hole conductivity, can reduce electron-hole recombination in the bulk or in the space charge region, increasing the number of minority carriers reaching the surface to perform oxygen reduction. Also, the increase in hole density that changed the Fermi level was confirmed by the shift of the flat band potential to the positive direction. Finally, according to our computational results, a simultaneous decrease in E_a by Li doping also contributed to photocurrent enhancement by improving the hole mobility of CuO.

While the impact of Li doping on the activation energy E_a and the impact on carrier density cannot be easily separated in our photocurrent measurements, the impact of Li doping on the activation energy has been discussed explicitly in dark resistivity measurements of Li doped CuO between a few K to 300 K. [135, 138] An order of magnitude decrease of the hopping activation energy with 16 at. % Li doping clearly confirmed the combined effect of E_a^{spin} and E_a^{e-ph} being lowered by Li doping, as the effect of E_a^{e-ph} alone cannot explain the observed order of magnitude decrease in the hopping activation energy based on our calculations. [135] This study clearly demonstrated that the effect of Li-doping on E_a^{spin} is still considerable at 300 K (because of the short-range magnetic couplings remaining above Néel temperature)[133, 158] and that Li-doping can play a critical role in improving the mobility of CuO at room temperature, which is relevant for its PEC applications.

2.5.4 Conclusions

In conclusion, we have studied in-depth hole conduction in pristine and Li-doped CuO by first-principles calculations accompanied by the PEC performance

of experimentally prepared CuO and Li-doped CuO electrodes. In pristine CuO, we have verified the existence of spin polarons (SP), which occur via the flip of a single Cu ion's spin so that the polaron may redistribute over several atoms, and this delocalization effect lowers the energy of the polaron state. We then showed how transport of SPs in CuO will involve a spin-flip hopping process and developed a theoretical framework of computing the activation energy which involves both electron-phonon and magnetic coupling contributions. Next, we displayed how Li doping in CuO generates shallow states above the valence band which pushes the Fermi level closer to the valence band maximum and improves hole concentrations in CuO. Then, we showed how Li doping improves hole hopping mobility in CuO by lowering the electron-phonon coupling contribution to the activation energy due to higher electronic screening. More importantly, we demonstrated that Li doping lowers the magnetic coupling contribution to the activation energy due to the destruction of magnetic interactions through the replacement of Cu ions with non-magnetic Li ions, culminating in a significantly lowered hopping barrier and increased hole mobility in Li-doped CuO. Finally, we prepared CuO and Li-doped CuO electrodes and compared their photoelectrochemical properties for O_2 reduction, where the changes in photocurrent and the onset of photocurrent can be directly related to changes in charge transport properties and the Fermi level, respectively. The experimental results show that Li doping enhances charge transport properties and shifted the Fermi level toward the valence band maximum while not affecting photon absorption, which agrees well with computational results. This work provides important insights on the mechanisms of the formation and transport of SPs and their effect on the charge transport properties of CuO and Li-doped CuO. Similar to Li doping, doping with other non-magnetic shallow acceptors may also simultaneously improve carrier concentration and hopping

mobility of magnetic oxides. In this case, shallow dopants can be ionized easily to increase carrier concentrations and increase dielectric screening, which weakens the charge-lattice interactions. Most importantly, non-magnetic dopants can break the magnetic couplings and lower the hopping barrier for SPs significantly, which is critical for improvement of hopping mobility. These insights offer effective strategies for the improvement of hopping conduction in magnetic oxides through atomic doping, which provides important guidance for materials design.

2.5.5 Computational Methods

Cupric oxide (CuO) assembles in a monoclinic structure with C2/c symmetry and a geometric unit cell consisting of only 8 atoms. To consider the correct magnetic interactions prevalent in CuO, a $\sqrt{2} \times 1 \times \sqrt{2}$ unit cell containing 16 atoms needs to be implemented (Figure S1).[156, 158, 165] Meanwhile, a $2 \times 3 \times 2$ supercell of 96 atoms was used for calculations considering polaron formation and doping. A final supercell of $2\sqrt{2} \times 3 \times 2\sqrt{2}$ with 192 atoms was used to confirm spin polaron formation size and charged cell correction.

It is well known that both local and semi-local exchange and correlation functionals in DFT cannot accurately describe the electron correlation in magnetic insulators, which results in a qualitatively incorrect electronic structure. To account for this issue, we applied the Hubbard U correction[11] with $U = 7.5$ eV, a well-established model for this material. [166, 167, 168, 169, 170] All calculations were carried out in the open-source plane wave code Quantum ESPRESSO [52] with ultrasoft LDA pseudopotentials,[53] unless otherwise noted. The choice of LSDA+U instead of GGA+U was made because GGA+U was unable to give the correct monoclinic structure of CuO, while LSDA+U yielded a geometry of CuO within 5% of experimental values. Nonetheless, LSDA+U and GGA+U provide

similar electronic structures (with the experimental geometry) and overall gave results in agreement with experimental expectations. Our calculations yielded that Cu^{2+} ions have a magnetic moment of 0.57 μ_B with a magnetic ordering according to Figure S1. Notably, the O atoms in this system share a non-negligible magnetic moment of 0.14 μ_B (in agreement with previous experiments[165] and theory[166]). We were also able to replicate the computed magnetic couplings at higher levels of theory with the LSDA+U method (see Table S1-S2).

2.6 Small Polarons Inducing Optical Transitions in Co_3O_4

In our 2019 work published in Physical Review Materials as a Rapid Communicaion [36], we demonstrated the origin and misconceptions behind optical transitions in Co_3O_4 due to the presence of small hole polarons which have active optical transitions below the energy of the true band-band transition. Polarons, conduction electrons or holes with self-induced lattice polarization, are known to exist in most transition metal oxides (TMO) and deeply affect their optical and carrier transport properties [171]. In these materials, much of the interest has been related to the role of small polarons (SPs) that form when the induced lattice polarization is localized in a volume on the order of the unit cell. In particular, for many important TMOs, including Fe_2O_3 [44, 47, 12], NiO [172, 173], Co_3O_4 [174, 175], MnO [176], $BiVO_4$ [106, 107, 18, 49], CuO [160, 35], it has been found that the formation of SPs is responsible for the low carrier mobility and conductivity, which hinders their practical application as electrochemical catalysts and photoelectrochemical (PEC) electrodes [33, 29, 177, 178, 179]. It is also well-established that the transport of SPs in these TMOs can be characterized through the thermally activated hopping conduction mechanism and a logarithmic temperature dependence of the materials carrier mobility [130].

Unlike the distinct signature of SPs on the carrier conduction discussed above, the effect of polarons on electronic structure and optical transitions in TMOs is rather complex and difficult to elucidate. For example, in several TMOs, such as WO_3 [180, 17], TiO_2 [181, 182, 183] and $SrTiO_3$ [184, 185], the presence of large polarons that are delocalized over several unit cells may lead to a strong band gap renormalization through electron-phonon coupling. By contrast, the formation

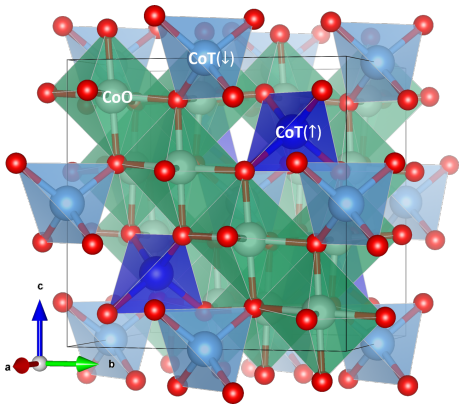

Figure 2.19: Normal spinel atomic structure of Co_3O_4. Octahedral Co are shown in green, tetrahedral Co are shown in blue/light blue (distinguishing spin polarization direction), and O are shown in red.

of SPs may introduce isolated gap states away from the band edges due to their spatially localized nature, which could be easily misinterpreted as band edges that define the fundamental band gap. A prime example is Fe_2O_3, where recent time-resolved spectroscopy experiments have shown that its mid-gap states are indeed associated with optically active polarons, which in turn lead to transition energies that are significantly lower than the fundamental band gap [78, 186]. This conclusion is also consistent with Lohaus *et al.* [79], where the authors showed that while the band gap of Fe_2O_3 is 2.2 eV, an effective gap of 1.75 eV is observed due to the formation of small polarons. Nonetheless, distinguishing mid-gap states due to SP formation from other sources such as defect-bound states [187, 188, 189] and surface states [190] is still not well understood in literature. Despite extensive experiments on these TMOs, theoretical studies of SP effects on electronic structure and optical properties of TMOs are limited. More importantly, challenges remain in first-principles methods that accurately describe polarons and electronic structure of TMOs.

In this paper, we discuss the role of SPs (hereinafter referred to as "polarons"

for simplicity) in tricobalt tetraoxide (Co_3O_4), an anti-ferromagnetic oxide with a normal spinel structure. Despite that Co_3O_4 has been extensively investigated for a wide range of technologies [191, 192, 193, 5, 194, 175, 195, 196], a fundamental understanding of the optical properties of this material remains largely lacking, and conflicting results have been reported, e.g., for the band gap of bulk Co_3O_4. For instance, a value of 1.5-1.7 eV has been commonly reported for the optical gap of Co_3O_4 [197, 198, 199, 200, 201, 202, 203]. On the other hand, several experimental studies conclude that, despite a transition being observed around 1.5-1.7 eV, the true band gap of Co_3O_4 is significantly smaller, yielding a value of around 0.7-0.9 eV [204, 205, 206, 207]. This conclusion, however, is not supported by time-resolved optical spectroscopy measurements, which suggest the state at $\sim$0.8 eV above the valence band maximum is a localized polaron state [199, 198, 208]. Along this direction, other experiments have indicated that the intrinsic carriers in Co_3O_4 are hole polarons that are characterized by a nearest-neighbor hopping conduction mechanism; and such a signature implies that hole polarons may affect the optical properties of Co_3O_4 in a similar way as in Fe_2O_3 [209, 210, 200, 197, 211, 212, 203, 213]. Collectively, the existing results indicate that much is left to be understood regarding the nature of the optical transitions near the band edge of Co_3O_4, and how it is related to polaron formation.

The aim of this work is to resolve the conflicting results in the literature on Co_3O_4, and provide a coherent description of its electronic structure, carrier conduction, and optical properties through first-principles calculations. In particular, we discuss the level of theory needed for a proper description of the electronic structure of the material. In addition, we elucidate the role of polaron formation on the electronic band gap and optical spectra of p-doped Co_3O_4, and we discuss how uniaxial strain can be used to distinguish polaron related

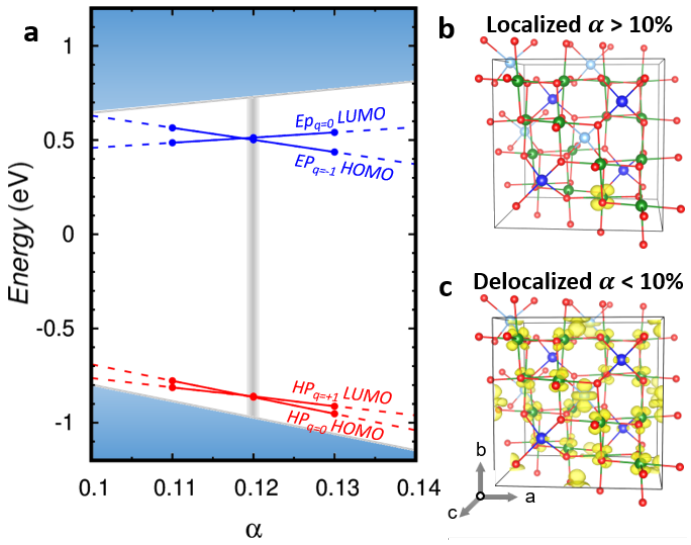

Figure 2.20: a. Generalized Koopmans' condition for electron polaron (EP) and hole polaron (HP) in Co_3O_4. The exact exchange α for the PBE0(α) method is varied until the condition $\text{HOMO}_q = \text{LUMO}_{q+1}$ (at fixed geometry where polaron has formed) is met. In both cases, we find that at an exact exchange of 0.12 Koopmans' condition is satisfied. The corresponding pristine gap is computed to be 1.70 eV. **b.** Localized and **c.** delocalized hole wavefunction, subject to the value of the exact exchange. Isosurface plots use a cutoff of 10% the maximum.

transitions in the optical spectra. This work provides a straightforward method for considering SP effects in the optical absorption, alongside unambiguous SP peak assignment in agreement with several previous experimental studies. This work will help to distinguish SP formation from other optical effects often considered instead (e.g. exciton formation, thermal broadening of optical spectra and electron-phonon renormalization of band edges) for TMOs in general. Our study presents a roadmap for first-principles calculations in the investigation of SP effects on optical absorption.

2.6.1 Computational Methods

We begin by discussing our computational strategy for addressing the electronic properties of Co_3O_4 (spinel structure shown in Figure 2.19). It is well known that density functional theory (DFT), with conventional local or semi-local exchange-correlation functionals, is not sufficient to provide a proper description of polarons in transition metal oxides and often severely underestimates the band gap of these materials [11]. In order to mitigate this issue, several approaches have been proposed, including DFT+U with an orbital specific Hubbard U correction, and hybrid functional that includes a fraction of Hartree-Fock exchange (α), hereinafter denoted as PBE0(α). However, these calculations are known to highly depend on the choice of the Hartree-Fock exchange or Hubbard U correction. For instance, a wide range between 0.8 and 2.0 eV has been reported in the literature for the band gap of Co_3O_4, depending on the level of theory employed [205]. In this context, it is also necessary to emphasize that, despite significant development has been made, establishing a first-principles approach that allows for an accurate prediction of the electronic properties of TMOs remains a significant challenge [214].

Here, we implement both hybrid functional and DFT+U calculations to provide an unbiased description of the electronic properties of Co_3O_4. Notably, in variation with previous hybrid functional calculations, we invoked the generalized Koopmans' condition to determine the value of α from first-principles. We stress that this strategy has been shown to successfully predict the band gap of materials with band gaps up to 14 eV and has been particularly successful for polaronic systems [215, 216, 217, 218]. Specifically, the generalized Koopmans' condition enforces the condition $\mathrm{IP}_q = \mathrm{EA}_{q+1}$ at a fixed geometry for an isolated state in the materials, where IP_q is the ionization potential of an occupied state at the

charge state q, whereas EA_{q+1} is the electron affinity of the same state when it is unoccupied at the charge state $q+1$. Here, we determine the value of α by enforcing the condition $IP_q = EA_{q+1}$ for both the hole and electron polaron (see Figure S1 for more details of the electron polaron), and we obtained a value of 0.12 for the Hartree-Fock exchange α in both cases, as shown in Figure 2.20. We note that hole polarons do not form for α below 10%, as illustrated in Figure 2.20b-c). The value of α determined in this manner is an intrinsic property of the bulk system, and the choice of defect used to enforce the Koopmans' condition is proper as long as it has minimum hybridization with the bulk Bloch states [219, 215, 216].

We then determined U parameters based on the hybrid functional results, and the stable formation of electron and hole polarons (see Table S1 for more details). In particular, we find that the use of U values of $U_{Co(O)} = 4$ eV and $U_{Co(T)} = 3$ eV provides consistent results with the Koopmans' compliant hybrid functional (band gap agrees within 0.1 eV), as well as a proper description of the electronic properties of the system, as discussed later in this communication. We also note that hole polarons do not form for U values below 2.5 eV (see Figure S2).

All the calculations were then carried out using the plane-wave code Quantum ESPRESSO [52] with norm-conserving pseudopotentials [54]. A plane wave cutoff of 100 Ry was used in all PBE+U calculations, while a reduced cutoff of 50 Ry was implemented for the more demanding hybrid functional calculations (geometry and electronic structure are converged at 50 Ry). The calculations were generally performed within the 56 atom cubic cell with a $2 \times 2 \times 2$ k-point mesh for integration over the Brillouin zone. In addition, a $\sqrt{2} \times \sqrt{2} \times 2$ supercell with 224 atoms was utilized for comparison, particularly to understand the finite-size effects on polaron formation. Nevertheless, we find that the wavefunc-

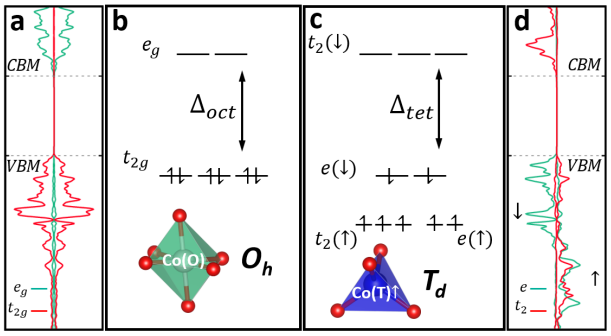

Figure 2.21: **a.** Projected density of states (PDOS) of Co(O) on t_{2g} and e_g orbitals. Schematic representation of the electronic configuration of **b.** octahedral Co^{3+} and **c.** tetrahedral Co^{2+} in Co_3O_4 due to a crystal field splitting (Δ_{oct} and Δ_{tet}, respectively). **d.** PDOS of Co(T) on t_2 and e orbitals. All the PDOS was computed with DFT+U.

tion character, energy level splitting, and band structure look largely unchanged between the 56 atom cubic cell and the 224 atom supercell (see Figure S3 for further details). In all calculations with electron or hole polarons, the charged cell correction scheme as developed in Ref. [69] was employed, which is necessary in order to remove the spurious interactions of the polarons with their periodic images and with the uniform compensating background charge [220]. For the rest of the manuscript, unless otherwise noted, the results presented here were obtained at the DFT+U level of theory that is computationally less demanding compared to hybrid functional calculations.

2.6.2 Electronic Structure of Pristine Co_3O_4

To set a baseline for the discussion of polaron effects in Co_3O_4, we briefly summarize the electronic structure of the pristine system. As shown in Figure 2.19, Co_3O_4 assembles in a normal spinel structure, where two thirds of Co occupy octahedral sites (denoted by Co(O)) and the remaining third occupy tetrahedral sites (denoted by Co(T)). We find that Co(O) exhibits a low-spin $3d^6$ orbital configu-

ration with the O_h symmetry, leading to filled t_{2g} and empty e_g bands, as shown in the calculated projected density of states (PDOS) and band diagram presented in Figure 2.21 a-b. On the other hand, Co(T) with the T_d symmetry forms a high-spin $3d^7$ configuration with a half-filled e_g band, yielding an overall magnetic moment of $\sim$3.2 μ_B as already reported in experiments [221]. These Co(T) sites experience an anti-ferromagnetic interaction mediated through a super-exchange of mutually bonded oxygen; in addition, the presence of a large Hund's spin exchange results in a splitting of the t_2 band. This is shown in Figure 2.21 c-d, where we find that the t_2 minority spin states are formed at a higher energy level, whereas all majority spin states occur at lower and similar energies [202, 222] (also see Figure S4 for further details). Overall, the behavior of the spin states and band splitting presented here are consistent with results reported in existing theoretical studies [222, 223].

2.6.3 Formation of Hole Polarons with Mid-Gap States

Next, we discuss the nature of polaron formation in Co_3O_4. Our calculations show that, among the Co(O) and Co(T) sites where hole polarons can form, the total energy of a hole polaron forming at Co(O) is lower than that of Co(T) by at least 70 meV. A more stable formation of the polaron on Co(O) is also reflected in the calculated density of states of Co_3O_4 where a larger contribution of Co(O) d states is found at the valence band edge compared to the Co(T) d states (see Figure S4). Finally, our conclusion is consistent with the experimental study reported by Ngamou *et al.* [209], where the authors show that the hopping of polarons takes place in the octahedral sites and are responsible for driving the electrical transport in the oxide. Collectively, these results indicate that the computational approach employed here provides a proper description of polaron

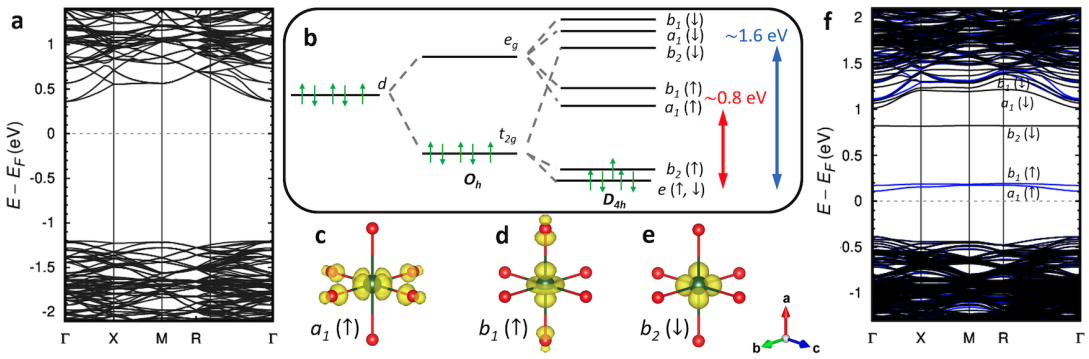

Figure 2.22: **a.** Pristine band structure of Co_3O_4 with a 224 atom supercell (primitive cell band structure shown in SI Figure S5). **b.** Hole polarons create a low-spin (LS) d^5 configuration at Co(O) along with a Jahn-Teller (JT) distortion which results in a D_{4h} configuration and the creation of several mid-gap states. **c-e.** Wavefunction isosurface plots (yellow cloud) of the three polaron induced states under hole formation of $a_1(\uparrow)(d_{x^2-y^2})$, $b_1(\uparrow)(d_{z^2})$, and $b_2(\downarrow)(d_{xy})$ character, respectively. Isosurface plots use a cutoff value of 10% the maximum. **f.** Band structure of Co_3O_4 with a hole polaron which shows several induced gap states (blue = spin up, black = spin down).

formation in Co_3O_4.

Beyond the findings on the thermodynamical stability of hole polaron formation in Co_3O_4, our calculations show that the hole polaron at Co(O) leads to several mid-gap states. As shown in Figure 2.22, we find that upon the hole polaron formation, Jahn-Teller (JT) distortion occurs at the Co(O) site due to an uneven occupation of the t_{2g} band, and splits the degeneracy of the O_h states. In addition, the uneven occupation of up/down states splits the spin degeneracy due to the on-site Coulomb repulsion of the d orbitals. Specifically, we find that the majority spin states (e.g. $b_2(\uparrow), a_1(\uparrow), b_1(\uparrow)$) are located at a lower energy, whereas the minority spin states (e.g. $b_2(\downarrow), a_1(\downarrow), b_1(\downarrow)$) are pushed higher in the energy. Such splitting and ordering is consistent with the previous time-resolved spectroscopy measurements of Co(O) [223, 201]. In addition, these mid-gap states are consistent with the experiment reported in Ref. [198], where it was found that

mid-gap excitations are associated with $a_1(\uparrow)$ and $b_1(\uparrow)$ states of Co(O). As a result, our analyses point to significant effects of hole polarons on the electronic structure of Co_3O_4, most notably in the formation of mid-gap states in a similar way as found in Fe_2O_3.

2.6.4 Small Polaron Induced Optical Transitions

We now turn to a more quantitative discussion of polaron effects on the electronic structure of Co_3O_4. In particular, we obtain a band gap of 1.6 eV and 1.7 eV with the current choice of U and α (respectively), which is in excellent agreement with the value of 1.5-1.7 eV reported in Refs. [197, 198, 199, 200, 201, 202, 203]. However, this is significantly larger than the result of 0.7-0.9 eV claimed by other experiments. [204, 205, 206, 207] We note that exciton binding energies are usually less than 150 meV in many TMOs [224, 225, 17], and we show later that the calculated optical spectra, by including excitonic effects, cannot explain the low energy transition at 0.7-0.9 eV. Interestingly, as shown in Figure 2.22b, at the current level of theory, we find that the mid-gap states are located at 0.8 eV away from the valence band maximum, and are associated with the hole polaron formation. This observation suggests that a scenario similar to the one observed for Fe_2O_3 may also occur in Co_3O_4, i.e., the true gap of Co_3O_4 is $\sim$1.6 eV, and the mid-gap states are responsible for the transitions found at $\sim$0.8 eV in the experimental optical absorption spectra [204, 205, 206, 207]. In order to verify our hypothesis and to further elucidate the role of polaron formation, we calculated the optical absorption spectra of Co_3O_4 with and without a hole polaron, and we compared the results with available experimental data. Absorption spectrum with a hole polaron was computed with a 56-atom supercell [226], which better represents experimental hole concentrations of p-type Co_3O_4 [199, 197] due to

abundant cation vacancies [210, 227].

Therefore, we computed the imaginary part of the dielectric function in the random phase approximation (RPA) with local field effects (as shown in Figure 5) and solving the Bethe-Salpeter equation that includes excitonic effects (as shown in SI Figures S8 and S9), as implemented in the YAMBO-code [228], using the single particle eigenvalues and wavefunctions derived from DFT+U. We note that this choice of starting point considers the balance between accuracy and computational cost, similar to this work in Ref. [229]. In addition, for a direct comparison with experimental measurements, we calculated the absorption coefficient from the dielectric function [230].

$$A(\omega) = \frac{\omega}{c} \frac{\epsilon_2(\omega)}{\sqrt{\frac{\epsilon_1(\omega)+\sqrt{\epsilon_1(\omega)^2+\epsilon_2(\omega)^2}}{2}}} \tag{2.15}$$

The calculated optical absorption spectra of Co_3O_4 are shown in Figure 2.23, together with the experimental spectrum. We find that the introduction of hole polarons leads to the formation of several lower energy optical transition peaks between 0.6 and 1.2 eV in Co_3O_4. More importantly, we find that, in sharp contrast to the result obtained for the pristine system, the spectrum computed for Co_3O_4 with a hole polaron is in very good agreement with experimental data, where three lower lying transitions were also found between 0.7 and 1.1 eV [204, 197, 198, 199]. Our analysis indicates that these transitions can be associated with those occur between the *p*-*d* hybridized dispersive valence states and the localized *d* states formed at the hole polaron site, for which the wavefunctions are illustrated in Figure 2.22 c-e. Collectively, these results clearly support the interpretation that the true optical gap of Co_3O_4 is $\sim$1.6 eV and that the optical transitions observed at $\sim$0.8 eV are due to hole polaron formation at Co(O) sites. We note

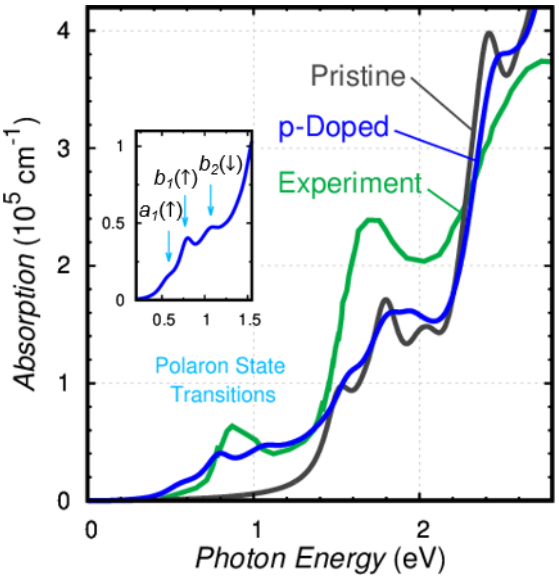

Figure 2.23: Optical absorption of Co_3O_4 in the pristine system (black) and the *p*-doped system (blue). Notably, only *p*-type doping i.e. the formation of holes, will cause mid-gap transitions below 1.6 eV, in agreement with experimental optical spectrum of Co_3O_4 shown in green [204]. The inset image displays the mid-gap transitions which are labeled according to the states formed from hole polaron formation as in Figure 2.22. (Theoretical spectrum is an average of spectra with light polarized in the [100], [010], and [001] directions.)

that electron polarons do not lead to the formation of low lying transitions (see Figure S6), indicative of the *p*-doped nature of the experimental system.

In order to rule out the possibility that the low energy transitions ∼0.8 eV are caused by large excitonic effects [231, 232, 233, 234], we also computed absorption spectra of pristine Co_3O_4 including excitonic effects by solving the Bethe-Salpeter Equation, as shown in SI Figure S7, S8. More detailed discussions can be found in SI. Overall, no extra peaks in the BSE spectra show up at the energy range below 1 eV for pristine Co_3O_4 (no hole polaron included), which confirms the excitonic effects do not explain the low energy transitions in the absence of SPs.

In addition, we note that we neglect electron-phonon coupling and thermal expansion effects on the band edge positions and absorption spectra at finite

temperature, as discussed in Refs. [235, 236]. For example, the absorption edge may be subject to a red-shift, in addition to an overall broadening of the spectra. This offers additional directions for future works. In any case, these effects will not lead to an additional peak well separated from the main absorption in a direct band-gap semiconductor like Co_3O_4; therefore, our conclusion on the small polaron contribution to the low energy optical transitions still holds.

2.6.5 Detecting Hole Polaron Transitions via Strain

Finally, we propose an experimentally viable method for distinguishing optical transitions involving localized polaron states from traditional band-band bulk state transitions. For Co_3O_4, the JT distortion upon the introduction of the hole polaron extends the Co-O bonds along the C_4 axis, and this distortion may occur along any of the bond axis that aligns with the [100], [010], [001] directions of the cubic unit cell. Such a three-fold degeneracy can be broken if uniaxial strain is applied to the system along one of the crystal lattice directions, which in turn may affect the optical absorption spectrum. In this regard, monitoring the change in the optical spectrum of Co_3O_4 in the presence of an uniaxial strain could potentially provide signatures of hole polarons associated with a specific JT distortion.

For demonstration, we considered a 1% tensile strain applied along the [100] direction. We find that the three-fold degeneracy in the polaron states is broken upon the introduction of the strain; in particular, polaron formation with the JT elongation along the [100] direction is lowered in the energy by 5 meV compared to those associated with the [010] or [001] directions. Here, to investigate the collective and individual effects of these polarons on the absorption spectrum, we computed a thermally averaged ensemble spectrum by using a Boltzmann

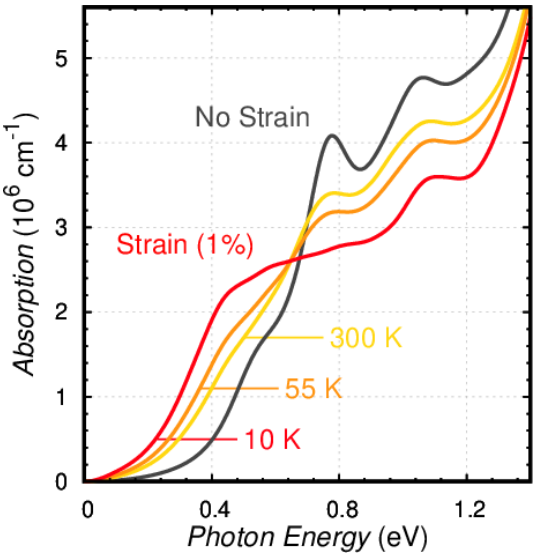

Figure 2.24: Optical absorption of p-doped Co_3O_4 under 1% uniaxial tensile strain along the [100] direction. Temperature dependence determines the probability for which direction the Jahn-Teller elongation will occur (as the degeneracy is removed under strain) and results in a red-shift of optical peaks related to the hole polaron.

probability distribution of the optical absorption obtained for each case:

$$P_i = \frac{e^{E_i/kT}}{\sum_i e^{E_i/kT}} \quad , \quad A(\omega) = \sum_i P_i \, A_i(\omega), \tag{2.16}$$

where E_i and A_i are the energy and absorption spectrum of the system containing a polaron in the state i (i denotes different JT elongation direction), respectively.

The calculated optical absorption spectrum presented in Figure 2.24 clearly shows a red-shift in the first peak that is associated with polarons. In particular, we find that at lower temperatures where kT is on the order of 5 meV or less, the resulting optical spectra follow that of the lowest energy polaron associated with JT elongation along the [100] direction. At higher temperatures, the clear red-shift remains, although a high temperature of 300 K is sufficient to quench the 5 meV energy difference between polaron states. In contrast to the transition associated

with hole polarons, we find that bulk band-band transitions at higher energy (above 1.5 eV) remain mostly unchanged upon uniaxial strain (see Figure S9). Accordingly, this allows one to clearly distinguish the local polaron state involved in optical transitions, whose JT distortion renders them quite sensitive to strain, from that of the band-band bulk state transitions which are insensitive to strain.

2.6.6 Conclusions

To summarize, we present a detailed investigation of the electronic structure and polaronic induced optical transitions in Co_3O_4 based on first-principles calculations. We resolved several contradicting findings in the literature related to the character of the charge carrier and band gap of the material. In particular, we show that the optical gap of pristine Co_3O_4 is 1.6 eV, whereas the lower lying transition around $\sim$0.8 eV is associated with the hole polaron, which was misinterpreted as the band edge of the material. We also demonstrated the important effects of uniaxial strain on the optical spectra of Co_3O_4, which in turn can be used to reveal the localized character of polaron-induced electronic states.

Our study also suggests a strategy for establishing a potential first-principles approach that can simultaneously achieve an accurate description of polaron states, electronic band structure and optical properties in polaronic magnetic oxides. Specifically, the generalized Koopmans' condition can be utilized to derive the fraction of exact exchange from first-principles, which in turn can be used in hybrid functional for investigating the electronic structure of the oxide. These hybrid functionals can also be used for benchmarking DFT-U calculations, which offer a much lower computational cost, or to provide inputs for higher level electronic structure methods, such as many-body perturbation theory within the GW approximation.

2.7 Combining Theory and Experiment

2.7.1 Oxygen Deficient $BiFeO_3$

Bismuth iron oxide, $BiFeO_3$, is a semiconductor with a rhombohedrally distorted perovskite structure that yields a large ferroelectric effect. [237] For this reason, it has been investigated as one of the most promising candidates for ferroelectric diode devices and ferroelectric photovoltaics. [237, 238, 239, 240] Recently, $BiFeO_3$ was also reported as a photoelectrode in a solar water-splitting cell. [241, 242, 243, 244, 245] In these reports, $BiFeO_3$ was demonstrated to have a relatively narrow bandgap of $\sim$2.2 eV and conduction band minimum (CBM) and valence band maximum (VBM) positions that straddle the water reduction and oxidation potentials, [241, 242] all of which are very attractive features for a photoelectrode in a water-splitting photoelectrochemical cell (PEC). Considering that Fe_2O_3, an extensively studied photoanode with a similar bandgap, has a CBM that is $\sim$200 mV more positive than the water reduction potential, [246] the shifts in the CBM and VBM to the negative direction constitute an important advantage of $BiFeO_3$ over Fe_2O_3. [33]

To date, both n-type and p-type $BiFeO_3$ photoelectrodes have been reported, [241, 242, 243, 244, 245] meaning that $BiFeO_3$ can serve as a photoanode or a photocathode, respectively. In these studies, the doping type varied without the introduction of external dopants, suggesting that the defects responsible for n-type and p-type $BiFeO_3$ can both readily form. [33] The defects that cause n-type behavior include oxygen vacancies, [247] and the defects that cause p-type behavior include Bi vacancies. [248]

Despite the many interesting and advantageous features shown for $BiFeO_3$ as a photoelectrode, there have been very few systematic investigations on the photo-

electrochemical properties of $BiFeO_3$. Because of its popularity as a ferroelectric material, most studies on $BiFeO_3$ photoelectrodes have focused on how the application of an external electric field on $BiFeO_3$ affects its photocurrent generation or on the conversion between *n*-type and *p*-type photocurrent. [244, 245, 249, 250] From a careful analysis of these papers, it appears that the $BiFeO_3$ electrodes used in these studies were very lightly doped. [33] For the purpose of accurately evaluating the potential of $BiFeO_3$ as a photoanode or a photocathode, optimally doped *n*-type and *p*-type $BiFeO_3$ electrodes need to be prepared and examined individually.

Considering that charge transport in many oxide-based photoanodes involves small polaron hopping, [37, 36, 35, 12, 18, 49] understanding the formation and transport of small polarons in $BiFeO_3$ is also critical. Unfortunately, while numerous theoretical studies on $BiFeO_3$ have been published to date, they have focused on its bulk polarization, [251, 252] photovoltaic effects, [253, 254] and multiferroic effects. [255, 256] Small electron polaron formation and its effects on dopant ionization energies and concentration of free carriers in $BiFeO_3$ have not yet been investigated theoretically.

In this work, we conducted combined experimental and theoretical studies on *n*-type $BiFeO_3$ photoanodes. For the experimental investigation, we prepared highly uniform $BiFeO_3$ photoanodes by electrodeposition and examined their photoelectrochemical properties and stability for use in a PEC. We then intentionally introduced oxygen vacancies into the pristine $BiFeO_3$ lattice and examined the effect on carrier concentration and photocurrent generation. The experimental results were compared with those of a computational study, which examined the formation of small polarons in $BiFeO_3$ and the effect of oxygen vacancies on small polaron formation and free carrier generation in $BiFeO_3$ for the first time. The

new experimental and computational results discussed in this study will significantly increase our fundamental understanding of $BiFeO_3$ for use as a photoanode material.

Density functional theory calculations were performed using the Quantum ESPRESSO package [52] with PBE+U exchange correlation functional, ultrasoft pseudopotentials, [53] and Hubbard U parameters of 2 eV on O $2p$ and 3 eV on Fe $3d$. All calculations were done using the hexagonal $BiFeO_3$ cell (space group: R3c), which we expanded to a $2 \times 2 \times 1$ supercell to avoid spurious interactions during defect calculations. A $2\times2\times2$ k-point grid was used to calculate the charge density, and a $4 \times 4 \times 4$ k-point grid was used for density of states. We applied a newly developed charge correction scheme [69] to calculations containing excess charge as implemented in JDFTx. [15] For the calculations used to investigate the effect of oxygen vacancies, a single oxygen atom was removed from a 120-atom supercell. Because 72 oxygen atoms are present in this supercell, this is equivalent to removing 1.39 atomic % oxygen (1.39 oxygen atoms out of 100 oxygen atoms), leading to the empirical formula of $BiFeO_{2.96}$.

Theoretical optical absorption spectra of $BiFeO_3$ with and without V_O were obtained by computing the imaginary part of the dielectric function in the random phase approximation with local field effects as implemented in the YAMBO code. [228] The input of this calculation came directly from our single particle eigenvalues and wavefunctions from DFT+U computed in Quantum ESPRESSO. The absorption spectrum (α) is related to the real and imaginary parts of dielectric function (ϵ_1 and ϵ_2, respectively) as shown in the equation below. [230]

$$\alpha(\omega) = \frac{\omega}{c} \frac{\epsilon_2(\omega)}{\sqrt{\frac{\epsilon_1(\omega)+\sqrt{\epsilon_1(\omega)^2+\epsilon_2(\omega)^2}}{2}}} \tag{2.17}$$

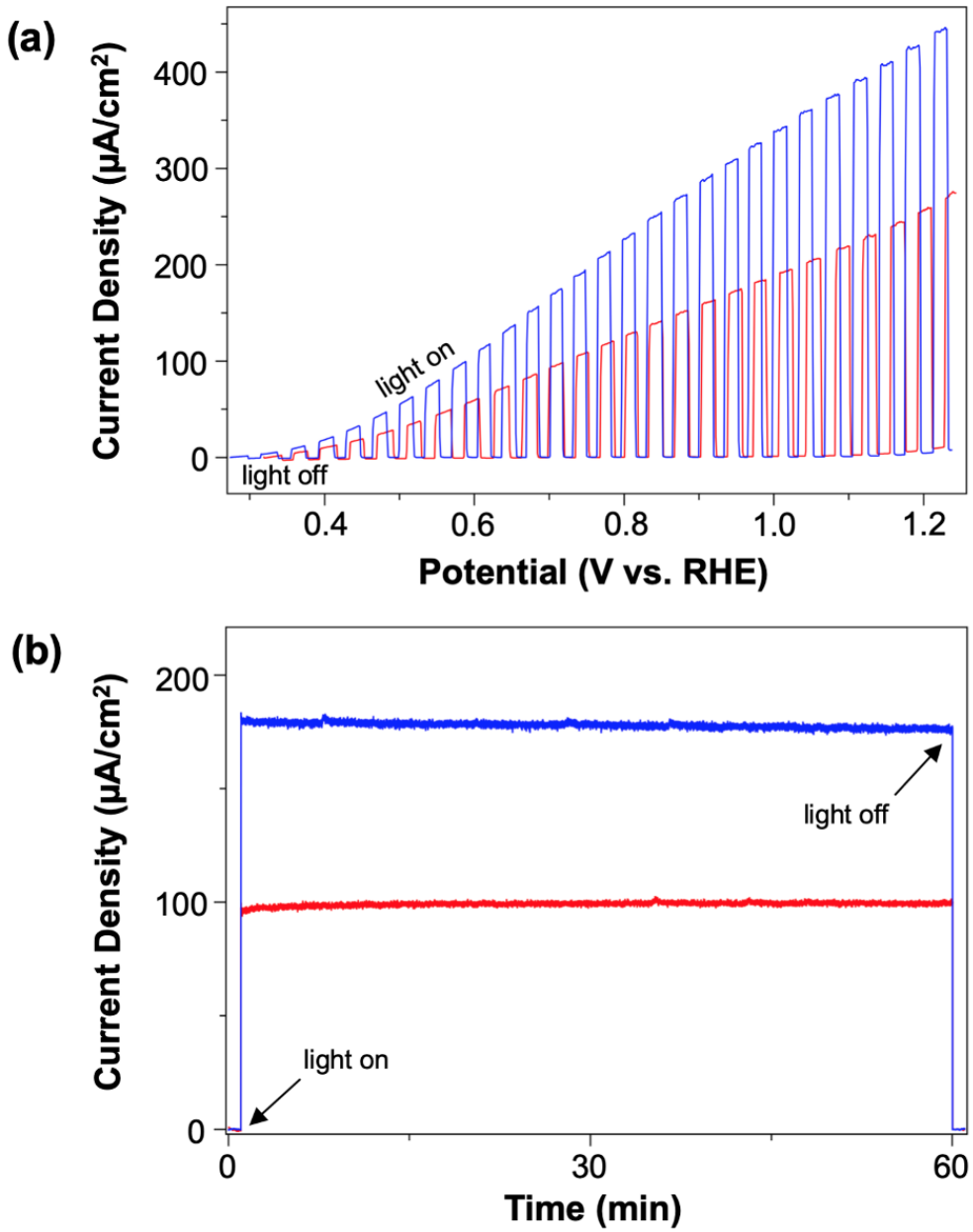

Figure 2.25: (**a**) J-V plots and (**b**) J-t plots at 0.8 V vs. RHE for pristine $BiFeO_3$ (red) and N_2-treated $BiFeO_3$ (blue) for sulfite oxidation. All measurements were obtained in pH 9.2 borate buffer containing 0.7 M sulfite under 1 sun illumination (100 mW/cm^2, AM 1.5 G).

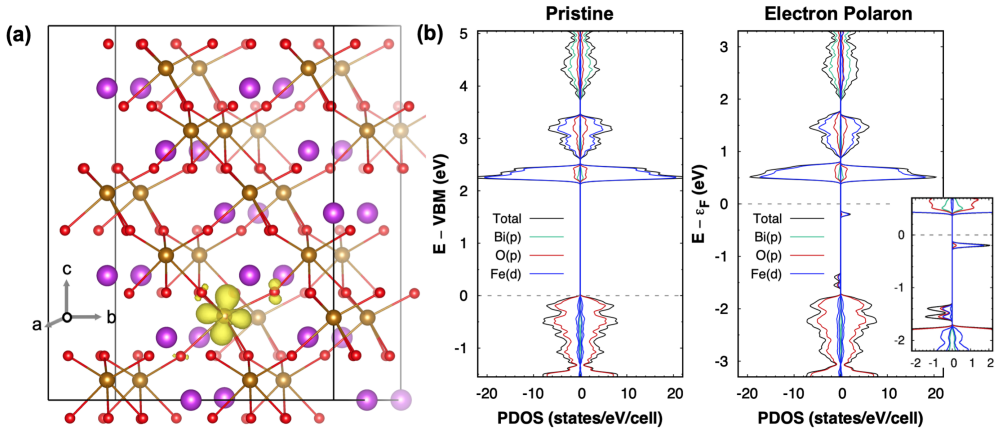

Figure 2.26: (**a**) Norm-squared wavefunction of the electron polaron (yellow cloud) shown as an isosurface in the $BiFeO_3$ lattice (purple = Bi, gold = Fe, red = O). Isosurface value is 1% of the maximum amplitude of the wavefunction; (**b**) projected density of states (PDOS) for $BiFeO_3$ before (left) and after (right) a single electron-polaron is introduced in a 120-atom supercell.

To gain additional insight into the photoelectrochemical properties of $BiFeO_3$, we conducted density functional theory (DFT) calculations to investigate the small polaron formation and its effect on defect ionization energy and free carrier concentration in $BiFeO_3$. First-principles calculations were carried out on $BiFeO_3$ using the DFT+U method (see Computational Methods for more information). The computed bandgap of $BiFeO_3$ was 2.2 eV, which is in great agreement with the experimentally measured value of the bandgap.

Due to strong electron-phonon interactions, carriers in many transition metal oxides are trapped by their self-induced lattice distortions, forming small polarons. [257] Small polarons conduct through the system via a thermally-activated hopping mechanism unlike carriers in covalent semiconductors, which conduct through conventional band mechanisms. [258, 259] Therefore, understanding and facilitating small polaron hopping are critical for the development of oxide-based photoelectrodes. [37, 36, 35, 18, 106, 107]

The formation of an electron polaron in pristine $BiFeO_3$ was simulated by

adding one extra electron into the pristine $BiFeO_3$ system and allowing the system to relax. We observed that the extra electron spontaneously localizes on a single Fe site, forming a small electron polaron as shown in Figure 2.26a. This creates a deep, localized state that lies 1 eV below the CBM of the pristine $BiFeO_3$ as shown in Figure 2.26b. The formation of similar localized electron polaron states has been observed in other Fe^{3+}-based oxides such as Fe_2O_3. [12]

The Fe^{3+} ions in $BiFeO_3$ have O_h crystal field splitting with $3d^5$ high-spin electron configuration. [260] Thus, the extra electron occupies an Fe t_{2g} state, and the small polaron state has mainly t_{2g} character. Furthermore, the presence of a small polaron on the Fe ion, which lowers its valency from +3 to +2, perturbs valence states and creates additional localized states above the VBM of the pristine $BiFeO_3$ (Figure 2.26b). These localized states have character of e_g orbitals of Fe^{2+} and $2p$ orbitals of oxygen. (The corresponding wavefunctions are shown in Figure S6.)

Previous theoretical studies on defect formation in $BiFeO_3$ reported that the oxygen vacancy is a very deep donor with an ionization energy greater than 1 eV, [247, 261, 262, 263] meaning that the oxygen vacancy cannot contribute to the generation of n-type carriers at room temperature. This disagrees with our experimental observation that the N_2-treated $BiFeO_3$ that contains more oxygen vacancies has a higher carrier density and generates significantly more photocurrent at room temperature. We note that previous theoretical studies did not consider the formation of small polarons in $BiFeO_3$ and their effects on defect ionization energies and carrier concentration. Employing recently developed methods, [12, 18] we revisited the formation of oxygen vacancies in $BiFeO_3$ to investigate their ionization energies with respect to the free polaron level in pristine $BiFeO_3$.

When an oxygen vacancy (V_O) is formed in the lattice of $BiFeO_3$, it introduces two electrons that spontaneously generate two small electron polaron states. These two states correspond to the two peaks shown ~0.8 eV below the CBM in the PDOS of $BiFeO_3$ in Figure 2.27a. As in the case of introducing a free electron-polaron, these polaron states have mainly t_{2g} character of Fe^{2+}. Due to attractive electrostatic interactions between the electron polarons and the V_O site, the most thermodynamically stable configuration is the one with the two electron-polarons located at the Fe sites nearest to the V_O, as shown in Figure 2.27b. The difference in energy of the V_O polarons seen in the PDOS is a result of their differing distances from the V_O (Figure S7). The introduction of V_O and the resulting small electron polarons also generate perturbed valence states above the VBM. These perturbed states are mainly composed of the e_g orbitals (*i.e.* $d_{x^2-y^2}$) of Fe^{2+} and $2p$ orbitals of oxygen (Figure S8). When absorption spectra of $BiFeO_3$ with and without V_O were simulated and compared (Figure S9), we found that the presence of the perturbed states above the VBM did not affect the absorption of $BiFeO_3$. This agrees with our experimental results.

In order to consider the effects of oxygen vacancies on the carrier concentration in $BiFeO_3$, it is necessary to compute the formation energy of the defect in each of its charge states q. Typically, the charge transition level of an electron donor from one charge state to a more positive charge state referenced to the CBM defines the ionization energy of the defect. However, in polaronic oxides, the feasibility of polaron hopping is determined not by the ionization energy of the defect with respect to the CBM, but by the ionization energy of the defect with respect to a free polaron state where the polaron is not bound to a defect. [12, 18] Therefore, the true ionization energy of small polarons is equal to the energy difference between the charge transition levels of the defects (solid red dots in

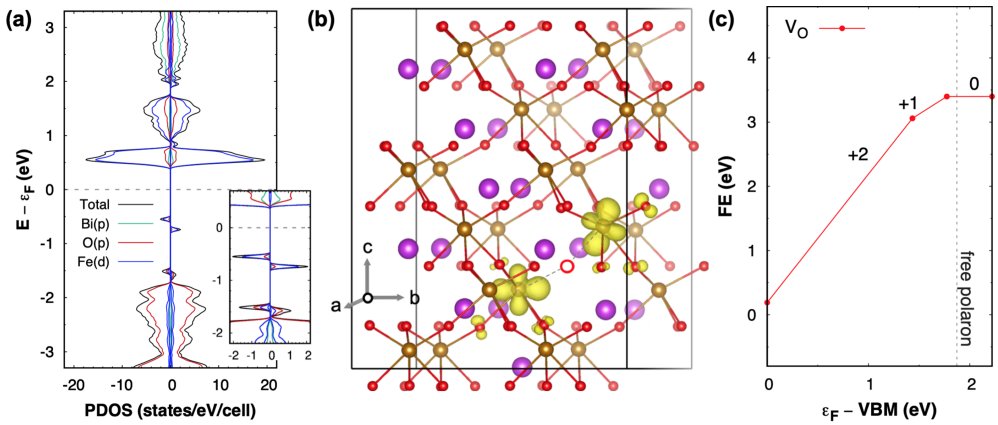

Figure 2.27: (**a**) Projected density of states (PDOS) for $BiFeO_3$ with a single oxygen vacancy (V_O) introduced into a 120-atom supercell; (**b**) Norm-squared wavefunction of the two electron-polarons (yellow regions surrounding Fe). Isosurface value is 1% of the maximum amplitude of the wavefunction. The V_O is indicated by a single empty red circle between the two electron-polarons; (**c**) Charge formation energy (FE) diagram of V_O in $BiFeO_3$.

Figure 2.27c) and the free polaron level (grey dashed line in Figure 2.27c). The free polaron energy level can be obtained from the formation energy of the pristine system with ($q = -1$) and without ($q = 0$) an extra electron. The Fermi level corresponding to the $\varepsilon^{0|-1}$ transition in the pristine system defines the free polaron level. [12, 18] The energy difference between the free polaron level and the CBM is the polaron binding energy.

Under this model, we computed the charge formation energy diagram of the V_O and its corresponding ionization energies. In an oxygen-rich environment, the formation energy of a neutral V_O is 3.4 eV, which agrees with previous calculations. [247, 261, 262, 263] We find that the V_O has two distinct charge transition levels corresponding to the (0/+1) and (+1/+2) transitions. The energies of these charge transition levels relative to the VBM (1.57 eV and 1.22 eV, respectively) are in excellent agreement with recent DFT+U calculations. [257] On the other hand, the positions of charge transition levels relative to the CBM of $BiFeO_3$ vary drastically depending on the choice of U, [247, 257, 262] which is a known

effect. However, their positions with respect to the free polaron level are relatively insensitive to the choice of U, which is similar to what was reported for the case of Sn-doped Fe_2O_3. [12] Comparing the charge transition levels of V_O to the free polaron level, we found energy differences of 99 and 438 meV for the first and second charge transition levels, respectively. The energy of the first charge transition level (0/+1) relative to the free polaron level is comparable to kT at room temperature (26 meV) and indicates that a fraction of the oxygen vacancies in $BiFeO_3$ can ionize at room temperature and contribute to an increased carrier concentration. A simple thermodynamic calculation (assuming a Boltzmann-like distribution) suggests that $\sim$2.05% of oxygen vacancies will be ionized to their +1 state at room temperature at thermal equilibrium. This result differs from previous reports that V_O in $BiFeO_3$ is a deep donor and cannot increase the carrier concentration. [247, 261, 262, 263]

Our theoretical result has clarified the role of oxygen vacancies in enhancing carrier concentrations in $BiFeO_3$, and it is consistent with our experimental findings. This study emphasizes that in polaronic oxides, the defect ionization energies need to be considered with respect to the free polaron level and not to the CBM to more accurately understand the role of defects in the charge transport properties.

To summarize, we performed combined experimental and theoretical investigations on n-type $BiFeO_3$ to evaluate its properties relevant to its use as a photoanode in a photoelectrochemical cell. In our experimental study, we developed a synthesis method to produce high-quality, uniform n-type $BiFeO_3$ photoanodes and examined their photoelectrochemical properties. A bandgap energy of $\sim$2.1 eV was determined for the $BiFeO_3$ photoanodes, and this value agreed well with the films' orange color. The $BiFeO_3$ photoanode showed a photocurrent onset po-

tential of 0.3 V vs. RHE for sulfite oxidation, which is equivalent to its flatband potential. This value is significantly more negative than that of other ternary Fe-based oxide photoanodes. Upon annealing under a N_2 environment to intentionally introduce more oxygen vacancies, the flatband potential was slightly shifted to the negative direction, and the photocurrent increased considerably. These results indicate that oxygen vacancies can contribute to an increase in carrier density, thus improving the charge transport properties of $BiFeO_3$. While the photocurrent reported in this study is one of the highest among those reported for $BiFeO_3$ photoanodes, the observed value was still far below that expected for a photoanode having a bandgap of 2.1 eV, suggesting that bulk recombination is a major limitation of $BiFeO_3$. Considering that nanostructuring other Fe^{3+}-containing photoanodes such as Fe_2O_3 that suffer from short hole-diffusion lengths can significantly increase electron-hole separation, nanostructuring $BiFeO_3$ is a logical next step to take to improve its photocurrent generation.

In our theoretical study, we showed for the first time that an extra electron in $BiFeO_3$ spontaneously localizes on an Fe^{3+} ion and forms a small polaron. The formation of the small polaron also perturbs valence states and creates additional localized states above the VBM of pristine $BiFeO_3$. When an oxygen vacancy is introduced into the $BiFeO_3$ lattice, it forms two electron-polarons at the two Fe sites nearest to the V_O site. By accurately referencing the charge transition level to the free electron polaron level instead of to the CBM in our charge formation energy calculations, we showed that the first ionization energy of the V_O is 99 meV, meaning that the V_O is capable of serving as a donor to enhance the carrier concentration of $BiFeO_3$. Overall, $BiFeO_3$ has many attractive properties for use as a photoanode in a water-splitting PEC, and we expect that strategies such as nanostructuring and substitutional doping that can introduce shallow donors

can continue to increase the photocurrent generation. Our combined investigation contributes to a fundamental understanding of the photoelectrochemical properties of $BiFeO_3$ that can aid future systematic investigations of both n-type and p-type $BiFeO_3$ photoelectrodes.

2.7.2 K Doping in $LaFeO_3$

Computational Methods Density functional theory calculations were performed using the Quantum ESPRESSO package [52] with PBE+U exchange and correlation functional, with a Hubbard U parameter on O $2p$ of 2 eV and Fe $3d$ of 3 eV and norm-conserving pseudopotential [54] with a plane wave energy cutoff of 80 Ry. A total energy convergence of at least 10^{-7} Ry was used for all self-consistent calculations while atomic forces were relaxed until a threshold of 10^{-3} Ry/au was met. Final calculations implemented a $2 \times 2 \times 2$ supercell consisting of 160 atoms with a k-point grid of $2 \times 2 \times 1$ with the cell parameters attained via a variable cell relaxation. To investigate the effect of K doping, 1 out of 32 La atoms was replaced with K atom, which is equivalent to 3 at. % K doping at the La site. This level of doping was chosen for computational studies because experimental studies showed that 3 at % K doping at the La site is optimal for enhancing the photoelectrochemical properties of $LaFeO_3$.

Effect of K Doping on Electronic Structure and Optical Absorption. $LaFeO_3$ is a charge transfer insulator with valence states mainly composed of O $2p$ and conduction states mainly composed of Fe $3d$ orbitals (Figure 2.28a). The electronic band structure of pristine $LaFeO_3$ shows a direct $\Gamma - \Gamma$ bandgap of 2.13 eV. We used Hubbard U parameters of 2 eV for O $2p$ and 3 eV for Fe $3d$, which enables the formation of both electron- and hole-polarons and results in a bandgap value of pristine $LaFeO_3$ close to the reported experimental value. [163]

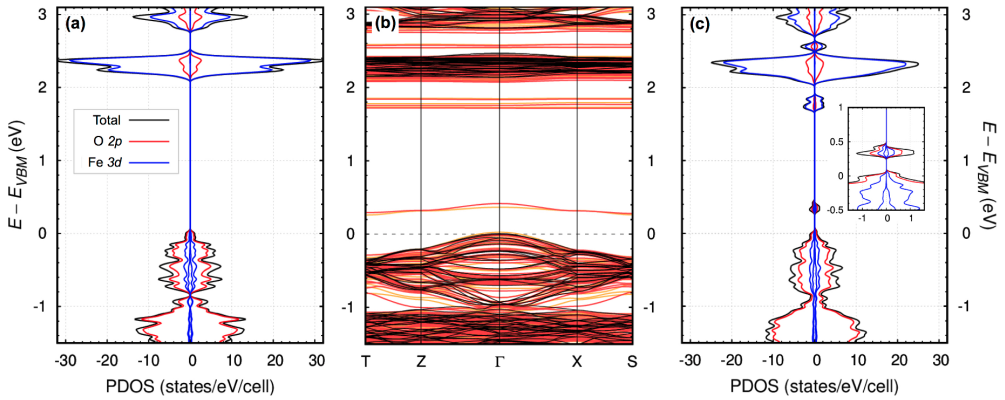

Figure 2.28: (**a**) Total (black) and projected (red for O $2p$ and blue for Fe $3d$) density of states of pristine $LaFeO_3$. The reference zero is chosen to be at the valence band maximum. (**b**) Band structure of pristine (black) and K-doped $LaFeO_3$ (red = spin up and orange = spin down). (**c**) Total (black) and projected (red for O $2p$ and blue for Fe $3d$) density of states of K-doped $LaFeO_3$. The inset image shows magnified hole-polaron states.

We confirmed that the major effects of K doping on the band structure of $LaFeO_3$ discussed here are not affected by the choice of U parameters as long as they are chosen to allow for the formation of both electron- and hole-polarons. [35, 18, 12, 106] For example, the major results obtained with Hubbard U parameters of 4 eV for O $2p$ and 5 eV for Fe $3d$ (Figure S1) are the same as those shown in Figure 2.28 although the exact energy levels of the band structures may vary.

After doping the system with K, we observed the formation of an isolated hole-polaron state, which is a hybridized state consisting of O $2p$ and Fe $3d_{x^2-y^2}$ located at 0.3 eV above the VBM (Figure 2.28 b-c). This suggests that the two holes generated by the replacement of La^{3+} with K^+ are localized on Fe atoms and their neighboring O atoms, [264] forming Fe^{4+}. This result agrees well with experimental observations that the electrical conduction and dipolar relaxation in $LaFeO_3$ are dominated by polaronic hole hopping between Fe^{4+} and Fe^{3+}. [265, 266] Figure 2.29a shows a structural unit of $LaFeO_3$ where eight Fe atoms numbered through 1 and 8 are located at the corners of a cube with a K atom at the center.

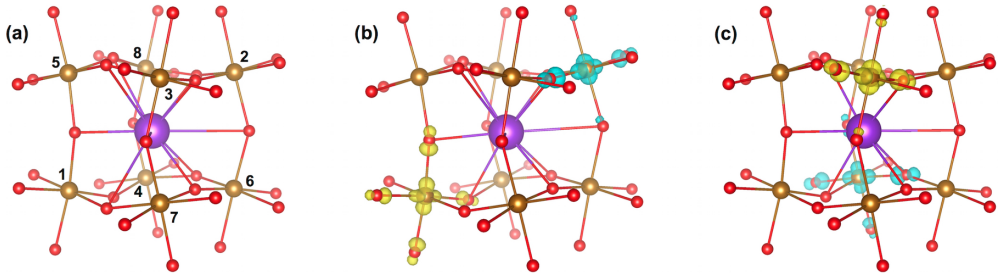

Figure 2.29: (**a**) A cube composed of eight Fe atoms at the corners numbered from 1 through 8 with a K atom at the center (K = purple, Fe = brown, O = red). (b-c) Hole-polaron wavefunction modulus with an isosurface at 10% of the maximum value for the spin up (yellow) and spin down (turquoise); (**b**) hole-polarons formed at the (1, 2) Fe pair, which are symmetrically identical to those formed at the (5, 6) Fe pair; (c) hole-polarons formed at the (3, 4) Fe pair, which are symmetrically identical to those formed at the (7, 8) Fe pair.

The most energetically preferred configurations of the two hole-polarons formed by K doping are those with the holes occupying Fe at the off-diagonal corners. Due to crystal symmetry, only two unique Fe-Fe diagonal positions are present as shown in Figure 2.29b-c (Table S1). Between these two configurations, the one shown in Figure 2.29b is more stable by 113 meV. Considering that our calculations were performed at 0 K and only included electronic energy without an entropy contribution, it is possible that a non-negligible concentration of hole-polarons formed in the sample at room temperature may exist in the configuration shown in Figure 2.29c.

Our calculations also showed that K doping decreases the bandgap by lowering the conduction band minimum (CBM) from 2.13 eV to 2.06 eV and additionally forms multiple highly localized states below the CBM (Figure 2.28b-c). We note that these states are formed not due to the presence of K but due to the free holes from K doping that form small polarons, which perturbed the system. (Even when free holes are introduced without K, the same states form.) To understand how these changes in electronic structure affect the optical properties of the system, we

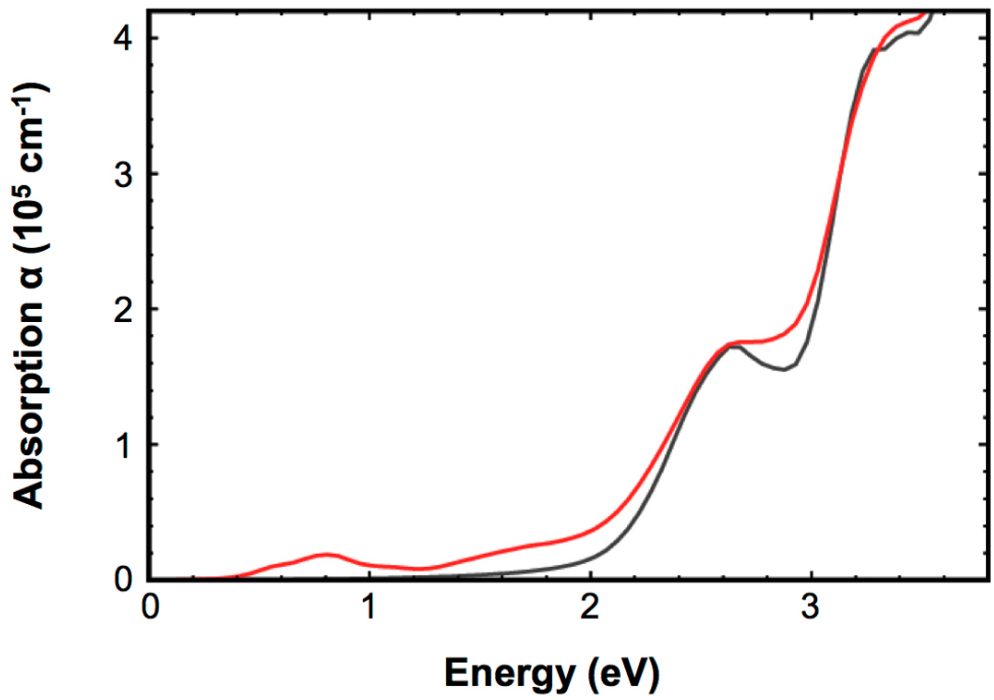

Figure 2.30: Calculated absorption spectra for pristine (black) and K-doped (red) $LaFeO_3$.

calculated the absorption spectra of pristine and K-doped $LaFeO_3$ (Figure 2.30). Because of the presence of optical anisotropy in the system, we averaged optical responses from light that was polarized along the a, b, c crystal axes. The results showed that K doping causes a negligible change in the high energy range ($\geq$ 2.4 eV) in terms of the position and intensity of the absorption peaks. However, K doping clearly enhances absorption in the low energy range ($<$ 2.4 eV) due to the lowering of the CBM and the introduction of perturbed states below the CBM. Since the solar spectrum contains a considerable number of photons near 2 eV, even a small increase in absorbance in this region may significantly increase the number of photons that can be utilized by $LaFeO_3$ for photocurrent generation. We note that we did not include excitonic effects in this calculation because in most transition metal oxides, the exciton binding energy is small (0.1 eV) and its change by doping is negligible. [49, 17, 267]

K as a Shallow Acceptor in $LaFeO_3$. Although K doping introduces two holes into the system, the experimental carrier concentration will only increase when the dopant site does not trap the holes within the system. A dopant is generally considered to be a trap if the defect ionization energy or the energy that is required to free a defect-bound polaron is much higher than kT. We computed the defect ionization energies and formation energies from first principles. In K-doped $LaFeO_3$, the $q = -1$ system (where one of the two holes from K substitution of La has been removed) is unstable leading to a direct $q = 0$ to $q = -2$ transition. Furthermore, the value of this charge transition level ($\varepsilon^{0|-2}$) is only 30 meV above the VBM. Since the energy required for this transition is comparable to kT at room temperature (25 meV), K can serve as a shallow acceptor. We also note that the ionization energy obtained from defect formation energies is not significantly different from the energy difference between the VBM and the position of the hole state in the PDOS (Figure 2.28c). This result indicates that the DFT+U level has largely corrected the delocalization errors that are known to occur at the semi-local DFT level. Additionally, it implies that the geometry relaxation at different charge states has minimum contribution. [216, 16] From these results we concluded that K doping can effectively increase the hole concentration in $LaFeO_3$.

Effects of K Doping on Atomic Structure. $LaFeO_3$ has a perovskite structure in which the La atoms are located at the center of a cube composed of eight Fe atoms at the corners that are octahedrally coordinated with O. However, the atoms in $LaFeO_3$ are slightly displaced from those of an ideal cubic perovskite structure, and $LaFeO_3$ has an orthorhombic Pnma structure with a G-type antiferromagnetic ordering on the Fe atoms. [268] Theoretically predicted cell parameters for pristine and K-doped $LaFeO_3$ are shown in Table 2.8. For K-doped $LaFeO_3$, the results for two configurations of hole-polaron formation shown

in Figure 2.29b-c are shown as Configuration 1 and Configuration 2, respectively.

System	a (Å)	b (Å)	c (Å)	Volume (Å^3)
Pristine	5.652	7.903	5.568	248.69
K-doped C1	5.644	7.887	5.569	247.91
K-doped C2	5.649	7.886	5.566	247.95

Table 2.8: Theoretically predicted cell parameters and band gap values for pristine $LaFeO_3$ and K-doped $LaFeO_3$.

Despite the fact that K^+ (164 pm) has a larger ionic radius than La^{3+} (136 pm), [108] the result shows that K doping (one K atom in the 160 atom cell) shrinks the unit cell volume by ∼0.3% for both configurations. This is because a fraction of Fe^{3+} (64.5 pm) is substituted by Fe^{4+} (58.5 pm) owing to the hole-polaron formation. To confirm this, we considered four different systems: (1) pristine sample with a neutral charge; (2) pristine sample plus two holes without K doping, giving a +2 charge; (3) K-doped minus two holes, giving a −2 charge; and (4) K-doped sample with corresponding Fe^{4+} formation with a neutral charge (Table S2). System 2 has the same number of Fe^{4+} ions as System 4, but La is not replaced with K. System 3 has no Fe^{4+} formation even though La is replaced with K. We found that System 2 (pristine sample plus two holes, +2 charge) showed a decreased cell volume due to Fe^{4+} formation, whereas System 3 (K-doped sample minus two holes, −2 charge) showed an increased cell volume because K^+ has a larger radius than La^{3+}. System 4 (K-doped sample with corresponding Fe^{4+} formation) showed consistency with the average cell volume of Systems 2 and 3 as expected. However, because the magnitude of cell shrinkage caused by the formation of Fe^{4+} is greater than that of expansion caused by the replacement of La by K, the cell volume of System 4 is smaller than that of the pristine sample (System 1).

In summary, we performed a combined theoretical and experimental investigation to examine the effect of substitutional K doping at the La site (3 at. %) of $LaFeO_3$. The theoretical study showed that K doping creates shallow acceptor levels above the VBM of $LaFeO_3$ and can effectively increase the majority carrier density. Furthermore, K doping decreased the bandgap by lowering the CBM and additionally generated multiple highly localized defect states below the CBM. The theoretical study also showed that the two holes generated by the replacement of La^{3+} with K^+ are localized on Fe atoms and their neighboring O atoms, forming Fe^{4+}. The most stable hole-polaron configurations around K were examined. In terms of structure, our theoretical study predicted that K doping results in a shrinkage of the unit cell owing to the conversion of Fe^{3+} to smaller Fe^{4+} even though K^+ has a large ionic radius than La^{3+}.

The results obtained from the theoretical studies were verified by experimentally preparing $LaFeO_3$ and K-doped (3 at. %) $LaFeO_3$ as high-quality, high-surface-area electrodes having the same morphology. The XRD patterns indeed showed a decrease in all cell parameters, which confirms the substitution of La^{3+} by K^+ and the resulting Fe^{4+} formation. The increase in Fe^{4+} concentration in K-doped $LaFeO_3$ was also supported by XPS. The UV-vis-NIR absorption spectra showed that K doping decreased the bandgap by $\sim$0.2 eV and enhanced the absorption below the bandgap as predicted by the electronic band structure and simulated optical response of K-doped $LaFeO_3$. Furthermore, Mott-Schottky analysis confirmed an increase in carrier density caused by K doping. Due to the increase in photon absorption and charge transport properties, K-doped $LaFeO_3$ generated a significantly increased photocurrent for O_2 reduction, which is a good measure of the increase in the number of surface-reaching electrons under illumination. K-doped $LaFeO_3$ also increased the photocurrent for water reduction. However,

the increase in this case was not significant due the poor catalytic ability of both the pristine and K-doped $LaFeO_3$ for water reduction, resulting in considerable surface recombination. The beneficial effect of the decreased bandgap of K-doped $LaFeO_3$ on photocurrent generation was confirmed by IPCE, which showed photocurrent generation below the bandgap of the pristine $LaFeO_3$. The enhanced photocurrent caused by K doping was also confirmed to be stable. This study demonstrated that substitutional doping of La^{3+} with K^+ offers an effective way to increase both photon absorption and charge transport properties that directly influence photocurrent generation by $LaFeO_3$. We plan to perform further investigations of doping at the Fe site as well as doping at the La site with other dopants that vary in nature (alkaline, alkaline earth, or transition metals) and valency to obtain a comprehensive understanding of the effect of composition tuning of *p*-type oxides with a perovskite structure.

Chapter 3

Designing Quantum Defects in Two Dimensional Materials

3.1 Overview

Quantum technologies offer exotic and impressive capabilities in computation, sensing, and information [269]. While several systems of quantum computation exist, defect based qubits offer a distinct advantage in their ability to operate optically and under room temperature conditions [270, 271, 272]. Furthermore defects in two-dimensional (2D) materials yield a higher-ceiling for defect based quantum technologies where spatially controlling doping, entangling qubits, and qubit tuning are all more attainable [273, 274]. In particular, two-dimensional hexagonal boron nitride (h-BN) has demonstrated that it can host defect-based single photon emitters (SPEs) [275] and qubits [276].

As such, my work has focused on the prediction of defects in h-BN for quantum applications. From a computational perspective, studying defects in 2D materials offers several technical challenges. In 2018, I was awarded an NSF scholarship for

studying quantum information science through a program known as QISE-NET. This program provides supplemental funding to perform ongoing research in collaboration with Argonne National Laboratory, so that we may study defects in h-BN (this was later highlighted in the UC Santa Cruz newsletter). In particular, these efforts culminated in our work from 2018, wherein we demonstrated how to compute the single-particle band gap of h-BN via a Koopmans' compliant hybrid functional approach which incorporates improved screening effects in our calculation but mitigates the expense of many-body theory based methods i.e. the GW approximation [216]. Additionally, this work demonstrated the layer dependence on defect ionization energies. Following this up, we then studied radiative and nonradiatiave recombination of defects in h-BN. One particularly interesting facet of this research in the demonstration of how significantly the nonradiative recombination of defects can be effected by strain, wherein we predicted the strain fingerprints of $N_B V_N$ which matches closely with subsequent experimental measurements. [277] Recently, I also implmented computing the zero-field splitting of $S \geq 1$ systems, an essential quantity in defect based-qubit systems like NV center in diamond. In addition, I have implemented computing intersystem crossing (necessary for spin initialization and readout) with spin-orbit coupling and electron-phonon interaction. With these computed static and dynamical properties, we are able to predict spin qubits read-out efficiency and new quantum spin defect systems in hexagonal boron nitride which can be potential candidates for spin-based quantum technologies.

3.2 Charge Defect Formation and Ionization Energies

In our 2018 work published in Physical Review Materials [216], we demonstrated methods of computing charge transition levels at various levels of theory and propose referencing to vacuum among other things as a way to achieve consistency at semi-local DFT, hybrid DFT, and GW. We also employ Koopmans' condition to achieve hybrid functionals which reproduce GW results. Two-dimensional (2D) materials provide the unique opportunity to scale future electronics smaller than ever believed physically possible, implying engineering 2D materials is a promising strategy that can meet the demands of future nanotechnologies [278]. As defects play a crucial role in the optical and electronic properties of these systems, the engineering of defects in 2D materials has sparked continuous interest [279, 280, 281, 282, 283, 284]. For example, defects in h-BN have been found to be the source of stable polarized and ultra-bright single-photon emissions at room temperature [285, 286, 273, 287]. Hence, the development of our understanding of defects in 2D materials will open up further possibilities for emerging applications in quantum information and nanotechnology with much better scalability than traditional defects in 3D materials.

Unlike in their 3D counterparts [288, 19, 289, 70, 290], first-principles techniques for calculating defect properties in 2D materials still face significant challenges. Specifically, eliminating the periodic charge interactions for charged defects in 2D materials requires a charge correction scheme that accounts for the weak and anisotropic dielectric screening of 2D systems [291, 292, 293]. Furthermore, several exchange-correlation functionals that provide accurate electronic structures for 3D bulk systems are no longer applicable to ultrathin 2D systems.

For example, the fraction of Fock exchange (α) in hybrid functionals can be approximated as the inverse of dielectric constant (ε_∞) of the material [294, 295], but this is problematic for ultrathin 2D materials where ε_∞ decreases to unity in the limit of infinite vacuum sizes (complete separation between periodic images). Therefore, the determination of α in hybrid functionals for 2D materials remains an open question. On the other hand, many body perturbation theory techniques (*e.g.* GW approximation) give accurate quasiparticle energies such as band gaps and band positions; however, high computational cost and slow convergence with respect to empty states make the screening of many defects in 2D materials impractical with conventional implementations [296, 297, 298, 299, 300, 301].

In our previous work [16, 69], we developed an efficient and accurate method that can give reliable charge corrections for total energies and electronic states of charged defects in 2D materials *without any supercell extrapolations*, and then provided accurate defect CTLs with the DFT+GW scheme [302, 303, 304, 305]. Such implementation is built on top of the WEST-code [306], Quantum-Espresso [52] and JDFTx [15] packages. In our GW calculations, we avoided explicit inclusion of empty states and inversion of dielectric matrices [306, 224, 307], while also speeding up vacuum size convergence with a 2D Coulomb truncation [308]. In this letter, we propose to solve two important issues for 2D materials. First, we determine which level of theory and which electron chemical potential reference one should use to calculate a CTL. Second, we show how to define the fraction of Fock exchange in hybrid functionals for accurate band edges and band gaps. In the end, we combine these two findings to obtain accurate defect ionization energies for 2D materials.

3.2.1 Methodology

Computational Methods In this work, all structural relaxations and total energy calculations were performed using open source plane wave code Quantum-ESPRESSO [52] with Perdew-Burke-Ernzerhof (PBE) [10] exchange-correlation functional, ONCV norm-conserving pseudopotentials [54, 55], a wavefunction cutoff of 70 Ry and a k-point mesh corresponding to $12 \times 12 \times 1$ or higher in the primitive cell. The vacuum between periodic images along non-periodic direction is at least 30 Bohr.

Once the structural parameters were determined, we performed a separate single-point calculation using a wavefunction cutoff of 45 Ry and hybrid functionals including HSE, B3PW91, PBE0 and PBE0(α) with a sufficient k-point mesh as large as 36×36. The band gap is determined from the difference between valence band maximum (VBM) and conduction band minimum (CBM). If the k-point of VBM or CBM is not included in the k-point mesh, it is interpolated between eigenvalues of the same band of nearby k-points.

A single point calculation using a wavefunction cutoff of 45 Ry and PBE functional was performed as the starting point for GW calculations. The GW calculations were performed using the WEST code [306]. We used the G_0W_0 approach with starting wavefunctions and eigenvalues at the PBE level of theory. We employed the contour deformation technique for frequency integration of the self energy. For the dielectric matrix calculation, the number of eigenpotentials (N_{PDEP}) was chosen to be $3N_{\mathrm{electron}}$, and we used $4N_{\mathrm{electron}}$ to validate its convergence. The final GW correction values were extrapolated between 9×9 and 12×12 k-point meshes to infinite k-points similar to Ref. [16].

The charge corrections [69] for the total energies and eigenvalues of charged defects at the DFT level employed the techniques developed in Ref. [69] and

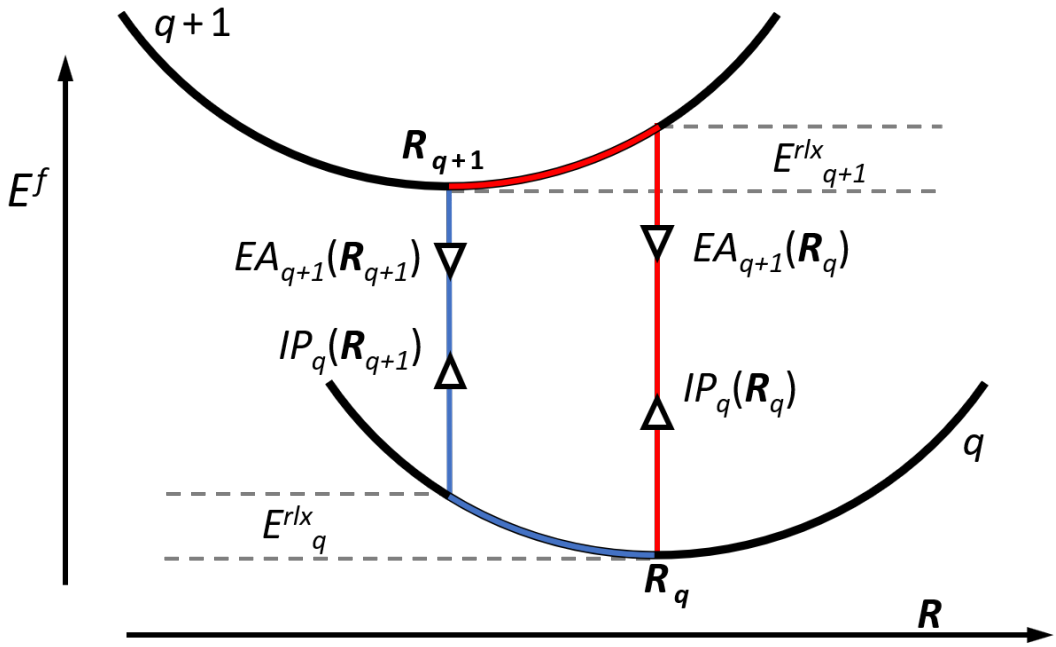

Figure 3.1: Schematic plot of the two paths (distinguished with blue/red color) that transition from charge state q to $q+1$. For each path, there is a corresponding vertical excitation, which can be computed either with EA_{q+1} or IP_q (noted with up/down arrowheads), as discussed in the main text.

in the SI section IV, which were implemented in the JDFTx code [15, 308, 309] (computed dielectric profiles are shown in the SI). Dielectric profiles are computed by applying finite electric fields following the procedure discussed in Ref. [16], with a smearing width of 1 Bohr (smearing widths of 0.5 to 4.0 Bohr yield identical charge corrections).

Thermodynamic Charge Transition Levels

A thermodynamic CTL is the value of electron chemical potential ε_F at which the stable charge state of the system changes, *e.g.* from q to $q+1$. Therefore, CTLs are calculated through the equivalency of the formation energies q and $q+1$,

given by Eq. (3.1) [19].

$$\begin{aligned}\varepsilon_{q+1|q} &= E_q^f(\mathbf{R}_q) - E_{q+1}^f(\mathbf{R}_{q+1}) \\ &= E_q(\mathbf{R}_q) - E_{q+1}(\mathbf{R}_{q+1}) - \varepsilon_F \end{aligned} \tag{3.1}$$

Here $E_q^f(\mathbf{R})$ is the defect formation energy with charge q and geometry $\mathbf{R}$, and $\mathbf{R}_q$ is the relaxed geometry of the system with charge q. $E_q(\mathbf{R})$ is the total energy that relates to $E_q^f(\mathbf{R})$ and ε_F following the definition of Eq. (1) in Ref. [16]. Diagrammatically, Eq. (3.1) is the energy difference between two potential surface minimua in position space $\mathbf{R}$, as shown in Fig. 3.1.

3.2.2 Implementing Quasiparticle Corrections in Defect Charge Transition Levels

It is well-known that local and semi-local functionals do not give accurate total energy differences between two charge states, where an electron removing (IP)/adding process (EA) is involved. An alternative approach [16] is to separate Eq. (3.1) into two parts: the vertical excitation energy between two charge states (q and q+1) at the same geometry ($\mathbf{R}$) (denoted as quasiparticle energies ε^{QP}) and the geometry relaxation energy at a fixed charge state (denoted with E^{rlx}). Since DFT is known to provide reliable geometry relaxation energies (if one corrects the fictitious charge interactions between periodic images as we did in Ref. [16]), this separation allows us to accurately calculate the vertical excitation energies with a higher level of theory appropriate for non-neutral excitations, such as the GW approximation.

One can separate Eq. (3.1) by two possible physical pathways from $E_q^f(\mathbf{R}_q)$ to $E_{q+1}^f(\mathbf{R}_{q+1})$ as shown in Fig. 3.1. One pathway (red path) occurs with a vertical

excitation at $\mathbf{R}_q$ ($E^f_{q+1}(\mathbf{R}_q) - E^f_q(\mathbf{R}_q)$) followed by a geometry relaxation at the charge state $q+1$ ($E^f_{q+1}(\mathbf{R}_{q+1}) - E^f_{q+1}(\mathbf{R}_q)$), shown in Eq. (3.2). The other pathway (blue path) occurs through the geometry relaxation at the charge state q plus a vertical excitation at $\mathbf{R}_{q+1}$, corresponding to Eq. (3.3).

$$\begin{aligned}\varepsilon_{q+1|q} &= \underbrace{E^f_q(\mathbf{R}_q) - E^f_{q+1}(\mathbf{R}_q)}_{\varepsilon^{QP}} + \underbrace{E^f_{q+1}(\mathbf{R}_q) - E^f_{q+1}(\mathbf{R}_{q+1})}_{E^{rlx}} \\ &= \varepsilon^{QP}_{q+1|q}(\mathbf{R}_q) + E^{rlx}_{q+1} \end{aligned} \tag{3.2}$$

$$\begin{aligned}\varepsilon_{q+1|q} &= \underbrace{E^f_q(\mathbf{R}_q) - E^f_q(\mathbf{R}_{q+1})}_{E^{rlx}} + \underbrace{E^f_q(\mathbf{R}_{q+1}) - E^f_{q+1}(\mathbf{R}_{q+1})}_{\varepsilon^{QP}} \\ &= E^{rlx}_q + \varepsilon^{QP}_{q+1|q}(\mathbf{R}_{q+1}) \end{aligned} \tag{3.3}$$

Note that all three equations (Eq. (3.1), (3.2), (3.3)) are exactly equivalent theoretically. Yet, in practice they may yield sizable differences, as discussed later.

Furthermore, the vertical excitation energies $\varepsilon^{QP}_{q+1|q}$ in Eq. (3.2) and Eq. (3.3) can be determined from either the ionization potential of the charge state q (IP_q) or the electron affinity of the charge state $q+1$ (EA_{q+1}) , as noted in Fig. 3.1 with up/down arrowheads. Note that we obtained IP and EA through eigenvalues at different levels of theory based on the Janak's theorem [310]. The difference between IP_q and EA_{q+1} is largely related to the delocalization or localization error at a particular level of theory, and serves as a stringent test for an exchange-correction scheme in electronic structure calculations [311].

Method		Defect			
		C_B	V_NC_B	C_N	V_NC_B
	CTL	(0/+1)	(0/+1)	(-1/0)	(-1/0)
PBE	Eq3.1	-3.63	-4.22	-3.54	-1.57
	Eq3.2	-3.61	-4.29	-3.51	-1.66
	Eq3.3	-3.64	-4.33	-3.49	-1.67
PBE0	Eq3.1	-3.65	-4.19	-3.50	-1.87
	Eq3.2	-3.60	-4.17	-3.50	-1.87
	Eq3.3	-3.62	-4.21	-3.50	-1.21*
G_0W_0	Eq3.2	-3.40	-4.29	-3.74	-1.74
	Eq3.3	-3.28	-4.22	-3.73	-1.70
		$IP_q(\mathbf{R}_q)$-$EA_{q+1}(\mathbf{R}_q)$			
PBE		2.68	2.60	2.75	2.50
PBE0		1.15	1.09	1.13	1.42
G_0W_0		0.04	0.20	0.03	0.19

Table 3.1: Charge transition levels (CTLs) relative to vacuum (in eV) of multiple defects in monolayer h-BN. These values are collected via three methods (Eq. (3.1-3.3)) at various levels of theory (PBE, PBE0, G_0W_0@PBE). The CTLs relative to vacuum are remarkably similar. The one exception, V_NC_B (-1/0) at PBE0 (marked with *) incidentally has a band inversion resulting in a defect level within the valence band, breaking the reliability of Eq. (3.3). We also show $IP_q(\mathbf{R}_q)-EA_{q+1}(\mathbf{R}_q)$ at different levels of theory. Note that at the G_0W_0 level, this difference is < 0.2 eV.

Therefore, we firstly compared the CTL with PBE, PBE0 and G_0W_0@PBE for three different defects in monolayer BN as shown in Table 3.1, where ε^{QP} is obtained by taking the average of IP_q and EA_{q+1} as:

$$\varepsilon^{QP}_{q+1|q}(\mathbf{R}) = \frac{1}{2}(EA_{q+1}(\mathbf{R}) + IP_q(\mathbf{R})) \tag{3.4}$$

Note that we propose to set ε_F equal to the vacuum level (determined by the electrostatic potential in the vacuum region of supercells) and use it as a reference

for Eq. (3.1). We found this choice (opposed to band edges) is particularly advantageous for obtaining consistent CTLs among different methods as shown in Table 3.1. (More computational details for G_0W_0@PBE can be found in SI, with similar numerical techniques and parameters used in Ref. [16]). There are several interesting observations from Table 3.1, as follows. First, we found excellent agreement (within 0.1 eV) among Eq. (3.1), (3.2) and (3.3) for each defect at each level of theory. Second, we found the results obtained among PBE, PBE0 and G_0W_0@PBE are also strikingly similar (within 0.2 eV) for each defect. This means the CTLs of 2D materials relative to vacuum are *not affected by the level of theory one chooses*. Note that the difference between IP_q and EA_{q+1} is more than 2 eV for PBE, reduced to 1 eV at PBE0 level ($\alpha = 0.25$), but less than 0.2 eV at G_0W_0@PBE, which indicates the delocalization error present with semi-local DFT has been mostly corrected at G_0W_0@PBE [311].

3.2.3 Generalized Koopman's Condition for Exact Exchange of 2D Materials

After we obtained reliable CTLs, in particular relative to vacuum, we focused on how to calculate accurate band edge positions and band gaps of 2D materials in order to determine defect ionization energies. Using the GW approximation, we obtained an accurate quasiparticle band gap (indirect at T→M) 6.01 eV for bulk h-BN (Table 3.2), in excellent agreement with the experimental fundamental electronic gap 6.08 ± 0.015 [312]. Nonetheless, GW is still too computationally demanding for materials' screening and computing forces is non-trivial. Therefore, the development of computationally affordable methods such as accurate non-empirical hybrid functionals for 2D materials is strongly desired.

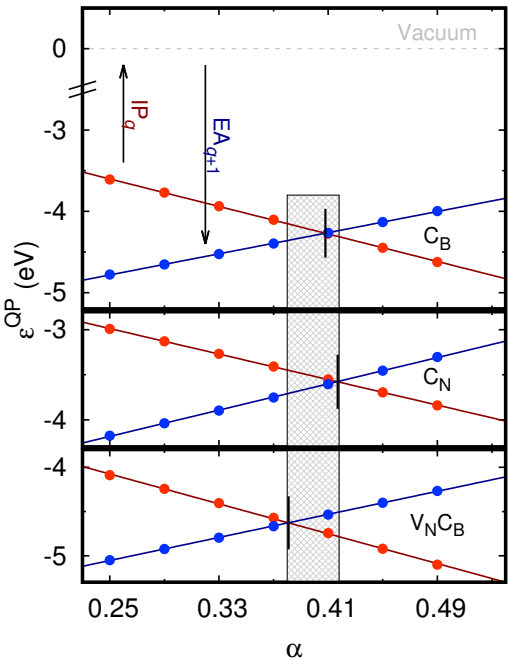

Figure 3.2: The IP at $q = 0$ and the EA at $q = +1$ for the defects C_B, C_N and V_NC_B in monolayer h-BN as a function of the fraction of Fock exchange α for PBE0(α). The predicted exchange constant ($\alpha = 0.409$, 0.41 and 0.382, respectively) is the corresponding crossing point where $EA_{q+1} = IP_q$.

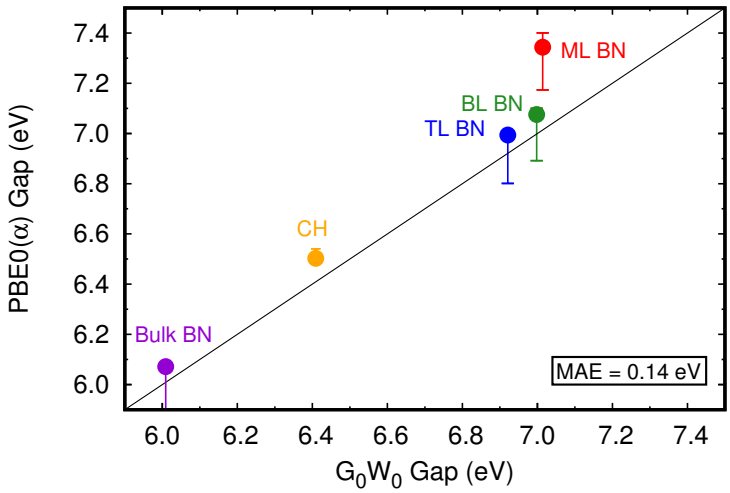

Figure 3.3: Comparing computed band gaps of *h*-BN (monolayer, bilayer, trilayer, bulk) and graphane with PBE0(α) versus those computed with G_0W_0@PBE . Overall we find that our PBE0(α) results agree very well with G_0W_0, yielding a MAE of 0.14 eV.

System	PBE	HSE	PBE0	B3PW	PBE0(α)	G_0W_0
Graphane	3.57 | $\Gamma \to \Gamma$	4.41 | $\Gamma \to \Gamma$	5.06 | $\Gamma \to \Gamma$	5.04 | $\Gamma \to \Gamma$	6.54 | $\Gamma \to \Gamma$	6.41 | $\Gamma \to \Gamma$
ML BN	4.71 | $K \to K$	5.70 | $K \to \Gamma$	6.33 | $K \to \Gamma$	6.33 | $K \to \Gamma$	7.34 | $K \to \Gamma$	7.01 | $K \to \Gamma$
BL BN	4.49 | $T \to M$	5.81 | $T \to M$	6.46 | $T \to \Gamma$	6.17 | $T \to M$	7.08 | $T \to \Gamma$	7.00 | $T \to \Gamma$
TL BN	4.36 | $T \to M$	5.68 | $T \to M$	6.40 | $T \to M$	6.03 | $T \to M$	7.01 | $T \to \Gamma$	6.92 | $T \to M$
Bulk BN	4.22 | $T \to M$	5.60 | $T \to M$	6.28 | $T \to M$	5.91 | $T \to M$	6.07 | $T \to M$	6.01 | $T \to M$
Exp.(Bulk BN)	6.08 ± 0.015					

Table 3.2: Band gaps for various pristine 2D materials. In general, PBE severely underestimates the gap. Hybrid functionals HSE, B3PW, and PBE0 ($\alpha = 0.25$) generally enlarge the bulk band gap, but still underestimate the gaps of ultrathin 2D systems compared with experiments and GW approximation. Only PBE0(α) with α satisfying $\mathrm{IP}_q = \mathrm{EA}_{q+1}$ of localized defects ($\mathrm{C_B}$) yield gaps in good agreement with experiment [312] and G_0W_0@PBE.

The generalized Koopmans' condition has been mostly used to determine the appropriate fraction of Fock exchange (α) for molecules and molecular crystals [313, 314, 315, 316, 317, 318, 319]. One recent work [215] enforced this condition (*i.e.* $\mathrm{EA}_{q+1} = \mathrm{IP}_q$) on defects in bulk semiconductors to obtain α and in turn predicted accurate electronic structure of the corresponding pristine bulk systems. The fundamental assumption is that the optimized α depends on the long range screening of the system and not on the nature of the probe defects. This condition is also valid for deep defects in 2D materials, where defect wavefunctions are well localized like molecule orbitals in the supercells, and their contribution to dielectric screening is negligible compared to the crystal environment. Another advantage of applying this condition to 2D systems is that both EA_{q+1} and IP_q can be exactly referenced to vacuum. In order to validate the applicability of the generalized Koopmans' condition to 2D materials, we used the defect $\mathrm{C_B}$ as a probe to determine α for *h*-BN ($\mathrm{B_C}$ for graphane). This method gives α of 0.409, 0.347, 0.324, 0.225 for monolayer, bilayer, trilayer and bulk *h*-BN, respectively. Note that the α value 0.225 for bulk h-BN, agrees well with the predicted α from the inverse of high frequency dielectric constant ($\alpha = 1/\varepsilon_\infty \approx 0.2$) [320], which supports the assumption that long-range screening determines α. We also investigated other defects $\mathrm{C_N}$ and $\mathrm{V_NC_B}$ as probes of α (their corresponding electronic structure can be found in SI).

Interestingly, we found that IP_q and EA_{q+1} from Kohn-Sham eigenvalues varied linearly with α. Fig. 3.2 shows this linearity for three defects in monolayer *h*-BN, and three defects predict very similar α, which justifies the insensitivity of α to the explicit defect. It is also notable that the slopes of IP_q and EA_{q+1} are opposite but nearly equal, explaining how the average of IP_q and EA_{q+1} as ε^{QP} for CTL in Eq. (3.2) and (3.3) works well (as shown in Table 3.1).

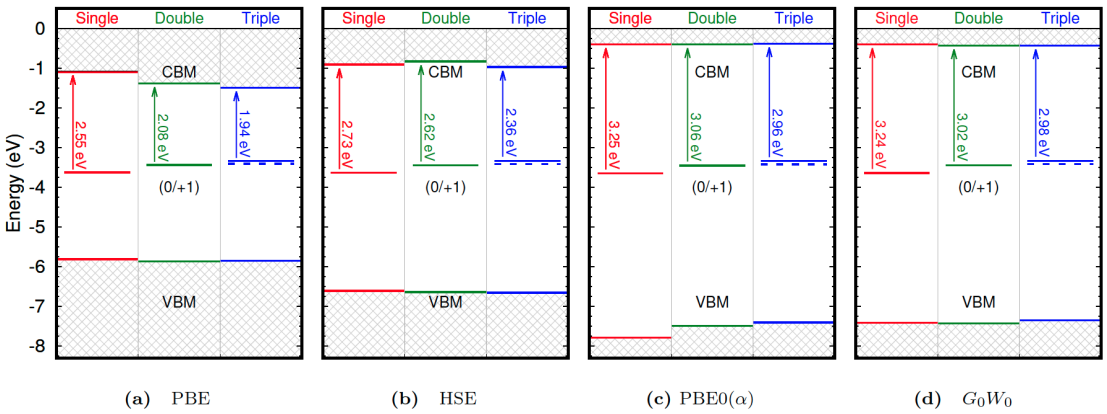

Figure 3.4: Charge transition level C_B (+1/0) in *h*-BN with different levels of theory. Defect charge transition levels gradually become shallower with lower ionization energies while increasing the number of layers (ionization energies are written adjacent to arrows from the CTL to CBM). Note that the defect CTLs are very similar relative to vacuum between different methods.

Most commonly, two-dimensional systems are synthesized with a few layers of the material, therefore understanding the effect of increasing thickness is essential to connect with realistic experiments. As such, we have computed the band gaps of monolayer, bilayer, trilayer and bulk *h*-BN, as well as graphane with several hybrid functionals including HSE, PBE0, B3PW and PBE0(α) (with α predicted earlier), as well as with G_0W_0@PBE for a reliable comparison (see Table 3.2). As anticipated, PBE strongly underestimated monolayer *h*-BN band gap: 4.71 eV with a direct transition at the K point. With any level of theory beyond PBE, monolayer *h*-BN is predicted to have a larger, indirect gap from K to Γ. In accordance with quantum confinement, we observed that the band gaps of *h*-BN obtained at B3PW, PBE0(α), and G_0W_0 show a sharp increase at ultrathin BN (monolayer to trilayer) compared to bulk BN. However, HSE and PBE0 provide almost the same band gaps between ultrathin and bulk BN. This is because there is a severe change in the dielectric screening from monolayer to bulk, and a different portion of Fock exchange must be instilled.

Using PBE0(α) we obtained results consistent with quantum confinement and in best agreement with our G_0W_0 calculations with a MAE of 0.14 eV (see SI Fig. 3). In addition, the B3PW functional [321, 322] provided a more accurate bulk BN band gap than PBE0 and HSE but still underestimated the band gaps of ultrathin BN. Therefore, the direct/indirect transitions and magnitude of the gaps from bulk to monolayer are provided accurately solely with PBE0(α) and G_0W_0. In brief, the results shown in Table 3.2 validate our method for determining accurate fundamental band gaps for 2D materials from first-principles. We note that calculated band edge positions relative to vacuum are also similar at PBE0(α) and G_0W_0 as shown in Fig. 3.4 and SI.

3.2.4 Defect Ionization Energies in 2D Materials

Finally, CTLs and ionization energies for C_B in h-BN computed at PBE, HSE, PBE0(α) and G_0W_0 levels of theory as a function of number of layers are shown in Fig. 3.4. Consistent with the findings in Table 3.1, CTLs changed less than 0.1 eV across different theoretical methods relative to vacuum. Interestingly, no clear trend and only small difference have been found in the band edge positions of h-BN from monolayer to triple layers. These results illustrate that one just needs to correct the band edge positions of pristine 2D materials with PBE0(α) or G_0W_0, and use CTLs determined from DFT with semi-local functionals, then the difference of the two yields accurate defect ionization energies in 2D materials. On another note, we found there is a clear monotonic decrease in the ionization energies of defects in BN with increasing number of layers, mostly contributed by CTLs' shift towards vacuum (shown in Fig. 3.4; also see SI Fig. 5). This effect can be understood as a result of increased dielectric screening with more layers of h-BN, and is consistent with the effect of dielectric environments on the ionization

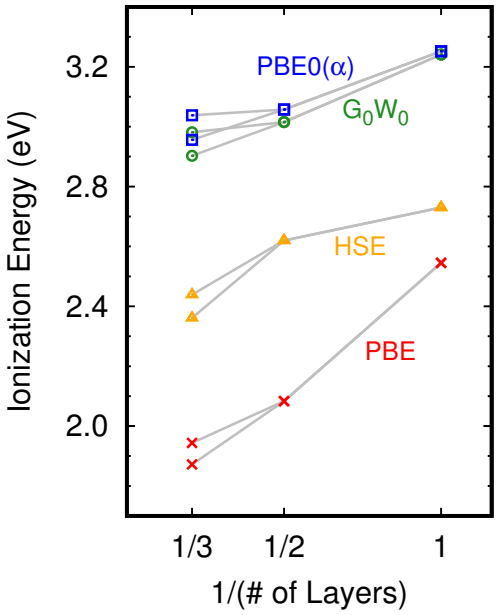

Figure 3.5: Ionization energies of C_B in h-BN with varying number of layers. It is observed that ionization energies decrease monotonically with increasing number of layers. Note that PBE0(α) and G_0W_0 give results in excellent agreement.

energies of MoS_2 [323].

3.2.5 Conclusions

In summary, we established fundamental principles to reliably and efficiently compute ionization energies for defects in 2D materials. Specifically, band edge positions of the pristine systems should be computed with our proposed PBE0(α) hybrid functional or GW approximations, and the defect CTL can be obtained reliably by standard DFT with semi-local functional, if relative to vacuum. We successfully applied the proposed methods for a variety of defects from monolayer to triple layer h-BN, as well as graphane. We also demonstrated that defect ionization energies decreased with increasing number of layers in h-BN, mainly due to enlarged dielectric screening. Our findings in this work suggest efficient and

accurate methods to compute defect ionization energies and electronic structures in 2D materials, which can be applied to screening new promising defects for quantum information and optoelectronic applications.

3.3 Carrier Recombination Mechanisms

3.3.1 Introduction

The engineering of spin defects in wide-band semiconductors offers a promising avenue for the development of quantum spin devices. [324, 325, 326, 282] They are among the few alternatives for quantum technologies that operate at room temperature. Deep defects in two-dimensional (2D) materials such as hexagonal boron nitride (h-BN) [327, 287, 328, 285, 275, 329, 330, 331, 332, 333, 334, 335, 336] and transition metal dichalcogenides (TMD) [337, 338] have proven to be promising single photon sources with polarized and ultrabright single photon emission at room temperature. These materials exhibit unprecedented potential for several applications, including large-scale nanophotonics and quantum information processing, [339, 340, 341, 342, 343] which in turn provide a new platform for exploring quantum phenomena. [282] In order for these defect centers to provide bright SPE, [324, 342] the radiative recombination rate (photon emitted) needs to be high, while the non-radiative recombination rate (no photon emitted) must be substantially lower to yield a high quantum efficiency. Furthermore, a weak electron-phonon coupling is also required to ensure long spin relaxation time for the application of qubit and stable single photon emission at room temperature.

Despite the importance of maximizing radiative rates for quantum information, the factors which determine the recombination process at defects in 2D materials are not understood experimentally or theoretically. Past theoretical studies have either focused on radiative recombination in pristine 2D materials [344, 16] or phonon assisted non-radiative recombination for defects in 3D wide band-gap semiconductors. [345, 346] Therefore, a fully comparative study of both recombination processes for defect centers in 2D materials is highly desired.

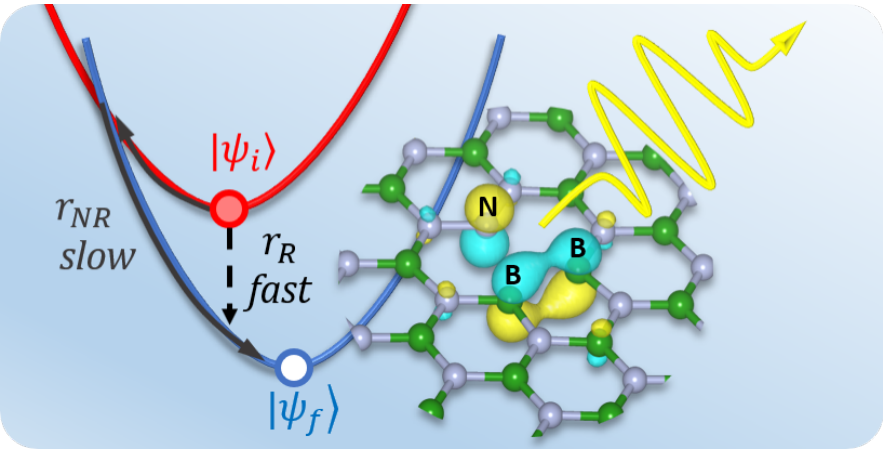

Figure 3.6: Schematic diagram of carrier recombination at the N_BV_N defect in monolayer *h*-BN. In order for a defect to be a robust single photon source, it is necessary to have the radiative recombination rates much higher than the non-radiative ones.

Furthermore, the high tunability of SPE allows them to be integrated within a vast array of applications. [287, 342] Among these methods, strain modulation is one of the most effective strategies, especially for low-dimensional materials which can work under large distortion. [347] For example, in 2D systems, some key electronic properties such as band gap, change by 1.5% under 1% uniaxial tension in TMD monolayers [348] or 6% under 1% uniaxial tension in phosphorene [349]. Additionally, the non-radiative process, which is intrinsically sensitive to lattice deformation (as it is phonon mediated), may exhibit even more drastic changes under strain.

In this communication, we first introduce the formalism of computing the radiative and non-radiative lifetime of defect excited states from first-principles. We then focus on comparing radiative and non-radiative processes of different transitions in a series of important defects in monolayer *h*-BN, where we discuss the dominant recombination processes and their implication on SPE efficiency. Finally, we show that applying strain to *h*-BN defects can effectively tune the

non-radiative rates and quantum yield of SPE.

The radiative and non-radiative transition rates between two electronic states under perturbation can be computed via Fermi's golden rule:

$$r_{if}^{R} = \frac{2\pi}{\hbar} g \left| \langle f|H^{R}|i\rangle \right|^{2} \delta(E_i - E_f), \tag{3.5}$$

$$r_{if}^{NR} = \frac{2\pi}{\hbar} g \sum_{n,m} p_{in} \left| \langle fm|H^{e-ph}|in\rangle \right|^{2} \delta(E_{in} - E_{fm}). \tag{3.6}$$

Here, r_{if}^{R} and r_{if}^{NR} denote the recombination rates between electronic states i and f via a radiative process (r_{if}^{R}) and non-radiative process (r_{if}^{NR}), respectively. g is the degeneracy factor of the final state, i.e. several equivalent energy-degenerate atomic configurations of the final state might exist. [350] For defects in 2D materials studied in this work, g factors are all equal to 1. H^{R} is the electron-photon coupling (electromagnetic) Hamiltonian and H^{e-ph} is the electron-phonon coupling Hamiltonian. A sum over phonon states n, m enters the non-radiative recombination process with an occupation number p_{in} of the vibronic state $|in\rangle$. For ground state calculations, we employed open source plane-wave code Quantum ESPRESSO [52] with ONCV norm conserving pseudopotentials [54, 55] and a supercell size of 6×6 or higher. Charge corrections for the total energies and eigenvalues of charged defects were applied by employing the techniques developed in Ref. [16, 69]. The total energies, defect formation energies and geometry were computed at both PBE and hybrid functional levels (the results presented in the main text are computed at PBE, and detailed comparison between two levels can be found in the Supporting Information (SI) Table S4). The band gaps of pristine h-BN are computed at $GW@PBE$ as done in our previous work [16], which are 6.01 eV for bulk and 7.01 eV for monolayer h-BN respectively. The exciton dipole moments and exciton energies as input for radiative lifetime were computed at many body perturbation theory with GW approximation for quasi-

particle energies [306, 224, 351] and then solving the Bethe-Salpeter equation with the Yambo-code [228], as well as Random Phase approximation with DFT eigenvalues (detailed comparison can be found in the SI, Table S3; the results in the main text are computed at DFT-RPA). More computational details and formulation of radiative rates r_{if}^{R} are discussed in the SI and Ref. [21].

The non-radiative rate is simplified by the static coupling approximation with a one-dimensional (1D) effective phonon approximation[345, 350, 352, 353, 354, 347, 355, 356, 357, 235, 358, 359, 360, 346, 361, 362, 363, 364] (the validation of 1D effective phonon approximation in h-BN is based on the similarity of Huang-Rhys factors between 1D effective phonon and all phonon calculations, as discussed in the SI, section IV):

$$r_{if}^{NR} = \frac{2\pi}{\hbar} g |W_{if}|^2 X_{if}(T), \tag{3.7}$$

$$X_{if}(T) = \sum_{n,m} p_{in} \left| \langle \phi_{fm}(\boldsymbol{R}) | Q - Q_a | \phi_{in}(\boldsymbol{R}) \rangle \right|^2 \times \delta(m\hbar\omega_f - n\hbar\omega_i + \Delta E_{if}), \tag{3.8}$$

$$W_{if} = \langle \psi_i(\mathbf{r}, \boldsymbol{R}) | \frac{\partial H}{\partial Q} | \psi_f(\mathbf{r}, \boldsymbol{R}) \rangle \Big|_{\boldsymbol{R}=\boldsymbol{R}_a}, \tag{3.9}$$

where r_{if}^{NR} is naturally separated into an electronic term W_{if} and a phonon term $X_{if}(T)$ with temperature dependence from thermal population (p_{in}). Here ΔE_{if} is the zero phonon line energy (ZPL), which can be measured experimentally by photoluminescence. We implemented the non-radiative recombination rates as postprocessing codes of Quantum ESPRESSO [52].

3.3.2 Defect-band versus defect-defect transitions in h-BN

A single defect may introduce several energy levels within the band gap of the host material. This yields the possibility for transitions to occur between

Table 3.3: Non-radiative lifetimes and capture coefficients of defects in h-BN and GaN through defect-band recombination(only for the hole capture processes $A^{-1} + h^{+} \rightarrow A^{0}$). For comparison a dominant defect-defect recombination at N_BV_N in monolayer h-BN is also listed. The capture coefficients C_p (with a unit of cm^2/s for 2D and cm^3/s for 3D systems) and lifetimes are reported at $T = 300$ K. Lifetimes are defined as the inverse of rates $\tau^{NR} = 1/r_{if}^{NR}$ and computed in 6×6 h-BN supercell or $2 \times 2 \times 2$ GaN supercell.

System	ZPL (eV)	ΔQ ($amu^{1/2}$Å)	$\hbar\omega_f$ (meV)	C_p (cm^n/s)	τ^{NR}
ML C_BV_N(2D)	5.78	0.58	86	10^{-32}	> 1 ms
ML $O_BO_BV_N$(2D)	4.26	0.84	85	10^{-29}	> 1 ms
ML N_BV_N(2D)	5.46	0.51	95	10^{-33}	> 1 ms
ML C_N(2D)	3.87	0.35	150	10^{-16}	> 1 ms
Bulk C_N(3D)	2.69	0.35	149	10^{-16}	6.6 μs
GaN-C_N(3D)	1.00	1.39	39	10^{-9}*	0.29 ps
ML N_BV_N(2D) (defect-defect)	2.04	0.53	100	10^{-4}	102 ps

* 7×10^{-10} in Ref. [350].

defect states ("defect-defect" transition), as well as from a defect state to a band edge ("defect-band" transition). The computed non-radiative lifetimes and capture coefficients of the most probable defect-band transitions for hole captures in multiple defects in monolayer and bulk h-BN as well as bulk GaN are listed in Table 3.3 (where X_BV_N (X=C, O, N) denotes X substitution of boron accompanied by a nitrogen vacancy). The capture coefficients are defined as a product of recombination rates r_{ij} with surface area or volume for 2D or 3D systems, respectively. The corresponding defect formation energies and configuration coordinate diagrams are presented in the SI, Figure S1. We find that all defect-band transitions in monolayer h-BN have very small rates (the corresponding lifetime exceeds milliseconds). This is in contrast to typical 3D bulk defects in other materials, such as GaN-C_N or GaN-($Zn_{Ga}V_N$), where the non-radiative lifetime is at the picosecond level with a similar defect concentration to h-BN. [360, 350, 365]

One key reason that non-radiative defect-band recombination in monolayer

h-BN is typically slow, is due to large energy differences between defect states and band edges ($\sim 4-6$ eV) as the ZPL shown in Table 3.3. [16, 216, 297] Nonetheless, other factors such as the effective phonon frequencies $\hbar\omega_f$ and the change of nuclear positions ΔQ can also affect the rates, as discussed later. For example, comparing monolayer BN-C_N with bulk BN-C_N, only the ZPL changes significantly (over 1 eV) and other parameters ($\hbar\omega_f$ and ΔQ) retain nearly constants, which ultimately leads to a two order of magnitude difference in their capture rates. Physically, the phonon-assisted non-radiative rate is dominated by a charge transfer process between initial and final state potential energy surfaces, and can be approximated by a classical Marcus' theory picture (see Figure 3.6). Given the form of the energy barrier for charge transfer, [347] a large energy difference between the two states (ZPL) results in an exponential drop in the transfer rate (although exceptions can be found [366, 367, 368, 346]). Therefore, in monolayer h-BN, the large ZPLs of defect-band transitions result in extremely slow non-radiative recombination processes (over milliseconds). On the other hand, several defects have allowed defect-defect transitions with viable non-radiative rates due to smaller energy differences, e.g. the N_BV_N (nitrogen substitution of boron accompanied by a nitrogen vacancy) defect-defect transition in monolayer h-BN (Table 3.4).

Hence, the remaining discussions are focused on defect-defect transitions in monolayer h-BN. Defect-defect non-radiative recombination is performed for neutral excited and ground state with constrained occupation number. The equilibrium geometry, ZPL and vibrational frequency can be also obtained at DFT with constrained occupation. More computational details for defect-defect nonradiative recombination can be found in SI, section III, Figure S2 and Table S4.

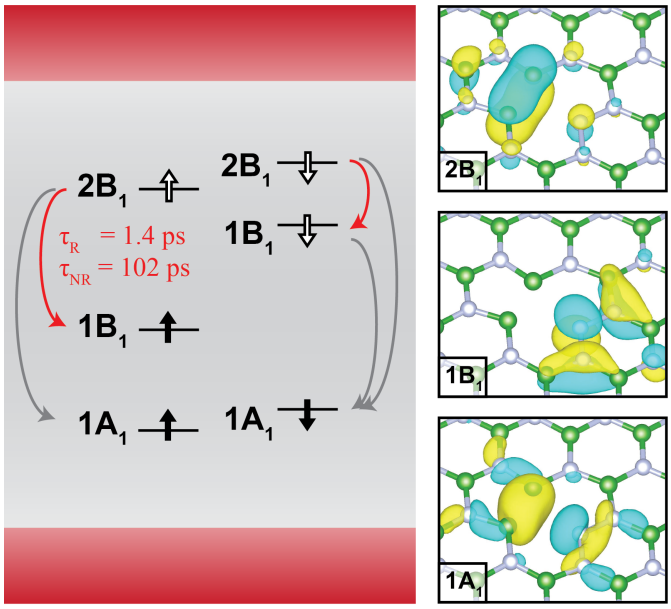

Figure 3.7: Defect levels and possible defect-defect transitions of N_BV_N in monolayer h-BN. Both up and down spin channels of the $2B_1/1B_1$ transitions are marked in red as they are optically allowed with light polarized along defect C_2 symmetry axis. The exact radiative (τ_R) and non-radiative (τ_{NR}) lifetimes are given for the spin up transition with a 6×6 supercell. The remaining transitions in gray are all optically forbidden and have very long radiative and non-radiative recombination lifetimes (exceeding 1 ms).

3.3.3 Competition between radiative and non-radiative recombination lifetime at h-BN defects

Considering a typical point defect such as N_BV_N which has been proposed as a promising defect for SPE, [331, 287, 286] we find it introduces several isolated energy levels that lead to multiple possible radiative and non-radiative defect-defect recombination pathways (as shown in Figure 3.7). However, we found only the transition between $1B_1 \uparrow$ and $2B_1 \uparrow$ (HOMO-LUMO transition for the majority spin channel) has a viably short radiative lifetime and non-radiative lifetime. All other processes have a non-radiative lifetime longer than ms, much slower than this transition which is at a picosecond level.

Table 3.4: Properties of defect-defect non-radiative recombination of the N_BV_N defect in monolayer h-BN. Non-radiative lifetimes are computed with a 6×6 supercell at 300 K and S_f denotes the ground-state Huang-Rhys factor.

Transition	ZPL (eV)	$\hbar\omega_f$ (meV)	k*	S_f	X_{if}	W_{if}	C_p (cm^2/s)	τ^{NR} (ps)
$2B_1 \uparrow$ / $1B_1 \uparrow$	2.04	100	20	5.3	1.3	0.38	10^{-4}	102
$1B_1 \downarrow$ / $1A_1 \downarrow$	1.33	58	23	16.6	10^{5}	10^{-7}	10^{-11}	$> 10^9$
$2B_1 \downarrow$ / $1A_1 \downarrow$	2.94	65	46	7.8	10^{-4}	10^{-6}	10^{-19}	$> 10^9$
$2B_1 \downarrow$ / $1B_1 \downarrow$	1.61	57	28	3.2	10^{-13}	0.03	10^{-19}	$> 10^9$

* $k = \Delta E_{if}/\hbar\omega_f$

The non-radiative transition rate is determined by multiple factors based on Eq. 3.7. The first factor is the phonon term X_{if}. As the ZPL for all defect-defect transitions are relatively small (less than 3 eV, unlike defect-band transitions), we analyze the subtle difference causing variation of X_{if} among different transitions, based on the relation: $X_{if} \propto e^{-S}\frac{S^k}{k!}$ where $k \approx \Delta E_{if}/\hbar\omega_f$ and S is the HR factor. [350]. Specifically ($k > S$ for all defect-defect transitions we study here), a high S implies a large electron-phonon coupling and generally will increase the phonon contribution X_{if}. For example, the HR factor for the $1B_1 \downarrow/1A_1 \downarrow$ transition (16.6) is several times larger than other transitions in Table 3.4 and therefore yields the largest X_{if} of 10^5 at 300 K. On the other hand, a high value of k means a large energy difference (ZPL) relative to the phonon frequency and will reduce phonon contribution X_{if}, similar to earlier discussions on defect-band transitions. The second factor is the electronic term W_{if}, which is proportional to the overlap between electronic wavefunctions $\langle\psi_i\rangle\,\psi_f$. Ultimately, only the $2B_1 \uparrow/1B_1 \uparrow$ transition has a reasonably large X_{if} and the largest W_{if}, which leads to a viable non-radiative recombination process with a lifetime of 102 ps at 300 K.

The radiative process is more straightforward to interpret as it is directly related to the symmetries of wavefunctions via the dipole transition matrix ele-

ments $\langle\psi_i|\mathbf{r}|\psi_f\rangle$. Computational details can be found in section VI and Table S3 in the SI. The corresponding transition section rules for radiative recombination of N_BV_N defect in h-BN are listed in Table S5. Both the $2B_1 \uparrow/1B_1 \uparrow$ transition and the $2B_1 \downarrow/1B_1 \downarrow$ transition are symmetry allowed, [286] resulting in short radiative lifetimes of 1.4 ps and 2.5 ps, respectively. This lifetime can be considered to be a lower-bound compared to that of experimental results, because a much higher defect concentration is adopted in practical calculations (1 defect in a 72-atom supercell, i.e. 1 defect per 2 nm^2, compared to order of one SPE per μm^2 in experiments [287]) and both radiative and non-radiative lifetimes will increase linearly with decreasing defect concentrations or increasing supercell size (see Ref. [354] and section V Table S1 and S2 in the SI). At the low concentration limit, we can consider the defect acts as an isolated molecule in the 2D plane [21], which gives an upper-bound of the actual lifetime, i.e. 40 ns for $2B_1 \uparrow/1B_1 \uparrow$ radiative lifetime at N_BV_N. This is in good agreement with the experimental radiative lifetime of monolayer h-BN SPE, which are measured to be on the order of ns.[287, 285, 275, 330] We note that different from the recombination rates, the capture coefficient is generally constant as a function of defect concentration or supercell sizes (see Table S1 and S2 in the SI).

The quantum yield of a SPE (excluding substrate effects) is defined as $\gamma_{if} = r_{if}^{R}/(r_{if}^{R} + r_{if}^{NR})$. [369, 370, 371] By comparing the radiative lifetimes with the non-radiative ones shown in Table 3.4 for the N_BV_N defect, we have $\gamma > 98\%$ which shows it has the potential to be a highly efficient quantum emitter. In practice, several other external effects can cause the quantum yield to be substantially lower. In particular, substrate recombination [372], photobleaching [373], and strain (discussed in the next section) are known to play the role of limiting the quantum yield of defect SPE.

3.3.4 Effect of strain on the non-radiative lifetime of defects in h-BN

Table 3.5: Properties of $1B_1 \uparrow - 2B_1 \uparrow$ defect-defect state transition for N_BV_N defect in monolayer h-BN under strain. Strain directions are shown in Figure 3.8. X_{if} and lifetime are reported at 300 K.

Strain	ZPL (eV)	ΔQ (Å)	$\hbar\omega_f$ (meV)	S_f	W_{if}	X_{if}	τ^{NR} (ps)
No strain	2.04	0.666	100	5.33	0.38	1.26	102
Biaxial -1%	2.08	0.613	105	4.69	0.39	0.28	429
Biaxial 1%	2.01	0.732	96	6.18	0.36	9.20	16
Uniaxial $\parallel -1\%$	2.02	0.637	102	4.96	0.39	0.95	127
Uniaxial $\parallel$ 1%	2.07	0.703	98	5.80	0.36	1.98	70
Uniaxial $\perp -1\%$	2.10	0.642	103	5.05	0.38	0.38	336
Uniaxial $\perp$1%	1.98	0.697	98	5.69	0.37	5.39	25

In this work, we discuss the impact of strain on non-radiative recombination (and leave other external effects for future study) with N_BV_N as an example. Presumably, strain will change the radiative lifetime little (orbital overlaps between initial and final states are largely preserved) compared to that of the non-radiative lifetime which can be strongly affected by changes in local structures. As shown in Figure 3.8, strain may be applied along the C_2 symmetry axis (denoted as $\parallel$ strain) or orthogonal to the symmetry axis (denoted as $\perp$ strain). We consider effects of strain along both directions as well as the combinatory effects of biaxial strain for the $2B_1 \uparrow / 1B_1 \uparrow$ transition (shown in Table 3.5).

As discussed earlier, the non-radiative recombination rate is composed of an electronic term W_{if} and a phonon term X_{if}. Because W_{if} is proportional to the wavefunction overlap, the change in W_{if} due to strain is found to be negligible, as shown in Figure 3.9a. However, there are significant changes of the phonon term X_{if} due to strain. We note that compressive strain indicates lattice shrinking ($-$); while tensile strain indicates lattice stretching ($+$) and induces opposite

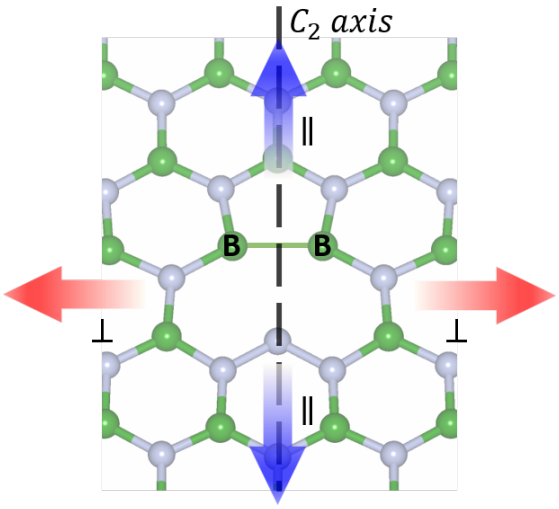

Figure 3.8: Illustration of the directions of uniaxial strain based on the C_{2v} symmetry of N_BV_N in h-BN. Uniaxial strains applied parallel (|| blue arrows) or perpendicular ($\perp$ red arrows) to the C_2 axis are considered. The optimized atomic structure of N_BV_N defect is also shown. The green balls denote B atoms and the grey balls denote N atoms.

changes on non-radiative rates from the former. Therefore, we only discuss compressive strain here. First, compressive strain decreased interatomic distances, which in turn decreased the change in the atomic coordination between initial and final states (ΔQ in Table 3.5). As such, under compressive strain, the HR factor $S = \omega_f \Delta Q^2/2\hbar$ decreased resulting in an exponential decrease of the phonon term X_{if}. Such trends occurred regardless of the direction of strain applied (i.e. $\perp$ or || to the C_2 axis). Second, a change in the ZPL also occurred under strain [275]. After the formation of the nitrogen vacancy, a weak B-B bond is formed perpendicular to the C_2 symmetric axis (see Figure 3.8). When compressive strain is applied perpendicular to the C_2 axis ($\perp$ strain), the ZPL is increased, due to larger bonding-antibonding splitting of the B-B bond that shifts up the $2B_1$ energy level (see Figure 3.7 for related wavefunctions and energy levels). As a result, for $\perp$ strain the change in ZPL and HR factor coincided and yielded an exponential decrease of X_{if} under compressive strain (red curve Figure 3.9b). In contrast, for ||

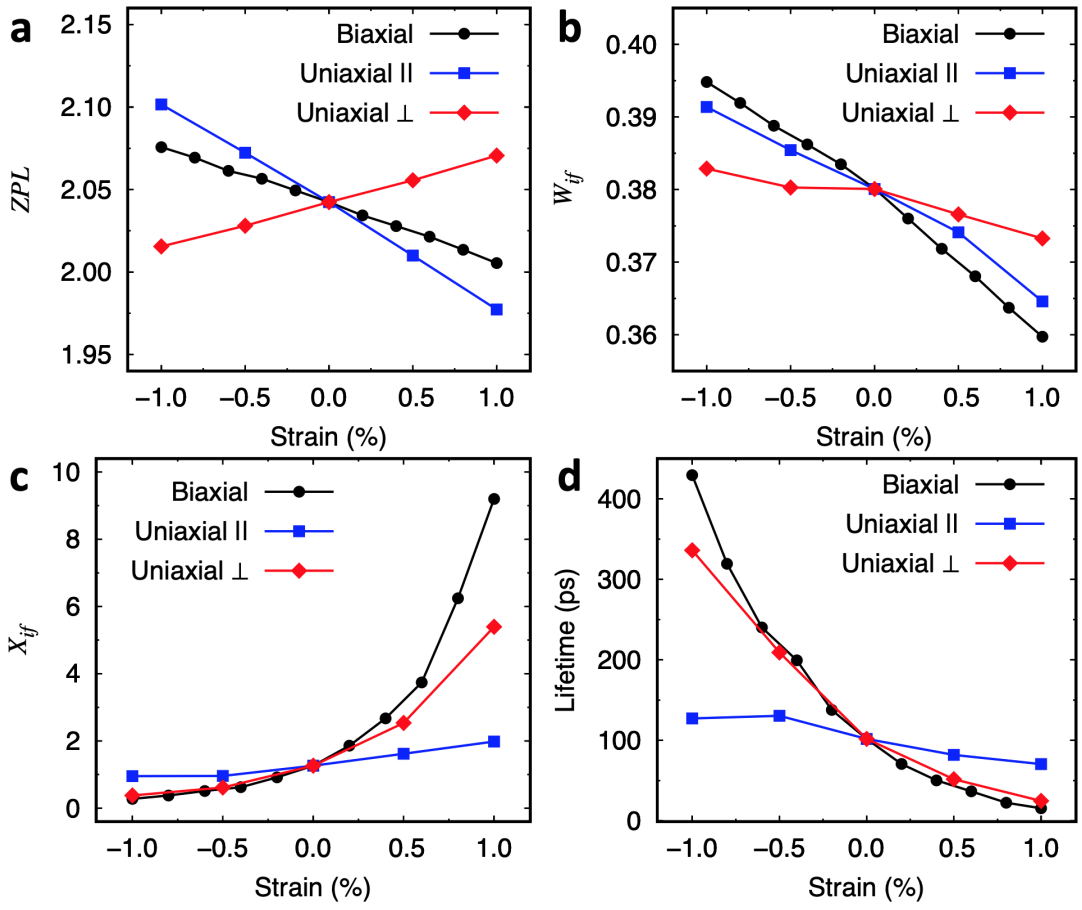

Figure 3.9: Strain induced properties related to non-radiative recombination lifetime of the $1B_1 - 2B_1$ defect-defect transition of N_BV_N in monolayer *h*-BN. Strain directions are shown in Figure 3.8.

strain, these changes counteracted each other resulting in a nearly constant value of X_{if} (blue curve Figure 3.9b). In addition, biaxial strain is a simple combinatory effect of || and $\perp$ strain, mostly dominated by the trend of $\perp$ strain (black curve Figure 3.9b). All in all, the exponential change in X_{if} for both biaxial and uniaxial $\perp$ strain resulted in exponential modification to the non-radiative lifetime of the defect, as black and red curves shown in Figure 3.9c. In particular, in the case of tensile biaxial strain, with 1%, the quantum yield decreased by 10% due to an order of magnitude decrease in non-radiative lifetime. This highlights the significant impact strain can have on the efficiency of defect SPE.

3.3.5 Conclusion

In summary, in this work we compared the radiative and phonon-assisted non-radiative recombinations at defects in wide bandgap 2D materials, using monolayer h-BN as a prototypical example. We found the radiative recombination rates far surpass the non-radiative ones, highlighting the potential of point defects in wide bandgap 2D materials as single photon emitters. Defect-band non-radiative recombinations all have negligible rates possibly due to large energy differences between initial and final states, and only a small subset of defect-defect non-radiative transitions are possible. Transitions vary on several orders of magnitude due to wavefunction symmetry, HR factor, as well as zero-phonon line (ZPL). Finally, we show that compressive or tensile strain up to 1% can alter the non-radiative lifetime by orders of magnitude. Hence, strain largely impacts the quantum yield of single photon emitters and alters the photon energy of the emitter for use towards specific optoelectronic applications. Our study provides important insights on the critical factors of defects in 2D materials as single photon emitters for quantum information applications.

3.4 Intersystem Crossing and Exciton-Defect Coupling of Spin Defects

In our 2021 work published in npj Computational Materials [374], we implemented and employed methods for computing static and dynamic properties of spin defects in h-BN, in particular zero-field splitting and intersystem crossing rates were computed. Using a vast array of methods we are able to identify new extrinsic dopants in h-BN as single photon emitters and spin defect qubits. Optically addressable defect-based qubits offer a distinct advantage in their ability to operate with high fidelity under room temperature conditions [270, 271]. Despite tremendous progress made in years of research, systems which exist today remain inadequate for real-world applications. The identification of stable single photon emitters in 2D materials has opened up a new playground for novel quantum phenomena and quantum technology applications, with improved scalability in device fabrication and a leverage in doping spatial control, qubit entanglement, and qubit tuning [375, 273]. In particular, hexagonal boron nitride (h-BN) has demonstrated that it can host stable defect-based single photon emitters (SPEs) [277, 376, 377, 23] and spin triplet defects [378, 379]. However, persistent challenges must be resolved before 2D quantum defects can become the most promising quantum information platform. These challenges include the undetermined chemical nature of existing SPEs[329, 377], difficulties in controlled generation of desired spin defects, and scarcity of reliable theoretical methods which can accurately predict critical physical parameters for defects in 2D materials due to their complex many-body interactions.

To circumvent these challenges, design of promising spin defects by high-integrity theoretical methods is urgently needed. Introducing extrinsic defects

can be unambiguously produced and controlled, which fundamentally solves the current issues of undetermined chemical nature of existing SPEs in 2D systems. As highlighted by Ref. [271, 380], promising spin qubit candidates should satisfy several essential criteria: deep defect levels, stable high spin states, large zero-field splitting, efficient radiative recombination, high intersystem crossing rates and long spin coherence and relaxation time. Using these criteria for theoretical screening can effectively identify promising candidates but requires theoretical development of first-principles methods, significantly beyond the static and mean-field level. For example, accurate defect charge transition levels in 2D materials necessitates careful treatment of defect charge corrections for removal of spurious charge interactions [291, 292, 293, 16] and electron correlations for non-neutral excitation, e.g. from GW approximations [16, 306] or Koopmans-compliant hybrid functionals [216, 381, 382, 215]. Optical excitation and exciton radiative lifetime must account for defect-exciton interactions, e.g. by solving the Bethe-Salpeter equation, due to large exciton binding energies in 2D systems [383, 384]. Spin-phonon relaxation time calls for a general theoretical approach to treat complex symmetry and state degeneracy of defective systems, along the line of recent development based on ab-initio density matrix approach [385]. Spin coherence time due to the nuclei spin and electron spin coupling can be accurately predicted for defects in solids by combining first-principles and spin Hamiltonian approaches [386, 387]. In the end, nonradiative processes, such as phonon-assisted nonradiative recombination, have been recently computed with first-principles electron-phonon couplings for defects in h-BN [388], and resulted in less competitive rates than corresponding radiative processes. However, the spin-orbit induced intersystem crossing as the key process for pure spin state initialization during qubit operation has not been investigated for spin defects in 2D materials

from first-principles in-depth.

This work has developed a complete theoretical framework which enables the design of spin defects based on the critical physical parameters mentioned above and highlighted in Figure D.1a. We employed state-of-the-art first-principles methods, focusing on many-body interaction such as defect-exciton couplings and dynamical processes through radiative and nonradiative recombinations. We developed methodology to compute nonradiative intersystem crossing rates with explicit overlap of phonon wavefunctions beyond current implementations in the Huang-Rhys approximation[24]. We showcase the discovery of transition metal complexes such as Ti and Mo with vacancy (Ti_{VV} and Mo_{VV}) to be spin triplet defects in *h*-BN, and the discovery of Si_{VV} to be a bright SPE in *h*-BN. We predict Ti_{VV} and Mo_{VV} are stable triplet defects in *h*-BN (which is rare considering the only known such defect is V_B^- [276]) with large zero-field splitting and spin-selective decay, which will set 2D quantum defects at a competitive stage with NV center in diamond for quantum technology applications.

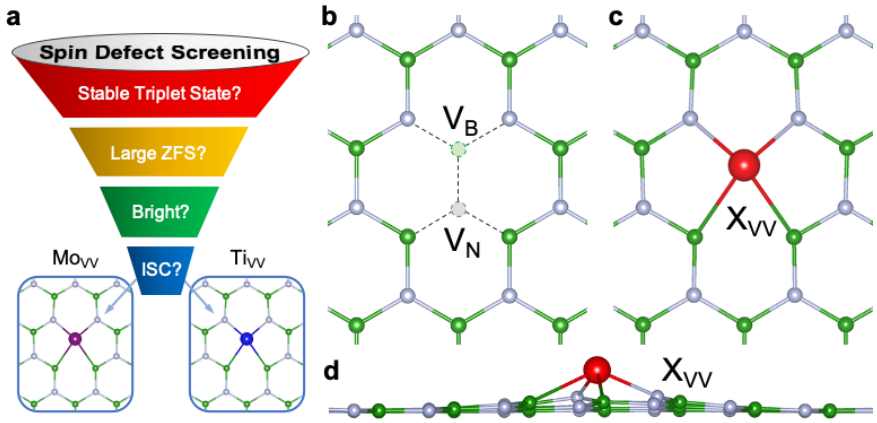

Figure 3.10: Screening of spin defects in *h*-BN. a Schematic of the screening criteria and workflow developed in this work, where we first search for defects with stable triplet ground state, followed by large zero-field splitting (ZFS), then "bright" optical transitions between defect states required for SPEs or qubit operation by photon, and at the end large intersystem crossing rate (ISC) critical for pure spin state initialization. **b** Divacancy site in *h*-BN corresponding to adjacent B and N vacancies (denoted by V_B and V_N). **c** Top-view and **d** Side-view of a typical doping configuration when placed at the divacancy site, denoted by X_{VV}. Atoms are distinguished by color: grey=N, green=B, purple=Mo, blue=Ti, red=X (a generic dopant).

In the development of spin qubits in 3D systems (e.g. diamond, SiC, and AlN), defects beyond *sp* dangling bonds from N or C have been explored. In particular, large metal ions plus anion vacancy in AlN and SiC were found to have potential as qubits due to triplet ground states and large zero-field splitting (ZFS) [389]. Similar defects may be explored in 2D materials [390], such as the systems shown in Figure D.1b-d. This opens up the possibility of overcoming the current limitations of uncontrolled and undetermined chemical nature of 2D defects, and unsatisfactory spin dependent properties of existing defects. In the following, we will start the computational screening of spin defects with static properties of the ground state (spin state, defect formation energy and ZFS) and the excited state (optical spectra), then we will discuss dynamical properties including radiative and nonradiative (phonon-assisted spin conserving and spin flip) processes, as the

flow chart shown in Figure D.1a. We will summarize the complete defect discovery procedure and discuss the outlook at the end.

3.4.1 Screening Triplet Spin Defects in h-BN

To identify stable qubits in h-BN, we start from screening neutral dopant-vacancy defects for a triplet ground state based on total energy calculations of different spin states at both semi-local PBE (Perdew–Burke-Ernzerhof) and hybrid functional levels. We considered the dopant substitution at a divacancy site in h-BN (Figure D.1b) for four different elemental groups. The results of this procedure are summarized in Supplementary Table 1 and Note 1. With additional supercell tests in Supplementary Table 2, our screening process finally yielded that only Mo_{VV} and Ti_{VV} have a stable triplet ground state. We further confirmed the thermodynamic charge stability of these defect candidates via calculations of defect formation energy and charge transition levels. As shown in Supplementary Figure 1, both Ti_{VV} and Mo_{VV} defects have a stable neutral ($q = 0$) region for a large range of Fermi level (ε_F), from 2.2 eV to 5.6 eV for Mo_{VV} and from 2.9 eV to 6.1 eV for Ti_{VV}. These neutral states will be stable in intrinsic h-BN systems or with weak p-type or n-type doping (see Supplementary Note 2).

With a confirmed triplet ground state, we next computed the two defects' zero-field splitting. A large ZFS is necessary to isolate the $m_s = \pm 1$ and $m_s = 0$ levels even at zero magnetic field allowing for controllable preparation of the spin qubit. Here we computed the contribution of spin-spin interaction to ZFS by implementing the plane-wave based method developed by Rayson et al. (see Methods section for details of implementation and benchmark on NV center in diamond) [391]. Meanwhile, the spin-orbit contribution to ZFS was computed with the ORCA code. We find that both defects have sizable ZFS including both

spin-spin and spin-orbit contributions (axial D parameter) of 19.4 GHz for Ti_{VV} and 5.5 GHz for Mo_{VV}, highlighting the potential for the basis of a spin qubit with optically detected magnetic resonance (ODMR) (see Supplementary Note 3 and Figure 2). They are notably larger than previously reported values for ZFS of other known spin defect in solids [389], although at a reasonable range considering large ZFS values (up to 1000 GHz) in transition-metal complex molecules [392].

3.4.2 Screening SPE Defects in h-BN

To identify single photon emitters in h-BN, we considered a separate screening process of these dopant-vacancy defects, targeting those with desirable optical properties. Namely, an SPE efficiently emits a single photon at a time at room temperature. Physically this corresponds to identifying defects which have a single bright intra-defect transition with high quantum efficiency (i.e. much faster radiative rates than nonradiative ones), for example current SPEs in h-BN have radiative lifetimes ∼1-10 ns and quantum efficiency over 50%. [393, 394]

Using these criteria we screened the defects by computing their optical transitions and radiative lifetime at Random Phase Approximation (RPA) (see Supplementary Note 4, Figure 3 and Table 3). This offers a cost-efficient first-pass to identify defects with bright transition and short radiative lifetime as potential candidates for SPEs. From this procedure, we found that C_{VV}(T), Si_{VV}(S), Si_{VV}(T), S_{VV}(S), Ge_{VV}(S) and Sn_{VV}(S) could be promising SPE defects ((T) denotes triplet; (S) denotes singlet), with a bright intra-defect transition and radiative lifetimes on the order of 10 ns, at the same order of magnitude of the SPEs' lifetime observed experimentally. [394] Among these, Si_{VV}(S) has the shortest radiative lifetime, and in addition, Si has recently been experimentally detected in h-BN with samples grown in chemical vapor deposition (the ground state of

Si_{VV} is also singlet).[395] Hence we will focus on Si_{VV} as an SPE candidate in the following sections as we compute optical and electronic properties at higher level of theory from many-body perturbation theory including accurate electron correlation and electron-hole interactions. Note that C_{VV} (commonly denoted C_BV_N) has also been suggested to be a SPE source in *h*-BN. [396]

3.4.3 Single-Particle Levels, Optical Spectra and Radiative Lifetime

The single-particle energy levels of Ti_{VV}, Mo_{VV} and Si_{VV} are shown in Figure 3.11. These levels are computed by many-body perturbation theory (G_0W_0) for accurate electron correlation, with hybrid functional (PBE0(α), $\alpha = 0.41$ based on the Koopmans' condition [216]) as the starting point to address self-interaction errors for 3*d* transition metal defects. [397, 398] For example, we find that both the wavefunction distribution and ordering of defect states can differ between PBE and PBE0(α) (see Supplementary Figure 4-6). The convergence test of G_0W_0 can been found in Supplementary Figure 7, Note 5, and Table 4. Importantly, the single particle levels in Figure 3.11 show there are well localized occupied and unoccupied defect states in the *h*-BN band gap, which yield the potential for intra-defect transitions.

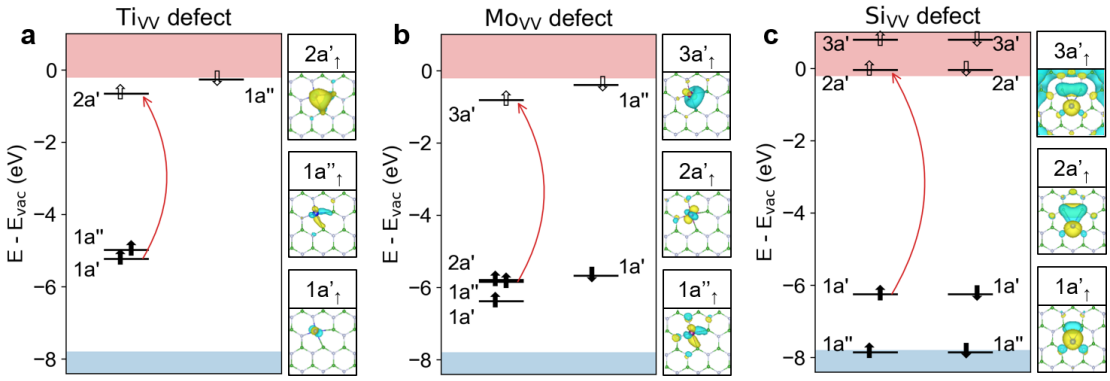

Figure 3.11: Single-particle levels and wavefunctions. Single-particle defect levels (horizontal black lines) of the (a) Ti_{VV}, (b) Mo_{VV}, and (c) Si_{VV} defects in h-BN, calculated at G_0W_0 with PBE0(α) starting wavefunctions. The blue/red area corresponds to the valence/conduction band of h-BN. States are labelled by their ordering and representation within the C_S group with up/down arrows indicating spin and filled/unfilled arrows indicating occupation. A red arrow is drawn to denote the intra-defect optical transition found in Figure 3.12. Defect wavefunctions at PBE0(α) are shown with an isosurface value 10% of the maximum. The blue and yellow color denotes different signs of wavefunctions.

Obtaining reliable optical properties of these two-dimensional materials necessitates solving the Bethe-Salpeter equation (BSE) to include excitonic effects due to their strong defect-exciton coupling, which is not included in RPA calculations (see comparison in Supplementary Figure 8 and Table 5). [224, 399, 400, 17] The BSE optical spectra are shown for each defect in Figure 3.12a-c (the related convergence tests can be found in Supplementary Figure 9-10). In each case we find an allowed intra-defect optical transition (corresponding to the lowest energy peak as labeled in Figure 3.12a-c, and red arrows in Figure 3.11). From the optical spectra we can compute their radiative lifetimes as detailed in the Methods section on Radiative Recombination. We find the transition metal defects' radiative lifetimes (tabulated in Table 3.6) are long, exceeding μs. Therefore, they are not good candidates for SPE. In addition, while they still are potential spin qubits with optically-allowed intra-defect transitions, optical readout of these

defects will be difficult. Referring to Table 3.6 and the expression of radiative lifetime in Eq. 1.14 we can see this is due to their low excitation energies (E_0, in the infrared region) and small dipole moment strength (μ^2_{e-h}). The latter is related to the tight localization of the excitonic wavefunction for Ti_{VV} and Mo_{VV} (shown in Figure 3.12d-f), as strong localization of the defect-bound exciton leads to weaker oscillator strength. [401]

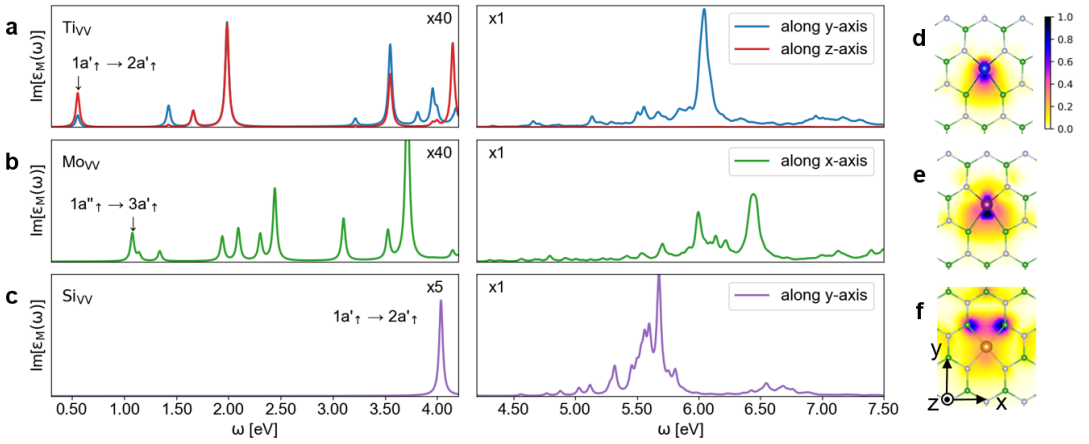

Figure 3.12: BSE optical spectra and exciton wavefunctions. Absorption spectra of the (a) Ti_{VV}, (b) Mo_{VV}, and (c) Si_{VV} defects in h-BN at the level of G_0W_0 + BSE@PBE0(α). The left and right panels provide absorption spectra for two different energy ranges, where the former is magnified by a factor of 40 for Ti_{VV} and Mo_{VV} and a factor of 5 for Si_{VV} for increasing visibility. A spectral broadening of 0.02 eV is applied. The exciton wavefunctions of (d) Ti_{VV}, (e) Mo_{VV} and (f) Si_{VV} are shown on the right for the first peak.

On the other hand, the optical properties of the Si_{VV} defect are quite promising for SPEs, as Figure 3.12c shows it has a very bright optical transition in the ultraviolet region. As a consequence, we find that the radiative lifetime (Table 3.6) for Si_{VV} is 22.8 ns at G_0W_0 + BSE@PBE0(α). We note that although the lifetime of Si_{VV} at the level of BSE is similar to that obtained at RPA (13.7 ns), the optical properties of 2D defects at RPA are still unreliable, due to the lack of excitonic effects. For example, the excitation energy (E_0) can deviate by ~1 eV and oscillator strengths (μ^2_{e-h}) can deviate by an order of magnitude (more details

can be found in Supplementary Table 5). Above all, the radiative lifetime of Si_{VV} is comparable to experimentally observed SPE defects in h-BN,[394] showing that Si_{VV} is a strong SPE defect candidate in h-BN.

Defect	E_0 (eV)	μ^2_{e-h} (bohr^2)	τ_R (ns)	E_b (eV)
Ti_{VV}	0.556	$2.81 * 10^{-2}$	$1.95 * 10^5$	4.018
Mo_{VV}	1.079	$2.29 * 10^{-2}$	$3.26 * 10^4$	3.965
Si_{VV}	4.036	$6.28 * 10^{-1}$	22.8	2.189
N_BV_N	2.408	1.87	35.9	2.428

Table 3.6: Optical excitation energy (E_0), modulus square of the transition dipole moment (μ^2_{e-h}), radiative lifetime (τ_R) and exciton binding energy (E_b) of several defects in h-BN at the level of theory of G_0W_0 + BSE@PBE0(α). The corresponding excitation transitions are $1a'_\uparrow \rightarrow 2a'_\uparrow$ for the Ti_{VV} defect, $1a''_\uparrow \rightarrow 3a'_\uparrow$ for the Mo_{VV} defect and $1a'_\uparrow \rightarrow 2a'_\uparrow$ for the Si_{VV} defect. For comparison, we include the results of N_BV_N (in-plane structure) from Ref. [388].

3.4.4 Multiplet Structure and Excited-State Dynamics

Finally, we discuss the excited-state dynamics of the spin qubit candidates Ti_{VV} and Mo_{VV} defects in h-BN, where the possibility of intersystem crossing is crucial. This can allow for polarization of the system to a particular spin state by optical pumping, required for realistic spin qubit operation.

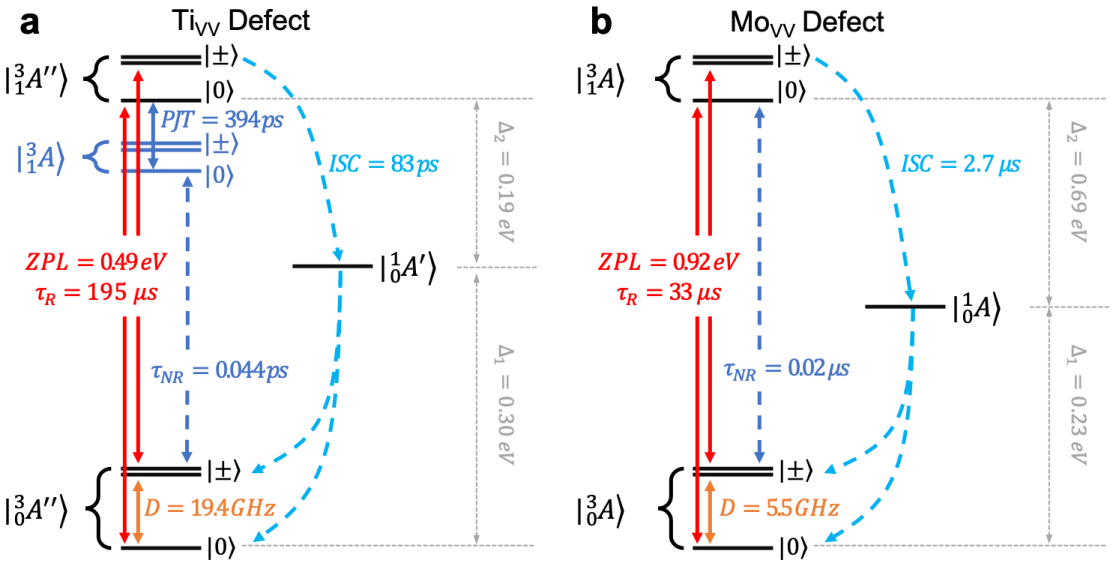

Figure 3.13: Multiplet structure of triplet defects. Multiplet structure and related radiative and nonradiative recombination rates of the (**a**) Ti_{VV} defect and the (**b**) Mo_{VV} defect in h-BN, computed at $T = 10K$. The radiative process is shown in red with zero-phonon line (ZPL) and radiative lifetime (τ_R); the ground state nonradiative recombination (τ_{NR}) is denoted with a dashed line in dark blue; and finally the intersystem crossing (ISC) to the singlet state from the triplet excited state is shown in light blue. The zero-field splitting (D) is denoted by the orange line. For the Ti_{VV} defect, the pseudo Jahn-Teller (PJT) process is shown with a solid line in dark blue.

An overview of the multiplet structure and excited-state dynamics is given in Figure 3.13 for the Ti_{VV} and Mo_{VV} defects. For both defects, the system will begin from a spin-conserved optical excitation from the triplet ground state to the triplet excited state, where next the excited state relaxation and recombination can go through several pathways. The excited state can directly return to the ground state via a radiative (red lines) or nonradiative process (dashed dark blue lines). For the Ti_{VV} defect shown in Figure 3.13a, we find the system may relax to another excited state with lower symmetry through a pseudo Jahn-Teller distortion (PJT; solid dark blue lines), and ultimately recombine back to the ground state nonradiatively. Most importantly, a third pathway is to nonradiatively relax to an intermediate singlet state through a spin-flip intersystem crossing (ISC), and

then again recombine back to the ground state (dashed light-blue lines). This ISC pathway is critical for the preparation of a pure spin state, similar to NV center in diamond. Below, we will discuss our results for the lifetime of each radiative or nonradiative process, in order to determine the most competitive pathway under the operation condition.

3.4.5 Direct Radiative and Nonradiative Recombination

First, we will consider the direct ground state recombination processes. Figure 3.14 shows the configuration diagram of the Ti_{VV} and Mo_{VV} defects. The zero-phonon line (ZPL) for direct recombination can be accurately computed by subtracting its vertical excitation energy computed at BSE (0.56 eV for Ti_{VV} and 1.08 eV for Mo_{VV}) by its relaxation energy in the excited state (i.e. Franck-Condon shift [402], ΔE_{FC} in Figure 3.14). This yields ZPLs of 0.53 eV and 0.91 eV for Ti_{VV} and Mo_{VV}, respectively. Although this method accurately includes both many-body effects and Franck-Condon shifts, it is difficult to evaluate ZPLs for the triplet to singlet-state transition currently. Therefore, we compared with the ZPLs computed by constrained occupation DFT (CDFT) method at PBE. This yields ZPLs of 0.49 eV and 0.92 eV for Ti_{VV} and Mo_{VV}, respectively, which are in great agreement with the ones obtained from BSE excitation energies subtracting ΔE_{FC} above. Lastly, the radiative lifetimes for these transitions are presented in Table 3.6 as discussed in the earlier section, which shows Ti_{VV} and Mo_{VV} have radiative lifetimes of 195 μs and 33 μs, respectively (red lines in Figure 3.13).

In terms of nonradiative properties, the small Huang-Rhys (S_f) for the $|^3_1A''\rangle$ to $|^3_0A''\rangle$ transition of the Ti_{VV} defect (0.91) implies extremely small electron-phonon coupling and potentially an even slower nonradiative process. On the other hand, S_f for the $|^3_1A\rangle$ to $|^3_0A\rangle$ transition of the Mo_{VV} defect is modest (3.53)

and may indicate a possible nonradiative decay. Following the formalism presented in Ref. [388], we computed the nonradiative lifetime of the ground state direct recombination (T = 10 K is chosen to compare with measurement at cryogenic temperatures [403]). Consistent with their Huang-Rhys factors, the nonradiative lifetime of Ti_{VV} is found to be 10 s, while the nonradiative lifetime of the Mo_{VV} defect is found to be 0.02 μs. The former lifetime is indicative of a forbidden transition; however, the Ti_{VV} defect also possesses a pseudo Jahn-Teller (PJT) effect in the triplet excited state (red curve in Figure 3.14a). Due to the PJT effect, the excited state (C_S, $|^3_1A''\rangle$) can relax to lower symmetry (C_1, $|^3_1A\rangle$) with a nonradiative lifetime of 394 ps (solid dark blue line in Figure 3.13a, additional details see Supplementary Note 9 and Figure 11). Afterward, nonradiative decay from $|^3_1A\rangle$ to the ground state ($|^3_0A''\rangle$) (dashed dark blue line in Figure 3.13a) exhibits a lifetime of 0.044 ps due to a large Huang-Rhys factor (14.95).

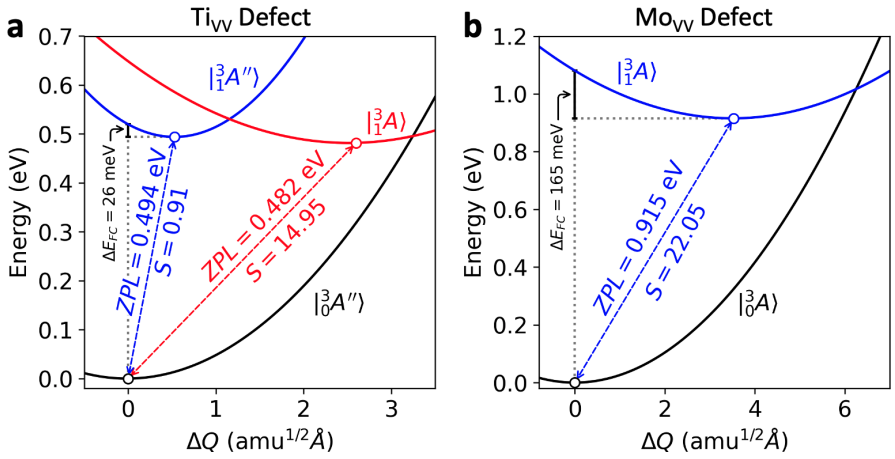

Figure 3.14: Configuration coordinate diagrams. Configuration diagram of the (**a**) Ti_{VV} defect and (**b**) Mo_{VV} defect in h-BN. The potential energy surfaces for each state are as follows: the triplet ground state in black, triplet excited state in blue, and for the Ti_{VV} defect the pseudo Jahn-Teller triplet excited state in red. The zero-phonon lines (ZPL) are given as the energetic separation between the minima of the respective potential energy surfaces, along with the corresponding Huang-Rhys factors (S). The dashed black line represents the vertical excitation energy between triplet ground and excited states, and ΔE_{FC} represents relaxation energy to equilibrium geometry at the excited state.

3.4.6 Spin-Orbit Coupling and Nonradiative Intersystem Crossing Rate

Lastly, we considered the possibility of an ISC between the triplet excited state and the singlet ground state for each defect, which is critical for spin qubit application. In order for a triplet to singlet transition to occur, a spin-flip process must take place. For ISC, typically spin-orbit coupling (SOC) can entangle triplet and singlet states yielding the possibility for a spin-flip transition. To validate our methods for computing SOC (see methods section), we first computed the SOC strengths for the NV center in diamond. We obtained SOC values of 4.0 GHz for the axial λ_z and 45 GHz for non-axial $\lambda_\perp$ in fair agreement with previously computed values and experimentally measured values [24, 404]. We then computed the SOC strength for the Ti_{VV} defect (λ_z = 149 GHz, $\lambda_\perp$ = 312 GHz) and the Mo_{VV} defect (λ_z = 16 GHz, $\lambda_\perp$ = 257 GHz). The value of $\lambda_\perp$ in particular leads to the potential for a spin-selective pathway for both defects, analogous to NV center in diamond.

To compute the ISC rate, we developed an approach which is a derivative of the nonradiative recombination formalism presented in Eq. 1.16:

$$\Gamma_{ISC} = 4\pi\hbar\lambda_\perp^2 \widetilde{X}_{if}(T) \tag{3.10}$$

$$\widetilde{X}_{if}(T) = \sum_{n,m} p_{in} \left|\langle \phi_{fm}(\mathbf{R})\rangle \, \phi_{in}(\mathbf{R})\right|^2 \delta(m\hbar\omega_f - n\hbar\omega_i + \Delta E_{if}) \tag{3.11}$$

Compared with previous formalism, [24] this method allows different values for initial state vibrational frequency (ω_i) and final state one (ω_f) through explicit calculations of phonon wavefunction overlap. Again to validate our methods we first computed the intersystem crossing rate for NV center in diamond. Using the experimental value for $\lambda_\perp$ we obtain an intersystem crossing rate for NV center in

Ti_{VV}	GSR	ZPL (eV)	S_f	W_{if} (eV/(amu$^{1/2}$Å))	τ_{NR} (ps)
	$\|^3_1A''\rangle \rightarrow \|^3_0A''\rangle$	0.494	0.91	1.02×10^{-1}	8.80×10^{12}
	$\|^3_1A\rangle \rightarrow \|^3_0A''\rangle$	0.482	14.95	1.91×10^{-2}	4.41×10^{-2}
	PJT	E_{JT} (eV)	S_f	δ_{JT} (eV)	τ^C_{NR} (ps)
	$\|^3_1A''\rangle \rightarrow \|^3_1A\rangle$	0.012	10.75	0.006	3.94×10^2
	ISC	ZPL (eV)	S_f	$\lambda_\perp$ (GHz)	τ_{ISC} (ps)
	$\|^3_1A''\rangle \rightarrow \|^1_0A'\rangle$	0.189	17.48	312	8.30×10^1
Mo_{VV}	GSR	ZPL (eV)	S_f	W_{if} (eV/(amu$^{1/2}$Å))	τ_{NR} (μs)
	$\|^3_1A\rangle \rightarrow \|^3_0A\rangle$	0.915	22.05	1.5×10^{-2}	0.02
	ISC	ZPL (eV)	S_f	$\lambda_\perp$ (GHz)	τ_{ISC} (μs)
	$\|^3_1A\rangle \rightarrow \|^1_0A\rangle$	0.682	7.22	257	2.7

Table 3.7: Various nonradiative recombination lifetimes along with relevant quantities for the Ti_{VV} and Mo_{VV} defects in h-BN, including ground state recombination (GSR), pseudo Jahn-Teller (PJT), and intersystem crossing (ISC).

diamond of 2.3 MHz which is in excellent agreement with the experimental value of 8 and 16 MHz [403]. In final, we obtain an intersystem crossing time of 83 ps for Ti_{VV} and 2.7 μs for Mo_{VV} as shown in Table 3.7 and light blue lines in Figure 3.13.

The results of all the nonradiative pathways for two spin defects are summarized in Table 3.7 and are displayed in Figure 3.13 along with the radiative pathway. We begin by summarizing the results for Ti_{VV} first and then discuss Mo_{VV} below. In short, for Ti_{VV} the spin conserved optical excitation from the triplet ground state $|^3_0A''\rangle$ to the triplet excited state $|^3_1A''\rangle$ cannot directly recombine nonradiatively due to a weak electron-phonon coupling between these states. In contrast, a nonradiative decay is possible via its PJT state ($|^3_1A\rangle$) with a lifetime of 394 ps. Finally, the process of intersystem crossing from the triplet excited state $|^3_1A''\rangle$ to the singlet state ($|^1_0A'\rangle$) is an order of magnitude faster (i.e. 83 ps) and is in-turn a dominant relaxation pathway. Therefore the Ti_{VV} defect in h-BN is predicted to have an expedient spin purification process due to a fast intersystem crossing with a rate of 12 GHz. We note that while the defect has a low optical quantum yield and is predicted to not be a good SPE candidate, it is still

noteworthy, as to date the only discovered triplet defect in h-BN is the negatively charged boron vacancy, which also does not exhibit SPE and has similarly low quantum efficiency. [378] Meanwhile, the leveraged control of an extrinsic dopant can offer advantages in spatial and chemical nature of defects.

For the Mo_{VV} defect, its direct nonradiative recombination lifetime from the triplet excited state $|^3_1A\rangle$ to the ground state $|^3_0A\rangle$ is 0.02 μs. While the comparison with its radiative lifetime (33 μs) is improved compared to the Ti_{VV} defect, it still is predicted to have low quantum efficiency. However, again the intersystem crossing between $|^3_1A\rangle$ and $|^1_0A\rangle$ is competitive with a lifetime of 2.7 μs. This rate (around MHz) is similar to diamond and implies a feasible intersystem crossing. Owing to its more ideal ZPL position ($\sim$1eV) and improved quantum efficiency, optical control of the Mo_{VV} defect is seen as more likely and may be further improved by other methods such as coupling to optical cavities [328, 405] and applying strain [388, 277].

3.4.7 Conclusion

In summary, we proposed a general theoretical framework for identifying and designing optically-addressable spin defects for the future development of quantum emitter and quantum qubit systems. We started from searching for defects with triplet ground state by DFT total energy calculations which allow for rapid identification of possible candidates. Here we found that the Ti_{VV} and Mo_{VV} defects in h-BN have a neutral triplet ground state. We then computed zero-field splitting of secondary spin quantum sublevels and found they are sizable for both defects, larger than that of NV center in diamond, enabling possible control of these levels for qubit operation. In addition, we screened for potential single photon emitters (SPEs) in h-BN based on allowed intra-defect transitions and

radiative lifetimes, leading to the discovery of Si_{VV}. Next the electronic structure and optical spectra of each defect were computed from many-body perturbation theory. Specifically, the Si_{VV} defect is shown to possess an exciton radiative lifetime similar to experimentally observed SPEs in h-BN and is a potential SPE candidate. Finally, we analyzed all possible radiative and nonradiative dynamical processes with first-principles rate calculations. In particular, we identified a dominant spin-selective decay pathway via intersystem crossing at the Ti_{VV} defect which gives a key advantage for initial pure spin state preparation and qubit operation. Meanwhile, for the Mo_{VV} defect we found that it has the benefit of improved quantum efficiency for more realistic optical control.

This work emphasizes that the theoretical discovery of spin defects requires careful treatment of many-body interactions and various radiative and nonradiative dynamical processes such as intersystem crossing. We demonstrate high potential of extrinsic spin defects in 2D host materials as qubits for quantum information science. Future work will involve further examination of spin coherence time and its dominant decoherence mechanism, as well as other spectroscopic fingerprints from first-principles calculations to facilitate experimental validation of these defects.

3.4.8 Computational Details

In this study, we used the open source plane-wave code Quantum ESPRESSO [52] to perform calculations on all structural relaxations and total energies with optimized norm-conserving Vanderbilt (ONCV) pseudopotentials [54] and a wavefunction cutoff of 50 Ry. A supercell size of 6×6 or higher was used in our calculations with a $3 \times 3 \times 1$ k-point mesh. Charged cell total energies were corrected to remove spurious charge interactions by employing the techniques developed in

Refs. [69, 16, 406] and implemented in the JDFTx code [15]. The total energies, charged defect formation energies and geometry were evaluated at the Perdew-Burke-Ernzerhof (PBE) level [10]. Single-point calculations with k-point meshes of $2 \times 2 \times 1$ and $3 \times 3 \times 1$ were performed using hybrid exchange-correlation functional PBE0(α), where the mixing parameter $\alpha = 0.41$ was determined by the generalized Koopmans' condition as discussed in Ref. [216, 215]. Moreover, we used the YAMBO code [228] to perform many-body perturbation theory with the GW approximation to compute the quasi-particle correction using PBE0(α) eigenvalues and wavefunctions as the starting point. The random phase approximation (RPA) and Bethe-Salpeter Equation (BSE) calculations were further solved on top of the GW approximation for the electron-hole interaction to investigate the optical properties of the defects, including absorption spectra and radiative lifetime.

3.4.9 Zero-Field Splitting

The first-order ZFS due to spin-spin interactions was computed for the dipole-dipole interactions of the electron spin:

$$H_{ss} = \frac{\mu_0}{4\pi} \frac{(g_e \hbar)^2}{r^5} \left[3(\mathbf{s}_1 \cdot \mathbf{r})(\mathbf{s}_2 \cdot \mathbf{r}) - (\mathbf{s}_1 \cdot \mathbf{s}_2) r^2 \right]. \tag{3.12}$$

Here, μ_0 is the magnetic permeability of vacuum, g_e is the electron gyromagnetic ratio, $\hbar$ is the Planck's constant, $\mathbf{s}_1$, $\mathbf{s}_2$ is the spin of first and second electron, respectively, and $\mathbf{r}$ is the displacement vector between these two electron. The spatial and spin dependence can be separated by introducing the effective total spin $\mathbf{S} = \sum_i \mathbf{s}_i$. This yields a Hamiltonian of the form $H_{ss} = \mathbf{S}^T \hat{\mathbf{D}} \mathbf{S}$, which introduces the traceless zero-field splitting tensor $\hat{\mathbf{D}}$. It is common to consider the axial and rhombic ZFS parameters D and E which can be acquired from the

$\hat{\mathbf{D}}$ tensor:

$$D = \frac{3}{2} D_{zz} \quad \text{and} \quad E = (D_{yy} - D_{xx})/2 \; . \tag{3.13}$$

Following the formalism of Rayson et al., [391] the ZFS tensor $\hat{\mathbf{D}}$ can be computed with periodic boundary conditions as:

$$D_{ab} = \frac{1}{2} \frac{\mu_0}{4\pi} (g_e \hbar)^2 \sum_{i>j} \chi_{ij} \, \langle \Psi_{ij}(\mathbf{r}_1, \mathbf{r}_2) | \frac{\mathbf{r}^2 \delta_{ab} - 3\mathbf{r}_a \mathbf{r}_b}{r^5} | \Psi_{ij}(\mathbf{r}_1, \mathbf{r}_2) \rangle \; . \tag{3.14}$$

Here the summation on pairs of i, j runs over all occupied spin-up and spin-down states, with χ_{ij} taking the value $+1$ for parallel spin and -1 for anti-parallel spin, and $\Psi_{ij}(\mathbf{r}_1, \mathbf{r}_2)$ is a two-particle Slater determinant constructed from the Kohn-Sham wavefunctions of the ith and jth states. This procedure was implemented as a post-processing code interfaced with Quantum ESPRESSO. To verify our implementation is accurate, we computed the ZFS of the NV center in diamond which has a well-established result. Using ONCV pseudopotentials, we obtained a ZFS of 3.0 GHz for NV center, in perfect agreement with previous reported results [389]. For heavy elements such as transition metals, spin-orbit (SO) coupling can have substantial contribution to zero-field splitting. Here, we also computed the SO contribution of the ZFS as implemented in the ORCA code [26, 407] (additional details can be found in Supplementary Note 10, Figure 12, and Table 6).

3.4.10 Spin-Orbit Coupling Constant

Spin-orbit coupling (SOC) can entangle triplet and singlet states yielding the possibility for a spin-flip transition. The SOC operator is given to zero-order

by [25]:

$$H_{so} = \frac{1}{2}\frac{1}{c^2 m_e^2}\sum_i \left(\nabla_i V \times \mathbf{p}_i\right)\mathbf{S}_i \tag{3.15}$$

where c is the speed of light, m_e is the mass of an electron, $\mathbf{p}$ and $\mathbf{S}$ are the momentum and spin of electron i and V is the nuclear potential energy. The spin-orbit interaction can be rewritten in terms of the angular momentum L and the SOC strength λ as [25],

$$H_{so} = \sum_i \lambda_\perp (L_{x,i}S_{x,i} + L_{y,i}S_{y,i}) + \lambda_z L_{z,i}S_{z,i}. \tag{3.16}$$

where $\lambda_\perp$ and λ_z denote the non-axial and axial SOC strength, respectively. The SOC strength was computed for the $\mathrm{Ti_{VV}}$ defect in h-BN using the ORCA code by TD-DFT [26, 27]. More computational details can be found in Supplementary Note 10.

Appendix A

Formalism of Nonradiative Recombination

A.1 Static Coupling

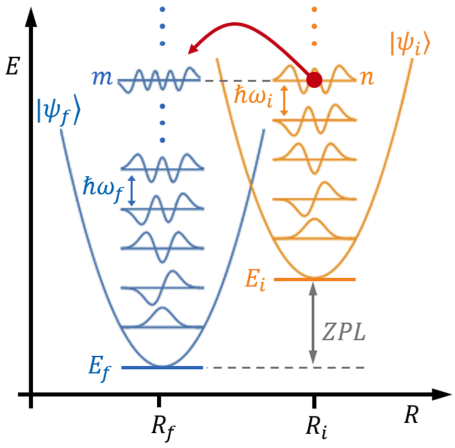

Figure A.1: Diagram of the transition between two vibronic states. The two quadratic curves represent the electronic states (i, f) and the vibrational modes present at each state are superimposed with states (n, m).

Here we consider a system which is initially in a vibronic state $|\Psi_{in}(r, R)\rangle$ and transitions to a final vibronic state $|\Psi_{fm}(r, R)\rangle$ with $i \neq f$. Here the indices

(i, f) denote the electronic state, while (n, m) denote the phonon state as shown schematically in Figure A.1. Within the Born-Oppenheimer approximation these states are a direct product of the electronic states $|\psi_{(i,f)}(r, R)\rangle$ and phonon states $|\phi_{(n,m)}(R)\rangle$.

$$|\Psi_{(in,fm)}(r, R)\rangle = |\psi_{(i,f)}(r, R)\phi_{(n,m)}(R)\rangle \tag{A.1}$$

The coordinate r denotes the spatial dependence of the electronic wavefunction $\psi_{(i,f)}$ and R is the configuration of atomic positions.

The probability of transitioning between vibronic state $|\Psi_{i,n}(r, R)\rangle$ to the state $|\Psi_{f,m}(r, R)\rangle$ is given by Fermi's Golden Rule:

$$\Gamma_{in\to fm} = \frac{2\pi}{\hbar} f(i, n)|V_{in,fm}|^2 \delta(E_{in} - E_{fm}) \tag{A.2}$$

Here $f(i, n)$ is the probability of occupying phonon state n when in the electronic state i, which follows a thermal Maxwell-Boltzmann distribution. The dirac delta function ensures the conservation of energy between vibronic states E_{in} and E_{fm}. And finally $V_{in,fm}$ is the electron phonon coupling matrix, discussed in more detail later.

If we wish to compute the collective transition rate between electronic states i and f this follows readily from Eq. (A.2).

$$\begin{aligned} \Gamma_{i\to f} &= \sum_{n,m} \Gamma_{in\to fm} \\ \Gamma_{i\to f} &= \frac{2\pi}{\hbar} \sum_{n,m} f(i, n)|V_{in,fm}|^2 \delta(E_{in} - E_{fm}) \end{aligned} \tag{A.3}$$

Here we have now summed over all possible initial and final phonon states (n and m) to give the full probability of transitioning from electronic state i to state f.

A term of particular interest in Eq. (A.3) is the electron-phonon coupling matrix $V_{in,fm}$. Within the static coupling approximation we approximate the electron-phonon coupling to first order in R. First consider the total Hamiltonian H_{tot} to first order in R about some position R_0 as:

$$H_{tot}(r,R) = H(r,R_0) + \sum_R \frac{\partial H}{\partial R}(R - R_0) \tag{A.4}$$

where H is the electron Hamiltonian, and the partial of H with respect to R is for every atomic position in 3D space. Meanwhile the electronic wavefunction is $\psi_i(r,R)$ to first order in R is given by

$$|\psi_i(r,R)\rangle = |\psi_i(r,R_0)\rangle + \sum_R (R - R_0)\,|\frac{\partial \psi_i}{\partial R}\rangle \tag{A.5}$$

where in Eq. (A.4-A.5) the evaluation of the derivative with respect to R at R_0 is implicit.

Using the approximations of Eq. (A.4-A.5), the electron-phonon coupling

matrix is given by:

$$
\begin{aligned}
V_{in,fm} &= \langle \Psi_{f,m}(r,R)|H_{tot}(r,R)|\Psi_{i,n}(r,R)\rangle \\
&= \langle \psi_f(r,R_0)\phi_{f,m}(R)|H_0|\psi_i(r,R_0)\phi_{i,n}(R)\rangle \\
&\quad + \sum_R \Bigg(\langle \psi_f(r,R_0)\phi_{f,m}(R)|\frac{\partial H}{\partial R}(R-R_0)|\psi_i(r,R_0)\phi_{i,n}(R)\rangle \\
&\quad + \langle \psi_f(r,R_0)\phi_{f,m}(R)|H_0(R-R_0)|\frac{\partial \psi_i}{\partial R}\phi_{i,n}(R)\rangle \\
&\quad + \langle \frac{\partial \psi_f}{\partial R}\phi_{f,m}(R)|(R-R_0)H_0|\psi_i(r,R_0)\phi_{i,n}(R)\rangle \Bigg) \\
&\quad + \mathcal{O}(R^2) \\
&= \sum_R \langle \phi_{f,m}(R)|(R-R_0)|\phi_{i,n}(R)\rangle \Bigg[\langle \psi_f(r,R_0)|\frac{\partial H}{\partial R}|\psi_i(r,R_0)\rangle \\
&\qquad + \langle \psi_f(r,R_0)|H_0|\frac{\partial \psi_i}{\partial R}\rangle + \langle \frac{\partial \psi_f}{\partial R}|H_0|\psi_i(r,R_0)\rangle \Bigg] \\
&= \sum_R \langle \phi_{f,m}(R)|(R-R_0)|\phi_{i,n}(R)\rangle \, \langle \psi_f(r,R_0)|\frac{\partial H}{\partial R}|\psi_i(r,R_0)\rangle \qquad \text{(A.6)}
\end{aligned}
$$

Where in the first step we have we have removed any terms of order R^2 (denoted with $\mathcal{O}(R^2)$). In the second step, the first term is removed do to orthogonality $\langle \psi_f|\psi_i\rangle = 0$, and the latter part is rewritten with the factorization of the electronic and phonon parts due to there independence on R and H, respectively. In the final step, we are left with only one term as the last two terms cancel (see Appendix). Thus, the static coupling approximation gives an electron-phonon coupling matrix of the form:

$$
V_{in,fm} = \sum_R \langle \phi_{f,m}(R)|(R-R_0)|\phi_{i,n}(R)\rangle \, \langle \psi_f(r,R_0)|\frac{\partial H}{\partial R}|\psi_i(r,R_0)\rangle \qquad \text{(A.7)}
$$

Alternatively, the electron-phonon coupling can instead be expressed in terms

of phonon modes Q_k,

$$V_{in,fm} = \sum_k \langle\psi_f(r,R_0)|\frac{\partial H}{\partial Q_k}|\psi_i(r,R_0)\rangle \langle\phi_{f,m}(R)|(Q_k - Q_{k,0})|\phi_{i,n}(R)\rangle \quad \text{(A.8)}$$

$$= \sum_k C_{if}^k \langle\phi_{f,m}(R)|\mathbf{Q}_k|\phi_{i,n}(R)\rangle \quad \text{(A.9)}$$

with

$$\mathbf{Q}_{i,k} = \frac{1}{\sqrt{M_k}} \sum_R M_R \mu_k(R) \mathbf{R}_i$$

$$\mathbf{Q}_{f,k} = \frac{1}{\sqrt{M_k}} \sum_R M_R \mu_k(R) \mathbf{R}_f \quad \text{(A.10)}$$

Here $\mathbf{R}_i = R_i - R_i(0)$ and $\mathbf{R}_f = R_f - R_f(0)$ is the displacement of the atomic positions from equilibrium. M_R is the mass of the atom located at position R, M_k is the reduced mass in the kth phonon mode, and $\mu_k(R)$ is the phonon mode displacement vector at position R.

In Eq. (A.9), we have defined the electron-electron coupling constants C_{if}^k.

$$C_{if}^k = \langle\psi_f(r,R_0)|\frac{\partial H}{\partial Q_k}|\psi_i(r,R_0)\rangle = \sum_R \mu_k(R) \langle\psi_f(r,R_0)|\frac{\partial H}{\partial R}|\psi_i(r,R_0)\rangle \quad \text{(A.11)}$$

Now for the full transition rate we have

$$\Gamma_{i\to f} = \frac{2\pi}{\hbar} \sum_{k_1,k_2} C_{if}^{k_1} C_{if}^{k_2} \Bigg(\sum_{n,m} f(i,n) \langle\phi_{i,n}(R)|\mathbf{Q}_{k_1}|\phi_{f,m}(R)\rangle \cdot \langle\phi_{f,m}(R)|\mathbf{Q}_{k_2}|\phi_{i,n}(R)\rangle \, \delta(\hbar\omega_{in} - \hbar\omega_{fm} - \Delta E_{if}) \Bigg) \quad \text{(A.12)}$$

If we use the integral form of the dirac delta function $\delta(x) = \frac{1}{2\pi}\int_{-\infty}^{\infty} e^{ixt}dt$ then we can reduce the phonon-phonon coupling piece of Eq. A.12 (see Appendix for

derivation):

$$\Gamma_{if} = \frac{2\pi}{\hbar} \sum_{k1,k2} C_{if}^{k_1} C_{if}^{k_2} \cdot A_{if}^{k1,k2} \tag{A.13}$$

where,

$$A_{if}^{k1,k2} = \frac{1}{2\pi\mathcal{Z}} \int_{-\infty}^{\infty} \chi_{if}^{k_1,k_2}(t,T) e^{-it\Delta E_{if}/\hbar}\, dt \tag{A.14}$$

$$\chi_{if}^{k_1,k_2}(t,T) = \mathrm{Tr}\left[\mathbf{Q}_{k_1} e^{-itH_f/\hbar} \mathbf{Q}_{k_2} e^{-(\beta\hbar - it)H_i/\hbar}\right] \tag{A.15}$$

A.2 Full-Phonon

This section discusses details of computing Eq. A.14 & A.15 in practice, following the implementation of [Shi 2015 PRB]. First of all we will assume that the phonon modes in states i and j are the same, so $k_1 = k_2 = k$. Next we introduce the following diagonal $(N_{vib} \times N_{vib})$ matrices:

$$a(\tau_\xi)_k = \frac{\omega_k}{\sinh\left(i\hbar\omega_k\tau_\xi\right)}, \quad c(\tau_\xi)_k = \omega_k \coth\left(i\hbar\omega_k\tau_\xi/2\right), \quad d(\tau_\xi)_k = \omega_k \tanh\left(i\hbar\omega_k\tau_\xi/2\right). \tag{A.16}$$

Where, $\xi = (i,j)$, $\tau_i = -t - i\beta$, $\tau_j = t$, and ω_k is the frequency of the kth harmonic oscillator. We then define matrices:

$$C(\tau_i,\tau_j)_k = c(\tau_i)_k + c(\tau_j)_k, \quad D(\tau_i,\tau_j)_k = d(\tau_i)_k + d(\tau_j)_k. \tag{A.17}$$

And also

$$D_{\mathrm{HT}} = -D^{-1} d(\tau_j)\mathbf{K}, \tag{A.18}$$

$$A_{\mathrm{HT}} = \frac{1}{2}(D^{-1} - C^{-1}) + D_{\mathrm{HT}}(D_{\mathrm{HT}})^T, \tag{A.19}$$

where

$$\mathbf{K}_k = \Delta Q_{ij,k} = \frac{1}{\sqrt{M_k}} \sum_R M_R \mu_k(R) \Delta R_{ij} \,. \tag{A.20}$$

This gives the final form:

$$\chi_{ij}^k(t,T) = \sqrt{\frac{\det\{[a(\tau_j)]\}\det\{[a(\tau_i)]\}}{(i\hbar)^{2N}\det\{(C)\}\det\{(D)\}}} \times \exp\left[-\mathbf{K}^T d(\tau_j)\mathbf{K} + \mathbf{K}^T d(\tau_j) D^{-1} d(\tau_i)\mathbf{K}\right](A_{\mathrm{HT}}) \tag{A.21}$$

One can then integrate Eq. A.14 to give the final phonon part.

A.3 Linear Response Theory

Here we consider the single particle Hamiltonian (h) to first order deviation in the one-dimensional effective coordinate (Q) as:

$$h = h_a + \frac{\partial h}{\partial Q}(Q - Q_a) \tag{A.22}$$

We can consider the latter term as a perturbation on the system where only the term $\frac{\partial h}{\partial Q}$ acts on the electronic states (Q acts on phonon states). Therefore, the first-order response of the electronic eigenstate (φ_m) is given by:

$$|\Delta\varphi_m\rangle = \sum_{n \neq m} |\varphi_n\rangle \frac{\langle\varphi_n| \frac{\partial h}{\partial Q} |\varphi_m\rangle}{\varepsilon_m - \varepsilon_n} \tag{A.23}$$

We now work to solve for $\langle\varphi_n| \frac{\partial h}{\partial Q} |\varphi_m\rangle$, the term we want to replace in the

current formalism. First consider a simple rewrite of Eq. A.23.

$$|\Delta\varphi_m\rangle = \left(\sum_{n\neq m} |\varphi_n\rangle \langle\varphi_n|\right) \frac{\frac{\partial h}{\partial Q}|\varphi_m\rangle}{\varepsilon_m - \varepsilon_n} \tag{A.24}$$

Evoking the completeness relation gives

$$|\Delta\varphi_m\rangle = \left(\mathbb{1} - |\varphi_m\rangle \langle\varphi_m|\right) \frac{\frac{\partial h}{\partial Q}|\varphi_m\rangle}{\varepsilon_m - \varepsilon_n} \tag{A.25}$$

Then taking the inner product with $\langle\varphi_n|$ and implementing the orthogonality of these states $\langle\varphi_n|\varphi_m\rangle = \delta_{nm}$ (in this case n and m differ, so $\langle\varphi_n|\varphi_m\rangle = 0$).

$$\langle\varphi_n|\Delta\varphi_m\rangle = \left(\langle\varphi_n| - \langle\varphi_n|\varphi_m\rangle \langle\varphi_m|\right) \frac{\frac{\partial h}{\partial Q}|\varphi_m\rangle}{\varepsilon_m - \varepsilon_n} \tag{A.26}$$

$$= \left(\langle\varphi_n|\right) \frac{\frac{\partial h}{\partial Q}|\varphi_m\rangle}{\varepsilon_m - \varepsilon_n} \tag{A.27}$$

$$= \frac{\langle\varphi_n| \frac{\partial h}{\partial Q}|\varphi_m\rangle}{\varepsilon_m - \varepsilon_n} \tag{A.28}$$

This gives the final form we desired ($n = i$ initial state; $m = f$ final state)

$$\langle\varphi_i| \frac{\partial h}{\partial Q}|\varphi_f\rangle = (\varepsilon_f - \varepsilon_i) \langle\varphi_i|\frac{\partial \varphi_f}{\partial Q}\rangle \tag{A.29}$$

Note that φ_f is also considered to change first order in Q and hence $|\Delta\varphi_f\rangle = |\frac{\partial\varphi_f}{\partial Q}\rangle$.

A.4 Supplemental Derivations

A.4.1 S1

Proof that

$$\langle\psi_f(r,R_0)|H_0|\frac{\partial\psi_i}{\partial R}\rangle + \langle\frac{\partial\psi_f}{\partial R}|H_0|\psi_i(r,R_0)\rangle = 0. \tag{A.30}$$

Consider,

$$\begin{aligned}
&\frac{\partial}{\partial R}\Big(\ \langle\psi_f(r,R_0)|H_0|\psi_i(r,R_0)\rangle\ \Big) = \qquad\qquad (A.31)\\
&\qquad\qquad \langle\frac{\partial\psi_f(r,R_0)}{\partial R}|H_0|\psi_i(r,R_0)\rangle + \langle\psi_f(r,R_0)|H_0|\frac{\partial\psi_i(r,R_0)}{\partial R}\rangle\\
&\qquad\qquad + \langle\psi_f(r,R_0)|\frac{\partial H_0}{\partial R}|\psi_i(r,R_0)\rangle\\
&0 = \langle\frac{\partial\psi_f(r,R_0)}{\partial R}|H_0|\psi_i(r,R_0)\rangle + \langle\psi_f(r,R_0)|H_0|\frac{\partial\psi_i(r,R_0)}{\partial R}\rangle + 0\\
&\Rightarrow \langle\frac{\partial\psi_f(r,R_0)}{\partial R}|H_0|\psi_i(r,R_0)\rangle + \langle\psi_f(r,R_0)|H_0|\frac{\partial\psi_i(r,R_0)}{\partial R}\rangle = 0 \qquad (A.32)
\end{aligned}$$

Here the left hand side is zero because $\langle\psi_f|\psi_i\rangle = 0$, while the final term on the right hand side is zero because $\partial H_0/\partial R = 0$.

A.4.2 S2

Below the mathematical steps which allow for the rewriting of Eq. (A.12) in terms of Eq. (A.13-A.15) are presented.

$$
\begin{aligned}
&\sum_{n,m} f(i,n)\,\langle\phi_{i,n}(R)|\mathbf{Q}_{k_1}|\phi_{f,m}(R)\rangle\cdot\langle\phi_{f,m}(R)|\mathbf{Q}_{k_2}|\phi_{i,n}(R)\rangle\,\delta(\hbar\omega_{fm}-\hbar\omega_{in}+\Delta E_{if}) \\
&= \frac{1}{2\pi\hbar\mathcal{Z}}\sum_{n,m} e^{-\beta\hbar\omega_{in}}\,\langle\phi_{i,n}(R)|\mathbf{Q}_{k_1}|\phi_{f,m}(R)\rangle\cdot\langle\phi_{f,m}(R)|\mathbf{Q}_{k_2}|\phi_{i,n}(R)\rangle \\
&\qquad\qquad \cdot\int_{-\infty}^{\infty} e^{it(\omega_{in}-\omega_{fm}-\Delta E_{if}/\hbar)}\,dt \\
&= \frac{1}{2\pi\hbar\mathcal{Z}}\int_{-\infty}^{\infty}\left(\sum_{n,m}\langle\phi_{i,n}(R)|\mathbf{Q}_{k_1}|\phi_{f,m}(R)\rangle\cdot\langle\phi_{f,m}(R)|\mathbf{Q}_{k_2}|\phi_{i,n}(R)\rangle\right. \\
&\qquad\qquad \left.\cdot\, e^{-(\beta\hbar-it)\omega_{in}-it\omega_{fm}-it\Delta E_{if}/\hbar)}\right)dt \\
&= \frac{1}{2\pi\hbar\mathcal{Z}}\int_{-\infty}^{\infty}\left(\sum_{n,m}\langle\phi_{i,n}(R)|\mathbf{Q}_{k_1}e^{-it\omega_{fm}}|\phi_{f,m}(R)\rangle\right. \\
&\qquad\qquad \left.\cdot\,\langle\phi_{f,m}(R)|\mathbf{Q}_{k_2}e^{-(\beta\hbar-it)\omega_{in}}|\phi_{i,n}(R)\rangle\,e^{-it\Delta E_{if}/\hbar)}\right)dt \\
&= \frac{1}{2\pi\hbar\mathcal{Z}}\int_{-\infty}^{\infty}\left(\sum_{n}\langle\phi_{i,n}(R)|\,\mathbf{Q}_{k_1}\right. \\
&\qquad\qquad \sum_{m} e^{-it\omega_{fm}}\,|\phi_{f,m}(R)\rangle\cdot\langle\phi_{f,m}(R)| \\
&\qquad\qquad \left.\mathbf{Q}_{k_2}e^{-(\beta\hbar-it)\omega_{in}}\,|\phi_{i,n}(R)\rangle\,e^{-it\Delta E_{if}/\hbar}\right)dt \\
&= \frac{1}{2\pi\hbar\mathcal{Z}}\int_{-\infty}^{\infty}\left(\sum_{n}\langle\phi_{i,n}(R)|\,\mathbf{Q}_{k_1}e^{-itH_f/\hbar}\mathbf{Q}_{k_2}e^{-(\beta\hbar-it)\omega_{in}}\,|\phi_{i,n}(R)\rangle\,e^{-it\Delta E_{if}/\hbar}\right)dt \\
&= \frac{1}{2\pi\hbar\mathcal{Z}}\int_{-\infty}^{\infty}\mathrm{Tr}\left[\mathbf{Q}_{k_1}e^{-itH_f/\hbar}\mathbf{Q}_{k_2}e^{-(\beta\hbar-it)H_i/\hbar}\right]e^{-it\Delta E_{if}/\hbar}\,dt
\end{aligned}
\tag{A.33}
$$

Plugging this piece back into Eq. A.12 gives the final condensed form of the transition rate.

$$\Gamma_{if} = \frac{2\pi}{\hbar}\sum_{k1,k2} C_{if}^{k_1}C_{if}^{k_2}\cdot A_{if}^{k1,k2} \tag{A.34}$$

Where we have shown that

$$A_{if}^{k1,k2} = \frac{1}{2\pi\mathcal{Z}} \int_{-\infty}^{\infty} \chi_{if}^{k_1,k_2}(t,T) e^{-it\Delta E_{if}/\hbar}\, dt \tag{A.35}$$

$$\chi_{if}^{k_1,k_2}(t,T) = \mathrm{Tr}\left[\mathbf{Q}_{k_1} e^{-itH_f/\hbar} \mathbf{Q}_{k_2} e^{-(\beta\hbar - it)H_i/\hbar}\right] \tag{A.36}$$

Appendix B

Semiclassical Transport Theory

B.1 Prelude

Carriers in several transition metal oxides such as Fe_2O_3, $BiVO_4$, as well as ABO_3 perovskites form what are known as polarons. A polaron is quasi-particle known for its tendency to self-trap due to large electron-phonon interactions. Aas the carrier moves through the lattice so due the surrounding lattice distortions as visualized in Figure B.1a. Due to this, polarons due not conduct via regular band conduction but instead they must hop from site to site in a process known as polaron hopping.

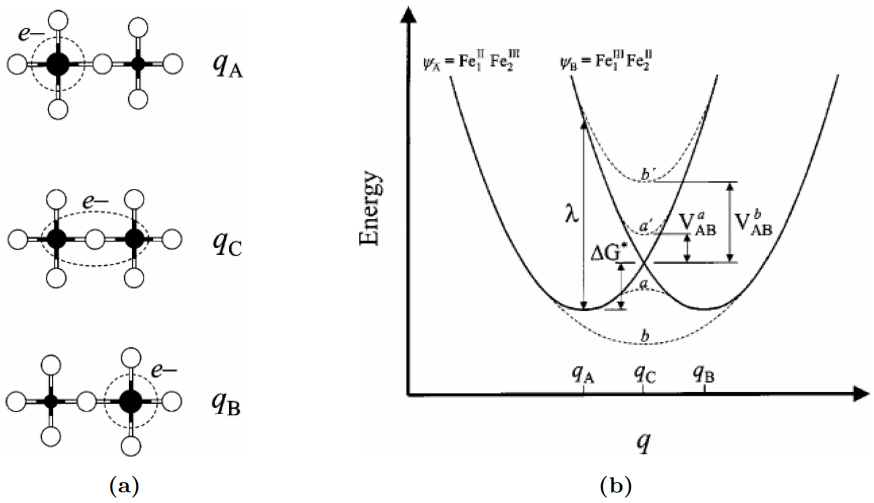

Figure B.1: (a) Top is the local geometry q_A, where the electron is localized on the left ion. As the electron moves through to the bottom configuration q_B, the local geometry distorts along with the movement of the electron. (b) These energy curves are plotted against the geometry of the lattice q, representing the potential energy well the electron is in if it is localized at either site A or site B. The height of the intersection of these curves, ΔG^*, represents the barrier the electron must overcome to hop from site A to site B. When coupling between the states is introduced then this activation energy is reduced by the amount of that coupling, V_{AB}.

The theory of transport for such systems has been developed by many but for the purposes of this report which hopes to key into the most essential concepts of activation transport, and although I have reviewed many works which I do not mention here, I will rather focus on the works of Newton and Sutin [408], as well as Landau [409] and Zener [410] (although both Landau and Zener are properly referenced here, I only used [410] since I could not find a translated copy of [409]). Over the past nearly 50+ years various bits and pieces of this overall theory have been implemented and modified with varying assumptions and approximations (often in literature without explicit mention of what approximations are being made). To make matters more complicated, citations on transport can often be inaccurate; in the sense that a report's citation for a theory or equation will not

be derived or fully motivated in the paper they cite! This can lead to a long look down some rabbit holes to find truly resourceful citations for this type of theory, but I guess that is the case with any research, I digress. Nonetheless, I believe the aforementioned citations properly explain the most important concepts of this theory and can explain the equations/approximations implemented in many recent works [73, 411, 412, 413, 414].

B.2 Semiclassical Model

The work of Newton and Sutin [408] begins with introducing the concept of a semiclassical model for the transition rate k_{sc} to approximate the true quantum mechanical transition rate:

$$k_{sc} = \kappa_{el}\Gamma_n k_{el} \sim k_{qm} \tag{B.1}$$

where κ_{el} is the thermally averaged electronic transmission coefficient and Γ_n is a thermally averaged nuclear tunneling factor. This semiclassical transition rate is proportional to the classical transition rate, k_{el} and is equivalent when the factors κ_{el} and Γ_n reach unity. To understand these factors, consider the spirit of Figure B.1a where the system is initially in state ψ_A and transport occurs if the state ψ_B is reached. The purposes of these factors is to introduce, respectively, non-adiabatic behavior where the system can remain a state ψ_A despite being brought to the crossing point (q_C in Figure B.1b) and quantum tunneling where the state ψ_B is reached without reaching the crossing point energy. In this sense we see that $0 \leq \kappa_{el} \leq 1$ and $\Gamma_n \geq 1$. From this we see there are perhaps three cases of transport to consider closely:

1. $\kappa_{el} = 1$ and $\Gamma_n = 1$

2. $\kappa_{el} \neq 1$ and $\Gamma_n = 1$

3. $\Gamma_n \neq 1$

Reviewing several works [73, 411, 412, 413, 414], shows that in most cases the latter of these cases is not often used and the assumption that $\Gamma_n \sim 1$ is made.

B.2.1 Case 1.

The first case pertains to that of a solely classical theory, *i.e.* if the crossing point configuration q_C is reached than the transition will occur, 100% of the time ($\kappa_{el} = 1$) and there is no chance of the transition occurring otherwise ($\Gamma_n = 1$). Therefore we have the transition rate is given by (in the high-temperature limit)

$$k_{el} = \nu_n e^{-E^{\ddagger}/k_B T} \tag{B.2}$$

where $E^{\ddagger}$ is the energy to bring q to the crossing point q_C and ν_n is an effective vibration frequency of the reactants. More details on the activation energy, $E^{\dagger}$ are discussed later.

B.2.2 Case 2.

In the second case we relax our assumptions and allow for the case that the system may not reach the final state ψ_B despite reaching the crossing point configuration ($\kappa_{el} \neq 1$). Now in this case the probability the system will undergo a transition from ψ_A to ψ_B is given by

$$\kappa_{el} = \frac{2P_{12}}{1 + P_{12}} \tag{B.3}$$

where P_{12} is the probability of the transition of $\psi_A \rightarrow \psi_B$ per single passage through the intersection region q_C. According to Landau-Zener P_{12} is given by (derivation given below)

$$P_{12} = 1 - \exp\left[-\frac{4\pi^2|H_{ab}|^2}{h\nu|F_A - F_B|}\right] \tag{B.4}$$

where F_A and F_B are the 'forces' acting on the two states and v is the average velocity the system moves through the intersection region. In most cases v is taken to be the Boltzmann averaged velocity $v_p = \sqrt{2k_BT/\pi\mu}$. Accordingly evaluating for a linear path tangent to the reaction coordinate at the crossing point gives $v|F_A - F_B| = 4\nu_n\sqrt{\lambda\pi k_BT}$ where λ is the reorganization energy (exact derivation not found). This gives a final formula for P_{12} in terms of parameters relevant to the problem.

$$P_{12} = 1 - \exp\left[-\frac{\pi^{3/2}|H_{ab}|^2}{h\nu\sqrt{\lambda\pi k_BT}}\right] \tag{B.5}$$

Plugging Eq. B.5 and Eq. B.3 into Eq. B.1 along with setting $\Gamma_n = 1$ gives the transition rate k_{sc}

$$k_{sc} = \frac{1 - \exp\left[-\frac{\pi^{3/2}|H_{ab}|^2}{h\nu\sqrt{\lambda\pi k_BT}}\right]}{1 - (1/2)\exp\left[-\frac{\pi^{3/2}|H_{ab}|^2}{h\nu\sqrt{\lambda\pi k_BT}}\right]}\nu_n e^{-E^{\ddagger}/k_BT} \tag{B.6}$$

It's important to notice a few cases dependent on the coupling constant H_{ab}. If H_{ab} is large (adiabatic regime) then $P_{12} = 1$ and likewise $\kappa_{el} = 1$ and we have recovered case 1 and if H_{ab} is small then $P_{12} < 1$ and $k_{el} < 1$ so we must use Eq. B.6 rather than Eq. B.2 (a plot of P_{12} along with κ_{el} is shown in Figure B.2.

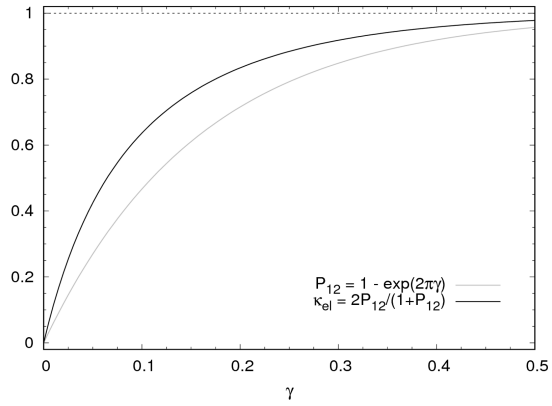

Figure B.2: How P_{12} and the transfer rate change with the coupling parameter γ.

B.3 Supplemental Derivations

B.3.1 Relation of $E^{\ddagger}$ with λ and H_{ab}

Consider the below Figure B.3, in this figure, these curves are drawn assuming that the potential energies are harmonic in q with identical curvature and displays the case where the process is not neutrothermal (curves with the same minima so $\Delta E = 0$). With these assumptions made one can express the activation energy $E^{\dagger}$ in terms of reorganization energy λ and the electron transfer energy ΔE, as shown below.

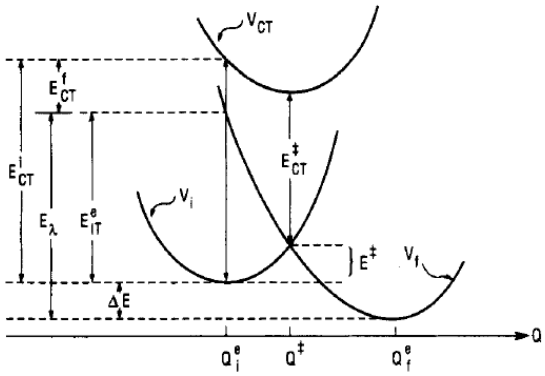

Figure B.3: Alternative schematic of the hopping barrier.

Let ψ_A have potential energy $V_A = q^2$ and let ψ_B have potential energy $V_B = (q-a)2 + b$. Initial conditions fix a and b

$$V_b(a) = \Delta E \quad \Rightarrow \quad b = \Delta E \tag{B.7}$$

$$V_b(0) = \lambda + \Delta E \quad \Rightarrow \quad a^2 = \lambda \tag{B.8}$$

Solving for the intercept of the potential energy surface q^*,

$$V_a(q^*) = V_b(q^*) \quad \Rightarrow \quad (q^*)^2 = (q^*)^2 - 2q^*q + a^2 + b \tag{B.9}$$

$$\Rightarrow \quad q^* = (a^2 + b)/2a \tag{B.10}$$

Plugging the intercept into $V_A(q)$ gives the activation energy,

$$E^\ddagger = V_A(q^*) = \Big[(a^2 + b)/2a\Big]^2 \tag{B.11}$$

Finally, plugging in a and b gives

$$E^\ddagger = \frac{(\lambda + \Delta E)^2}{4\lambda} \tag{B.12}$$

In any case where the initial and final configurations are equivalent or nearly equivalent such that $\Delta E \ll \lambda$, then our expression reduces to $E^\ddagger \sim \lambda/4$. If we wish to include a correction of the electronic coupling $|H_{ab}|$ (as shown in Figure B.1b), we need only subtract this from our above expression to get a final expression for the activation energy.

$$E^\ddagger = \frac{(\lambda + \Delta E)^2}{4\lambda} - |H_{ab}| \tag{B.13}$$

B.3.2 Probability of transfer P_{12}

Consider ψ_A and ψ_B as before and the process of transport from ψ_A to ψ_B. Initially in this process the configuration is in the state ψ_A but with finite velocity at any subsequent time it is in a linear combination of these states:

$$\psi(t) = A(t)\psi_A + B(t)\psi_B \tag{B.14}$$

As time evolves in the transport $A(t)$ will go from 1 to 0 and $B(t)$ will go from 0 to 1. Furthermore along this transition E_B will become less than E_A and so ψ_B will be more stable than ψ_A. Consider an alternative basis of wavefunctions ϕ_1 and ϕ_2 which are linear combinations of ψ_A and ψ_B, where for all t, the energy of the state ϕ_1 is less than that of ϕ_2. These new states no longer satisfy the Hamiltonian but rather,

$$\begin{bmatrix} H\phi_1 = \epsilon_1 + \epsilon_{12}\phi_2 \\ H\phi_2 = \epsilon_{12} + \epsilon_2\phi_2 \end{bmatrix}, \tag{B.15}$$

where ϵ_{12} is the electronic coupling constant (such as H_{ab} or V_{ab}). We then impose the following assumptions so that explicit functions of $A(t)$ and $B(t)$ can be obtained:

1. ϵ_{12} relative kinetic energy of the two systems

2. the transition region is small so that $\epsilon_1 - \epsilon_2$ is a linear function of time and ϵ_{12}, ϕ_1 and ϕ_2 are independent of time:

$$\frac{2\pi}{h}(\epsilon_1 - \epsilon_2) = \alpha t\,, \quad \dot{\epsilon}_{12} = \dot{\phi}_1 = \dot{\phi}_2 = 0\,. \tag{B.16}$$

We now want to solve the Schrödinger equation and for later reasons we will rewrite the coefficents $A(t)$ and $B(t)$ in terms of new coefficients $C_1(t)$ and $C_2(t)$:

$$\left(H - \frac{h}{2\pi i}\frac{\partial}{\partial t}\right)\left[C_1(t)\exp\left(\frac{2\pi i}{h}\int \epsilon_1\, dt\right)\phi_1 + C_2(t)\exp\left(\frac{2\pi i}{h}\int \epsilon_2\, dt\right)\phi_2\right] \quad \text{(B.17)}$$

Using the assumptions we made above this reduces into two coupled first-order differential equations:

$$\frac{h}{2\pi i}\frac{\partial C_1}{\partial t} = \epsilon_{12}\,\exp\left[-\frac{2\pi i}{h}\int(\epsilon_1 - \epsilon_2)\, dt\right] C_2 \quad \text{(B.18)}$$

$$\frac{h}{2\pi i}\frac{\partial C_2}{\partial t} = \epsilon_{12}\,\exp\left[\frac{2\pi i}{h}\int(\epsilon_1 - \epsilon_2)\, dt\right] C_1 \quad \text{(B.19)}$$

If we are initially in the state ψ_A or ϕ_1 then

$$|C_1(-\infty)| = 1 \quad \text{and} \quad C_2(-\infty) = 0 \quad \text{(B.20)}$$

Note that $|C_1(\infty)|$ is the probability of transfer and therefore we only need the asymptotic solutions of Eq. B.18 and Eq. B.19. Plugging in Eq. B.19 into Eq. B.18 gives a single differential equation for C_1,

$$\frac{d^2C_1}{dt^2} + \left(\frac{2\pi i}{h}(\epsilon_1 - \epsilon_2) - \frac{\dot{\epsilon}_{12}}{\epsilon_{12}}\right)\frac{dC_1}{dt} + \left(\frac{2\pi\epsilon_{12}}{h}\right)^2 C_1 = 0 \quad \text{(B.21)}$$

Imposing Eq. B.16 and rewriting $C_1 = \exp[-(\pi i/h)\int(\epsilon_1 - \epsilon_2)dt]U_1$ and $f = (2\pi\epsilon_{12}/h)$ reduces this to the Weber equation:

$$\frac{d^2U_1}{dt^2} + \left(f^2 - \frac{i\alpha}{2} + \frac{\alpha^2}{4}t^2\right)U_1 = 0 \quad \text{(B.22)}$$

The solution to this differential equation is known, but is not simple! Referring to the asymptotic forms we indeed find that

$$P_{12} = |C_1(\infty)|^2 = 1 - \exp(-2\pi\gamma)\,, \quad \text{where} \quad \gamma = \frac{2\pi}{h}\frac{\epsilon_{12}}{|\frac{d}{dt}(\epsilon_1 - \epsilon_2)|} \tag{B.23}$$

Finally, the recognition that

$$\left|\frac{dE}{dt}\right| = \left|\frac{dE}{dx}\frac{dx}{dt}\right| \quad \Rightarrow \quad \left|\frac{d}{dt}(\epsilon_1 - \epsilon_2)\right| = v|F_A - F_B| \tag{B.24}$$

allows us to rewrite Eq. B.23 as

$$P_{12} = 1 - \exp\left[-\frac{4\pi^2|H_{ab}|^2}{hv|F_A - F_B|}\right] \tag{B.25}$$

which is precisely Eq. B.5.

Appendix C

Zero-Field Splitting

C.1 Dipole-Dipole Spin Hamiltonian

This section follows chapter 6 in Ref. [415] closely. Here is a method for computing spin-spin contribution of the zero-field splitting from Kohn-Sham orbitals at defect centers with high spin ($S > 1$). Originally, we consider the spin-spin interaction of two dipole moments $\hat{\mathbf{S}}_1$ and $\hat{\mathbf{S}}_2$, separated by $\mathbf{r}$:

$$\hat{\mathcal{H}}_D = \frac{\mu_0}{4\pi} g^2 \mu_B^2 \left[\frac{\hat{\mathbf{S}}_1 \cdot \hat{\mathbf{S}}_2}{r^3} - 3\frac{(\hat{\mathbf{S}}_1 \cdot \mathbf{r})(\hat{\mathbf{S}}_2 \cdot \mathbf{r})}{r^5} \right] \tag{C.1}$$

where g is the electron g-factor and μ_B is the Bohr magneton. Expanding scalar products gives:

$$\begin{aligned} \hat{\mathcal{H}}_D = & \frac{\mu_0}{4\pi} \frac{g^2 \mu_B^2}{r^5} \Big[(r^2 - 3x^2)\hat{S}_{1x}\hat{S}_{2x} + (r^2 - 3y^2)\hat{S}_{1y}\hat{S}_{2y} + (r^2 - 3z^2)\hat{S}_{1z}\hat{S}_{2z} \\ & - 3xy(\hat{S}_{1x}\hat{S}_{2y} + \hat{S}_{1y}\hat{S}_{2x}) - 3xz(\hat{S}_{1x}\hat{S}_{2z} + \hat{S}_{1z}\hat{S}_{2x}) - 3yz(\hat{S}_{1y}\hat{S}_{2z} + \hat{S}_{1z}\hat{S}_{2y}) \Big]. \end{aligned} \tag{C.2}$$

Now we seek to convert from the operators $\hat{\mathbf{S}}_1$ and $\hat{\mathbf{S}}_2$ to the combinatory $\hat{\mathbf{S}} = \hat{\mathbf{S}}_1 + \hat{\mathbf{S}}_2$. It easily shown (see appendix) that:

$$\hat{S}_{1x}\hat{S}_{2x} = \frac{1}{2}\hat{S}_x^2 - \frac{1}{4}\mathbb{1} \tag{C.3}$$

and

$$\hat{S}_{1x}\hat{S}_{2y} + \hat{S}_{1y}\hat{S}_{2x} = \frac{1}{2}(\hat{S}_x\hat{S}_y + \hat{S}_y\hat{S}_x)\,. \tag{C.4}$$

Inserting Eq. C.3 and Eq. C.4 into Eq. C.2 gives:

$$\begin{aligned}\hat{\mathcal{H}}_D =& \frac{\mu_0}{4\pi}\frac{g^2\mu_B^2}{r^5}\frac{1}{2}\Big[(r^2-3x^2)\hat{S}_x^2 + (r^2-3y^2)\hat{S}_y^2 + (r^2-3z^2)\hat{S}_z^2 \\ &- 3xy(\hat{S}_x\hat{S}_y + \hat{S}_y\hat{S}_x) - 3xz(\hat{S}_x\hat{S}_z + \hat{S}_z\hat{S}_x) - 3yz(\hat{S}_y\hat{S}_z + \hat{S}_z\hat{S}_y)\Big]\,.\end{aligned} \tag{C.5}$$

which is analogous to Eq. C.2 but is in terms of a single spin operator $\hat{\mathbf{S}}$. Therefore Eq. C.5 can be converted into a typical spin-hamiltonian form where $\langle\,\rangle$ represents integration over real space wavefunctions.

$$\hat{\mathcal{H}}_D = \hat{\mathbf{S}}^T \cdot \mathbf{D} \cdot \hat{\mathbf{S}} \tag{C.6}$$

$$\mathbf{D} = \frac{\mu_0}{8\pi} g^2\mu_B^2 \begin{bmatrix} \langle\frac{r^2-3x^2}{r^5}\rangle & \langle\frac{-3xy}{r^5}\rangle & \langle\frac{-3xz}{r^5}\rangle \\ & \langle\frac{r^2-3y^2}{r^5}\rangle & \langle\frac{-3yz}{r^5}\rangle \\ & & \langle\frac{r^2-3z^2}{r^5}\rangle \end{bmatrix} \qquad \hat{\mathbf{S}} = \begin{bmatrix} \hat{S}_x \\ \hat{S}_y \\ \hat{S}_z \end{bmatrix} \tag{C.7}$$

C.2 Two Particle Wavefunctions from DFT Calculations

This section follows Ref. [391] exactly. Here we are interested in the evaluation of integrals of the form:

$$I_{ab} = \iint \rho(\mathbf{r}_1, \mathbf{r}_2) f_{ab}(\mathbf{r}_1 - \mathbf{r}_2)\, d\mathbf{r}_1\, d\mathbf{r}_2\,, \tag{C.8}$$

with

$$f_{ab}(\mathbf{r}_1 - \mathbf{r}_2) = \frac{r^2\delta_{ab} - 3r_a r_b}{r^5}\,, \tag{C.9}$$

$\mathbf{r} = \mathbf{r}_1 - \mathbf{r}_2$ and $a, b \in \{x, y, z\}$. Here $\rho(\mathbf{r}_1, \mathbf{r}_2)$ is the two-particle charge density which is constructed by the anti-symmetric product of single particle orbitals:

$$\Psi(\mathbf{r}_1, \mathbf{r}_2) = \frac{1}{\sqrt{2}}\left[\psi_i(\mathbf{r}_1)\psi_j(\mathbf{r}_2) - \psi_i(\mathbf{r}_2)\psi_j(\mathbf{r}_1)\right]\,. \tag{C.10}$$

And thus the two particle charge density is given by (note f_{ab} is symmetric under particle exchange):

$$\rho(\mathbf{r}_1, \mathbf{r}_2) = \left[\psi_i^*(\mathbf{r}_1)\psi_j^*(\mathbf{r}_2)\psi_i(\mathbf{r}_1)\psi_j(\mathbf{r}_2) - \psi_i^*(\mathbf{r}_2)\psi_j^*(\mathbf{r}_1)\psi_i(\mathbf{r}_1)\psi_j(\mathbf{r}_2)\right]\,. \tag{C.11}$$

Here we alleviate the expense in this calculation by expanding $\rho(\mathbf{r}_1, \mathbf{r}_2)$ in terms of plane waves and thus circumventing the cost from direct integration. This expansion gives

$$\rho(\mathbf{r}_1, \mathbf{r}_2) = \sum_{\mathbf{G}_1, \mathbf{G}_2} \rho(\mathbf{G}_1, \mathbf{G}_2) e^{i\mathbf{G}_1\cdot\mathbf{r}_1} e^{i\mathbf{G}_2\cdot\mathbf{r}_2} \tag{C.12}$$

and thus

$$I_{ab} = \frac{1}{8} \sum_{\mathbf{G}_1,\mathbf{G}_2} \rho(\mathbf{G}_1,\mathbf{G}_2) \iint e^{i[\mathbf{r}\cdot(\mathbf{G}_1-\mathbf{G}_2)]/2} e^{i[\mathbf{R}\cdot(\mathbf{G}_1+\mathbf{G}_2)]/2} f_{ab}(\mathbf{r})\, d\mathbf{r}\, d\mathbf{R}\,, \tag{C.13}$$

where $\mathbf{r} = \frac{1}{2}(\mathbf{r}_1 - \mathbf{r}_2)$ and $\mathbf{R} = \frac{1}{2}(\mathbf{r}_1 + \mathbf{r}_2)$, with $d\mathbf{r}_1\, d\mathbf{r}_2 = 1/2\, d\mathbf{r}\, d\mathbf{R}$. The integration over $\mathbf{R}$ can be done directly and yields $8\Omega\delta_{\mathbf{G}_1,-\mathbf{G}_2}$. Therefore $\mathbf{G}_1 = -\mathbf{G}_2 = \mathbf{G}$ and Eq. C.13 simplifies to

$$I_{ab} = \Omega \sum_{\mathbf{G}} \rho(\mathbf{G},-\mathbf{G}) \int e^{i\mathbf{G}\cdot\mathbf{r}} f_{ab}(\mathbf{r})\, d\mathbf{r}\,, \tag{C.14}$$

where Ω is the volume of the unit cell. The integration over r is slightly more tricky but can still be evaluated to give the final result (see appendix for integration over $\mathbf{R}$ and $\mathbf{r}$)

$$I_{ab} = 4\pi\Omega \sum_{\mathbf{G}} \rho(\mathbf{G},-\mathbf{G}) \left(\frac{G_a G_b}{G^2} - \frac{\delta_{ab}}{3} \right)\,, \tag{C.15}$$

where

$$D_{ab} = \frac{\mu_0}{4\pi} g^2 \mu_B^2 \left[\frac{1}{2} I_{ab} \right]\,. \tag{C.16}$$

Therefore the spin-spin Hamiltonian is given by (Ref. [416])

$$\hat{\mathcal{H}}_D = D \left(\hat{S}_z^2 - \frac{S(S+1)}{3} \right) + E \left(\frac{\hat{S}_+^2 + \hat{S}_-^2}{2} \right)\,, \tag{C.17}$$

with

$$D = \frac{3}{2} D_{zz}\,, \quad E = \frac{D_{yy} - D_{xx}}{2}\,, \quad \hat{S}_\pm = \hat{S}_x \pm i\, \hat{S}_y \tag{C.18}$$

C.3 Beyond two-band result

Consider a two particle wavefunction built of parallel spin electrons with $i \neq j$:

$$\Psi^{\alpha}(1,2) = \frac{1}{\sqrt{2}} \begin{bmatrix} \psi_i^{\alpha}(1) & \psi_j^{\alpha}(1) \\ \psi_i^{\alpha}(2) & \psi_j^{\alpha}(2) \end{bmatrix} \tag{C.19}$$

$$= \frac{1}{\sqrt{2}} \left[\psi_i^{\alpha}(1)\psi_j^{\alpha}(2) - \psi_i^{\alpha}(2)\psi_j^{\alpha}(1) \right] \tag{C.20}$$

The corresponding two particle density is:

$$\rho^{\alpha} = \Psi^{\alpha}(1,2)^* \Psi^{\alpha}(1,2) \tag{C.21}$$

$$= \frac{1}{2} \Big[|\psi_i^{\alpha}(1)|^2 |\psi_j^{\alpha}(2)|^2 + |\psi_i^{\alpha}(2)|^2 |\psi_j^{\alpha}(1)|^2 \tag{C.22}$$

$$- \psi_i^{\alpha}(1)^* \psi_j^{\alpha}(2)^* \psi_i^{\alpha}(2)\psi_j^{\alpha}(1) - \psi_i^{\alpha}(2)^* \psi_j^{\alpha}(1)^* \psi_i^{\alpha}(1)\psi_j^{\alpha}(2) \Big]$$

Consider a two particle wavefunction built of anti-parallel spin electrons with $i \neq j$:

$$\Psi^{\alpha\beta}(1,2) = \frac{1}{\sqrt{2}} \begin{bmatrix} \psi_i^{\alpha}(1) & \psi_j^{\beta}(1) \\ \psi_i^{\alpha}(2) & \psi_j^{\beta}(2) \end{bmatrix} \tag{C.23}$$

$$= \frac{1}{\sqrt{2}} \left[\psi_i^{\alpha}(1)\psi_j^{\beta}(2) - \psi_i^{\alpha}(2)\psi_j^{\beta}(1) \right] \tag{C.24}$$

The corresponding two particle density is:

$$\rho^{\alpha\beta} = \Psi^{\alpha\beta}(1,2)^*\Psi^{\alpha\beta}(1,2) \tag{C.25}$$

$$= \frac{1}{2}\Big[|\psi_i^\alpha(1)|^2|\psi_j^\beta(2)|^2 + |\psi_i^\alpha(2)|^2|\psi_j^\beta(1)|^2 \tag{C.26}$$

$$- \psi_i^\alpha(1)^*\psi_j^\beta(2)^*\psi_i^\alpha(2)\psi_j^\beta(1) - \psi_i^\alpha(2)^*\psi_j^\beta(1)^*\psi_i^\alpha(1)\psi_j^\beta(2)\Big]$$

$$= \frac{1}{2}\Big[|\psi_i^\alpha(1)|^2|\psi_j^\beta(2)|^2 + |\psi_i^\alpha(2)|^2|\psi_j^\beta(1)|^2\Big] \tag{C.27}$$

The full many-particle D tensor including spin operator terms is given by (see Eq. 18 of Ref. [391] and Eq. 31 of Ref. [417]):

$$D_{ab} = \frac{1}{S(2S-1)}\left[\sum_{i>j}\langle\Psi|f_{ab}(\mathbf{r}_i,\mathbf{r}_j)(2\hat{S}_{i_z}\hat{S}_{j_z} - \hat{S}_{i_x}\hat{S}_{j_x} - \hat{S}_{i_y}\hat{S}_{j_y})|\Psi\rangle\right] \tag{C.28}$$

$$= \frac{1}{S(2S-1)}\Big[\frac{1}{2}\sum_{i>j}\langle\Psi|f_{ab}(\mathbf{r}_i,\mathbf{r}_j)\hat{\sigma}_{i_z}\hat{\sigma}_{j_z}|\Psi\rangle \tag{C.29}$$

$$- \frac{1}{4}\sum_{i>j}\langle\Psi|f_{ab}(\mathbf{r}_i,\mathbf{r}_j)\hat{\sigma}_{i_x}\hat{\sigma}_{j_x}|\Psi\rangle - \frac{1}{4}\sum_{i>j}\langle\Psi|f_{ab}(\mathbf{r}_i,\mathbf{r}_j)\hat{\sigma}_{i_y}\hat{\sigma}_{j_y}|\Psi\rangle\Big]$$

Recalling that $\hat{\sigma}_z|\pm\rangle = \pm|\pm\rangle$, $\hat{\sigma}_x|\pm\rangle = |\mp\rangle$, and $\hat{\sigma}_y|\pm\rangle = \pm i|\mp\rangle$. We have:

$$\text{for parallel spin states:} \qquad \hat{\sigma}_{i_z}\hat{\sigma}_{j_z} = 1,\ \hat{\sigma}_{i_x}\hat{\sigma}_{j_x} = 1,\ \hat{\sigma}_{i_y}\hat{\sigma}_{j_y} = -1, \tag{C.30}$$

$$\text{for anti-parallel spin states:} \qquad \hat{\sigma}_{i_z}\hat{\sigma}_{j_z} = -1,\ \hat{\sigma}_{i_x}\hat{\sigma}_{j_x} = 1,\ \hat{\sigma}_{i_y}\hat{\sigma}_{j_y} = 1. \tag{C.31}$$

Now we consider each term in Eq. C.29, first for the case of parallel spins then in the case of anti-parallel spins.

Parallel spins ($\hat{\sigma}_{i_z}\hat{\sigma}_{j_z}$ term):

$$(\hat{\sigma}_{i_z}\hat{\sigma}_{j_z})\rho^{\alpha} = \Psi^{\alpha}(1,2)^{*}(\hat{\sigma}_{i_z}\hat{\sigma}_{j_z})\Psi^{\alpha}(1,2) \tag{C.32}$$

$$= \Psi^{\alpha}(1,2)^{*}\Psi^{\alpha}(1,2) \tag{C.33}$$

$$= \frac{1}{2}\Big[|\psi_i^{\alpha}(1)|^2|\psi_j^{\alpha}(2)|^2 + |\psi_i^{\alpha}(2)|^2|\psi_j^{\alpha}(1)|^2 - \psi_i^{\alpha}(1)^{*}\psi_j^{\alpha}(2)^{*}\psi_i^{\alpha}(2)\psi_j^{\alpha}(1) - \psi_i^{\alpha}(2)^{*}\psi_j^{\alpha}(1)^{*}\psi_i^{\alpha}(1)\psi_j^{\alpha}(2)\Big] \tag{C.34}$$

$$f_{ab}(1,2)(\hat{\sigma}_{i_z}\hat{\sigma}_{j_z})\rho^{\alpha} = J_{ij}^{\alpha} - K_{ij}^{\alpha} \tag{C.35}$$

Parallel spins ($\hat{\sigma}_{i_x}\hat{\sigma}_{j_x} + \hat{\sigma}_{i_y}\hat{\sigma}_{j_y}$ term):

$$(\hat{\sigma}_{i_x}\hat{\sigma}_{j_x} + \hat{\sigma}_{i_y}\hat{\sigma}_{j_y})\rho^{\alpha} = \Psi^{\alpha}(1,2)^{*}(\hat{\sigma}_{i_x}\hat{\sigma}_{j_x} + \hat{\sigma}_{i_y}\hat{\sigma}_{j_y})\Psi^{\alpha}(1,2) \tag{C.36}$$

$$= \Psi^{\alpha}(1,2)^{*}\Psi^{\beta}(1,2) - \Psi^{\alpha}(1,2)^{*}\Psi^{\beta}(1,2) \tag{C.37}$$

$$f_{ab}(1,2)(\hat{\sigma}_{i_x}\hat{\sigma}_{j_x} + \hat{\sigma}_{i_y}\hat{\sigma}_{j_y})\rho^{\alpha} = 0 \tag{C.38}$$

Anti-parallel spins ($\hat{\sigma}_{i_z}\hat{\sigma}_{j_z}$ term):

$$(\hat{\sigma}_{i_z}\hat{\sigma}_{j_z})\rho^{\alpha\beta} = \Psi^{\alpha\beta}(1,2)^{*}(\hat{\sigma}_{i_z}\hat{\sigma}_{j_z})\Psi^{\alpha\beta}(1,2) \tag{C.39}$$

$$= -\Psi^{\alpha\beta}(1,2)^{*}\Psi^{\alpha\beta}(1,2) \tag{C.40}$$

$$= -\frac{1}{2}\Big[|\psi_i^{\alpha}(1)|^2|\psi_j^{\beta}(2)|^2 + |\psi_i^{\alpha}(2)|^2|\psi_j^{\beta}(1)|^2\Big] \tag{C.41}$$

$$f_{ab}(1,2)(\hat{\sigma}_{i_z}\hat{\sigma}_{j_z})\rho^{\alpha\beta} = -J_{ij}^{\alpha\beta} \tag{C.42}$$

Anti-parallel spins ($\hat{\sigma}_{i_x}\hat{\sigma}_{j_x} + \hat{\sigma}_{i_y}\hat{\sigma}_{j_y}$ term):

$$(\hat{\sigma}_{i_x}\hat{\sigma}_{j_x} + \hat{\sigma}_{i_y}\hat{\sigma}_{j_y})\rho^{\alpha\beta} = \Psi^{\alpha\beta}(1,2)^*(\hat{\sigma}_{i_x}\hat{\sigma}_{j_x} + \hat{\sigma}_{i_y}\hat{\sigma}_{j_y})\Psi^{\alpha\beta}(1,2) \tag{C.43}$$

$$= 2\Psi^{\alpha\beta}(1,2)^*\Psi^{\beta\alpha}(1,2) \tag{C.44}$$

$$= \Big[\psi_i^\alpha(1)^*\psi_i^\beta(1)\psi_j^\beta(2)^*\psi_j^\alpha(2) \tag{C.45}$$

$$+ \psi_i^\alpha(2)^*\psi_i^\beta(2)\psi_j^\beta(1)^*\psi_j^\alpha(1)$$

$$- \psi_i^\alpha(1)^*\psi_j^\beta(2)^*\psi_i^\beta(2)\psi_j^\alpha(1)$$

$$- \psi_i^\alpha(2)^*\psi_j^\beta(1)^*\psi_i^\beta(1)\psi_j^\alpha(2)\Big]$$

$$f_{ab}(1,2)(\hat{\sigma}_{i_x}\hat{\sigma}_{j_x} + \hat{\sigma}_{i_y}\hat{\sigma}_{j_y})\rho^{\alpha\beta} = -2K_{ij}^{\alpha\beta} \tag{C.46}$$

Plugging Eq. C.35 (both up and down), Eq. C.38, Eq. C.42, and Eq. C.46 into Eq. C.29 gives:

$$D_{ab} = \frac{1}{2S(2S-1)}\left[(\sum_{i>j}^{\alpha} J_{ij}^\alpha - K_{ij}^\alpha) + (\sum_{i>j}^{\beta} J_{ij}^\beta - K_{ij}^\beta) + (\sum_{i>j}^{\alpha\beta} -J_{ij}^{\alpha\beta}) - \frac{1}{2}(\sum_{i>j}^{\alpha\beta} -2K_{ij}^{\alpha\beta})\right] \tag{C.47}$$

Origin of each term: Eq. C.35 Eq. C.35 Eq. C.42 Eq. C.46

Therefore in final we have:

$$D_{ab} = \frac{1}{2S(2S-1)}\sum_{i>j}\chi_{ij}(J_{ij} - K_{ij}) \tag{C.48}$$

Note that the inclusion of an anti-parallel $i = j$ term is theoretically possible but

resolves to zero. This is because in this case the J and K term will cancel:

$$K_{ii}^{\alpha\beta} = f_{ab}(1,2)\Big[\psi_i^{\alpha}(1)^*\psi_i^{\beta}(2)^*\psi_i^{\beta}(2)\psi_i^{\alpha}(1) + \psi_i^{\alpha}(2)^*\psi_i^{\beta}(1)^*\psi_i^{\beta}(1)\psi_i^{\alpha}(2)\Big] \quad \text{(C.49)}$$

$$= f_{ab}(1,2)\Big[|\psi_i^{\alpha}(1)|^2|\psi_i^{\beta}(2)|^2 + |\psi_i^{\alpha}(2)|^2|\psi_i^{\beta}(1)|^2\Big] \quad \text{(C.50)}$$

$$= J_{ii}^{\alpha\beta} \quad \text{(C.51)}$$

C.4 Important notes

Spin Contamination One very important drawback when approximating the multielectron wavefunction with Kohn-Sham wavefunctions as in Eq. C.10 is the affect of spin-contamination. In principle, the sum over multiple states above may not be necessary and terms where $i = j$ for anti-parallel should cancel to zero. However, due to the construction of a Slater determinant from spin-unrestricted DFT calculations, the wavefunctions are no longer eigenfunctions of the total spin operator S^2, thereby introducing error into the calculation of ZFS (see Ref. [418] for more detail). Hence a more appropriate form of Eq. C.48 should be written as:

$$D_{ab} = \frac{1}{S(2S-1)}\left[\frac{1}{2}(\sum_{i>j}^{\alpha} J_{ij}^{\alpha} - K_{ij}^{\alpha}) + \frac{1}{2}(\sum_{i>j}^{\beta} J_{ij}^{\beta} - K_{ij}^{\beta}) - \frac{1}{2}(\sum_{i}^{\alpha}\sum_{j}^{\beta} J_{ij}^{\alpha\beta} - K_{ij}^{\alpha\beta})\right] \quad \text{(C.52)}$$

Therefore there are $\binom{\alpha+\beta}{2}$ number of $J_{ij} - K_{ij}$ terms to be computed. This form is more explicit to what is actually implemented in the code.

Convert G vectors to Cartesian A second important note, is that in most plane-wave basis codes the G-vectors will be defined in 3D on a crystal basis (so the components are simple integers). However, when computing the sum in

Eq. C.15 it is essential (for non-simple cubic systems) to convert the G-vectors to the Cartesian basis. For example if $g = (n, l, m)$ in the crystal basis $(n, l, m \in \mathbb{Z})$, we can convert it to it's Cartesian form as:

$$\begin{bmatrix} b_{1x} & b_{2x} & b_{3x} \\ b_{1y} & b_{2y} & b_{3y} \\ b_{1z} & b_{2z} & b_{3z} \end{bmatrix} \begin{bmatrix} n \\ l \\ m \end{bmatrix} = \begin{bmatrix} nb_{1x} + lb_{2x} + mb_{3x} \\ nb_{1y} + lb_{2y} + mb_{3y} \\ nb_{1z} + lb_{2z} + mb_{3z} \end{bmatrix} \tag{C.53}$$

Diagonalize D_{ab} The resulting matrix from the approach detailed above will be in the Cartesian basis and therefore in order to obtain the ZFS parameters D_x, D_y, D_z, one must compute the eigenvalues and eigenvectors of the matrix D_{ab}. The eigenvector corresponding to D_z is known as the principal axis and can be identified as the eigenvector with the largest eigenvalue (and should also be fairly recognizable given the symmetry of the defect and the orientation of the defect orbitals). In many cases, such as cases with C_{3v}, or D_{3h} symmetry, etc. the eigenvalues D_x and D_y will be equivalent. Distinguishing the two can be done in terms of considering the cross product of their eigenvectors ($\hat{v}_{D_x}$ and $\hat{v}_{D_y}$, respectively) should satisfy $\hat{v}_{D_x} \times \hat{v}_{D_y} = \hat{v}_{D_z}$.

C.5 Supplemental Derivation

Proof of Eq. C.3 Recall $\hat{S}_x = \hat{S}_{1x} + \hat{S}_{2x}$ and $[\hat{S}_{1x}, \hat{S}_{2x}] = 0$.

$$\hat{S}_x^2 = \hat{S}_{1x}^2 + \hat{S}_{2x}^2 + 2\hat{S}_{1x}\hat{S}_{2x} \tag{C.54}$$

Therefore,

$$\hat{S}_{1x}\hat{S}_{2x} = \frac{1}{2}\hat{S}_x^2 - (\hat{S}_{1x}^2 + \hat{S}_{2x}^2)\,, \tag{C.55}$$

and since $\hat{S}_{1x}$ and $\hat{S}_{2x}$ represent individual pauli matrices, it can be easily shown that $\hat{S}_{1x}^2 = \hat{S}_{2x}^2 = (1/2)^2$. This gives:

$$\hat{S}_{1x}\hat{S}_{2x} = \frac{1}{2}\hat{S}_x^2 - \frac{1}{4}\mathbb{1}\,. \tag{C.56}$$

The same is true for (y, z) and components.

Proof of Eq. C.4 The anti-commutator (denoted as $\{,\}$) of $\hat{S}_x$ and $\hat{S}_y$ is given by

$$\begin{aligned}
\{\hat{S}_x, \hat{S}_y\} &= \hat{S}_x\hat{S}_y + \hat{S}_y\hat{S}_x \\
&= (\hat{S}_{1x} + \hat{S}_{2x})(\hat{S}_{1y} + \hat{S}_{2y}) + (\hat{S}_{1y} + \hat{S}_{2y})(\hat{S}_{1x} + \hat{S}_{2x}) \\
&= \hat{S}_{1x}\hat{S}_{1y} + \hat{S}_{1y}\hat{S}_{1x} + \hat{S}_{2x}\hat{S}_{2y} + \hat{S}_{2y}\hat{S}_{2x} + \hat{S}_{1x}\hat{S}_{2y} + \hat{S}_{2x}\hat{S}_{1y} + \hat{S}_{1y}\hat{S}_{2x} + \hat{S}_{2y}\hat{S}_{1x} \\
&= \{\hat{S}_{1x}, \hat{S}_{1y}\} + \{\hat{S}_{2x}, \hat{S}_{2y}\} + 2(\hat{S}_{1x}\hat{S}_{2y} + \hat{S}_{1y}\hat{S}_{2x}) \\
&= 2(\hat{S}_{1x}\hat{S}_{2y} + \hat{S}_{1y}\hat{S}_{2x})\,.
\end{aligned} \tag{C.57}$$

Where the anti-commutator relation $\{\hat{S}_{1a}, \hat{S}_{1b}\} = 0$ for $a \neq b$ was used and we have shown

$$\hat{S}_{1x}\hat{S}_{2y} + \hat{S}_{1y}\hat{S}_{2x} = \frac{1}{2}(\hat{S}_x\hat{S}_y + \hat{S}_y\hat{S}_x)\,. \tag{C.58}$$

The same is true for other combinations of (x, y, z).

Substitution between Eq. C.8 and Eq. C.13 The transformation of co-

ordinates requires calculating the Jacobian for integration.

$$\begin{aligned} dr_{1x}\, dr_{2x} &= \begin{vmatrix} \partial r_{1x}/\partial r_x & \partial r_{1x}/\partial R_x \\ \partial r_{2x}/\partial r_x & \partial r_{2x}/\partial R_x \end{vmatrix} dr_x\, dR_x \\ &= \begin{vmatrix} 1/2 & 1/2 \\ -1/2 & 1/2 \end{vmatrix} dr_x\, dR_x \\ &= \frac{1}{2}\, dr_x\, dR_x \end{aligned} \tag{C.59}$$

Repeating for y and z components gives a total factor of $1/8$.

Integration over R in Eq. C.13 Consider the part of I_{ab} from Eq. C.13 which depends on R:

$$I_{\mathbf{R}} = \int_{\Omega} e^{i[\mathbf{R}\cdot(\mathbf{G}_1+\mathbf{G}_2)]/2}\, d\mathbf{R} \tag{C.60}$$

For simplicity consider the x component which integrates over lattice vector ($\mathbf{a}$):

$$\begin{aligned} I_{R_x} &= \int_0^a e^{i[R_x(G_{1x}+G_{2x})]/2}\, dR_x \\ &= \frac{-2i}{G_{1x}+G_{2x}} \left[e^{i[a(G_{1x}+G_{2x})]/2} - 1 \right] \end{aligned} \tag{C.61}$$

As $\mathbf{G}_1$ and $\mathbf{G}_2$ represent reciprocal lattice vectors they both have the form:

$$\mathbf{G} = v_1\mathbf{b}_1 + v_2\mathbf{b}_2 + v_3\mathbf{b}_3 \tag{C.62}$$

where the reciprocal lattice vectors $\mathbf{b}_i$ obey the property $\mathbf{b}_i \cdot \mathbf{a}_j = 2\pi\delta_{ij}$. This will result in

$$I_{R_x} = \frac{-2i}{G_{1x}+G_{2x}} \left[e^{2\pi ik} - 1 \right] \tag{C.63}$$

where $k \in \mathbb{Z}$. Therefore the integral equates to zero except under the condition that $G_{1x} = G_{2x}$. In this limit we have:

$$\lim_{\eta \to 0} \frac{-2i}{\eta} \left[e^{ia\eta} - 1 \right] \overset{LH}{=} \lim_{\eta \to 0} -2i(ia)e^{ia\eta}$$
$$= 2a \tag{C.64}$$

Carrying out the integration over y and z will result in the volume of the unit cell and force $G_1 = G_2$. This gives the final result:

$$I_{\mathbf{R}} = \int_{\Omega} e^{i[\mathbf{R}\cdot(\mathbf{G}_1+\mathbf{G}_2)]/2} \, d\mathbf{R} = 8\Omega\delta_{\mathbf{G}_1,\mathbf{G}_2} \tag{C.65}$$

Integration over r in Eq. C.14 Consider the solution to the following integral:

$$\int e^{i\mathbf{G}\cdot\mathbf{r}} \frac{1}{|\mathbf{r}-\mathbf{C}|} \, d\mathbf{r} = \frac{4\pi}{G^2} e^{i\mathbf{G}\cdot\mathbf{C}} \, . \tag{C.66}$$

Taking the second derivative ($a, b \in \{x, y, z\}$):

$$-\frac{\partial^2}{\partial C_a \partial C_b} \int e^{i\mathbf{G}\cdot\mathbf{r}} \frac{1}{|\mathbf{r}-\mathbf{C}|} \, d\mathbf{r} = \frac{4\pi G_a G_b}{G^2} e^{i\mathbf{G}\cdot\mathbf{C}} \, . \tag{C.67}$$

Meanwhile,

$$-\frac{\partial^2}{\partial C_a \partial C_b} \frac{1}{|\mathbf{r}-\mathbf{C}|} = \frac{\delta_{ab}}{r^3} - \frac{3r'_a r'_b}{r^5} + \frac{4\pi\delta_{ab}}{3}\delta(\mathbf{r}) \, . \tag{C.68}$$

Therefore,

$$\int e^{i\mathbf{G}\cdot\mathbf{r}} \frac{r^2\delta_{ab} - 3r'_a r'_b}{r^5} \, d\mathbf{r} = \frac{4\pi G_a G_b}{G^2} e^{i\mathbf{G}\cdot\mathbf{C}} + \frac{4\pi}{3}\delta_{ab} \, , \tag{C.69}$$

and the final form fo I_{ab} is obtained:

$$I_{ab} = 4\pi\Omega \sum_{\mathbf{G}} \rho(\mathbf{G}, -\mathbf{G}) \left(\frac{G_a G_b}{G^2} - \frac{\delta_{ab}}{3} \right) \tag{C.70}$$

Convolution Theorem

Consider the Fourier transform of ψ.

$$\psi(\mathbf{r}) = \frac{1}{\Omega} \sum_{\mathbf{G}} \psi(\mathbf{G})\, e^{i\mathbf{G}\cdot\mathbf{r}} \qquad \text{and} \qquad \psi(\mathbf{G}) = \int_{\Omega} \psi(\mathbf{r})\, e^{-i\mathbf{G}\cdot\mathbf{r}}\, d\mathbf{r} \tag{C.71}$$

The product $\psi_j^*(\mathbf{r})\psi_i(\mathbf{r})$ therefore has the form:

$$\psi_j^*(\mathbf{r})\psi_i(\mathbf{r}) = \frac{1}{\Omega^2} \left(\sum_{\mathbf{G}'} \psi_i(\mathbf{G}') e^{i\mathbf{G}'\cdot\mathbf{r}} \right) \left(\sum_{\mathbf{G}''} \psi_j^*(\mathbf{G}'') e^{-i\mathbf{G}''\cdot\mathbf{r}} \right) . \tag{C.72}$$

The Fourier transform of the product of these wavefunctions is thus given by:

$$\begin{aligned}
\mathcal{F}\left\{ \psi_j^*(\mathbf{r})\psi_i(\mathbf{r}) \right\} &= \frac{1}{\Omega^2} \int_{\Omega} \left[\left(\sum_{\mathbf{G}'} \psi_i(\mathbf{G}') e^{i\mathbf{G}'\cdot\mathbf{r}} \right) \left(\sum_{\mathbf{G}''} \psi_j^*(\mathbf{G}'') e^{-i\mathbf{G}''\cdot\mathbf{r}} \right) \right] e^{-i\mathbf{G}\cdot\mathbf{r}}\, d\mathbf{r} \\
&= \frac{1}{\Omega^2} \sum_{\mathbf{G}'} \psi_i(\mathbf{G}') \left[\sum_{\mathbf{G}''} \psi_j^*(\mathbf{G}'') \left(\int_{\Omega} e^{i(\mathbf{G}'-\mathbf{G}''-\mathbf{G})\cdot\mathbf{r}}\, d\mathbf{r} \right) \right] \\
&= \frac{1}{\Omega} \sum_{\mathbf{G}'} \psi_i(\mathbf{G}') \left[\sum_{\mathbf{G}''} \psi_j^*(\mathbf{G}'')\, \delta(\mathbf{G}' - \mathbf{G}'' - \mathbf{G}) \right] \\
&= \frac{1}{\Omega} \sum_{\mathbf{G}'} \psi_i(\mathbf{G}') \psi_j^*(\mathbf{G} - \mathbf{G}') .
\end{aligned} \tag{C.73}$$

Therefore we can compute $f_1(\mathbf{G})$, $f_2(\mathbf{G})$, $f_3(\mathbf{G})$ as:

$$\begin{gathered}
f_1(\mathbf{G}) = \frac{1}{\Omega} \sum_{\mathbf{G}'} \psi_1^*(\mathbf{G} - \mathbf{G}')\psi_1(\mathbf{G}') , \quad f_2(\mathbf{G}) = \frac{1}{\Omega} \sum_{\mathbf{G}'} \psi_2^*(\mathbf{G} - \mathbf{G}')\psi_2(\mathbf{G}') , \\
f_3(\mathbf{G}) = \frac{1}{\Omega} \sum_{\mathbf{G}'} \psi_1^*(\mathbf{G} - \mathbf{G}')\psi_2(\mathbf{G}') .
\end{gathered} \tag{C.74}$$

Appendix D

Photoluminescence

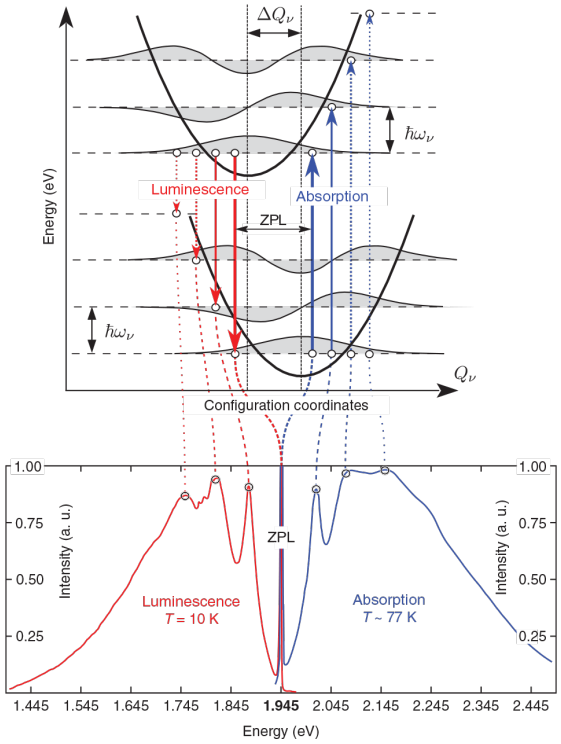

Figure D.1: Top, schematic representation of two adiabatic potential energy surfaces with various vibronic levels with energetic separation ($\hbar\omega$). Bottom, luminescence (red) and absoprtion (blue) spectra of NV center in diamond. This diagram provides an amazing visual representation so I borrowed it from Ref. [419], a fantastic reference for the NV center.

D.1 Normalized Photoluminescence

Following Ref. [345], at $T = 0$K the absolute luminescence intensity $I(\hbar\omega)$ (photons per unit time per unit energy) for a single emitter is given by:

$$I(\hbar\omega) = \frac{n_D \omega^3}{3\epsilon_0 \pi c^3 \hbar} |\vec{\mu}_{eg}|^2 \sum_m |\langle \chi_{gm} | \chi_{e0} \rangle|^2 \, \delta(E_{ZPL} - E_{gm} - \hbar\omega) \,. \tag{D.1}$$

Here n_D is the refractive index ($n = \sqrt{\epsilon}$); χ_{e0} and χ_{gm} are vibrational levels of the excited and ground state with energy E_{e0} and E_{gm} (with $E_{ZPL} = E_{e0} - E_{g0}$). Here we assume the Franck-Condon approximation holds, i.e. the transition dipole moment $|\vec{\mu}_{eg}|$ depends weakly on the lattice parameters. A prefactor of ω^3 arises from the density of states of photons that cause the spontaneous emission ($\sim \omega^2$ – Pg. 465 Ashcroft & Mermin: Debye model) and the perturbing electric field ($|\vec{E}|^2 \sim \omega$).

If only the normalized luminescence is desired (experimentally the absolute intensity is difficult), then we can consider the normalized luminescence intensity, defined as

$$L(\hbar\omega) = C\omega^3 \, A(\hbar\omega) \,, \tag{D.2}$$

where

$$A(\hbar\omega) = \sum_m |\langle \chi_{gm} | \chi_{e0} \rangle|^2 \, \delta(E_{ZPL} - E_{gm} - \hbar\omega) \tag{D.3}$$

is the optical spectral function, and C is a normalization constant.

D.2 The optical spectral function

In Ref. [345], the direct calculation of Eq. D.3 is avoided. We assume: (1) normal modes that contribute the luminescence are those of the solid with the defect (opposed to bulk modes without the defect) and (2) the modes of the excited state are identical to the ground state. Using a generating function approach in which the main quantity to compute directly from first-principles results is the HR function:

$$S(\hbar\omega) = \sum_k S_k \delta(\hbar\omega - \hbar\omega_k)\,, \tag{D.4}$$

where

$$S_k = \omega_k\, q_k^2/(2\hbar) \tag{D.5}$$

are partial Huang-Rhys (HR) factors and

$$q_k = \sum_i \sqrt{m_i}\,(\vec{R}_{e;i} - \vec{R}_{g;i}) \cdot \Delta\vec{r}_{k;i} \tag{D.6}$$

are generalized coordinates in vibrational mode k ($\Delta\vec{r}_{k;i}$ is a normalized vector that describes the displacement of ion i in phonon mode k). The larger the dot product between the normalized phonon mode k and the displacement vector $(\vec{R}_{e;i} - \vec{R}_{g;i})$; the greater the contribution of mode k to the overall HR function in equation D.4. From $S(\hbar\omega)$ we can compute $A(\hbar\omega)$ as:

$$A(E_{ZPL} - \hbar\omega) = \frac{1}{2\pi}\int_{-\infty}^{\infty} G(t)\, e^{i\omega t - \gamma|t|}\, dt \tag{D.7}$$

with the generating function $G(t)$ defined as

$$G(t) = e^{S(t)-S(0)}\,, \tag{D.8}$$

where $S(t)$ is the Fourier transform of the HR function

$$S(t) = \int_0^\infty S(\hbar\omega)e^{-i\omega t}\,d(\hbar\omega)\,. \tag{D.9}$$

A broadening of the ZPL γ enters the form of the photoluminescence in Eq. D.7 and can be chosen to reproduce the experimental ZPL width. This procedure of computing photoluminescence is implemented here: `https://github.com/Ping-Group-UCSC/PL-code`.

D.3 Additional Derivations

The form of the spectral function:

$$A(\hbar\omega) = \sum_m |\,\langle\chi_{gm}|\chi_{e0}\rangle\,|^2\delta(E_{ZPL} - E_{gm} - \hbar\omega) \tag{D.10}$$

isn't quite exact, in fact while the quantum number m represents the state of a vibrational mode, in a solid crystal (in 3D space) has 3N vibrational modes which we denoted by k. More exactly:

$$A(\hbar\omega) = \sum_k\sum_m |\,\langle\chi^k_{gm}|\chi^k_{e0}\rangle\,|^2\delta(E_{ZPL} - E^k_{gm} - \hbar\omega) \tag{D.11}$$

where E^k_{gm} is actually $E^k_{gm} = E^k_{gm} - E^k_{e0}$ but since we have assumed g and e have the same vibrational states $k_g = k_e$ and so $E^k_{gm} = (m+1/2)\hbar\omega_k - (0+1/2)\hbar\omega_k = m\hbar\omega_k$.

Hence,

$$A(\hbar\omega) = \sum_k \sum_m |\langle \chi^k_{gm} | \chi^k_{e0} \rangle|^2 \delta(E_{ZPL} - m\hbar\omega_k - \hbar\omega) \tag{D.12}$$

or

$$A(E_{ZPL} - \hbar\omega) = \sum_k \sum_m |\langle \chi^k_{gm} | \chi^k_{e0} \rangle|^2 \delta(\hbar\omega - m\hbar\omega_k) \tag{D.13}$$

Now focusing on the phonon overlap:

$$\sum_m |\langle \chi^k_{gm} | \chi^k_{e0} \rangle|^2 \tag{D.14}$$

The solution of this overlap is [420]

$$|\langle \chi^k_{gm} | \chi^k_{e0} \rangle|^2 = e^{-S_k} \frac{S_k^m}{m!} \tag{D.15}$$

in addition

$$\sum_m |\langle \chi^k_{gm} | \chi^k_{e0} \rangle|^2 = e^{-S_k} \sum_m \frac{(S_k)^m}{m!} = e^{-S_k} \left(e^{S_k}\right) = 1 \tag{D.16}$$

where

$$S_k = \omega_k q_k^2 / 2\hbar \tag{D.17}$$

The spectral density $S(\hbar\omega)$ is defined as:

$$S(\hbar\omega) = \sum_k S_k \delta(\hbar\omega - \hbar\omega_k) = \sum_k \frac{\omega_k q_k^2}{2\hbar} \delta(\hbar\omega - \hbar\omega_k) \tag{D.18}$$

Note: $\chi_{gm}(Q) = \chi_{em}(Q - Q_0 + \Delta Q)$ when $\Delta Q = Q_0$

Appendix E

Optical Properties

E.1 Macroscopic Dielectric Function

See Ref. [421, 422, 423] for additional details. Within the Alder-Wiser formulation (consistent with KS approach for periodic boundary conditions) the irreducible polarizability is given by:

$$\chi^0_{\mathbf{G},\mathbf{G}'}(\mathbf{q}) = -\frac{4}{(2\pi)^3}\sum_{v,c}\int_{BZ} d\mathbf{k}\frac{\langle \mathbf{k}+\mathbf{q},c|\, e^{i(\mathbf{q}+\mathbf{G})\cdot r}\,|\mathbf{k},v\rangle\,\langle \mathbf{k},v|\, e^{-i(\mathbf{q}+\mathbf{G}')\cdot r}\,|\mathbf{k}+\mathbf{q},c\rangle}{E_c(\mathbf{k}+\mathbf{q}) - E_v(\mathbf{k})} \tag{E.1}$$

Note the compressed notation used here $f_{\mathbf{G},\mathbf{G}'}(\mathbf{q}) = f(\mathbf{G}+\mathbf{q},\mathbf{G}'+\mathbf{q})$.

E.1.1 Independent-Particle-Approximation

The simplest approach, known as the independent-particle approximation is to directly compute the dielectric matrix ϵ from the irreducible polarizability.

$$\epsilon_{\mathbf{G},\mathbf{G}'}(\mathbf{q}) = \delta_{\mathbf{G},\mathbf{G}'} - v_{\mathbf{G}}(\mathbf{q})\chi^0_{\mathbf{G},\mathbf{G}'}(\mathbf{q}) \tag{E.2}$$

Here $v_{\mathbf{G}}(\mathbf{q})$ is the simple Hartree kernel.

$$v_{\mathbf{G}}(\mathbf{q}) = \frac{4\pi}{|\mathbf{q}+\mathbf{G}|^2} \tag{E.3}$$

Therefore, within the independent-particle approximation, the macroscopic dielectric function (long-wavelength limit of the $\mathbf{G} = \mathbf{G}' = 0$ element) is given by:

$$\epsilon_M = \lim_{q\to 0} \epsilon_{0,0}(\mathbf{q}) \tag{E.4}$$

E.1.2 Random-Phase-Approximation

In reality, the irreducible polarizability should be fed into a Dyson equation for the reducible polarizability which includes the Hartree term explicitly in the polarizability.

$$\chi_{\mathbf{G},\mathbf{G}'}(\mathbf{q}) = \chi^0_{\mathbf{G},\mathbf{G}'}(\mathbf{q}) + \sum_{G_1,G_2} \chi^0_{\mathbf{G},\mathbf{G}_1}(\mathbf{q})\Big[v_{\mathbf{G}_1}(\mathbf{q})\delta_{\mathbf{G}_1,\mathbf{G}_2}\Big]\chi_{\mathbf{G}_2,\mathbf{G}'}(\mathbf{q}) \tag{E.5}$$

Then the dielectric matrix is provided by a calculation reminiscent of Eq. E.2.

$$\epsilon^{-1}_{\mathbf{G},\mathbf{G}'}(\mathbf{q}) = \delta_{\mathbf{G},\mathbf{G}'} + v_{\mathbf{G}}(\mathbf{q})\chi_{\mathbf{G},\mathbf{G}'}(\mathbf{q}) \tag{E.6}$$

An important difference is that here the inverse of the dielectric matrix is computed and therefore an inversion is necessary to obtain the final macroscopic dielectric function.

$$\epsilon_M = \lim_{q\to 0} \frac{1}{\epsilon^{-1}_{0,0}(\mathbf{q})} \tag{E.7}$$

E.2 Absorption spectra

Follows Jackson Ch. 7 [230]. A polarized plane wave electromagnetic field has the general form

$$\tilde{E}(z,t) = \hat{n}\,\tilde{E}_0 e^{i\tilde{k}z - i\omega t} \tag{E.8}$$

This gives the wave vector to be

$$\tilde{k} = \omega\sqrt{\mu\tilde{\epsilon}} = \frac{\omega}{c}\sqrt{\frac{\mu\tilde{\epsilon}}{\mu_0\epsilon_0}} \simeq \frac{\omega}{c}\sqrt{\tilde{\epsilon}_r} \tag{E.9}$$

where $\mu \simeq \mu_0$, and $\tilde{\epsilon}_r \equiv \tilde{\epsilon}/\epsilon_0$. Within a medium the dielectric constant $\tilde{\epsilon}_r$ can take a complex form and therefore so will $\tilde{k}$.

$$\tilde{k} = \beta + i\,\frac{\alpha}{2} \tag{E.10}$$

Plugging this into Eq. E.8, we see that α is responsible for the attenuation of the wave within the medium.

$$\tilde{E}(z,t) = \hat{n}\,\tilde{E}_0 e^{-\alpha z/2} e^{i\beta z - i\omega t} \tag{E.11}$$

The intensity of the beam is proportional to the square of the electric field and so we see the intensity dies exponentially with α as it travels a distance z in the medium.

$$I(z) \propto e^{-\alpha z} \tag{E.12}$$

For this reason α is known as the absorption coefficient and is responsible for the energy transfer of light to the medium due to the medium's dielectric response ϵ_r.

A direct relation between α and $\tilde{\epsilon}_r$ can be obtained with some algebra:

$$\tilde{k} = \beta + i\,\frac{\alpha}{2} = \frac{\omega}{c}\sqrt{\tilde{\epsilon_r}} \tag{E.13}$$

$$\Rightarrow \tilde{k}^2 = \beta^2 - \frac{\alpha^2}{4} + i\,\beta\alpha = \frac{\omega^2}{c^2}\tilde{\epsilon_r} \tag{E.14}$$

Relating real and imaginary parts and taking $\tilde{\epsilon}_r = \epsilon_1 + i\,\epsilon_2$, we have:

$$\beta^2 - \frac{\alpha^2}{4} = \frac{\omega^2}{c^2}\epsilon_1 \tag{E.15}$$

$$\beta\alpha = \frac{\omega^2}{c^2}\epsilon_2 \tag{E.16}$$

Multiplying by β^2 and inserting where appropriate we have

$$\beta^4 - \left(\frac{\omega^2}{c^2}\epsilon_1\right)\beta^2 - \left(\frac{\omega^4}{c^4}\epsilon_2^2\right) = 0 \tag{E.17}$$

This is a biquadratic function whose solutions resemble that of the quadratic function. In this case our solutions are given by ($\beta > 0$ and $\beta \in \mathbb{R}$):

$$\beta = \sqrt{\frac{\frac{\omega^2}{c^2}\epsilon_1 + \sqrt{\frac{\omega^4}{c^4}\epsilon_1^2 + \frac{\omega^4}{c^4}\epsilon_2^2}}{2}} \tag{E.18}$$

$$\beta = \frac{\omega}{c}\sqrt{\frac{\epsilon_1 + \sqrt{\epsilon_1^2 + \epsilon_2^2}}{2}} \tag{E.19}$$

Finally, the absorption coefficient (up to $\mu \simeq \mu_0$):

$$\alpha(\omega) = \frac{\omega}{c}\frac{\epsilon_2(\omega)}{\sqrt{\frac{\epsilon_1(\omega) + \sqrt{\epsilon_1^2(\omega) + \epsilon_2^2(\omega)}}{2}}} \tag{E.20}$$

Unless the absorption is very strong, we have $\epsilon_1 \gg \epsilon_2$ and can write the absorption coefficient in the simple form:

$$\alpha(\omega) \simeq \frac{\omega}{c}\frac{\epsilon_2(\omega)}{\sqrt{\epsilon_1(\omega)}} \tag{E.21}$$

E.3 Additional forms of the absorption coefficient

$$\begin{aligned}
\alpha(\omega) &= \frac{2\omega}{c}k(\omega) && \text{(E.22)}\\
&= \frac{2\omega}{c}\mathrm{Im}\left(\sqrt{\epsilon(\omega)}\right) && \text{(E.23)}\\
&= \frac{2\omega}{c}\mathrm{Im}\left(\sqrt{\epsilon_1(\omega)+\epsilon_2(\omega)}\right) && \text{(E.24)}\\
&= \frac{\omega}{c}\sqrt{2(|\epsilon(\omega)|-\epsilon_1(\omega))} && \text{(E.25)}\\
&= \frac{\omega}{c}\sqrt{2(|\epsilon(\omega)|-\epsilon_1(\omega))}\frac{\sqrt{|\epsilon(\omega)|+\epsilon_1(\omega)}}{\sqrt{|\epsilon(\omega)|+\epsilon_1(\omega)}} && \text{(E.26)}\\
&= \frac{\omega}{c}\frac{\sqrt{2(|\epsilon(\omega)|^2-\epsilon_1(\omega)^2)}}{\sqrt{|\epsilon(\omega)|+\epsilon_1(\omega)}} && \text{(E.27)}\\
&= \frac{\omega}{c}\frac{\sqrt{(\epsilon_1(\omega)^2+\epsilon_2(\omega)^2)-\epsilon_1(\omega)^2}}{\sqrt{\frac{|\epsilon(\omega)|+\epsilon_1(\omega)}{2}}} && \text{(E.28)}\\
&= \frac{\omega}{c}\frac{\epsilon_2(\omega)}{\sqrt{\frac{|\epsilon(\omega)|+\epsilon_1(\omega)}{2}}} && \text{(E.29)}\\
&= \frac{\omega}{c}\frac{\epsilon_2(\omega)}{\sqrt{\frac{\epsilon_1(\omega)+\sqrt{\epsilon_1(\omega)^2+\epsilon_2(\omega)^2}}{2}}} && \text{(E.30)}
\end{aligned}$$

Appendix F

Why we may average IP & EA

From Janak's Theorem the IP and EA of a system are defined in terms of the derivative of the total energy of the system:

$$\mathrm{EA}(q) = -\left.\frac{\partial E}{\partial n}\right|_{n=q^+} \tag{F.1}$$

$$\mathrm{IP}(q+1) = -\left.\frac{\partial E}{\partial n}\right|_{n=(q+1)^-} \tag{F.2}$$

Within the framework of DFT (with local and semi-local functionals), energy is a continuous and smooth functional of the number of electrons in the system $E[n]$. As shown in Figure 1, this leads to inconsistency between the eigenvalues of the q and $q+1$ system (resulting in $\mathrm{IP}(q+1) \neq \mathrm{EA}(q)$). In particular, both the IP and EA will be incorrect at local and semi-local levels of theory. We can however, approximate the true eigenvalue between the q and $q+1$ state by averaging the value of the DFT eigenvalue over the range q to $q+1$. In practice this would require having an analytic form of the value of the eigenvalue in terms of electron number. While this is certainly doable, we can obtain a fast approximation easily by first assuming the total energy as quadratic in electron number (*this is the*

second order approximation we make):

$$E[n] = E_0 + E_1 n + E_2 n^2 \tag{F.3}$$

From Janak's theorem we can then obtain $\varepsilon[n]$:

$$\varepsilon[n] = E_1 + 2E_2 n \tag{F.4}$$

We can then simply compute the average of $\varepsilon[n]$ over the range q to $q+1$ (denoted as $\varepsilon_{q|q+1}$):

$$\varepsilon_{q|q+1} = \frac{1}{(q+1)-q} \int_q^{q+1} \varepsilon[n]\, dn = E_1 + 2E_2(q + 1/2) \tag{F.5}$$

Since $\varepsilon[n]$ is linear this is identical to the average of $\varepsilon[n]$ at the points q and $q+1$:

$$\varepsilon_{q|q+1} = \frac{1}{2} \left(\varepsilon[q+1] + \varepsilon[q]\right) = E_1 + 2E_2(q + 1/2) \tag{F.6}$$

Therefore from Eq. F.6 and Eq. F.1-F.2 we have:

$$\varepsilon_{q|q+1} = \frac{1}{2} \left(\mathrm{EA}(q) + \mathrm{IP}(q+1)\right) \tag{F.7}$$

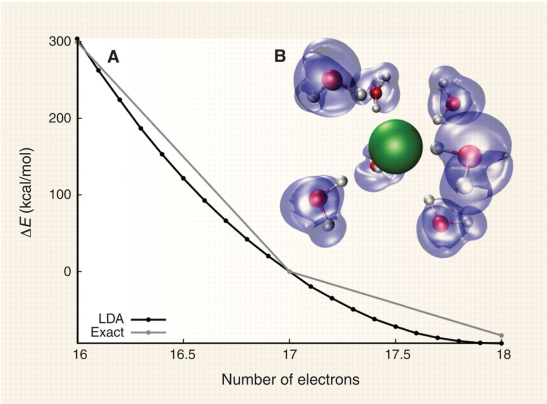

Figure F.1: Delocalization error in LDA, taken from Ref. [424].

Bibliography

[1] "U.S. Energy Information Administration." https://www.eia.gov/totalenergy/.

[2] "U.S. Renewable Energy Factsheet." http://css.umich.edu/factsheets/us-renewable-energy-factsheet.

[3] C. C. McCrory, S. Jung, I. M. Ferrer, S. M. Chatman, J. C. Peters, and T. F. Jaramillo, "Benchmarking Hydrogen Evolving Reaction and Oxygen Evolving Reaction Electrocatalysts for Solar Water Splitting Devices," *Journal of the American Chemical Society*, vol. 137, no. 13, pp. 4347–4357, 2015.

[4] L.-F. Huang, J. R. Scully, and J. M. Rondinelli, "Modeling Corrosion with First-Principles Electrochemical Phase Diagrams," *Annual Review of Materials Research*, vol. 49, 2019.

[5] A. Wang, S. Kadam, H. Li, S. Shi, and Y. Qi, "Review on Modeling of the Anode Solid Electrolyte Interphase (SEI) for Lithium-Ion Batteries," *npj Computational Materials*, vol. 4, no. 1, p. 15, 2018.

[6] "Quantum information science." https://www.energy.gov/science/initiatives/quantum-information-science.

[7] P. Hohenberg and W. Kohn, "Inhomogeneous electron gas," *Physical review*, vol. 136, no. 3B, p. B864, 1964.

[8] R. M. Martin, *Electronic structure: basic theory and practical methods*. Cambridge university press, 2020.

[9] W. Kohn and L. J. Sham, "Self-consistent equations including exchange and correlation effects," *Physical review*, vol. 140, no. 4A, p. A1133, 1965.

[10] J. P. Perdew, K. Burke, and M. Ernzerhof, "Generalized gradient approximation made simple," *Physical review letters*, vol. 77, no. 18, p. 3865, 1996.

[11] S. Dudarev, G. Botton, S. Savrasov, C. Humphreys, and A. Sutton, "Electron-energy-loss spectra and the structural stability of nickel oxide: An lsda+u study," *Physical Review B*, vol. 57, no. 3, p. 1505, 1998.

[12] T. J. Smart and Y. Ping, "Effect of defects on the small polaron formation and transport properties of hematite from first-principles calculations," *Journal of Physics: Condensed Matter*, vol. 29, no. 39, p. 394006, 2017.

[13] J. Kang and L.-W. Wang, "High defect tolerance in lead halide perovskite cspbbr3," *The journal of physical chemistry letters*, vol. 8, no. 2, pp. 489–493, 2017.

[14] S. Li, Z. Shi, F. Zhang, L. Wang, Z. Ma, D. Yang, Z. Yao, D. Wu, T.-T. Xu, Y. Tian, *et al.*, "Sodium doping-enhanced emission efficiency and stability of cspbbr3 nanocrystals for white light-emitting devices," *Chemistry of Materials*, vol. 31, no. 11, pp. 3917–3928, 2019.

[15] R. Sundararaman, K. Letchworth-Weaver, K. A. Schwarz, D. Gunceler, Y. Ozhabes, and T. Arias, "JDFTx: software for joint density-functional theory," *SoftwareX*, vol. 6, pp. 278 – 284, 2017.

[16] F. Wu, A. Galatas, R. Sundararaman, D. Rocca, and Y. Ping, "First-principles engineering of charged defects for two-dimensional quantum technologies," *Physical Review Materials*, vol. 1, no. 7, p. 071001, 2017.

[17] Y. Ping, D. Rocca, and G. Galli, "Optical properties of tungsten trioxide from first-principles calculations," *Physical Review B*, vol. 87, p. 165203, Apr 2013.

[18] H. Seo, Y. Ping, and G. Galli, "Role of point defects in enhancing the conductivity of $BiVO_4$," *Chemistry of Materials*, vol. 30, no. 21, pp. 7793–7802, 2018.

[19] C. Freysoldt, B. Grabowski, T. Hickel, J. Neugebauer, G. Kresse, A. Janotti, and C. G. Van de Walle, "First-principles calculations for point defects in solids," *Reviews of Modern Physics*, vol. 86, no. 1, p. 253, 2014.

[20] J. Lee and S. Han, "Thermodynamics of native point defects in α-Fe_2O_3: an ab initio study," *Physical Chemistry Chemical Physics*, vol. 15, no. 43, pp. 18906–18914, 2013.

[21] F. Wu, D. Rocca, and Y. Ping, "Dimensionality and anisotropicity dependence of radiative recombination in nanostructured phosphorene," *Journal of Materials Chemistry C*, vol. 7, no. 41, pp. 12891–12897, 2019.

[22] S. Gupta, J.-H. Yang, and B. I. Yakobson, "Two-level quantum systems in two-dimensional materials for single photon emission," *Nano Lett.*, vol. 19, no. 1, pp. 408–414, 2018.

[23] M. Mackoit-Sinkevičienė, M. Maciaszek, C. G. Van de Walle, and A. Alkauskas, "Carbon dimer defect as a source of the 4.1 ev luminescence in hexagonal boron nitride," *Appl. Phys. Lett.*, vol. 115, no. 21, p. 212101, 2019.

[24] G. Thiering and A. Gali, "Ab initio calculation of spin-orbit coupling for an nv center in diamond exhibiting dynamic jahn-teller effect," *Phys. Rev. B*, vol. 96, no. 8, p. 081115, 2017.

[25] J. R. Maze, A. Gali, E. Togan, Y. Chu, A. Trifonov, E. Kaxiras, and M. D. Lukin, "Properties of nitrogen-vacancy centers in diamond: the group theoretic approach," *New J. Phys.*, vol. 13, no. 2, p. 025025, 2011.

[26] F. Neese, "The orca program system," *WIREs Comput. Mol. Sci.*, vol. 2, no. 1, pp. 73–78, 2012.

[27] B. de Souza, G. Farias, F. Neese, and R. Izsák, "Predicting phosphorescence rates of light organic molecules using time-dependent density functional theory and the path integral approach to dynamics," *J. Chem. Theory Comput.*, vol. 15, no. 3, pp. 1896–1904, 2019.

[28] T. Yao, X. An, H. Han, J. Q. Chen, and C. Li, "Photoelectrocatalytic materials for solar water splitting," *Advanced Energy Materials*, vol. 8, no. 21, p. 1800210, 2018.

[29] Y. Tachibana, L. Vayssieres, and J. R. Durrant, "Artificial photosynthesis for solar water-splitting," *Nature Photonics*, vol. 6, no. 8, p. 511, 2012.

[30] M. G. Walter, E. L. Warren, J. R. McKone, S. W. Boettcher, Q. Mi, E. A. Santori, and N. S. Lewis, "Solar water splitting cells," *Chemical reviews*, vol. 110, no. 11, pp. 6446–6473, 2010.

[31] J. H. Kim and J. S. Lee, "Elaborately modified bivo4 photoanodes for solar water splitting," *Advanced Materials*, vol. 31, no. 20, p. 1806938, 2019.

[32] A. G. Tamirat, J. Rick, A. A. Dubale, W.-N. Su, and B.-J. Hwang, "Using hematite for photoelectrochemical water splitting: a review of current progress and challenges," *Nanoscale Horizons*, vol. 1, no. 4, pp. 243–267, 2016.

[33] D. K. Lee, D. Lee, M. A. Lumley, and K.-S. Choi, "Progress on ternary oxide-based photoanodes for use in photoelectrochemical cells for solar water splitting," *Chemical Society Reviews*, vol. 48, no. 7, pp. 2126–2157, 2019.

[34] A. Bosman and H. Van Daal, "Small-polaron versus band conduction in some transition-metal oxides," *Advances in Physics*, vol. 19, no. 77, pp. 1–117, 1970.

[35] T. J. Smart, A. C. Cardiel, F. Wu, K.-S. Choi, and Y. Ping, "Mechanistic insights of enhanced spin polaron conduction in cuo through atomic doping," *npj Computational Materials*, vol. 4, no. 1, pp. 1–8, 2018.

[36] T. J. Smart, T. A. Pham, Y. Ping, and T. Ogitsu, "Optical absorption induced by small polaron formation in transition metal oxides: The case of co 3 o 4," *Physical Review Materials*, vol. 3, no. 10, p. 102401, 2019.

[37] G. P. Wheeler, V. U. Baltazar, T. J. Smart, A. Radmilovic, Y. Ping, and K.-S. Choi, "Combined theoretical and experimental investigations of atomic doping to enhance photon absorption and carrier transport of lafeo3 photocathodes," *Chemistry of Materials*, vol. 31, no. 15, pp. 5890–5899, 2019.

[38] A. Radmilovic, T. J. Smart, Y. Ping, and K.-S. Choi, "Combined experimental and theoretical investigations of n-type bifeo3 for use as a photoanode in a photoelectrochemical cell," *Chemistry of Materials*, vol. 32, no. 7, pp. 3262–3270, 2020.

[39] B. Lu, T. J. Smart, D. Qin, J. E. Lu, N. Wang, L. Chen, Y. Peng, Y. Ping, and S. Chen, "Nitrogen and iron-codoped carbon hollow nanotubules as high-performance catalysts toward oxygen reduction reaction: a combined experimental and theoretical study," *Chemistry of Materials*, vol. 29, no. 13, pp. 5617–5628, 2017.

[40] T. Kou, T. Smart, B. Yao, I. Chen, D. Thota, Y. Ping, and Y. Li, "Theoretical and experimental insight into the effect of nitrogen doping on hydrogen evolution activity of ni3s2 in alkaline medium," *Advanced Energy Materials*, vol. 8, no. 19, p. 1703538, 2018.

[41] T. Kou, M. Chen, F. Wu, T. J. Smart, S. Wang, Y. Wu, Y. Zhang, S. Li, S. Lall, Z. Zhang, *et al.*, "Carbon doping switching on the hydrogen adsorption activity of nio for hydrogen evolution reaction," *Nature communications*, vol. 11, no. 1, pp. 1–10, 2020.

[42] B. Lu, L. Guo, F. Wu, Y. Peng, J. E. Lu, T. J. Smart, N. Wang, Y. Z. Finfrock, D. Morris, P. Zhang, *et al.*, "Ruthenium atomically dispersed in carbon outperforms platinum toward hydrogen evolution in alkaline media," *Nature communications*, vol. 10, no. 1, pp. 1–11, 2019.

[43] B. D. Alexander, P. J. Kulesza, I. Rutkowska, R. Solarska, and J. Augustynski, "Metal oxide photoanodes for solar hydrogen production," *Journal of Materials Chemistry*, vol. 18, no. 20, pp. 2298–2303, 2008.

[44] K. Sivula, F. Le Formal, and M. Grätzel, "Solar water splitting: progress using hematite (α-Fe_2O_3) photoelectrodes," *ChemSusChem*, vol. 4, no. 4, pp. 432–449, 2011.

[45] J. A. Glasscock, P. R. Barnes, I. C. Plumb, and N. Savvides, "Enhancement of photoelectrochemical hydrogen production from hematite thin films by the introduction of ti and si," *The Journal of Physical Chemistry C*, vol. 111, no. 44, pp. 16477–16488, 2007.

[46] M. Forster, R. J. Potter, Y. Ling, Y. Yang, D. R. Klug, Y. Li, and A. J. Cowan, "Oxygen deficient α-fe 2 o 3 photoelectrodes: A balance between enhanced electrical properties and trap-mediated losses," *Chemical science*, vol. 6, no. 7, pp. 4009–4016, 2015.

[47] Y. Ling, G. Wang, D. A. Wheeler, J. Z. Zhang, and Y. Li, "Sn-doped hematite nanostructures for photoelectrochemical water splitting," *Nano Letters*, vol. 11, no. 5, pp. 2119–2125, 2011.

[48] G. Wang, Y. Ling, D. A. Wheeler, K. E. George, K. Horsley, C. Heske, J. Z. Zhang, and Y. Li, "Facile synthesis of highly photoactive α-fe2o3-based films for water oxidation," *Nano letters*, vol. 11, no. 8, pp. 3503–3509, 2011.

[49] T. W. Kim, Y. Ping, G. A. Galli, and K.-S. Choi, "Simultaneous enhancements in photon absorption and charge transport of bismuth vanadate photoanodes for solar water splitting," *Nature Communications*, vol. 6, p. 8769, 2015.

[50] Z. Zhou, P. Huo, L. Guo, and O. V. Prezhdo, "Understanding hematite doping with group iv elements: a dft+ u study," *The Journal of Physical Chemistry C*, vol. 119, no. 47, pp. 26303–26310, 2015.

[51] P. Liao, M. C. Toroker, and E. A. Carter, "Electron transport in pure and doped hematite," *Nano Letters*, vol. 11, no. 4, pp. 1775–1781, 2011.

[52] P. Giannozzi, S. Baroni, N. Bonini, M. Calandra, R. Car, C. Cavazzoni, D. Ceresoli, G. L. Chiarotti, M. Cococcioni, I. Dabo, A. Dal Corso, S. de Gironcoli, S. Fabris, G. Fratesi, R. Gebauer, U. Gerstmann, C. Gougoussis, A. Kokalj, M. Lazzeri, L. Martin-Samos, N. Marzari, F. Mauri, R. Mazzarello, S. Paolini, A. Pasquarello, L. Paulatto, C. Sbraccia, S. Scandolo, G. Sclauzero, A. P. Seitsonen, A. Smogunov, P. Umari, and R. M. Wentzcovitch, "QUANTUM ESPRESSO: A Modular and Open-Source Software Project for Quantum Simulations of Materials.," *Journal of Physics: Condensed Matter*, vol. 21, p. 395502, sep 2009.

[53] K. F. Garrity, J. W. Bennett, K. M. Rabe, and D. Vanderbilt, "Pseudopotentials for high-throughput dft calculations," *Computational Materials Science*, vol. 81, pp. 446–452, 2014.

[54] D. R. Hamann, "Optimized Norm-Conserving Vanderbilt Pseudopotentials," *Physical Review B*, vol. 88, p. 085117, aug 2013.

[55] M. Schlipf and F. Gygi, "Optimization Algorithm for the Generation of ONCV Pseudopotentials," *Computer Physics Communications*, vol. 196, pp. 36–44, 2015.

[56] M. Methfessel and A. Paxton, "High-precision sampling for brillouin-zone integration in metals," *Physical Review B*, vol. 40, no. 6, p. 3616, 1989.

[57] L. Pauling and S. B. Hendricks, "The crystal structures of hematite and corundum," *Journal of the American Chemical Society*, vol. 47, no. 3, pp. 781–790, 1925.

[58] L. W. Finger and R. M. Hazen, "Crystal structure and isothermal compression of fe2o3, cr2o3, and v2o3 to 50 kbars," *Journal of Applied Physics*, vol. 51, no. 10, pp. 5362–5367, 1980.

[59] N. Adelstein, J. B. Neaton, M. Asta, and L. C. De Jonghe, "Density functional theory based calculation of small-polaron mobility in hematite," *Physical Review B*, vol. 89, no. 24, p. 245115, 2014.

[60] J. Coey and G. Sawatzky, "A study of hyperfine interactions in the system (fe1-xrhx) 2o3 using the mossbauer effect (bonding parameters)," *Journal of Physics C: Solid State Physics*, vol. 4, no. 15, p. 2386, 1971.

[61] B. Gilbert, C. Frandsen, E. R. Maxey, and D. M. Sherman, "Band-gap measurements of bulk and nanoscale hematite by soft x-ray spectroscopy," *Physical Review B*, vol. 79, p. 035108, Jan 2009.

[62] G. Dräger, W. Czolbe, and J. Leiro, "High-energy-spectroscopy studies of a charge-transfer insulator: X-ray spectra of α-fe 2 o 3," *Physical Review B*, vol. 45, no. 15, p. 8283, 1992.

[63] M. Catti, G. Valerio, and R. Dovesi, "Theoretical study of electronic, magnetic, and structural properties of α-fe 2 o 3 (hematite)," *Physical Review B*, vol. 51, no. 12, p. 7441, 1995.

[64] C. E. Cava, L. S. Roman, and C. Persson, "Effects of native defects on the structural and magnetic properties of hematite α-fe 2 o 3," *Physical Review B*, vol. 88, no. 4, p. 045136, 2013.

[65] N. J. Mosey, P. Liao, and E. A. Carter, "Rotationally invariant ab initio evaluation of coulomb and exchange parameters for dft+ u calculations," *The Journal of Chemical Physics*, vol. 129, no. 1, p. 014103, 2008.

[66] G. Rollmann, A. Rohrbach, P. Entel, and J. Hafner, "First-principles calculation of the structure and magnetic phases of hematite," *Physical Review B*, vol. 69, p. 165107, Apr 2004.

[67] I. Austin and N. F. Mott, "Polarons in crystalline and non-crystalline materials," *Advances in physics*, vol. 18, no. 71, pp. 41–102, 1969.

[68] R. Eglitis, "Ab initio calculations of srtio 3, batio 3, pbtio 3, catio 3, srzro 3, pbzro 3 and bazro 3 (001),(011) and (111) surfaces as well as f centers, polarons, ktn solid solutions and nb impurities therein," *International Journal of Modern Physics B*, vol. 28, no. 17, p. 1430009, 2014.

[69] R. Sundararaman and Y. Ping, "First-principles electrostatic potentials for reliable alignment at interfaces and defects," *The Journal of Chemical Physics*, vol. 146, no. 10, p. 104109, 2017.

[70] Y. Kumagai and F. Oba, "Electrostatics-based finite-size corrections for first-principles point defect calculations," *Physical Review B*, vol. 89, p. 195205, May 2014.

[71] A. Janotti, J. B. Varley, M. Choi, and C. G. Van de Walle, "Vacancies and small polarons in srtio 3," *Physical Review B*, vol. 90, no. 8, p. 085202, 2014.

[72] S. A. Ansari, M. M. Khan, M. O. Ansari, and M. H. Cho, "Nitrogen-doped titanium dioxide (n-doped tio 2) for visible light photocatalysis," *New Journal of Chemistry*, vol. 40, no. 4, pp. 3000–3009, 2016.

[73] K. M. Rosso, D. M. Smith, and M. Dupuis, "An ab initio model of electron transport in hematite (α-fe 2 o 3) basal planes," *The Journal of Chemical Physics*, vol. 118, no. 14, pp. 6455–6466, 2003.

[74] A. Einstein, *Investigations on the Theory of the Brownian Movement*. Courier Corporation, 1956.

[75] Z. Zhang, I. Karimata, H. Nagashima, S. Muto, K. Ohara, K. Sugimoto, and T. Tachikawa, "Interfacial oxygen vacancies yielding long-lived holes in hematite mesocrystal-based photoanodes," *Nature communications*, vol. 10, no. 1, pp. 1–12, 2019.

[76] Y. Yang, S. Niu, D. Han, T. Liu, G. Wang, and Y. Li, "Progress in developing metal oxide nanomaterials for photoelectrochemical water splitting," *Advanced Energy Materials*, vol. 7, no. 19, p. 1700555, 2017.

[77] R. Dieckmann, "Point defects and transport in haematite (Fe_2O_3-ε)," *Philosophical Magazine A*, vol. 68, no. 4, pp. 725–745, 1993.

[78] L. M. Carneiro, S. K. Cushing, C. Liu, Y. Su, P. Yang, A. P. Alivisatos, and S. R. Leone, "Excitation-wavelength-dependent small polaron trapping of photoexcited carriers in α-Fe_2O_3," *Nature Materials*, vol. 16, no. 8, p. 819, 2017.

[79] C. Lohaus, A. Klein, and W. Jaegermann, "Limitation of fermi level shifts by polaron defect states in hematite photoelectrodes," *Nature Communications*, vol. 9, p. 4309, 2018.

[80] Y. Ling, G. Wang, J. Reddy, C. Wang, J. Z. Zhang, and Y. Li, "The influence of oxygen content on the thermal activation of hematite nanowires," *Angewandte Chemie*, vol. 124, no. 17, pp. 4150–4155, 2012.

[81] M. Rioult, H. Magnan, D. Stanescu, and A. Barbier, "Single crystalline hematite films for solar water splitting: Ti-doping and thickness effects," *The Journal of Physical Chemistry C*, vol. 118, no. 6, pp. 3007–3014, 2014.

[82] K. D. Malviya, D. Klotz, H. Dotan, D. Shlenkevich, A. Tsyganok, H. Mor, and A. Rothschild, "Influence of ti doping levels on the photoelectrochemical properties of thin-film hematite (α-Fe_2O_3) photoanodes," *The Journal of Physical Chemistry C*, vol. 121, no. 8, pp. 4206–4213, 2017.

[83] N. T. Hahn and C. B. Mullins, "Photoelectrochemical performance of nanostructured ti-and sn-doped α-Fe_2O_3 photoanodes," *Chemistry of Materials*, vol. 22, no. 23, pp. 6474–6482, 2010.

[84] O. Zandi, B. M. Klahr, and T. W. Hamann, "Highly photoactive ti-doped α-Fe_2O_3 thin film electrodes: resurrection of the dead layer," *Energy & Environmental Science*, vol. 6, no. 2, pp. 634–642, 2013.

[85] J. Liu, Y. Cai, Z. Tian, G. Ruan, Y. Ye, C. Liang, and G. Shao, "Highly oriented ge-doped hematite nanosheet arrays for photoelectrochemical water oxidation," *Nano Energy*, vol. 9, pp. 282–290, 2014.

[86] A. Annamalai, R. Sandström, E. Gracia-Espino, N. Boulanger, J.-F. Boily, I. Mühlbacher, A. Shchukarev, and T. Wågberg, "Influence of sb5+ as a double donor on hematite (fe3+) photoanodes for surface-enhanced photoelectrochemical water oxidation," *ACS applied materials & interfaces*, vol. 10, no. 19, pp. 16467–16473, 2018.

[87] C. Sanchez, K. Sieber, and G. Somorjai, "The photoelectrochemistry of niobium doped α-fe2o3," *Journal of electroanalytical chemistry and interfacial electrochemistry*, vol. 252, no. 2, pp. 269–290, 1988.

[88] M. Li, Y. Yang, Y. Ling, W. Qiu, F. Wang, T. Liu, Y. Song, X. Liu, P. Fang, Y. Tong, *et al.*, "Morphology and doping engineering of sn-doped hematite nanowire photoanodes," *Nano Letters*, vol. 17, no. 4, pp. 2490–2495, 2017.

[89] C. Tian, W. Li, Y. Lin, Z. Yang, L. Wang, Y. Du, H. Xiao, L. Qiao, J.-Y. Zhang, L. Chen, *et al.*, "Electronic structure, optical properties and

photoelectrochemical activity of sn doped Fe_2O_3 thin films," *The Journal of Physical Chemistry C*, vol. 124, no. 23, pp. 12548–12558, 2020.

[90] Y. Yang, M. Forster, Y. Ling, G. Wang, T. Zhai, Y. Tong, A. J. Cowan, and Y. Li, "Acid treatment enables suppression of electron–hole recombination in hematite for photoelectrochemical water splitting," *Angewandte Chemie*, vol. 128, no. 10, pp. 3464–3468, 2016.

[91] Z. Fu, T. Jiang, Z. Liu, D. Wang, L. Wang, and T. Xie, "Highly photoactive ti-doped α-Fe_2O_3 nanorod arrays photoanode prepared by a hydrothermal method for photoelectrochemical water splitting," *Electrochimica Acta*, vol. 129, pp. 358–363, 2014.

[92] Y. Ye, Q. Wang, J. Lu, C. Liu, and Y. Yang, "The generalized thermodynamic rule for phase selection in multicomponent alloys," *Intermetallics*, vol. 59, pp. 75–80, 2015.

[93] Y. Ye, Q. Wang, J. Lu, C. Liu, and Y. Yang, "High-entropy alloy: challenges and prospects," *Materials Today*, vol. 19, no. 6, pp. 349–362, 2016.

[94] T. J. Smart, V. Urena Baltazar, M. Chen, B. Yao, K. Mayford, F. Bridges, Y. Li, and Y. Ping, "Doping bottleneck in hematite: multipole clustering by small polarons," *Chemistry of Materials*, vol. In Press, 2021.

[95] P. Biswas, A. Ainabayev, A. Zhussupbekova, F. Jose, R. O'Connor, A. Kaisha, B. Walls, and I. V. Shvets, "Tuning of oxygen vacancy-induced electrical conductivity in ti-doped hematite films and its impact on photoelectrochemical water splitting," *Scientific Reports*, vol. 10, no. 1, pp. 1–9, 2020.

[96] P. Kumar, P. Sharma, R. Shrivastav, S. Dass, and V. R. Satsangi, "Electrodeposited zirconium-doped α-Fe_2O_3 thin film for photoelectrochemical water splitting," *International Journal of Hydrogen Energy*, vol. 36, no. 4, pp. 2777–2784, 2011.

[97] T.-Y. Yang, H.-Y. Kang, U. Sim, Y.-J. Lee, J.-H. Lee, B. Koo, K. T. Nam, and Y.-C. Joo, "A new hematite photoanode doping strategy for solar water splitting: oxygen vacancy generation," *Physical Chemistry Chemical Physics*, vol. 15, no. 6, pp. 2117–2124, 2013.

[98] J. Liu, C. Liang, G. Xu, Z. Tian, G. Shao, and L. Zhang, "Ge-doped hematite nanosheets with tunable doping level, structure and improved photoelectrochemical performance," *Nano Energy*, vol. 2, no. 3, pp. 328–336, 2013.

[99] A. Walsh and A. Zunger, "Instilling defect tolerance in new compounds," *Nature Materials*, vol. 16, no. 10, pp. 964–967, 2017.

[100] K. Bindu, K. Ajith, and H. Nagaraja, "Electrical, dielectric and magnetic properties of sn-doped hematite (α-snxfe2-xo3) nanoplates synthesized by microwave-assisted method," *Journal of Alloys and Compounds*, vol. 735, pp. 847–854, 2018.

[101] Z. Zhou, R. Long, and O. V. Prezhdo, "Why silicon doping accelerates electron polaron diffusion in hematite," *Journal of the American Chemical Society*, vol. 141, no. 51, pp. 20222–20233, 2019.

[102] S. Onari, T. Arai, and K. Kudo, "Infrared lattice vibrations and dielectric dispersion in α- Fe_2O_3," *Physical Review B*, vol. 16, no. 4, p. 1717, 1977.

[103] H. S. Nabi, R. J. Harrison, and R. Pentcheva, "Magnetic coupling parameters at an oxide-oxide interface from first principles: Fe_2O_3-$FeTiO_3$," *Physical Review B*, vol. 81, no. 21, p. 214432, 2010.

[104] W. Bao, W. Zhang, H. Li, S. Zheng, and Q. Zhai, "A first-principles study of titanium oxide clusters formation and evolution in a steel matrix," *RSC Advances*, vol. 7, no. 82, pp. 52296–52303, 2017.

[105] C. Mackeen, F. Bridges, L. Kovács, and J. Castillo-Torres, "Substitution of er, in, and hf in linbo 3: Evidence for multiple defect distributions about dopant sites," *Physical Review Materials*, vol. 2, no. 9, p. 093602, 2018.

[106] F. Wu and Y. Ping, "Combining landau–zener theory and kinetic monte carlo sampling for small polaron mobility of doped $BiVO_4$ from first-principles," *Journal of Materials Chemistry A*, vol. 6, no. 41, pp. 20025–20036, 2018.

[107] W. Zhang, F. Wu, J. Li, D. Yan, J. Tao, Y. Ping, and M. Liu, "Unconventional relation between charge transport and photocurrent via boosting small polaron hopping for photoelectrochemical water splitting," *ACS Energy Letters*, vol. 3, no. 9, pp. 2232–2239, 2018.

[108] R. D. Shannon, "Revised effective ionic radii and systematic studies of interatomic distances in halides and chalcogenides," *Acta Crystallographica A*, vol. 32, no. 5, pp. 751–767, 1976.

[109] M. Zhang, W. Luo, Z. Li, T. Yu, and Z. Zou, "Improved photoelectrochemical responses of si and ti codoped α-Fe_2O_3 photoanode films," *Applied Physics Letters*, vol. 97, no. 4, p. 042105, 2010.

[110] N. Mirbagheri, D. Wang, C. Peng, J. Wang, Q. Huang, C. Fan, and E. E. Ferapontova, "Visible light driven photoelectrochemical water oxidation by zn-and ti-doped hematite nanostructures," *ACS Catalysis*, vol. 4, no. 6, pp. 2006–2015, 2014.

[111] H. Pan, X. Meng, D. Liu, S. Li, and G. Qin, "(ti/zr, n) codoped hematite for enhancing the photoelectrochemical activity of water splitting," *Physical Chemistry Chemical Physics*, vol. 17, no. 34, pp. 22179–22186, 2015.

[112] J. Cai, H. Chen, C. Liu, S. Yin, H. Li, L. Xu, H. Liu, and Q. Xie, "Engineered sn-and mg-doped hematite photoanodes for efficient photoelectrochemical water oxidation," *Dalton Transactions*, vol. 49, no. 32, pp. 11282–11289, 2020.

[113] C. Zhou, Z. Sanders-Bellis, T. J. Smart, W. Zhang, L. Zhang, Y. Ping, and M. Liu, "Interstitial lithium doping in bivo4 thin film photoanode for enhanced solar water splitting activity," *Chemistry of Materials*, vol. 32, no. 15, pp. 6401–6409, 2020.

[114] Y. J. Jang, J.-W. Jang, S. H. Choi, J. Y. Kim, J. H. Kim, D. H. Youn, W. Y. Kim, S. Han, and J. S. Lee, "Tree branch-shaped cupric oxide for highly effective photoelectrochemical water reduction," *Nanoscale*, vol. 7, no. 17, pp. 7624–7631, 2015.

[115] F. Koffyberg and F. Benko, "A photoelectrochemical determination of the position of the conduction and valence band edges of p-type cuo," *Journal of Applied Physics*, vol. 53, no. 2, pp. 1173–1177, 1982.

[116] C.-Y. Chiang, Y. Shin, K. Aroh, and S. Ehrman, "Copper oxide photocathodes prepared by a solution based process," *international journal of hydrogen energy*, vol. 37, no. 10, pp. 8232–8239, 2012.

[117] M. Izaki, M. Nagai, K. Maeda, F. B. Mohamad, K. Motomura, J. Sasano, T. Shinagawa, and S. Watase, "Electrodeposition of 1.4-ev-bandgap p-copper (ii) oxide film with excellent photoactivity," *Journal of The Electrochemical Society*, vol. 158, no. 9, p. D578, 2011.

[118] J. S. Sagu, T. N. Peiris, and K. U. Wijayantha, "Rapid and simple potentiostatic deposition of copper (ii) oxide thin films," *Electrochemistry Communications*, vol. 42, pp. 68–71, 2014.

[119] S. Masudy-Panah, R. Siavash Moakhar, C. S. Chua, H. R. Tan, T. I. Wong, D. Chi, and G. K. Dalapati, "Nanocrystal engineering of sputter-grown cuo photocathode for visible-light-driven electrochemical water splitting," *ACS applied materials & interfaces*, vol. 8, no. 2, pp. 1206–1213, 2016.

[120] J. G. Lee, D.-Y. Kim, J.-H. Lee, M.-w. Kim, S. An, H. S. Jo, C. Nervi, S. S. Al-Deyab, M. T. Swihart, and S. S. Yoon, "Scalable binder-free supersonic cold spraying of nanotextured cupric oxide (cuo) films as efficient photocathodes," *ACS applied materials & interfaces*, vol. 8, no. 24, pp. 15406–15414, 2016.

[121] X. Guo, P. Diao, D. Xu, S. Huang, Y. Yang, T. Jin, Q. Wu, M. Xiang, and M. Zhang, "Cuo/pd composite photocathodes for photoelectrochemical hydrogen evolution reaction," *international journal of hydrogen energy*, vol. 39, no. 15, pp. 7686–7696, 2014.

[122] S. Emin, F. Abdi, M. Fanetti, W. Peng, W. Smith, K. Sivula, B. Dam, and M. Valant, "A novel approach for the preparation of textured cuo thin films from electrodeposited cucl and cubr," *Journal of Electroanalytical Chemistry*, vol. 717, pp. 243–249, 2014.

[123] W. Septina, R. R. Prabhakar, R. Wick, T. Moehl, and S. D. Tilley, "Stabilized solar hydrogen production with cuo/cds heterojunction thin film photocathodes," *Chemistry of Materials*, vol. 29, no. 4, pp. 1735–1743, 2017.

[124] T. K. Wong, S. Zhuk, S. Masudy-Panah, and G. K. Dalapati, "Current status and future prospects of copper oxide heterojunction solar cells," *Materials*, vol. 9, no. 4, p. 271, 2016.

[125] M. Poloju, N. Jayababu, and M. R. Reddy, "Improved gas sensing performance of al doped zno/cuo nanocomposite based ammonia gas sensor," *Materials Science and Engineering: B*, vol. 227, pp. 61–67, 2018.

[126] A. Rydosz, W. Maziarz, T. Pisarkiewicz, K. Wincza, and S. Gruszczyński, "Nano-thin cuo films doped with au and pd for gas sensors applications," in *2013 International Conference on Informatics, Electronics and Vision (ICIEV)*, pp. 1–5, IEEE, 2013.

[127] A. J. Rettie, W. D. Chemelewski, D. Emin, and C. B. Mullins, "Unravelling small-polaron transport in metal oxide photoelectrodes," *The journal of physical chemistry letters*, vol. 7, no. 3, pp. 471–479, 2016.

[128] A. J. Rettie, H. C. Lee, L. G. Marshall, J.-F. Lin, C. Capan, J. Lindemuth, J. S. McCloy, J. Zhou, A. J. Bard, and C. B. Mullins, "Combined charge carrier transport and photoelectrochemical characterization of bivo4 single crystals: intrinsic behavior of a complex metal oxide," *Journal of the American Chemical Society*, vol. 135, no. 30, pp. 11389–11396, 2013.

[129] J. T. Devreese, "Polarons," *Encycl. Appl. Phys.*, vol. 14, no. cond-mat/0004497, pp. 383–409, 1996.

[130] N. Mott, "Conduction in glasses containing transition metal ions," *Journal of Non-Crystalline Solids*, vol. 1, no. 1, pp. 1–17, 1968.

[131] A. Samokhvalov, N. Viglin, B. Gizhevskij, N. Loshkareva, V. Osipov, N. Solin, and Y. P. Sukhorukov, "Low-mobility charge carriers in cuo," *Zhurnal Eksperimentalnoi i Teoreticheskoi Fiziki*, vol. 103, no. 3, pp. 951–961, 1993.

[132] J. Wu, B. Yin, F. Wu, Y. Myung, and P. Banerjee, "Charge transport in single cuo nanowires," *Applied Physics Letters*, vol. 105, no. 18, p. 183506, 2014.

[133] X.-G. Zheng, C.-N. Xu, E. Tanaka, Y. Tomokiyo, H. Yamada, Y. Soejima, Y. Yamamura, and T. Tsuji, "Evidence of charge stripes, charge-spin-orbital coupling and phase transition in a simple copper oxide cuo," *Journal of the Physical Society of Japan*, vol. 70, no. 4, pp. 1054–1063, 2001.

[134] Y. K. Jeong and G. M. Choi, "Nonstoichiometry and electrical conduction of cuo," *Journal of Physics and Chemistry of Solids*, vol. 57, no. 1, pp. 81–84, 1996.

[135] X. Zheng, Y. Kodama, K. Saito, E. Tanaka, Y. Tomokiyo, H. Yamada, and C. Xu, "Fast suppression of antiferromagnetism in cu 1- x li x o," *Physical Review B*, vol. 69, no. 9, p. 094510, 2004.

[136] S. Masudy-Panah, K. Radhakrishnan, H. R. Tan, R. Yi, T. I. Wong, and G. K. Dalapati, "Titanium doped cupric oxide for photovoltaic application," *Solar Energy Materials and Solar Cells*, vol. 140, pp. 266–274, 2015.

[137] Y.-H. Choi, D.-H. Kim, and S.-H. Hong, "p-type aliovalent li (i) or fe (iii)-doped cuo hollow spheres self-organized by cationic complex ink printing: structural and gas sensing characteristics," *Sensors and Actuators B: Chemical*, vol. 243, pp. 262–270, 2017.

[138] K. H. Gao, Z. Q. Li, T. Du, E. Y. Jiang, and Y. X. Li, "Ferromagnetic properties of bulk cu 1- x mn x o magnetic semiconductors," *Physical Review B*, vol. 75, no. 17, p. 174444, 2007.

[139] S. Masudy-Panah, K. Radhakrishnan, A. Kumar, T. I. Wong, R. Yi, and G. K. Dalapati, "Optical bandgap widening and phase transformation of nitrogen doped cupric oxide," *Journal of Applied Physics*, vol. 118, no. 22, p. 225301, 2015.

[140] X. Zheng, H. Yamada, D. J. Scanderbeg, M. B. Maple, and C. Xu, "Effect of hole doping in li x cu 1- x o," *Physical Review B*, vol. 67, no. 21, p. 214516, 2003.

[141] C.-Y. Chiang, Y. Shin, and S. Ehrman, "Dopant effects on conductivity in copper oxide photoelectrochemical cells," *Applied Energy*, vol. 164, pp. 1039–1042, 2016.

[142] C.-Y. Chiang, Y. Shin, and S. Ehrman, "Li doped cuo film electrodes for photoelectrochemical cells," *Journal of The Electrochemical Society*, vol. 159, no. 2, p. B227, 2011.

[143] P. Chand, A. Gaur, A. Kumar, and U. K. Gaur, "Structural and optical study of li doped cuo thin films on si (1 0 0) substrate deposited by pulsed laser deposition," *Applied surface science*, vol. 307, pp. 280–286, 2014.

[144] J. Ghijsen, L.-H. Tjeng, J. van Elp, H. Eskes, J. Westerink, G. A. Sawatzky, and M. T. Czyzyk, "Electronic structure of cu 2 o and cuo," *Physical Review B*, vol. 38, no. 16, p. 11322, 1988.

[145] P. De Gennes, "Interactions indirectes entre couches 4f dans les métaux de terres rares," *Journal de Physique et le Radium*, vol. 23, no. 8-9, pp. 510–521, 1962.

[146] D. Vigren, "Mobility of the self-trapped paramagnetic spin polaron," *Journal of Physics C: Solid State Physics*, vol. 6, no. 6, p. 967, 1973.

[147] N. Mott, "Polaron models of high-temperature superconductors," *Journal of Physics: Condensed Matter*, vol. 5, no. 22, p. 3487, 1993.

[148] A. Chernyshev and R. Wood, "Models and methods of high-tc superconductivity: Some frontal aspects vol 1 ed jk srivastava and sm rao hauppauge, ny," 2003.

[149] J. P. Lu and Q. Si, "Spin polarons in high-t c copper oxides: Differences between electron-and hole-doped systems," *Physical Review B*, vol. 42, no. 1, p. 950, 1990.

[150] K. Yonemitsu, A. Bishop, and J. Lorenzana, "Sensitivity of doping states in the copper oxides to electron-lattice coupling," *Physical review letters*, vol. 69, no. 6, p. 965, 1992.

[151] A. Alexandrov and N. Mott, "Bipolarons," *Reports on Progress in Physics*, vol. 57, no. 12, p. 1197, 1994.

[152] R. Wood and J. Cooke, "d 9 spin-polaron theory of high-t c superconductivity," *Physical Review B*, vol. 45, no. 10, p. 5585, 1992.

[153] M. B. Goldey, N. P. Brawand, M. V́oŕos, and G. Galli, "Charge transport in nanostructured materials: implementation and verification of constrained density functional theory," *Journal of chemical theory and computation*, vol. 13, no. 6, pp. 2581–2590, 2017.

[154] B. Kaduk, T. Kowalczyk, and T. Van Voorhis, "Constrained density functional theory," *Chemical reviews*, vol. 112, no. 1, pp. 321–370, 2012.

[155] X. Rocquefelte, M.-H. Whangbo, A. Villesuzanne, S. Jobic, F. Tran, K. Schwarz, and P. Blaha, "Short-range magnetic order and temperature-dependent properties of cupric oxide," *Journal of Physics: Condensed Matter*, vol. 22, no. 4, p. 045502, 2010.

[156] X. Rocquefelte, K. Schwarz, and P. Blaha, "Theoretical investigation of the magnetic exchange interactions in copper (ii) oxides under chemical and physical pressures," *Scientific reports*, vol. 2, no. 1, pp. 1–5, 2012.

[157] X. Rocquefelte, K. Schwarz, P. Blaha, S. Kumar, and J. Van Den Brink, "Room-temperature spin-spiral multiferroicity in high-pressure cupric oxide," *Nature communications*, vol. 4, no. 1, pp. 1–7, 2013.

[158] B. Yang, T. Thurston, J. Tranquada, and G. Shirane, "Magnetic neutron scattering study of single-crystal cupric oxide," *Physical Review B*, vol. 39, no. 7, p. 4343, 1989.

[159] X. Gonze and C. Lee, "Dynamical matrices, born effective charges, dielectric permittivity tensors, and interatomic force constants from density-functional perturbation theory," *Physical Review B*, vol. 55, no. 16, p. 10355, 1997.

[160] A. C. Cardiel, K. J. McDonald, and K.-S. Choi, "Electrochemical growth of copper hydroxy double salt films and their conversion to nanostructured p-type cuo photocathodes," *Langmuir*, vol. 33, no. 37, pp. 9262–9270, 2017.

[161] D. Kang, J. C. Hill, Y. Park, and K.-S. Choi, "Photoelectrochemical properties and photostabilities of high surface area cubi2o4 and ag-doped cubi2o4 photocathodes," *Chemistry of Materials*, vol. 28, no. 12, pp. 4331–4340, 2016.

[162] C. G. Read, Y. Park, and K.-S. Choi, "Electrochemical synthesis of p-type cufeo2 electrodes for use in a photoelectrochemical cell," *The journal of physical chemistry letters*, vol. 3, no. 14, pp. 1872–1876, 2012.

[163] G. P. Wheeler and K.-S. Choi, "Photoelectrochemical properties and stability of nanoporous p-type lafeo3 photoelectrodes prepared by electrodeposition," *ACS Energy Letters*, vol. 2, no. 10, pp. 2378–2382, 2017.

[164] A. J. Nozik, "Photoelectrochemistry: applications to solar energy conversion," *Annual review of physical chemistry*, vol. 29, no. 1, pp. 189–222, 1978.

[165] J. Forsyth, P. Brown, and B. Wanklyn, "Magnetism in cupric oxide," *Journal of Physics C: Solid State Physics*, vol. 21, no. 15, p. 2917, 1988.

[166] Y. Peng, Z. Zhang, T. Viet Pham, Y. Zhao, P. Wu, and J. Wang, "Density functional theory analysis of dopants in cupric oxide," *Journal of Applied Physics*, vol. 111, no. 10, p. 103708, 2012.

[167] Y. Peng, J. Zheng, P. Wu, and J. Wang, "Ab-initio study of donor-acceptor codoping for n-type cuo," *Journal of Applied Physics*, vol. 116, no. 16, p. 163704, 2014.

[168] M. Heinemann, B. Eifert, and C. Heiliger, "Band structure and phase stability of the copper oxides cu 2 o, cuo, and cu 4 o 3," *Physical Review B*, vol. 87, no. 11, p. 115111, 2013.

[169] L. Debbichi, M. Marco de Lucas, J. Pierson, and P. Kruger, "Vibrational properties of cuo and cu4o3 from first-principles calculations, and raman and infrared spectroscopy," *The Journal of Physical Chemistry C*, vol. 116, no. 18, pp. 10232–10237, 2012.

[170] D. Wu, Q. Zhang, and M. Tao, "Lsda+ u study of cupric oxide: Electronic structure and native point defects," *Physical Review B*, vol. 73, no. 23, p. 235206, 2006.

[171] M. Reticcioli, U. Diebold, G. Kresse, and C. Franchini, "Small polarons in transition metal oxides," *Handbook of Materials Modeling: Applications: Current and Emerging Materials*, pp. 1–39, 2019.

[172] M. Gong, W. Zhou, M.-C. Tsai, J. Zhou, M. Guan, M.-C. Lin, B. Zhang, Y. Hu, D.-Y. Wang, J. Yang, S. J. Pennycook, B.-J. Hwang, and H. Dai, "Nanoscale nickel oxide/nickel heterostructures for active hydrogen evolution electrocatalysis," *Nature Communications*, vol. 5, p. 4695, 2014.

[173] C. Hu, K. Chu, Y. Zhao, and W. Y. Teoh, "Efficient photoelectrochemical water splitting over anodized p-type nio porous films," *ACS Applied Materials & Interfaces*, vol. 6, no. 21, pp. 18558–18568, 2014.

[174] Z. Wang, H. Liu, R. Ge, X. Ren, J. Ren, D. Yang, L. Zhang, and X. Sun, "Phosphorus-doped Co_3O_4 nanowire array: A highly efficient bifunctional electrocatalyst for overall water splitting," *ACS Catalysis*, vol. 8, no. 3, pp. 2236–2241, 2018.

[175] A. Aijaz, J. Masa, C. Rösler, W. Xia, P. Weide, A. J. Botz, R. A. Fischer, W. Schuhmann, and M. Muhler, "Co@Co_3O_4 encapsulated in carbon nanotube-grafted nitrogen-doped carbon polyhedra as an advanced bifunctional oxygen electrode," *Angewandte Chemie International Edition*, vol. 55, no. 12, pp. 4087–4091, 2016.

[176] K. Jin, A. Chu, J. Park, D. Jeong, S. E. Jerng, U. Sim, H.-Y. Jeong, C. W. Lee, Y.-S. Park, K. D. Yang, G. K. Pradhan, D. Kim, N.-E. Sung, S. H. Kim, and K. T. Nam, "Partially oxidized sub-10 nm mno nanocrystals with high activity for water oxidation catalysis," *Scientific Reports*, vol. 5, p. 10279, 2015.

[177] I. Roger, M. A. Shipman, and M. D. Symes, "Earth-abundant catalysts for electrochemical and photoelectrochemical water splitting," *Nature Reviews Chemistry*, vol. 1, no. 1, p. 0003, 2017.

[178] Y. Yan, B. Y. Xia, B. Zhao, and X. Wang, "A review on noble-metal-free bifunctional heterogeneous catalysts for overall electrochemical water splitting," *Journal of Materials Chemistry A*, vol. 4, no. 45, pp. 17587–17603, 2016.

[179] P. Liao and E. A. Carter, "New concepts and modeling strategies to design and evaluate photo-electro-catalysts based on transition metal oxides," *Chemical Society Reviews*, vol. 42, no. 6, pp. 2401–2422, 2013.

[180] M. Gerosa, F. Gygi, M. Govoni, and G. Galli, "The role of defects and excess surface charges at finite temperature for optimizing oxide photoabsorbers," *Nature Materials*, vol. 17, no. 12, p. 1122, 2018.

[181] B. Yan, D. Wan, X. Chi, C. Li, M. R. Motapothula, S. Hooda, P. Yang, Z. Huang, S. Zeng, A. G. Ramesh, S. J. Pennycook, A. Rusydi, Ariando, J. Martin, and T. Venkatesan, "Anatase TiO_2–a model system for large polaron transport," *ACS Applied Materials & Interfaces*, vol. 10, no. 44, pp. 38201–38208, 2018.

[182] S. Moser, L. Moreschini, J. Jaćimović, O. S. Barišić, H. Berger, A. Magrez, Y. J. Chang, K. S. Kim, A. Bostwick, E. Rotenberg, L. Forró, and M. Grioni, "Tunable polaronic conduction in anatase tio_2," *Physical Review Letters*, vol. 110, p. 196403, May 2013.

[183] W. Kang and M. S. Hybertsen, "Quasiparticle and optical properties of rutile and anatase tio_2," *Physical Review B*, vol. 82, p. 085203, Aug 2010.

[184] C. Verdi, F. Caruso, and F. Giustino, "Origin of the crossover from polarons to fermi liquids in transition metal oxides," *Nature Communications*, vol. 8, p. 15769, 2017.

[185] Z. Wang, S. McKeown Walker, A. Tamai, Y. Wang, Z. Ristic, F. Y. Bruno, A. de la Torre, S. Riccò, N. C. Plumb, M. Shi, P. Hlawenka, J. Sánchez-Barriga, A. Varykhalov, T. K. Kim, M. Hoesch, P. D. C. King, W. Meevasana, U. Diebold, J. Mesot, B. Moritz, T. P. Devereaux, M. Radovic, and F. Baumberger, "Tailoring the nature and strength of electron-phonon interactions in the $SrTiO_3$(001) 2d electron liquid," *Nature Materials*, vol. 15, p. 835, Apr 2016.

[186] S. Biswas, J. Husek, S. Londo, and L. R. Baker, "Ultrafast electron trapping and defect-mediated recombination in nio probed by femtosecond extreme ultraviolet reflection–absorption spectroscopy," *The Journal of Physical Chemistry Letters*, vol. 9, no. 17, pp. 5047–5054, 2018.

[187] M. N. Huda, A. Walsh, Y. Yan, S.-H. Wei, and M. M. Al-Jassim, "Electronic, structural, and magnetic effects of 3 d transition metals in hematite," *Journal of Applied Physics*, vol. 107, no. 12, p. 123712, 2010.

[188] O. Neufeld and M. C. Toroker, "Platinum-doped α-fe2o3 for enhanced water splitting efficiency: a dft+ u study," *The Journal of Physical Chemistry C*, vol. 119, no. 11, pp. 5836–5847, 2015.

[189] A. Sanson, A. Zaltron, N. Argiolas, C. Sada, M. Bazzan, W. Schmidt, and S. Sanna, "Polaronic deformation at the fe 2+/3+ impurity site in fe: Linbo 3 crystals," *Physical Review B*, vol. 91, no. 9, p. 094109, 2015.

[190] N. Yatom, O. Neufeld, and M. Caspary Toroker, "Toward settling the debate on the role of fe2o3 surface states for water splitting," *The Journal of Physical Chemistry C*, vol. 119, no. 44, pp. 24789–24795, 2015.

[191] Z.-S. Wu, W. Ren, L. Wen, L. Gao, J. Zhao, Z. Chen, G. Zhou, F. Li, and H.-M. Cheng, "Graphene anchored with Co_3O_4 nanoparticles as anode of lithium ion batteries with enhanced reversible capacity and cyclic performance," *ACS Nano*, vol. 4, no. 6, pp. 3187–3194, 2010.

[192] W.-Y. Li, L.-N. Xu, and J. Chen, "Co_3O_4 nanomaterials in lithium-ion batteries and gas sensors," *Advanced Functional Materials*, vol. 15, no. 5, pp. 851–857, 2005.

[193] T. Y. Ma, S. Dai, M. Jaroniec, and S. Z. Qiao, "Metal–organic framework derived hybrid Co_3O_4-carbon porous nanowire arrays as reversible oxygen evolution electrodes," *Journal of the American Chemical Society*, vol. 136, no. 39, pp. 13925–13931, 2014.

[194] M. Hamdani, R. Singh, and P. Chartier, "Co_3O_4 and co-based spinel oxides bifunctional oxygen electrodes," *International Journal of Electrochemical Sciences*, vol. 5, no. 4, pp. 556–577, 2010.

[195] S. K. Meher and G. R. Rao, "Ultralayered Co_3O_4 for high-performance supercapacitor applications," *The Journal of Physical Chemistry C*, vol. 115, no. 31, pp. 15646–15654, 2011.

[196] X.-h. Xia, J.-p. Tu, Y.-j. Mai, X.-l. Wang, C.-d. Gu, and X.-b. Zhao, "Self-supported hydrothermal synthesized hollow Co_3O_4 nanowire arrays with high supercapacitor capacitance," *Journal of Materials Chemistry*, vol. 21, no. 25, pp. 9319–9325, 2011.

[197] C. Lohaus, J. Morasch, J. Brötz, A. Klein, and W. Jaegermann, "Investigations on rf-magnetron sputtered Co_3O_4 thin films regarding the solar energy conversion properties," *Journal of Physics D: Applied Physics*, vol. 49, no. 15, p. 155306, 2016.

[198] C.-M. Jiang, L. R. Baker, J. M. Lucas, J. Vura-Weis, A. P. Alivisatos, and S. R. Leone, "Characterization of photo-induced charge transfer and hot carrier relaxation pathways in spinel cobalt oxide (Co_3O_4)," *The Journal of Physical Chemistry C*, vol. 118, no. 39, pp. 22774–22784, 2014.

[199] M. M. Waegele, H. Q. Doan, and T. Cuk, "Long-lived photoexcited carrier synamics of d–d excitations in spinel ordered Co_3O_4," *The Journal of Physical Chemistry C*, vol. 118, no. 7, pp. 3426–3432, 2014.

[200] V. Shinde, S. Mahadik, T. Gujar, and C. Lokhande, "Supercapacitive cobalt oxide (Co_3O_4) thin films by spray pyrolysis," *Applied Surface Science*, vol. 252, no. 20, pp. 7487–7492, 2006.

[201] I. Belova, Y. E. Roginskaya, R. Shifrina, S. Gagarin, Y. V. Plekhanov, and Y. N. Venevtsev, "Co (iii) ions high-spin configuration in nonstoichiometric Co_3O_4 films," *Solid State Communications*, vol. 47, no. 8, pp. 577–584, 1983.

[202] A. Lima, "Interpretation of the optical absorption spectrum of Co_3O_4 with normal spinel structure from first principles calculations," *Journal of Physics and Chemistry of Solids*, vol. 75, no. 1, pp. 148–152, 2014.

[203] C.-S. Cheng, M. Serizawa, H. Sakata, and T. Hirayama, "Electrical conductivity of Co_3O_4 films prepared by chemical vapour deposition," *Materials Chemistry and Physics*, vol. 53, no. 3, pp. 225–230, 1998.

[204] L. Qiao, H. Y. Xiao, H. Meyer, J. Sun, C. M. Rouleau, A. A. Puretzky, D. B. Geohegan, I. N. Ivanov, M. Yoon, W. J. Weber, and M. D. Biegalski, "Nature of the band gap and origin of the electro-/photo-activity of Co_3O_4," *Journal of Materials Chemistry C*, vol. 1, no. 31, pp. 4628–4633, 2013.

[205] V. Singh, M. Kosa, K. Majhi, and D. T. Major, "Putting dft to the test: A first-principles study of electronic, magnetic, and optical properties of Co_3O_4," *Journal of Chemical Theory and Computation*, vol. 11, no. 1, pp. 64–72, 2014.

[206] O. Sousa, J. Lima, A. Lima, and M. Lalic, "Theoretical study of structural, electronic and magnetic properties of the spinel Co_3O_4 under the pressure from 0 to 30 gpa," *Journal of Magnetism and Magnetic Materials*, vol. 484, pp. 21–30, 2019.

[207] J. Martens, W. Peeters, H. Van Noort, and M. Erman, "Optical, magneto-optical and mössbauer spectroscopy on Co^{3+} substituted cobalt ferrite $Co^{2+}Fe_{2-x}Co_x^{3+}O_4$ $(0 \leq x \leq 2)$," *Journal of Physics and Chemistry of Solids*, vol. 46, no. 4, pp. 411–416, 1985.

[208] D. A. Wheeler, G. Wang, Y. Ling, Y. Li, and J. Z. Zhang, "Nanostructured hematite: Synthesis, characterization, charge carrier dynamics, and photoelectrochemical properties," *Energy & Environmental Science*, vol. 5, no. 5, pp. 6682–6702, 2012.

[209] P. H. T. Ngamou and N. Bahlawane, "Influence of the arrangement of the octahedrally coordinated trivalent cobalt cations on the electrical charge transport and surface reactivity," *Chemistry of Materials*, vol. 22, no. 14, pp. 4158–4165, 2010.

[210] F. Tronel, L. Guerlou-Demourgues, M. Ménétrier, L. Croguennec, L. Goubault, P. Bernard, and C. Delmas, "New spinel cobalt oxides, potential conductive additives for the positive electrode of ni-mh batteries," *Chemistry of Materials*, vol. 18, no. 25, pp. 5840–5851, 2006.

[211] P. Sahoo, H. Djieutedjeu, and P. F. Poudeu, "Co_3O_4 nanostructures: The effect of synthesis conditions on particles size, magnetism and transport properties," *Journal of Materials Chemistry A*, vol. 1, no. 47, pp. 15022–15030, 2013.

[212] T. D. Sparks, A. Gurlo, M. W. Gaultois, and D. R. Clarke, "Revised model for thermopower and site inversion in Co_3O_4 spinel," *Physical Review B*, vol. 98, no. 2, p. 024108, 2018.

[213] K. Koumoto and H. Yanagida, "Electrical conduction in pure and li-substituted Co_3O_4," *Journal of the American Ceramic Society*, vol. 64, no. 11, p. C156, 1981.

[214] P. R. Kent and G. Kotliar, "Toward a predictive theory of correlated materials," *Science*, vol. 361, no. 6400, pp. 348–354, 2018.

[215] G. Miceli, W. Chen, I. Reshetnyak, and A. Pasquarello, "Nonempirical hybrid functionals for band gaps and polaronic distortions in solids," *Physical Review B*, vol. 97, no. 12, p. 121112, 2018.

[216] T. J. Smart, F. Wu, M. Govoni, and Y. Ping, "Fundamental principles for calculating charged defect ionization energies in ultrathin two-dimensional materials," *Physical Review Materials*, vol. 2, no. 12, p. 124002, 2018.

[217] Q. Liu, Q. Yao, Z. Kelly, C. Pasco, T. McQueen, S. Lany, and A. Zunger, "Electron doping of proposed kagome quantum spin liquid produces localized states in the band gap," *Physical Review Letters*, vol. 121, no. 18, p. 186402, 2018.

[218] S. Lany, "Predicting polaronic defect states by means of generalized koopmans density functional calculations," *Physica Status Solidi B*, vol. 248, no. 5, pp. 1052–1060, 2011.

[219] T. Bischoff, I. Reshetnyak, and A. Pasquarello, "Adjustable potential probes for band-gap predictions of extended systems through nonempirical hybrid functionals," *Physical Review B*, vol. 99, no. 20, p. 201114, 2019.

[220] S. Kokott, S. V. Levchenko, P. Rinke, and M. Scheffler, "First-principles supercell calculations of small polarons with proper account for long-range polarization effects," *New Journal of Physics*, vol. 20, no. 3, p. 033023, 2018.

[221] W. Roth, "The magnetic structure of Co_3O_4," *Journal of Physics and Chemistry of Solids*, vol. 25, no. 1, pp. 1–10, 1964.

[222] J. Chen, X. Wu, and A. Selloni, "Electronic structure and bonding properties of cobalt oxide in the spinel structure," *Physical Review B*, vol. 83, no. 24, p. 245204, 2011.

[223] M.-S. Wu, B. Xu, and C.-Y. Ouyang, "Manipulation of spin-flip in Co_3O_4: A first principles study," *Journal of Materials Science*, vol. 51, no. 9, pp. 4691–4696, 2016.

[224] Y. Ping, D. Rocca, and G. Galli, "Electronic excitations in light absorbers for photoelectrochemical energy conversion: First principles calculations based on many body perturbation theory," *Chemical Society Reviews*, vol. 42, no. 6, pp. 2437–2469, 2013.

[225] T. Le Bahers, M. Rérat, and P. Sautet, "Semiconductors used in photovoltaic and photocatalytic devices: Assessing fundamental properties from dft," *The Journal of Physical Chemistry C*, vol. 118, no. 12, pp. 5997–6008, 2014.

[226] The typical concentration of cobalt vacancies is 5% [210, 227], which corresponds to a hole concentration or 10% and 15 % for Co(T) and Co(O) vacancies, respectively. In this regard, it is reasonable to simulate hole polarons in Co_3O_4 using a 56-atom supercell that yields a hole concentration of 12.5% for a proper representation of the experimental systems.

[227] G. Godillot, L. Guerlou-Demourgues, L. Croguennec, K. Shaju, and C. Delmas, "Effect of temperature on structure and electronic properties of nanometric spinel-type cobalt oxides," *The Journal of Physical Chemistry C*, vol. 117, no. 18, pp. 9065–9075, 2013.

[228] A. Marini, C. Hogan, M. Grüning, and D. Varsano, "Yambo: An ab initio tool for excited state calculations," *Computer Physics Communications*, vol. 180, no. 8, pp. 1392 – 1403, 2009.

[229] C. Rödl and F. Bechstedt, "Optical and energy-loss spectra of the antiferromagnetic transition metal oxides mno, feo, coo, and nio including quasiparticle and excitonic effects," *Physical Review B*, vol. 86, p. 235122, Dec 2012.

[230] J. D. Jackson, *Classical Electrodynamics*. New York: Wiley, 1999.

[231] R. Laskowski, N. E. Christensen, P. Blaha, and B. Palanivel, "Strong excitonic effects in $cualo_2$ delafossite transparent conductive oxides," *Physical Review B*, vol. 79, p. 165209, Apr 2009.

[232] F. Bruneval, N. Vast, L. Reining, M. Izquierdo, F. Sirotti, and N. Barrett, "Exchange and correlation effects in electronic excitations of cu_2O," *Physical Review Letter*, vol. 97, p. 267601, Dec 2006.

[233] J. Wiktor, I. Reshetnyak, M. Strach, M. Scarongella, R. Buonsanti, and A. Pasquarello, "Sizable excitonic effects undermining the photocatalytic efficiency of β-cu2v2o7," *The Journal of Physical Chemistry Letters*, vol. 9, no. 19, pp. 5698–5703, 2018.

[234] C. Rödl and F. Bechstedt, "Optical and energy-loss spectra of the antiferromagnetic transition metal oxides mno, feo, coo, and nio including quasiparticle and excitonic effects," *Physical Review B*, vol. 86, p. 235122, Dec 2012.

[235] B. Monserrat, C. E. Dreyer, and K. M. Rabe, "Phonon-assisted optical absorption in basno 3 from first principles," *Physical Review B*, vol. 97, no. 10, p. 104310, 2018.

[236] I. Bravić and B. Monserrat, "Finite temperature optoelectronic properties of bas from first principles," *Physical Review Materials*, vol. 3, no. 6, p. 065402, 2019.

[237] T. Choi, S. Lee, Y. Choi, V. Kiryukhin, and S.-W. Cheong, "Switchable ferroelectric diode and photovoltaic effect in bifeo3," *Science*, vol. 324, no. 5923, pp. 63–66, 2009.

[238] H. Yi, T. Choi, S. Choi, Y. S. Oh, and S.-W. Cheong, "Mechanism of the switchable photovoltaic effect in ferroelectric bifeo3," *Advanced Materials*, vol. 23, no. 30, pp. 3403–3407, 2011.

[239] L. You, F. Zheng, L. Fang, Y. Zhou, L. Z. Tan, Z. Zhang, G. Ma, D. Schmidt, A. Rusydi, L. Wang, *et al.*, "Enhancing ferroelectric photovoltaic effect by polar order engineering," *Science advances*, vol. 4, no. 7, p. eaat3438, 2018.

[240] J. E. Spanier, V. M. Fridkin, A. M. Rappe, A. R. Akbashev, A. Polemi, Y. Qi, Z. Gu, S. M. Young, C. J. Hawley, D. Imbrenda, *et al.*, "Power conversion efficiency exceeding the shockley–queisser limit in a ferroelectric insulator," *Nature Photonics*, vol. 10, no. 9, pp. 611–616, 2016.

[241] H. Shen, X. Zhou, W. Dong, X. Su, L. Fang, X. Wu, and M. Shen, "Dual role of tio2 buffer layer in pt catalyzed bifeo3 photocathodes: Efficiency enhancement and surface protection," *Applied Physics Letters*, vol. 111, no. 12, p. 123901, 2017.

[242] P. Yilmaz, D. Yeo, H. Chang, L. Loh, and S. Dunn, "Perovskite bifeo3 thin film photocathode performance with visible light activity," *Nanotechnology*, vol. 27, no. 34, p. 345402, 2016.

[243] S. J. Moniz, C. S. Blackman, P. Southern, P. M. Weaver, J. Tang, and C. J. Carmalt, "Visible-light driven water splitting over bifeo 3 photoanodes grown via the lpcvd reaction of [bi (o t bu) 3] and [fe (o t bu) 3] 2 and enhanced with a surface nickel oxygen evolution catalyst," *Nanoscale*, vol. 7, no. 39, pp. 16343–16353, 2015.

[244] J. Song, T. L. Kim, J. Lee, S. Y. Cho, J. Cha, S. Y. Jeong, H. An, W. S. Kim, Y.-S. Jung, J. Park, *et al.*, "Domain-engineered bifeo 3 thin-film photoanodes for highly enhanced ferroelectric solar water splitting," *Nano Research*, vol. 11, no. 2, pp. 642–655, 2018.

[245] Q. Liu, Y. Zhou, L. You, J. Wang, M. Shen, and L. Fang, "Enhanced ferroelectric photoelectrochemical properties of polycrystalline bifeo3 film by decorating with ag nanoparticles," *Applied Physics Letters*, vol. 108, no. 2, p. 022902, 2016.

[246] K. Sivula and R. Van De Krol, "Semiconducting materials for photoelectrochemical energy conversion," *Nature Reviews Materials*, vol. 1, no. 2, pp. 1–16, 2016.

[247] T. R. Paudel, S. S. Jaswal, and E. Y. Tsymbal, "Intrinsic defects in multiferroic bifeo 3 and their effect on magnetism," *Physical Review B*, vol. 85, no. 10, p. 104409, 2012.

[248] T. Rojac, A. Bencan, G. Drazic, N. Sakamoto, H. Ursic, B. Jancar, G. Tavcar, M. Makarovic, J. Walker, B. Malic, *et al.*, "Domain-wall conduction in ferroelectric bifeo 3 controlled by accumulation of charged defects," *Nature materials*, vol. 16, no. 3, pp. 322–327, 2017.

[249] D. Cao, Z. Wang, L. Wen, Y. Mi, and Y. Lei, "Switchable charge-transfer in the photoelectrochemical energy-conversion process of ferroelectric bifeo3 photoelectrodes," *Angewandte Chemie*, vol. 126, no. 41, pp. 11207–11211, 2014.

[250] Y.-L. Huang, W. S. Chang, C. N. Van, H.-J. Liu, K.-A. Tsai, J.-W. Chen, H.-H. Kuo, W.-Y. Tzeng, Y.-C. Chen, C.-L. Wu, *et al.*, "Tunable photoelectrochemical performance of au/bifeo 3 heterostructure," *Nanoscale*, vol. 8, no. 34, pp. 15795–15801, 2016.

[251] D. Kan, V. Anbusathaiah, and I. Takeuchi, "Chemical substitution-induced ferroelectric polarization rotation in bifeo3," *Advanced Materials*, vol. 23, no. 15, pp. 1765–1769, 2011.

[252] J. Neaton, C. Ederer, U. Waghmare, N. Spaldin, and K. Rabe, "First-principles study of spontaneous polarization in multiferroic bi fe o 3," *Physical Review B*, vol. 71, no. 1, p. 014113, 2005.

[253] S. M. Young, F. Zheng, and A. M. Rappe, "First-principles calculation of the bulk photovoltaic effect in bismuth ferrite," *Physical review letters*, vol. 109, no. 23, p. 236601, 2012.

[254] S. Liu, I. Grinberg, and A. M. Rappe, "Development of a bond-valence based interatomic potential for bifeo3 for accurate molecular dynamics simulations," *Journal of Physics: Condensed Matter*, vol. 25, no. 10, p. 102202, 2013.

[255] D. Wang, J. Weerasinghe, and L. Bellaiche, "Atomistic molecular dynamic simulations of multiferroics," *Physical review letters*, vol. 109, no. 6, p. 067203, 2012.

[256] C.-M. Chang, B. Mani, S. Lisenkov, and I. Ponomareva, "Prediction of electromagnons in antiferromagnetic ferroelectrics from first-principles: The case of bifeo3," *Ferroelectrics*, vol. 494, no. 1, pp. 68–75, 2016.

[257] G. Geneste, C. Paillard, and B. Dkhil, "Polarons, vacancies, vacancy associations, and defect states in multiferroic bifeo 3," *Physical Review B*, vol. 99, no. 2, p. 024104, 2019.

[258] J. Lu, A. Günther, F. Schrettle, F. Mayr, S. Krohns, P. Lunkenheimer, A. Pimenov, V. Travkin, A. Mukhin, and A. Loidl, "On the room temperature multiferroic bifeo 3: magnetic, dielectric and thermal properties," *The European Physical Journal B*, vol. 75, no. 4, pp. 451–460, 2010.

[259] F. Gheorghiu, M. Calugaru, A. Ianculescu, V. Musteata, and L. Mitoseriu, "Preparation and functional characterization of bifeo3 ceramics: A comparative study of the dielectric properties," *Solid state sciences*, vol. 23, pp. 79–87, 2013.

[260] P. Baettig, C. Ederer, and N. A. Spaldin, "First principles study of the multiferroics bi fe o 3, bi 2 fe cr o 6, and bi cr o 3: Structure, polarization, and magnetic ordering temperature," *Physical Review B*, vol. 72, no. 21, p. 214105, 2005.

[261] A. Kay, I. Cesar, and M. Grätzel, "New benchmark for water photooxidation by nanostructured α-fe2o3 films," *Journal of the American Chemical Society*, vol. 128, no. 49, pp. 15714–15721, 2006.

[262] Z. Zhang, P. Wu, L. Chen, and J. Wang, "Density functional theory plus u study of vacancy formations in bismuth ferrite," *Applied Physics Letters*, vol. 96, no. 23, p. 232906, 2010.

[263] T. Shimada, T. Matsui, T. Xu, K. Arisue, Y. Zhang, J. Wang, and T. Kitamura, "Multiferroic nature of intrinsic point defects in bifeo 3: A hybrid hartree-fock density functional study," *Physical Review B*, vol. 93, no. 17, p. 174107, 2016.

[264] Z. Zhu, H. Peelaers, and C. G. Van de Walle, "Electronic and protonic conduction in lafeo 3," *Journal of Materials Chemistry A*, vol. 5, no. 29, pp. 15367–15379, 2017.

[265] M. Idrees, M. Nadeem, M. Atif, M. Siddique, M. Mehmood, and M. Hassan, "Origin of colossal dielectric response in lafeo3," *Acta Materialia*, vol. 59, no. 4, pp. 1338–1345, 2011.

[266] J. Mizusaki, T. Sasamoto, W. R. Cannon, and H. K. Bowen, "Electronic conductivity, seebeck coefficient, and defect structure of la1-xsrxfeo3 (x= 0. l, 0.25)," *Journal of the American Ceramic Society*, vol. 66, no. 4, pp. 247–252, 1983.

[267] Y. Ping and G. Galli, "Optimizing the band edges of tungsten trioxide for water oxidation: a first-principles study," *The Journal of Physical Chemistry C*, vol. 118, no. 12, pp. 6019–6028, 2014.

[268] G. L. Beausoleil, P. Price, D. Thomsen, A. Punnoose, R. Ubic, S. Misture, and D. P. Butt, "Thermal expansion of alkaline-doped lanthanum ferrite near the néel temperature," *Journal of the American Ceramic Society*, vol. 97, no. 1, pp. 228–234, 2014.

[269] J. A. N. Malik, "Science advocacy drives passage of us national quantum initiative act," *MRS Bulletin*, vol. 44, no. 3, pp. 158–159, 2019.

[270] W. F. Koehl, B. B. Buckley, F. J. Heremans, G. Calusine, and D. D. Awschalom, "Room temperature coherent control of defect spin qubits in silicon carbide," *Nature*, vol. 479, no. 7371, pp. 84–87, 2011.

[271] J. Weber, W. Koehl, J. Varley, A. Janotti, B. Buckley, C. Van de Walle, and D. D. Awschalom, "Quantum computing with defects," *P. Natl. Acad. Sci. USA*, vol. 107, no. 19, pp. 8513–8518, 2010.

[272] A. L. Falk, B. B. Buckley, G. Calusine, W. F. Koehl, V. V. Dobrovitski, A. Politi, C. A. Zorman, P. X.-L. Feng, and D. D. Awschalom, "Polytype control of spin qubits in silicon carbide," *Nature communications*, vol. 4, no. 1, pp. 1–7, 2013.

[273] I. Aharonovich and M. Toth, "Quantum emitters in two dimensions," *Science*, vol. 358, no. 6360, pp. 170–171, 2017.

[274] A. Sajid, M. J. Ford, and J. R. Reimers, "Single-photon emitters in hexagonal boron nitride: a review of progress," *Reports on Progress in Physics*, vol. 83, no. 4, p. 044501, 2020.

[275] G. Grosso, H. Moon, B. Lienhard, S. Ali, D. K. Efetov, M. M. Furchi, P. Jarillo-Herrero, M. J. Ford, I. Aharonovich, and D. Englund, "Tunable and high-purity room temperature single-photon emission from atomic defects in hexagonal boron nitride," *Nat. Commun.*, vol. 8, no. 1, p. 705, 2017.

[276] A. Gottscholl, M. Kianinia, V. Soltamov, S. Orlinskii, G. Mamin, C. Bradac, C. Kasper, K. Krambrock, A. Sperlich, M. Toth, *et al.*, "Initialization and read-out of intrinsic spin defects in a van der waals crystal at room temperature," *Nat. Mater.*, vol. 19, no. 5, pp. 540–545, 2020.

[277] N. Mendelson, M. Doherty, M. Toth, I. Aharonovich, and T. T. Tran, "Strain-induced modification of the optical characteristics of quantum emitters in hexagonal boron nitride," *Adv. Mater.*, vol. 32, no. 21, p. 1908316, 2020.

[278] S. Z. Butler, S. M. Hollen, L. Cao, Y. Cui, J. A. Gupta, H. R. Gutiérrez, T. F. Heinz, S. S. Hong, J. Huang, A. F. Ismach, E. Johnston-Halperin, M. Kuno, V. V. Plashnitsa, R. D. Robinson, R. S. Ruoff, S. Salahuddin, J. Shan, L. Shi, M. G. Spencer, M. Terrones, W. Windl, and J. E. Goldberger, "Progress, challenges, and opportunities in two-dimensional materials beyond graphene," *ACS Nano*, vol. 7, no. 4, pp. 2898–2926, 2013.

[279] D. Wang, X.-B. Li, D. Han, W. Q. Tian, and H.-B. Sun, "Engineering two-dimensional electronics by semiconductor defects," *Nano Today*, vol. 16, pp. 30–45, 2017.

[280] J. Hong, C. Jin, J. Yuan, and Z. Zhang, "Atomic defects in two-dimensional materials: From single-atom spectroscopy to functionalities in opto-/electronics, nanomagnetism, and catalysis," *Advanced Materials*, vol. 29, no. 14, p. 1606434, 2017.

[281] Z. Lin, B. R. Carvalho, E. Kahn, R. Lv, R. Rao, H. Terrones, M. A. Pimenta, and M. Terrones, "Defect engineering of two-dimensional transition metal dichalcogenides," *2D Materials*, vol. 3, no. 2, p. 022002, 2016.

[282] C. E. Dreyer, A. Alkauskas, J. L. Lyons, A. Janotti, and C. G. Van de Walle, "First-principles calculations of point defects for quantum technologies," *Annual Review of Materials Research*, vol. 48, pp. 1–26, 2018.

[283] L. Weston, D. Wickramaratne, M. Mackoit, A. Alkauskas, and C. Van de Walle, "Native point defects and impurities in hexagonal boron nitride," *Phys. Rev. B*, vol. 97, no. 21, p. 214104, 2018.

[284] S. A. Tawfik, S. Ali, M. Fronzi, M. Kianinia, T. T. Tran, C. Stampfl, I. Aharonovich, M. Toth, and M. J. Ford, "First-principles investigation of quantum emission from hbn defects," *Nanoscale*, vol. 9, no. 36, pp. 13575–13582, 2017.

[285] R. Bourrellier, S. Meuret, A. Tararan, O. Stéphan, M. Kociak, L. H. Tizei, and A. Zobelli, "Bright uv single photon emission at point defects in h-bn," *Nano Lett.*, vol. 16, no. 7, pp. 4317–4321, 2016.

[286] M. Abdi, J.-P. Chou, A. Gali, and M. B. Plenio, "Color centers in hexagonal boron nitride monolayers: a group theory and ab initio analysis," *ACS Photonics*, vol. 5, no. 5, pp. 1967–1976, 2018.

[287] T. T. Tran, K. Bray, M. J. Ford, M. Toth, and I. Aharonovich, "Quantum emission from hexagonal boron nitride monolayers," *Nature Nanotechnology*, vol. 11, no. 1, pp. 37–41, 2016.

[288] C. Freysoldt, J. Neugebauer, and C. G. Van de Walle, "Fully ab initio finite-size corrections for charged-defect supercell calculations," *Physical review letters*, vol. 102, no. 1, p. 016402, 2009.

[289] D. Vinichenko, M. G. Sensoy, C. M. Friend, and E. Kaxiras, "Accurate formation energies of charged defects in solids: a systematic approach," *Physical Review B*, vol. 95, no. 23, p. 235310, 2017.

[290] H.-P. Komsa and A. Pasquarello, "Finite-size supercell correction for charged defects at surfaces and interfaces," *Phys. Rev. Lett.*, vol. 110, p. 095505, Feb 2013.

[291] H.-P. Komsa, N. Berseneva, A. V. Krasheninnikov, and R. M. Nieminen, "Charged point defects in the flatland: Accurate formation energy calculations in two-dimensional materials," *Physical Review X*, vol. 4, no. 3, p. 031044, 2014.

[292] H.-P. Komsa, N. Berseneva, A. V. Krasheninnikov, and R. M. Nieminen, "Erratum: Charged point defects in the flatland: Accurate formation energy calculations in two-dimensional materials [phys. rev. x 4, 031044 (2014)]," *Physical Review X*, vol. 8, no. 3, p. 039902, 2018.

[293] D. Wang, D. Han, X.-B. Li, S.-Y. Xie, N.-K. Chen, W. Q. Tian, D. West, H.-B. Sun, and S. Zhang, "Determination of formation and ionization energies of charged defects in two-dimensional materials," *Physical review letters*, vol. 114, no. 19, p. 196801, 2015.

[294] A. Alkauskas, P. Broqvist, and A. Pasquarello, "Defect levels through hybrid density functionals: Insights and applications," *Phys. Status Solidi B*, vol. 248, no. 4, pp. 775–789, 2011.

[295] J. H. Skone, M. Govoni, and G. Galli, "Self-consistent hybrid functional for condensed systems," *Phys. Rev. B*, vol. 89, p. 195112, 2014.

[296] D. Y. Qiu, H. Felipe, and S. G. Louie, "Screening and many-body effects in two-dimensional crystals: Monolayer mos 2," *Physical Review B*, vol. 93, no. 23, p. 235435, 2016.

[297] F. A. Rasmussen, P. S. Schmidt, K. T. Winther, and K. S. Thygesen, "Efficient many-body calculations for two-dimensional materials using exact limits for the screened potential: Band gaps of mos 2, h-bn, and phosphorene," *Physical Review B*, vol. 94, no. 15, p. 155406, 2016.

[298] K. S. Thygesen, "Calculating excitons, plasmons, and quasiparticles in 2d materials and van der waals heterostructures," *2D Materials*, vol. 4, no. 2, p. 022004, 2017.

[299] F. Hüser, T. Olsen, and K. S. Thygesen, "Quasiparticle gw calculations for solids, molecules, and two-dimensional materials," *Physical Review B*, vol. 87, no. 23, p. 235132, 2013.

[300] C. Attaccalite, M. Bockstedte, A. Marini, A. Rubio, and L. Wirtz, "Coupling of excitons and defect states in boron-nitride nanostructures," *Physical Review B*, vol. 83, no. 14, p. 144115, 2011.

[301] H. Felipe, D. Y. Qiu, and S. G. Louie, "Nonuniform sampling schemes of the brillouin zone for many-electron perturbation-theory calculations in reduced dimensionality," *Physical Review B*, vol. 95, no. 3, p. 035109, 2017.

[302] A. Malashevich, M. Jain, and S. G. Louie, "First-principles dft+ g w study of oxygen vacancies in rutile tio 2," *Physical Review B*, vol. 89, no. 7, p. 075205, 2014.

[303] W. Chen and A. Pasquarello, "Correspondence of defect energy levels in hybrid density functional theory and many-body perturbation theory," *Physical Review B*, vol. 88, no. 11, p. 115104, 2013.

[304] W. Chen and A. Pasquarello, "First-principles determination of defect energy levels through hybrid density functionals and gw," *Journal of Physics: Condensed Matter*, vol. 27, no. 13, p. 133202, 2015.

[305] W. Chen and A. Pasquarello, "Accuracy of g w for calculating defect energy levels in solids," *Physical Review B*, vol. 96, no. 2, p. 020101, 2017.

[306] M. Govoni and G. Galli, "Large scale gw calculations," *J. Chem. Theory Comput.*, vol. 11, no. 6, pp. 2680–2696, 2015.

[307] T. A. Pham, H.-V. Nguyen, D. Rocca, and G. Galli, "*gw* calculations using the spectral decomposition of the dielectric matrix: Verification, validation, and comparison of methods," *Phys. Rev. B*, vol. 87, p. 155148, 2013.

[308] S. Ismail-Beigi and T. Arias, "New algebraic formulation of density functional calculation," *Computer Physics Communications*, vol. 128, no. 1-2, pp. 1–45, 2000.

[309] T. A. Arias, M. Payne, and J. Joannopoulos, "Ab initio molecular dynamics: Analytically continued energy functionals and insights into iterative solutions," *Physical Review Letters*, vol. 69, no. 7, p. 1077, 1992.

[310] J. F. Janak, "Proof that $\frac{\partial e}{\partial n_i} = \epsilon$ in density-functional theory," *Phys. Rev. B*, vol. 18, pp. 7165–7168, 1978.

[311] F. Bruneval, "G w approximation of the many-body problem and changes in the particle number," *Physical review letters*, vol. 103, no. 17, p. 176403, 2009.

[312] G. Cassabois, P. Valvin, and B. Gil, "Hexagonal boron nitride is an indirect bandgap semiconductor," *Nat. Photonics*, vol. 10, no. 4, pp. 262–266, 2016.

[313] V. Atalla, I. Y. Zhang, O. T. Hofmann, X. Ren, P. Rinke, and M. Scheffler, "Enforcing the linear behavior of the total energy with hybrid functionals: Implications for charge transfer, interaction energies, and the random-phase approximation," *Phys. Rev. B*, vol. 94, p. 035140, 2016.

[314] T. Körzdörfer and J.-L. Bredas, "Organic electronic materials: recent advances in the dft description of the ground and excited states using tuned range-separated hybrid functionals," *Accounts of chemical research*, vol. 47, no. 11, pp. 3284–3291, 2014.

[315] S. Refaely-Abramson, S. Sharifzadeh, N. Govind, J. Autschbach, J. B. Neaton, R. Baer, and L. Kronik, "Quasiparticle spectra from a nonempirical optimally tuned range-separated hybrid density functional," *Physical review letters*, vol. 109, no. 22, p. 226405, 2012.

[316] N. Sai, P. F. Barbara, and K. Leung, "Hole localization in molecular crystals from hybrid density functional theory," *Phys. Rev. Lett.*, vol. 106, p. 226403, 2011.

[317] A. J. Cohen, P. Mori-Sánchez, and W. Yang, "Development of exchange-correlation functionals with minimal many-electron self-interaction error," *J. Chem. Phys.*, vol. 126, no. 19, p. 191109, 2007.

[318] M. Pinheiro, M. J. Caldas, P. Rinke, V. Blum, and M. Scheffler, "Length dependence of ionization potentials of transacetylenes: Internally consistent dft/gw approach," *Phys. Rev. B*, vol. 92, p. 195134, 2015.

[319] J. Ma and L.-W. Wang, "Using wannier functions to improve solid band gap predictions in density functional theory," *Scientific Reports*, vol. 6, p. 24924, 2016.

[320] V. W. Brar, M. S. Jang, M. Sherrott, S. Kim, J. J. Lopez, L. B. Kim, M. Choi, and H. Atwater, "Hybrid surface-phonon-plasmon polariton modes in graphene/monolayer h-bn heterostructures," *Nano Lett.*, vol. 14, no. 7, pp. 3876–3880, 2014.

[321] A. D. Becke, "Density-functional thermochemistry. iii. the role of exact exchange," *J. Chem. Phys.*, vol. 98, no. 7, pp. 5648–5652, 1993.

[322] J. M. Crowley, J. Tahir-Kheli, and W. A. Goddard III, "Resolution of the band gap prediction problem for materials design," *J. Phys. Chem. Lett.*, vol. 7, no. 7, pp. 1198–1203, 2016.

[323] J.-Y. Noh, H. Kim, M. Park, and Y.-S. Kim, "Deep-to-shallow level transition of re and nb dopants in monolayer mos 2 with dielectric environments," *Phys. Rev. B*, vol. 92, no. 11, p. 115431, 2015.

[324] I. Aharonovich, S. Castelletto, D. Simpson, C. Su, A. Greentree, and S. Prawer, "Diamond-based single-photon emitters," *Reports on progress in Physics*, vol. 74, no. 7, p. 076501, 2011.

[325] T. D. Ladd, F. Jelezko, R. Laflamme, Y. Nakamura, C. Monroe, and J. L. O'Brien, "Quantum computers," *Nature*, vol. 464, no. 7285, p. 45, 2010.

[326] H. Seo, M. Govoni, and G. Galli, "Design of defect spins in piezoelectric aluminum nitride for solid-state hybrid quantum technologies," *Sci. Rep.*, vol. 6, p. 20803, 2016.

[327] I. Aharonovich and E. Neu, "Diamond nanophotonics," *Advanced Optical Materials*, vol. 2, no. 10, pp. 911–928, 2014.

[328] S. Kim, J. E. Fröch, J. Christian, M. Straw, J. Bishop, D. Totonjian, K. Watanabe, T. Taniguchi, M. Toth, and I. Aharonovich, "Photonic crystal cavities from hexagonal boron nitride," *Nat. Commun.*, vol. 9, no. 1, p. 2623, 2018.

[329] X. Li, G. D. Shepard, A. Cupo, N. Camporeale, K. Shayan, Y. Luo, V. Meunier, and S. Strauf, "Nonmagnetic quantum emitters in boron nitride with ultranarrow and sideband-free emission spectra," *ACS Nano*, vol. 11, no. 7, pp. 6652–6660, 2017.

[330] A. L. Exarhos, D. A. Hopper, R. R. Grote, A. Alkauskas, and L. C. Bassett, "Optical signatures of quantum emitters in suspended hexagonal boron nitride," *ACS Nano*, vol. 11, no. 3, pp. 3328–3336, 2017.

[331] A. L. Exarhos, D. A. Hopper, R. N. Patel, M. W. Doherty, and L. C. Bassett, "Magnetic-field-dependent quantum emission in hexagonal boron nitride at room temperature," *Nat. Commun.*, vol. 10, no. 1, p. 222, 2019.

[332] L. Museur, E. Feldbach, and A. Kanaev, "Defect-related photoluminescence of hexagonal boron nitride," *Phys. Rev. B*, vol. 78, p. 155204, Oct 2008.

[333] B. Sontheimer, M. Braun, N. Nikolay, N. Sadzak, I. Aharonovich, and O. Benson, "Photodynamics of quantum emitters in hexagonal boron nitride revealed by low-temperature spectroscopy," *Phys. Rev. B*, vol. 96, p. 121202, Sep 2017.

[334] N. R. Jungwirth, B. Calderon, Y. Ji, M. G. Spencer, M. E. Flatté, and G. D. Fuchs, "Temperature dependence of wavelength selectable zero-phonon emission from single defects in hexagonal boron nitride," *Nano Lett.*, vol. 16, no. 10, pp. 6052–6057, 2016.

[335] N. R. Jungwirth and G. D. Fuchs, "Optical absorption and emission mechanisms of single defects in hexagonal boron nitride," *Phys. Rev. Lett.*, vol. 119, p. 057401, Jul 2017.

[336] G. Noh, D. Choi, J.-H. Kim, D.-G. Im, Y.-H. Kim, H. Seo, and J. Lee, "Stark tuning of single-photon emitters in hexagonal boron nitride," *Nano letters*, vol. 18, no. 8, pp. 4710–4715, 2018.

[337] K. F. Mak and J. Shan, "Photonics and optoelectronics of 2d semiconductor transition metal dichalcogenides," *Nat. Photonics*, vol. 10, no. 4, p. 216, 2016.

[338] C. Palacios-Berraquero, D. M. Kara, A. R.-P. Montblanch, M. Barbone, P. Latawiec, D. Yoon, A. K. Ott, M. Loncar, A. C. Ferrari, and M. Atatüre, "Large-scale quantum-emitter arrays in atomically thin semiconductors," *Nat. Commun.*, vol. 8, p. 15093, 2017.

[339] A. Beveratos, R. Brouri, T. Gacoin, A. Villing, J.-P. Poizat, and P. Grangier, "Single photon quantum cryptography," *Phys. Rev. Lett.*, vol. 89, p. 187901, Oct 2002.

[340] J. L. O'Brien, A. Furusawa, and J. Vučković, "Photonic quantum technologies," *Nature Photonics*, vol. 3, no. 12, p. 687, 2009.

[341] V. Scarani, H. Bechmann-Pasquinucci, N. J. Cerf, M. Dušek, N. Lütkenhaus, and M. Peev, "The security of practical quantum key distribution," *Rev. Mod. Phys.*, vol. 81, pp. 1301–1350, Sep 2009.

[342] I. Aharonovich, D. Englund, and M. Toth, "Solid-state single-photon emitters," *Nature Photonics*, vol. 10, no. 10, p. 631, 2016.

[343] T. Vogl, G. Campbell, B. C. Buchler, Y. Lu, and P. K. Lam, "Fabrication and deterministic transfer of high-quality quantum emitters in hexagonal boron nitride," *ACS Photonics*, vol. 5, no. 6, pp. 2305–2312, 2018.

[344] M. Palummo, M. Bernardi, and J. C. Grossman, "Exciton radiative lifetimes in two-dimensional transition metal dichalcogenides," *Nano Lett.*, vol. 15, no. 5, pp. 2794–2800, 2015.

[345] A. Alkauskas, B. B. Buckley, D. D. Awschalom, and C. G. Van de Walle, "First-principles theory of the luminescence lineshape for the triplet transition in diamond nv centres," *New Journal of Physics*, vol. 16, no. 7, p. 073026, 2014.

[346] L. Shi, K. Xu, and L.-W. Wang, "Comparative study of ab initio nonradiative recombination rate calculations under different formalisms," *Phys. Rev. B*, vol. 91, p. 205315, May 2015.

[347] N. P. Brawand, M. Vörös, and G. Galli, "Surface dangling bonds are a cause of b-type blinking in si nanoparticles," *Nanoscale*, vol. 7, no. 8, pp. 3737–3744, 2015.

[348] C.-H. Chang, X. Fan, S.-H. Lin, and J.-L. Kuo, "Orbital analysis of electronic structure and phonon dispersion in mos_2, $mose_2$, ws_2, and wse_2 monolayers under strain," *Phys. Rev. B*, vol. 88, p. 195420, Nov 2013.

[349] X. Peng, Q. Wei, and A. Copple, "Strain-engineered direct-indirect band gap transition and its mechanism in two-dimensional phosphorene," *Phys. Rev. B*, vol. 90, p. 085402, Aug 2014.

[350] A. Alkauskas, Q. Yan, and C. G. Van de Walle, "First-principles theory of nonradiative carrier capture via multiphonon emission," *Phys. Rev. B*, vol. 90, p. 075202, Aug 2014.

[351] H.-V. Nguyen, T. A. Pham, D. Rocca, and G. Galli, "Improving accuracy and efficiency of calculations of photoemission spectra within the many-body perturbation theory," *Phys. Rev. B*, vol. 85, p. 081101, 2012.

[352] G. D. Barmparis, Y. S. Puzyrev, X.-G. Zhang, and S. T. Pantelides, "Theory of inelastic multiphonon scattering and carrier capture by defects in semiconductors: Application to capture cross sections," *Phys. Rev. B*, vol. 92, p. 214111, Dec 2015.

[353] A. Alkauskas, J. L. Lyons, D. Steiauf, and C. G. Van de Walle, "First-principles calculations of luminescence spectrum line shapes for defects in semiconductors: The example of gan and ZnO," *Phys. Rev. Lett.*, vol. 109, p. 267401, Dec 2012.

[354] A. Alkauskas, M. D. McCluskey, and C. G. Van de Walle, "Tutorial: Defects in semiconductors—combining experiment and theory," *Journal of Applied Physics*, vol. 119, no. 18, p. 181101, 2016.

[355] F. Giustino, "Electron-phonon interactions from first principles," *Reviews of Modern Physics*, vol. 89, no. 1, p. 015003, 2017.

[356] C. H. Henry and D. V. Lang, "Nonradiative capture and recombination by multiphonon emission in gaas and gap," *Phys. Rev. B*, vol. 15, pp. 989–1016, Jan 1977.

[357] D. W. Howgate, "Calculation of nonradiative electron transition rates in a lattice-localized-electron system," *Phys. Rev.*, vol. 177, pp. 1358–1369, Jan 1969.

[358] R. Pässler, "Description of nonradiative multiphonon transitions in the static coupling scheme," *Czechoslovak Journal of Physics B*, vol. 24, no. 3, pp. 322–339, 1974.

[359] R. Pässler, "Relationships between the nonradiative multiphonon carrier-capture properties of deep charged and neutral centres in semiconductors," *physica status solidi (b)*, vol. 78, no. 2, pp. 625–635, 1976.

[360] L. Shi and L.-W. Wang, "Ab initio calculations of deep-level carrier nonradiative recombination rates in bulk semiconductors," *Phys. Rev. Lett.*, vol. 109, p. 245501, Dec 2012.

[361] D. Wickramaratne, J.-X. Shen, A. Alkauskas, and C. G. Van de Walle, "Comment on "comparative study of ab initio nonradiative recombination rate calculations under different formalisms"," *Phys. Rev. B*, vol. 97, p. 077301, Feb 2018.

[362] L. Shi, K. Xu, and L.-W. Wang, "Reply to "comment on 'comparative study of ab initio nonradiative recombination rate calculations under different formalisms' "," *Phys. Rev. B*, vol. 97, p. 077302, Feb 2018.

[363] J.-H. Yang, L. Shi, L.-W. Wang, and S.-H. Wei, "Non-radiative carrier recombination enhanced by two-level process: a first-principles study," *Sci. Rep.*, vol. 6, p. 21712, 2016.

[364] A. M. Stoneham, *Theory of Defects in Solids: Electronic Structure of Defects in Insulators and Semiconductors*. Oxford University Press, 2001.

[365] M. A. Reshchikov, "Carrier-capture characteristics of point defects in gan and zno," in *AIP Conference Proceedings*, vol. 1583, pp. 127–131, American Institute of Physics, 2014.

[366] G. Nan, X. Yang, L. Wang, Z. Shuai, and Y. Zhao, "Nuclear tunneling effects of charge transport in rubrene, tetracene, and pentacene," *Phys. Rev. B*, vol. 79, p. 115203, Mar 2009.

[367] J. Jortner, "Temperature dependent activation energy for electron transfer between biological molecules," *J. Chem. Phys.*, vol. 64, no. 12, pp. 4860–4867, 1976.

[368] R. Pässler, "Nonradiative multiphonon transitions described by static versus adiabatic coupling scheme in comparison with landau-zener's theory," *Czechoslovak Journal of Physics B*, vol. 32, no. 8, pp. 846–883, 1982.

[369] J. I. Pankove, *Optical Processes in Semiconductors*. Courier Corporation, 1975.

[370] T. Chevallier, A. Benayad, G. Le Blevennec, and F. Chandezon, "Method to determine radiative and non-radiative defects applied to AgInS2–ZnS luminescent nanocrystals," *Phys. Chem. Chem. Phys.*, vol. 19, pp. 2359–2363, 2017.

[371] Y. Hamanaka, K. Ozawa, and T. Kuzuya, "Enhancement of donor–acceptor pair emissions in colloidal agins2 quantum dots with high concentrations of defects," *J. Phys. Chem. C*, vol. 118, no. 26, pp. 14562–14568, 2014.

[372] M. R. Rosenberger, H.-J. Chuang, K. M. McCreary, C. H. Li, and B. T. Jonker, "Electrical characterization of discrete defects and impact of defect density on photoluminescence in monolayer ws2," *ACS Nano*, vol. 12, no. 2, pp. 1793–1800, 2018.

[373] L. Martínez, T. Pelini, V. Waselowski, J. Maze, B. Gil, G. Cassabois, and V. Jacques, "Efficient single photon emission from a high-purity hexagonal boron nitride crystal," *Phys. Rev. B*, vol. 94, no. 12, p. 121405, 2016.

[374] T. J. Smart, K. Li, J. Xu, and Y. Ping, "Intersystem crossing and exciton–defect coupling of spin defects in hexagonal boron nitride," *npj Computational Materials*, vol. 7, no. 1, pp. 1–8, 2021.

[375] X. Liu and M. C. Hersam, "2d materials for quantum information science," *Nat. Rev. Mater.*, vol. 4, no. 10, pp. 669–684, 2019.

[376] M. A. Feldman, A. Puretzky, L. Lindsay, E. Tucker, D. P. Briggs, P. G. Evans, R. F. Haglund, and B. J. Lawrie, "Phonon-induced multicolor correlations in hbn single-photon emitters," *Phys. Rev. B*, vol. 99, no. 2, p. 020101, 2019.

[377] D. Yim, M. Yu, G. Noh, J. Lee, and H. Seo, "Polarization and localization of single-photon emitters in hexagonal boron nitride wrinkles," *ACS Appl. Mater. Inter.*, vol. 12, no. 32, pp. 36362–36369, 2020.

[378] M. Kianinia, S. White, J. E. Fröch, C. Bradac, and I. Aharonovich, "Generation of spin defects in hexagonal boron nitride," *ACS Photonics*, vol. 7, no. 8, pp. 2147–2152, 2020.

[379] M. Turiansky, A. Alkauskas, and C. Van de Walle, "Spinning up quantum defects in 2d materials," *Nature materials*, vol. 19, no. 5, pp. 487–489, 2020.

[380] V. Ivády, I. A. Abrikosov, and A. Gali, "First principles calculation of spin-related quantities for point defect qubit research," *npj Comp. Mater.*, vol. 4, no. 1, pp. 1–13, 2018.

[381] N. L. Nguyen, N. Colonna, A. Ferretti, and N. Marzari, "Koopmans-compliant spectral functionals for extended systems," *Phys. Rev. X*, vol. 8, p. 021051, May 2018.

[382] M. Weng, S. Li, J. Zheng, F. Pan, and L.-W. Wang, "Wannier koopmans method calculations of 2d material band gaps," *J. Chem. Phys. Lett.*, vol. 9, no. 2, pp. 281–285, 2018.

[383] S. Refaely-Abramson, D. Y. Qiu, S. G. Louie, and J. B. Neaton, "Defect-induced modification of low-lying excitons and valley selectivity in monolayer transition metal dichalcogenides," *Phys. Rev. Lett.*, vol. 121, p. 167402, 2018.

[384] S. Gao, H.-Y. Chen, and M. Bernardi, "Radiative properties and excitons of candidate defect emitters in hexagonal boron nitride," *arXiv:2007.10547*, 2020.

[385] J. Xu, A. Habib, S. Kumar, F. Wu, R. Sundararaman, and Y. Ping, "Spin-phonon relaxation from a universal ab initio density-matrix approach," *Nat. Commun.*, vol. 11, no. 1, pp. 1–10, 2020.

[386] H. Seo, A. L. Falk, P. V. Klimov, K. C. Miao, G. Galli, and D. D. Awschalom, "Quantum decoherence dynamics of divacancy spins in silicon carbide," *Nat. Commun.*, vol. 7, no. 1, pp. 1–9, 2016.

[387] M. Ye, H. Seo, and G. Galli, "Spin coherence in two-dimensional materials," *npj Comp. Mater.*, vol. 5, no. 1, pp. 1–6, 2019.

[388] F. Wu, T. J. Smart, J. Xu, and Y. Ping, "Carrier recombination mechanism at defects in wide band gap two-dimensional materials from first principles," *Phys. Rev. B*, vol. 100, no. 8, p. 081407, 2019.

[389] H. Seo, H. Ma, M. Govoni, and G. Galli, "Designing defect-based qubit candidates in wide-gap binary semiconductors for solid-state quantum technologies," *Phys. Rev. Mater.*, vol. 1, no. 7, p. 075002, 2017.

[390] M. E. Turiansky, A. Alkauskas, L. C. Bassett, and C. G. Van de Walle, "Dangling bonds in hexagonal boron nitride as single-photon emitters," *Phys. Rev. Lett.*, vol. 123, no. 12, p. 127401, 2019.

[391] M. Rayson and P. Briddon, "First principles method for the calculation of zero-field splitting tensors in periodic systems," *Phys. Rev. B*, vol. 77, no. 3, p. 035119, 2008.

[392] E. M. Zolnhofer, G. B. Wijeratne, T. A. Jackson, S. Fortier, F. W. Heinemann, K. Meyer, J. Krzystek, A. Ozarowski, D. J. Mindiola, and J. Telser, "Electronic structure and magnetic properties of a titanium (ii) coordination complex," *Inorg. Chem.*, vol. 59, no. 9, pp. 6187–6201, 2020.

[393] T. T. Tran, C. Elbadawi, D. Totonjian, C. J. Lobo, G. Grosso, H. Moon, D. R. Englund, M. J. Ford, I. Aharonovich, and M. Toth, "Robust multicolor single photon emission from point defects in hexagonal boron nitride," *ACS Nano*, vol. 10, no. 8, pp. 7331–7338, 2016.

[394] A. W. Schell, H. Takashima, T. T. Tran, I. Aharonovich, and S. Takeuchi, "Coupling quantum emitters in 2d materials with tapered fibers," *ACS Photonics*, vol. 4, no. 4, pp. 761–767, 2017.

[395] M. R. Ahmadpour Monazam, U. Ludacka, H.-P. Komsa, and J. Kotakoski, "Substitutional si impurities in monolayer hexagonal boron nitride," *Appl. Phys. Lett.*, vol. 115, no. 7, p. 071604, 2019.

[396] A. Sajid and K. S. Thygesen, "Vncb defect as source of single photon emission from hexagonal boron nitride," *2D Mater.*, vol. 7, no. 3, p. 031007, 2020.

[397] F. Fuchs, J. Furthmüller, F. Bechstedt, M. Shishkin, and G. Kresse, "Quasiparticle band structure based on a generalized kohn-sham scheme," *Phys. Rev. B*, vol. 76, no. 11, p. 115109, 2007.

[398] F. Bechstedt, *Many-Body Approach to Electronic Excitations*. Springer-Verlag: Berlin, 2016.

[399] D. Rocca, Y. Ping, R. Gebauer, and G. Galli, "Solution of the bethe-salpeter equation without empty electronic states: Application to the absorption spectra of bulk systems," *Phys. Rev. B*, vol. 85, p. 045116, 2012.

[400] Y. Ping, D. Rocca, D. Lu, and G. Galli, "Ab initio calculations of absorption spectra of semiconducting nanowires within many-body perturbation theory," *Phys. Rev. B*, vol. 85, p. 035316, 2012.

[401] J. Hours, P. Senellart, E. Peter, A. Cavanna, and J. Bloch, "Exciton radiative lifetime controlled by the lateral confinement energy in a single quantum dot," *Phys. Rev. B*, vol. 71, no. 16, p. 161306, 2005.

[402] C. G. Van de Walle and J. Neugebauer, "First-principles calculations for defects and impurities: Applications to iii-nitrides," *J. Appl. Phys.*, vol. 95, no. 8, pp. 3851–3879, 2004.

[403] M. L. Goldman, A. Sipahigil, M. Doherty, N. Y. Yao, S. Bennett, M. Markham, D. Twitchen, N. Manson, A. Kubanek, and M. D. Lukin, "Phonon-induced population dynamics and intersystem crossing in nitrogen-vacancy centers," *Phys. Rev. Lett.*, vol. 114, no. 14, p. 145502, 2015.

[404] L. C. Bassett, F. J. Heremans, D. J. Christle, C. G. Yale, G. Burkard, B. B. Buckley, and D. D. Awschalom, "Ultrafast optical control of orbital and spin dynamics in a solid-state defect," *Science*, vol. 345, no. 6202, pp. 1333–1337, 2014.

[405] T. Zhong, J. M. Kindem, J. G. Bartholomew, J. Rochman, I. Craiciu, V. Verma, S. W. Nam, F. Marsili, M. D. Shaw, A. D. Beyer, *et al.*, "Optically addressing single rare-earth ions in a nanophotonic cavity," *Phys. Rev. Lett.*, vol. 121, no. 18, p. 183603, 2018.

[406] D. Wang and R. Sundararaman, "Layer dependence of defect charge transition levels in two-dimensional materials," *Phys. Rev. B*, vol. 101, no. 5, p. 054103, 2020.

[407] F. Neese, "Calculation of the zero-field splitting tensor on the basis of hybrid density functional and hartree-fock theory," *J. Chem. Phys.*, vol. 127, no. 16, p. 164112, 2007.

[408] B. S. Brunschwig, J. Logan, M. D. Newton, and N. Sutin, "A semiclassical treatment of electron-exchange reactions. application to the hexaaquoiron (ii)-hexaaquoiron (iii) system," *Journal of the American Chemical Society*, vol. 102, no. 18, pp. 5798–5809, 1980.

[409] L. Landau, "Zur theorie der energieubertragung. ii," *Physikalische Zeitschrift der Sowjetunion*, vol. 2, pp. 46–51, 1932.

[410] C. Zener, "Non-adiabatic crossing of energy levels," *Proceedings of the Royal Society of London. Series A, Containing Papers of a Mathematical and Physical Character*, vol. 137, no. 833, pp. 696–702, 1932.

[411] N. A. Deskins and M. Dupuis, "Electron transport via polaron hopping in bulk ti o 2: A density functional theory characterization," *Physical Review B*, vol. 75, no. 19, p. 195212, 2007.

[412] H. Oberhofer and J. Blumberger, "Revisiting electronic couplings and incoherent hopping models for electron transport in crystalline c 60 at ambient temperatures," *Physical Chemistry Chemical Physics*, vol. 14, no. 40, pp. 13846–13852, 2012.

[413] F. Gajdos, H. Oberhofer, M. Dupuis, and J. Blumberger, "On the inapplicability of electron-hopping models for the organic semiconductor phenyl-c61-butyric acid methyl ester (pcbm)," *The journal of physical chemistry letters*, vol. 4, no. 6, pp. 1012–1017, 2013.

[414] J. Blumberger and K. P. McKenna, "Constrained density functional theory applied to electron tunnelling between defects in mgo," *Physical Chemistry Chemical Physics*, vol. 15, no. 6, pp. 2184–2196, 2013.

[415] J. A. Weil and J. R. Bolton, *Electron paramagnetic resonance: elementary theory and practical applications*. John Wiley & Sons, 2007.

[416] V. Ivády, T. Simon, J. R. Maze, I. Abrikosov, and A. Gali, "Pressure and temperature dependence of the zero-field splitting in the ground state of nv centers in diamond: A first-principles study," *Physical Review B*, vol. 90, no. 23, p. 235205, 2014.

[417] D. Ganyushin and F. Neese, "First-principles calculations of zero-field splitting parameters," *The Journal of chemical physics*, vol. 125, no. 2, p. 024103, 2006.

[418] T. Biktagirov, W. G. Schmidt, and U. Gerstmann, "Calculation of spin-spin zero-field splitting within periodic boundary conditions: towards all-electron accuracy," *Phys. Rev. B*, vol. 97, no. 11, p. 115135, 2018.

[419] Á. Gali, "Ab initio theory of the nitrogen-vacancy center in diamond," *Nanophotonics*, vol. 8, no. 11, pp. 1907–1943, 2019.

[420] G. Davies, "The jahn-teller effect and vibronic coupling at deep levels in diamond," *Reports on Progress in Physics*, vol. 44, no. 7, p. 787, 1981.

[421] S. L. Adler, "Quantum theory of the dielectric constant in real solids," *Physical Review*, vol. 126, no. 2, p. 413, 1962.

[422] N. Wiser, "Dielectric constant with local field effects included," *Physical Review*, vol. 129, no. 1, p. 62, 1963.

[423] S. Baroni and R. Resta, "Ab initio calculation of the macroscopic dielectric constant in silicon," *Physical Review B*, vol. 33, no. 10, p. 7017, 1986.

[424] A. J. Cohen, P. Mori-Sánchez, and W. Yang, "Insights into current limitations of density functional theory," *Science*, vol. 321, no. 5890, pp. 792–794, 2008.

[425] J. Towns, T. Cockerill, M. Dahan, I. Foster, K. Gaither, A. Grimshaw, V. Hazlewood, S. Lathrop, D. Lifka, G. D. Peterson, R. Roskies, J. R. Scott, and N. Wilkins-Diehr, "Xsede: Accelerating scientific discovery," *Computing in Science and Engineering*, vol. 16, pp. 62–74, Sept.-Oct. 2014.

[426] L. Wang, T. Maxisch, and G. Ceder, "Oxidation energies of transition metal oxides within the gga+ u framework," *Physical Review B*, vol. 73, no. 19, p. 195107, 2006.

[427] T. J. Smart, M. Chen, V. Urena Baltazar, Y. Li, and Y. Ping, "Interplay of defects, dopants, and small polarons on carrier concentrations in hematite," *In Preparation*, 2021.

[428] D. Lee, V. U. Baltazar, T. J. Smart, Y. Ping, and K.-S. Choi, "Electrochemical oxidation of metal–catechol complexes as a new synthesis route to the high-quality ternary photoelectrodes: A case study of fe2tio5 photoanodes," *ACS Applied Materials & Interfaces*, vol. 12, no. 26, pp. 29275–29284, 2020.

[429] S. Shinde, R. Bansode, C. Bhosale, and K. Rajpure, "Physical properties of hematite α-Fe_2O_3 thin films: application to photoelectrochemical solar cells," *Journal of Semiconductors*, vol. 32, no. 1, p. 013001, 2011.

[430] T. Hisatomi and K. Domen, "Reaction systems for solar hydrogen production via water splitting with particulate semiconductor photocatalysts," *Nature Catalysis*, vol. 2, no. 5, pp. 387–399, 2019.

[431] G. Zhao, K. Rui, S. X. Dou, and W. Sun, "Heterostructures for electrochemical hydrogen evolution reaction: a review," *Advanced Functional Materials*, vol. 28, no. 43, p. 1803291, 2018.

[432] M. Chen, T. J. Smart, S. Wang, T. Kou, D. Lin, Y. Ping, and Y. Li, "The coupling of experiments with density functional theory in the studies of the electrochemical hydrogen evolution reaction," *Journal of Materials Chemistry A*, vol. 8, no. 18, pp. 8783–8812, 2020.

[433] E. Pastor, J.-S. Park, L. Steier, S. Kim, M. Grätzel, J. R. Durrant, A. Walsh, and A. A. Bakulin, "In situ observation of picosecond polaron self-localisation in α-Fe_2O_3 photoelectrochemical cells," *Nature Communications*, vol. 10, no. 1, pp. 1–7, 2019.

[434] A. Pu, J. Deng, M. Li, J. Gao, H. Zhang, Y. Hao, J. Zhong, and X. Sun, "Coupling ti-doping and oxygen vacancies in hematite nanostructures for solar water oxidation with high efficiency," *Journal of Materials chemistry A*, vol. 2, no. 8, pp. 2491–2497, 2014.

[435] A. Annamalai, A. Subramanian, U. Kang, H. Park, S. H. Choi, and J. S. Jang, "Activation of hematite photoanodes for solar water splitting: effect of fto deformation," *The Journal of Physical Chemistry C*, vol. 119, no. 7, pp. 3810–3817, 2015.

[436] K. Atkinson, R. W. Grimes, M. R. Levy, Z. L. Coull, and T. English, "Accommodation of impurities in α-al2o3, α-cr2o3 and α-fe2o3," *Journal of the European Ceramic Society*, vol. 23, no. 16, pp. 3059–3070, 2003.

[437] I. Ayub, F. J. Berry, R. L. Bilsborrow, Ö. Helgason, R. C. Mercader, E. A. Moore, S. J. Stewart, and P. G. Wynn, "Influence of zinc doping on the structural and magnetic properties of α-Fe_2O_3," *Journal of Solid State Chemistry*, vol. 156, no. 2, pp. 408–414, 2001.

[438] F. J. Berry, A. Bohórquez, and E. A. Moore, "Rationalisation of defect structure of tin-and titanium-doped α-Fe_2O_3 using interatomic potential calculations," *Solid State Communications*, vol. 109, no. 3, pp. 207–211, 1998.

[439] X. Lu, Y. Zeng, M. Yu, T. Zhai, C. Liang, S. Xie, M.-S. Balogun, and Y. Tong, "Oxygen-deficient hematite nanorods as high-performance and novel negative electrodes for flexible asymmetric supercapacitors," *Advanced Materials*, vol. 26, no. 19, pp. 3148–3155, 2014.

[440] T. Jiang, F. Bu, X. Feng, I. Shakir, G. Hao, and Y. Xu, "Porous fe2o3 nanoframeworks encapsulated within three-dimensional graphene as high-performance flexible anode for lithium-ion battery," *ACS Nano*, vol. 11, no. 5, pp. 5140–5147, 2017.

[441] A. L. Ankudinov and J. Rehr, "Relativistic calculations of spin-dependent x-ray-absorption spectra," *Physical Review B*, vol. 56, no. 4, p. R1712, 1997.

[442] C. H. Booth, *R-Space X-ray Absorption Package*, 2010. http://lise.lbl.gov/RSXAP.

[443] E. A. Stern, "Number of relevant independent points in x-ray-absorption fine-structure spectra," *Physical Review B*, vol. 48, p. 9825, 1993.

[444] W. H. McMaster, *Compilation of X-ray Cross Sections*. UCRL-50174 Sec. II, Rev. 1, Berkeley: Lawrence Radiation Laboratory, University of California, 1969. url=http://books.google.com/books?id=8VHzmgEACAAJ.

[445] A. Schleife, M. D. Neumann, N. Esser, Z. Galazka, A. Gottwald, J. Nixdorf, R. Goldhahn, and M. Feneberg, "Optical properties of in2o3 from experiment and first-principles theory: influence of lattice screening," *New Journal of Physics*, vol. 20, p. 053016, may 2018.

[446] S. Angelov, E. Zhecheva, R. Stoyanova, and M. Atanasov, "Bulk defects in Co_3O_4, pure and slightly doped with lithium, revealed by epr of the tetrahedral Co^{2+} ions," *Journal of Physics and Chemistry of Solids*, vol. 51, no. 10, pp. 1157–1161, 1990.

[447] D. Wood and J. Remeika, "Optical absorption of tetrahedral Co^{3+} and Co^{2+} in garnets," *The Journal of Chemical Physics*, vol. 46, no. 9, pp. 3595–3602, 1967.

[448] S. B. Cho, E. S. Sim, and Y.-C. Chung, "Elucidating the unintentional p-type nature of spinel Co_3O_4: A defect study using ab-initio calculation," *Journal of the European Ceramic Society*, vol. 38, no. 2, pp. 629–635, 2018.

[449] P. Liao and E. A. Carter, "Testing variations of the gw approximation on strongly correlated transition metal oxides: Hematite (α-Fe_2O_3) as a benchmark," *Physical Chemistry Chemical Physics*, vol. 13, no. 33, pp. 15189–15199, 2011.

[450] J. H. Kim and J. S. Lee, "$BiVO_4$-based heterostructured photocatalysts for solar water splitting: A review," *Energy and Environment Focus*, vol. 3, no. 4, pp. 339–353, 2014.

[451] A. A. Ismail and D. W. Bahnemann, "Photochemical splitting of water for hydrogen production by photocatalysis: A review," *Solar Energy Materials and Solar Cells*, vol. 128, pp. 85–101, 2014.

[452] M. Ni, M. K. Leung, D. Y. Leung, and K. Sumathy, "A review and recent developments in photocatalytic water-splitting using TiO_2 for hydrogen production," *Renewable and Sustainable Energy Reviews*, vol. 11, no. 3, pp. 401–425, 2007.

[453] N. Mendelson, D. Chugh, T. S. Cheng, A. Gottscholl, H. Long, C. J. Mellor, A. Zettl, V. Dyakonov, P. H. Beton, S. V. Novikov, *et al.*, "Identifying carbon as the source of visible single photon emission from hexagonal boron nitride," *arXiv:2003.00949*, 2020.

[454] T. Biktagirov and U. Gerstmann, "Spin-orbit driven electrical manipulation of the zero-field splitting in high-spin centers in solids," *Phys. Rev. Research*, vol. 2, no. 2, p. 023071, 2020.

[455] J. Loubser and J. van Wyk, "Electron spin resonance in the study of diamond," *Rep. Prog. Phys.*, vol. 41, no. 8, p. 1201, 1978.

[456] B. C. Rose, G. Thiering, A. M. Tyryshkin, A. M. Edmonds, M. L. Markham, A. Gali, S. A. Lyon, and N. P. de Leon, "Strongly anisotropic spin relaxation in the neutral silicon vacancy center in diamond," *Phys. Rev. B*, vol. 98, no. 23, p. 235140, 2018.

[457] W. Kirmse, *Carbene Chemistry*, vol. 1. Elsevier, 2013.

[458] R. W. Godby and R. Needs, "Metal-insulator transition in kohn-sham theory and quasiparticle theory," *Phys. Rev. Lett.*, vol. 62, no. 10, p. 1169, 1989.

[459] A. Oschlies, R. Godby, and R. Needs, "Gw self-energy calculations of carrier-induced band-gap narrowing in n-type silicon," *Phys. Rev. B*, vol. 51, no. 3, p. 1527, 1995.

[460] C. A. Rozzi, D. Varsano, A. Marini, E. K. Gross, and A. Rubio, "Exact coulomb cutoff technique for supercell calculations," *Phys. Rev. B*, vol. 73, no. 20, p. 205119, 2006.

[461] H.-Y. Chen, D. Sangalli, and M. Bernardi, "Exciton-phonon interaction and relaxation times from first principles," *Phys. Rev. Lett.*, vol. 125, no. 10, p. 107401, 2020.

[462] G. Thiering and A. Gali, "Theory of the optical spin-polarization loop of the nitrogen-vacancy center in diamond," *Phys. Rev. B*, vol. 98, no. 8, p. 085207, 2018.

[463] G. B. Wijeratne, E. M. Zolnhofer, S. Fortier, L. N. Grant, P. J. Carroll, C.-H. Chen, K. Meyer, J. Krzystek, A. Ozarowski, T. A. Jackson, *et al.*, "Electronic structure and reactivity of a well-defined mononuclear complex of ti (ii)," *Inorg. Chem.*, vol. 54, no. 21, pp. 10380–10397, 2015.

[464] Ò. Àrias, K. Brandhorst, D. Baabe, M. Freytag, P. G. Jones, and M. Tamm, "Formation of paramagnetic metallacyclobutadienes by reaction of diaminoacetylenes with molybdenum alkylidyne complexes," *Dalton T.*, vol. 46, no. 14, pp. 4737–4748, 2017.

[465] X. Bu, Y. Gao, S. Zhang, and Y. Tian, "Amorphous cerium phosphate on p-doped fe2o3 nanosheets for efficient photoelectrochemical water oxidation," *Chemical Engineering Journal*, vol. 355, pp. 910–919, 2019.